

University of Strathclyde

Department of Electronic and Electrical Engineering

**Calibration and Design of UHF Partial Discharge Sensors
using
Finite-Difference Time-Domain Modelling**

by

Asnor Mazuan bin Ishak

A thesis presented in fulfilment of the requirements for the degree of
Doctor of Philosophy

2013

COPYRIGHT DECLARATION

This thesis is the result of the author's original research. It has been composed by the author and has not been previously submitted for examination which has led to the award of a degree.

The copyright of this thesis belongs to the author under the terms of the United Kingdom Copyright Acts as qualified by University of Strathclyde Regulation 3.50. Due acknowledgement must always be made of the use of any material contained in, or derived from, this thesis.

Signed:

Date: 25/11/13

ACKNOWLEDGMENTS

Firstly, I would like to acknowledge my supervisor, Prof. Martin D. Judd for his remarkable and excellent support. His encouragement has helped me through solving difficult problems during my research. I am also grateful to my colleagues in the High Voltage Technologies Group who like to share and exchange ideas in improving my experimental and simulated results.

Many thanks to my financial support, Ministry of Higher Education Malaysia and Universiti Pertahanan Nasional Malaysia (UPNM) who are taking care of my welfare over the years.

Finally, a special thanks to my family for their guidance and patience toward completing this thesis. I would like to dedicate this thesis to them.

ABSTRACT

Electric power supply involves three main stages which are generation, transmission and distribution. Properly maintained electrical equipment at each stage can assure the supply is continuous at all time to customers and it is important for safety requirements where fire and explosion accidents can be eliminated. The electrical equipment includes generators, motors, power transformers and switchgear. Electrical discharges (small sparks) which usually occur in defective insulation system of electrical equipment can cause equipment failure or even explosion if the discharges are not detected and treated in an appropriate time. The discharges generate electromagnetic waves which can be detected using ultra-high frequency (UHF) sensors. A lot of research have been done to design effective and low cost UHF sensors for different applications in high voltage systems. UHF sensor manufacturers are required to meet certain sensitivity standards so that the sensors are able to detect the minimum level of discharges and at certain frequency range. Manufacturers will fabricate a new sensor and then measure the sensitivity of the sensor using a calibration system. If the sensor does not achieve the minimum sensitivity standard, manufacturers will fabricate another one after changing certain parameters of the sensor that could improve the response and then the sensor will be characterised again. This repetitive and expensive process can be eliminated using numerical electromagnetic simulation to design and calibrate the sensor. Finite-difference time-domain (FDTD) method is a computational technique that can be used to design UHF sensors and predict the sensitivity of the sensors. In this study, a calibration system was modelled using FDTD technique to predict the responses of several existing UHF partial discharge sensors. The simulated calibration system was simplified to overcome the complex design of the experimental calibration system. However, the main function of the system was retained in the simulation. The performance of the simulated calibration system was validated by comparing the experimental responses of physical sensors with the simulated results. The percentage difference between the measured and simulated responses of the existing sensors is 7.65% on absolute average with standard deviation of 2.99. The factors that affect the responses of the sensors for examples, the electrical property of insulating materials and sensor sizes have been studied using this method. A new UHF partial discharge sensor was designed and modelled using FDTD

simulation and then fabricated for testing. The measured and simulated responses of the sensor showed good agreement. Design variations of the same sensor were simulated to improve the sensor response. Then, the optimum simulated response and simplest design to manufacture was chosen as the final design of the sensor. The experimental and simulated results of the sensor also showed excellent agreement. The FDTD method can also study the characteristics of electromagnetic wave propagation generated by PD source in power transformer.

ACRONYMS

FDTD	Finite-difference time-domain
FFT	Fast Fourier transform
GIS	Gas insulated substation
GIT	Gas insulated transformer
GTEM	Gigahertz transverse electromagnetic
HV	High voltage
HFCT	High frequency current transformer
PD	Partial discharge
PDIV	Partial discharge inception voltage
PEC	Perfect electric conductor
PML	Perfectly matched layer
PTFE	Polytetrafluoroethylene
PVC	Polyvinylchloride
TEM	Transverse electromagnetic
UHF	Ultra-high frequency

TABLE OF CONTENTS

Chapter 1: Introduction.....	1
1.1 Field of Research.....	1
1.2 Overview of the Thesis.....	2
1.3 Summary of Novel Contributions.....	5
1.4 Published Papers.....	6
Chapter 2: Partial Discharges in High Voltage Systems	7
2.1 Introduction of Partial Discharges.....	7
2.1.1 Partial Discharge Mechanisms.....	10
2.1.1.1 Gas Discharges.....	10
2.1.1.2 Liquid Discharges.....	11
2.1.1.3 Solid Discharges.....	12
2.1.2 Types of Partial Discharges.....	12
2.2 Types of Partial Discharge Detection.....	14
2.2.1 Motivation for PD Detection.....	14
2.2.2 Conventional Partial Discharge Detection.....	14
2.2.3 Unconventional Partial Discharge Detection.....	17
2.2.3.1 Chemical Partial Discharge Detection.....	17
2.2.3.2 Acoustic Partial Discharge Detection.....	26
2.2.3.3 Electromagnetic Partial Discharge Detection.....	29
2.3 Conclusion.....	34
Chapter 3: Ultra High Frequency (UHF) Partial Discharge Detection	35
3.1 UHF Partial Discharge Sensors for GIS Application.....	35

3.2	UHF Partial Discharge Sensors for High Voltage Transformer Application	45
3.3	Conclusion.....	51
Chapter 4: UHF Partial Discharge Sensor Calibration.....		52
4.1	Assessing the Sensitivity of UHF Sensors.....	52
4.2	Double Cone GIS System	56
4.2.1	The Model of UHF PD Sensor as a Capacitor	59
4.2.2	The Model of UHF PD Sensor as an Antenna	61
4.3	Monopole Cone Calibration System.....	64
4.4	TEM Calibration of UHF Partial Discharge Sensors	66
4.5	Conclusion.....	72
Chapter 5: GTEM Calibration of UHF Partial Discharge Sensors		74
5.1	The Structures of Calibration Cell.....	75
5.2	The Parameters of Incident Step Excitation.....	77
5.3	Laboratory Calibration of UHF Partial Discharge Sensors using GTEM cell....	78
5.4	Conclusion.....	88
Chapter 6: FDTD Modelling of Electromagnetic Waves.....		89
6.1	Introduction of FDTD Method.....	89
6.2	Partial Discharge Propagation in Transformer using FDTD Method.....	96
6.3	Predicting Frequency Responses of UHF PD Sensors using FDTD Method ...	105
6.4	Study of Factors that Affect the Sensitivity of UHF PD Sensors	116
6.4.1	Relative Permittivity of Dielectric Materials	117
6.4.2	Geometry of the Sensors	118
6.5	Conclusion.....	121

Chapter 7: Development of a Novel UHF PD Sensor using FDTD Simulation	122
7.1 Modelling a Novel External Disc-Type UHF PD Sensor.....	122
7.2 Fabricating a Novel Disc-Type UHF PD Sensor	128
7.3 Improving the Novel External Disc-Type UHF PD Sensor.....	135
7.3.1 Different Relative Permittivity of Half-Nylon Part.....	135
7.3.2 Four Earth Rods.....	138
7.4 Frequency Response Analysis of the Improved Design Sensor.....	145
7.5 Simulated Calibration System and Parallel Plates Application	149
7.6 Conclusion.....	154
8. Conclusions.....	156
9. Future Works.....	159
Appendices	160
Appendix 1	169
Appendix 2	169
Appendix 3	174
References	175

Chapter 1: Introduction

1.1 Field of Research

The first application of ultra-high frequency (UHF) partial discharge (PD) sensors was to detect and locate defects in gas insulated substation (GIS). Recently, UHF sensors have been used in PD diagnosis for power transformers. A lot of researchers and manufacturers design effective UHF PD sensors for the application of power transformers. The general types of UHF sensors that can detect electromagnetic waves from PD sources are disc, spiral, monopole and probe types. Designing sensors for specific applications currently involves repetitive manufacturing and testing stages with the aim to achieve the desired target or output. These processes can be reduced or eliminated by modelling, testing and optimising the design of UHF sensors using high performance software.

The objectives of this research are to:

- Study the application of finite-difference time-domain (FDTD) high frequency electromagnetic methods in modelling and calibrating UHF PD sensors.
- Model the existing structures in the laboratory which are the gigahertz transverse electromagnetic (GTEM) calibration cell that been used to measure the responses of UHF PD sensors such as 25 mm reference monopole probe, experimental disc-type PD sensor, monopole-type PD sensor and conventional disc-type PD sensor using FDTD method.
- Compare the simulated frequency responses of the sensors with the experimental results to assess accuracy of the modelling approach.
- Investigate the effect of relative permittivity of insulating materials and geometry of the sensors on the sensitivities of UHF PD sensors, through various parametric studies.

- Design an entirely new external disc-type UHF PD sensor using the FDTD method and then fabricate the sensor. The simulated and experimental responses of the sensor will be compared and discussed. The effects of the rotational positions of sensor output connector with respect to the arriving electromagnetic signal and dielectric part of the disc sensor on the sensitivity will be explained.

1.2 Overview of the Thesis

Partial discharge (PD) is a type of localised electrical discharge due to transient ionisation in an insulation system when the electric field level exceeds a certain critical value that depends on the material properties. The insulation system of high voltage equipment (switchgear, power cables, motors, generators and power transformers) could have PD because of manufacturing defects, installation defects, over-current, contaminants, ageing and others. It is important to maintain and monitor the PD levels in order to have continued power supply to the customers. It is a challenge to all electrical diagnostic engineers to locate the source of PD in high voltage equipment. UHF PD sensors are very effective and helpful devices to detect and locate PD sources in high voltage equipment.

This thesis describes the modelling of UHF PD sensors and their associated calibration system using an electromagnetic FDTD method. The work described in this thesis is presented in six chapters, as below:

Chapter 1: This thesis begins by describing the objectives of the research and its novel contributions. The published papers based on this research are listed which consist of an IEEE journal paper and 5 conference papers.

Chapter 2: Starts by explaining the meaning of PD followed by an outline of its mechanisms and the basic types of PD. The conventional PD measurement is described where a measuring instrument is coupled to the PD source through direct electrical circuit connection. Unconventional PD measurements are briefly summarised that involve chemical, acoustic and electromagnetic PD measurement. Sensors used to detect PD level

in unconventional PD measurement are often not connected physically to the unit being tested.

Chapter 3: This chapter is devoted to an introduction of different types of UHF PD sensors for GIS application and high voltage transformer application. Essentially, there are two families of UHF PD sensors, which are internal-type sensor and external-type sensor. The location of PD sources and defect types in high voltage equipment can be predicted using the UHF PD sensors.

Chapter 4: Calibration schemes for UHF PD sensors are reported. A general overview of three types of UHF sensor calibration systems is provided, namely: double cone GIS system, cone calibration system, and opened transverse electromagnetic (TEM) calibration cell. These calibration systems are exposed to reflected signal and external noise from surrounding environment. This chapter also explained that UHF PD sensor is better represented as an antenna than capacitive sensor.

Chapter 5: The operation of an enclosed TEM (gigahertz transverse electromagnetic, GTEM) calibration cell is discussed. This system can eliminate the reflected signal by applying time-domain gating to the output voltage (in time-domain) of the sensors. The responses of four existing sensors are experimentally measured using the GTEM calibration system.

Chapter 6: The FDTD method and the application of FDTD techniques in simulating PD signals in power transformer are explained at the beginning of this chapter. A simplified calibration system is modelled using FDTD software that represents GTEM calibration system. The predicted response of existing sensor designs using XFDTD software and the factors that affect these responses are presented. At the end of this chapter, the experimental and simulated results of sensor responses are discussed. Since the percentage difference between the experimental and simulated results of the existing sensors is small, the validity of the modelling technique is established.

Chapter 7: Lastly, this chapter is focused on designing a novel external disc-type UHF PD sensor using FDTD method. The sensor was fabricated based on the designed

modelling which predicts the highest sensitivity. Horizontal position of the output voltage connection indicates the better position with higher sensor response compared with the vertical position of the output connection. The same sensor was further improved in terms of its frequency response and directionality. Adding four earth rods between the sensor disc and the cover increases the response and even improves the mechanical strength of the sensor. At the last section, the effects of parallel-plates calibration system are investigated. Sensor responses of UHF PD sensors measured using GTEM calibration system are not suitable to be predicted using parallel plates calibration system as the percentage differences are higher.

UHF PD sensors are useful to detect and locate PD sources in the insulation system of high voltage equipment. Different types of PD sources can be predicted using pattern recognition of the measured PD signals. One of the methods to calibrate the sensors is by using experimental GTEM calibration system where the system can be simulated using electromagnetic FDTD method. The measured and simulated responses of the sensors demonstrate that the FDTD method is an effective tool to model and calibrate the sensors. A novel external disc-type UHF PD sensor was modelled entirely using the FDTD technique. The technique offers the capability of designing UHF PD sensors effectively by choosing the best simulated parameters for the sensors such as the effective size of the sensors and the cheapest dielectric materials. Comparing alternative types of numerical methods is important to understand the modelling benefit of certain system.

1.3 Summary of Novel Contributions

In the process of conducting the research, some novel contributions have been accomplished, which are listed below:

- Incorporating models of UHF PD sensors into FDTD simulations is novel in that the output is a predicted voltage that can be compared directly with experimental measurements with minor error. Modelling a calibration system using FDTD method which is used to accurately simulate the time-domain and frequency-domain responses of UHF PD sensors. The sloped modelling of a calibration cell and localised meshing improve the simulated results of the sensors.
- Designing using FDTD method and validating the simulated calibration system by testing the response of a novel external disc-type UHF PD sensor.
- The relative permittivity of insulating materials, the geometry of UHF PD sensors and the orientation of the sensor can influence the average sensitivities of the sensors in predictable ways using FDTD method.
- Modelling a power transformer tank using FDTD technique to study the characteristics of electromagnetic wave propagation generated by PD source.

Due to high performance of computational system nowadays, simulating a sensor calibration system is possible which only takes a few minutes. Modelling UHF PD sensors using the FDTD technique will be a valuable design tool to improve sensor response, speed up the design process, reduce the cost of fabricating a new sensor, and allow for installation in a wider range of high voltage equipment.

1.4 Published Papers

During the study, a journal paper (see Appendix 1) and 5 conference papers have been published which related to the understanding of FDTD modelling for PD detection system. The details of the papers are listed below:

Journal Paper

1. A. M. Ishak, P. C. Baker, W. H. Siew, and M. D. Judd, “Characterizing the Sensitivity of UHF Partial Discharge Sensors using FDTD Modeling”, *IEEE Sensors Journal*, vol. 13, pp. 3025 – 3031, Aug. 2013.

Conference Papers

2. A. M. Ishak, M. D. Judd, and W. H. Siew, “Validating the Response of UHF Partial Discharge Sensor Using FDTD Method”, *Progress In Electromagnetics Research Symposium (PIERS)*, Taipei, Mar. 25th-28th, 2013.
3. A. M. Ishak, M. D. Judd, W. H. Siew, and P. C. Baker, “Evaluation of FDTD Modelling as a Tool for Predicting the Response of UHF Partial Discharge Sensors”, *IEEE International Symposium on Electrical Insulation (ISEI)*, San Juan, Puerto Rico, Jun. 10th – 13th, 2012.
4. A. M. Ishak, M. D. Judd, and W. H. Siew, “Simulated and Measured Frequency Response of Disc-Type UHF Partial Discharge Sensors”, *Universities High Voltage Network (UHVnet) Colloquium*, University of Leicester, Jan. 18th – 19th, 2012.
5. A. M. Ishak, M. D. Judd, and W. H. Siew, “Full Wave Modelling of Partial Discharge Phenomena in Power Transformers using FDTD Methods”, *Universities High Voltage Network (UHVnet) Colloquium*, Winchester, Jan. 18th – 19th, 2011.
6. A. M. Ishak, M. D. Judd and W. H. Siew, “A Study of UHF Partial Discharge Signal Propagation in Power Transformers using FDTD Modelling”, *Proceedings of the 45th International Universities’ Power Engineering Conference (UPEC)*, Cardiff, Wales, UK, Aug. 31st – Sept. 3rd, 2010.

Chapter 2: Partial Discharges in High Voltage Systems

Small electrical sparks that occur in the insulation system of high voltage equipment are known as partial discharges. Partial Discharge (PD) levels are important indicators in electrical testing and monitoring of high voltage equipment. They can be used to evaluate the integrity of equipment insulation. Therefore, it is important to observe the general information on PD such as (i) the characteristics of PD activities, (ii) the mechanisms of PDs that can occur in different types of insulating media such as gas, liquid and solid insulating materials, (iii) types of PDs, and (iv) methods to detect the occurrence of PDs, for example, conventional detection and unconventional detection.

2.1 Introduction of Partial Discharges

There are progressive increases in the demand to reduce maintenance costs of power utility companies, maximize the life span of electrical equipment and decrease the unplanned outage events. The condition of high voltage electrical apparatus can be related to the insulation condition. The occurrence of defects in the insulation system can drastically degrade the insulation properties. The degradation is usually because of aging processes caused by electrical, thermal and mechanical stresses. But sometimes, it is also because of manufacturing defects and installation deficiencies.

Partial discharge (PD) is a localized electric discharge that only partially bridges the insulation system resulting from ionization when the electric field stress exceeds the dielectric strength [1]. Although the amplitude of the discharges is usually small, they can cause progressive deterioration and lead to equipment failure.

The apparent charge (Q) of PD is expressed in coulombs, usually in the picocoulombs (pC) range. The charge is measured when PDs are first observed in the test object at the lowest applied voltage which also known as partial discharge inception voltage (PDIV) [2]. IEC 61294 stated that PDIV of an insulating liquid occurs when PD charge equals to or exceeding 100 pC for a specific test geometry [3]. The PDIV measurement was done

based on specific test cell arrangement such as needle-sphere configuration, 3 μm radius of needle tip, and electrode gap of 50 ± 1 mm. The magnitude of PD charges and PDIVs can vary experimentally depending on the arrangement of the test objects, the types of insulating materials and others. Pattanadech [4] investigated PD characteristics in mineral oil using needle-plane and needle-sphere electrode arrangements, as shown in Figure 2.1. The measured PD charges were more than 200 pC but dependent on the tip radius of the needles and electrode configurations. The charge quantities and PDIV values increased as the needle tip radii were increased from 10 μm to 40 μm , as shown in Table 2.1. It was also shown that needle-sphere configuration gave higher value of PD charges and PDIVs than needle-plane configuration. Pompili [5] reported that PD charges can also be measured below 100 pC at applied voltage of 30 kV in three different dielectric liquids for liquid filled transformer which are natural ester, synthetic ester, and mineral oil. The needle-plane electrode system with 30 mm spacing between them and needle tip radius of 20 μm were used to generate the PD source. PD charge is also measured using the maximum apparent charge for a selected time interval of applied voltage [6]. The detected pulse discharge has a short rise time, in nanosecond (ns) range [7], and its frequency spectrum may range between kilohertz (kHz) and gigahertz (GHz) range. For example, the frequency range of PD signals in transformer oil is between 400 MHz and 800 MHz [8]. These studies demonstrate that the measurement of PD apparent charge can be influenced by (i) test cell arrangement such as the types of electrodes, electrode gaps and the diameters of electrodes; and different types of insulating materials such as natural ester, synthetic ester and mineral oil.

During the operation of electrical equipment, electric arc may take place in insulation system due to insulation defects or voltage impulses from lightning and switching operations. The arc appearance may degrade the performance of the insulation system and lead to insulation failures. The next section describes generally the breakdown mechanism in the insulation system; types of partial discharges; and PD measurement.

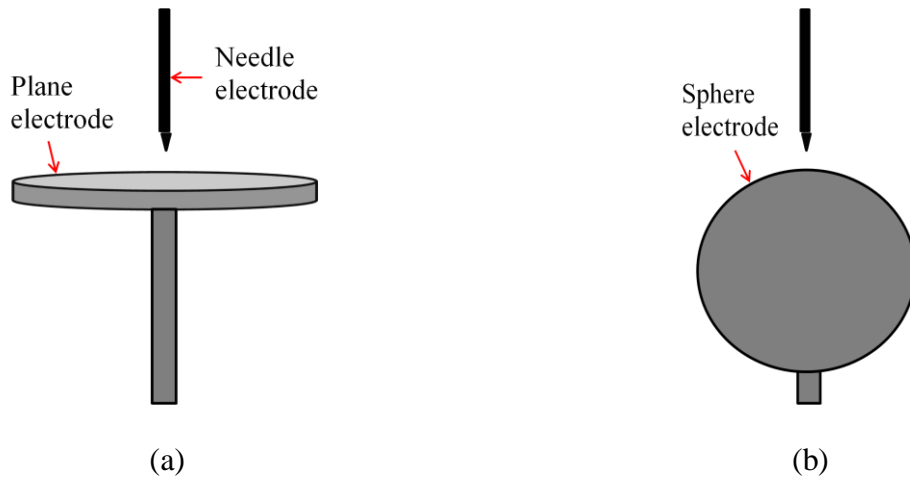


Figure 2.1: Electrode configurations: (a) needle-plane electrode and (b) needle-sphere electrode.

Table 2.1

The measured PDIV values and PD charges of the electrode systems in mineral oil [4].

Needle tip radius (μm)	Grounded electrode		PDIV (kV)	PD charge (pC)
10	Plane diameter (mm)	50.0	35.9	255
		75.0	36.3	286
	Sphere diameter (mm)	50.8	42.4	315
		76.2	37.2	311
20	Plane diameter (mm)	50.0	39.0	314
		75.0	40.2	360
	Sphere diameter (mm)	50.8	45.3	365
		76.2	41.0	383
40	Plane diameter (mm)	50.0	48.6	539
		75.0	48.1	561
	Sphere diameter (mm)	50.8	> 50.0	> 550
		76.2	48.6	568

2.1.1 Partial Discharge Mechanisms

PD mechanisms can lead to the failure of dielectric materials due to the generation of a conducting channel across the insulation. In electrical breakdown, a sufficiently high electric field and free electron, ion or foreign particles are the important initiating agents for PD. PD mechanisms can occur in gas, liquid and solid dielectrics.

2.1.1.1 Gas Discharges

Townsend [9] conducted experiments on the growth of electric currents between two parallel electrodes which then led to gas breakdown. He discovered that the current initially increases proportional to the applied direct voltage and then remains about constant at saturated current level, I_S . At higher voltage, the current increases above the saturated level at an exponential rate, as depicted in Figure 2.2, until breakdown occurs. The current increases exponentially due to ionisation of the gas by electron collision. As uniform electric field increases, more free electrons are emitted and then accelerated. This causes more collisions occur between electrons and gas molecules which then electron multiplication happens causing avalanche.

PD phenomena in gas (air) has been explained by Barbieri [10] where the propagation of the discharges can be clearly observed through a sample transparent dielectric. Okubo [11] investigated gas discharge characteristics with different electrode configurations for 15 mm electrode gap in gas chamber. Helium (He) and argon (Ar) gases were used as they are significant residual gases in space environment. Needle-plane configuration generated the highest electric field distribution along vacuum electrode gap, followed by rod-plane, cone-plane, and sphere-plane configurations. PDIV magnitudes in He and Ar gases varied with pressure. The PDIV levels decrease between the gas pressure range of 1 Pa and 100 Pa, and then the levels increase between 100 Pa and 100 kPa. Mizuno [12] studied the breakdown voltages of a rubber covered rod in air chamber which is possible to replace bare conductor in GIS tank. The breakdown voltage of the covered rod in air chamber can reach about 8.5 kV/mm, compared with the breakdown voltage of SF₆ gas, 8.9 kV/mm [13].

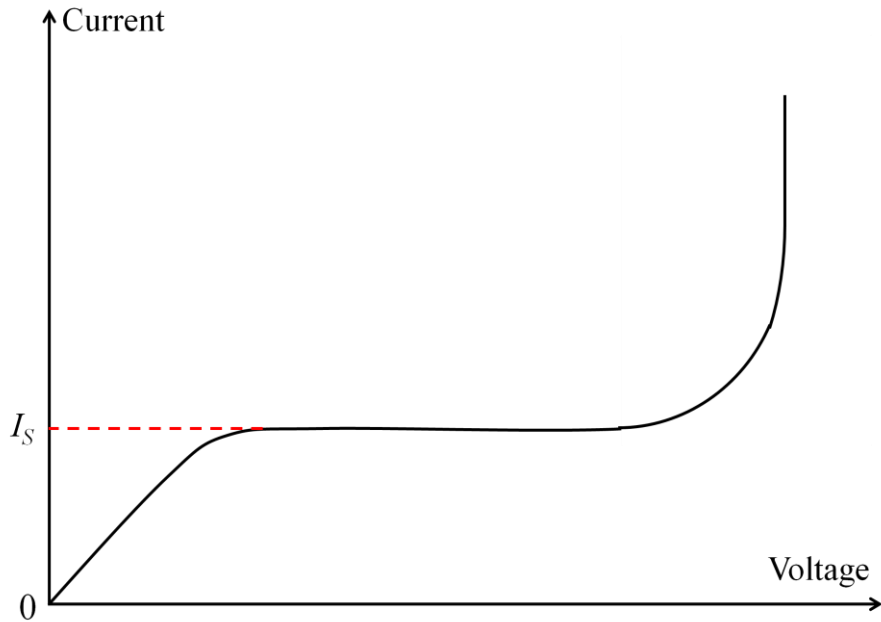


Figure 2.2: The voltage-current relationship in gas breakdown mechanism where I_s is the saturated current (after [9]).

2.1.1.2 Liquid Discharges

PD mechanism in liquid can be explained based on avalanche ionisation by electron collision which is an extension of gaseous breakdown mechanism; and the presence of foreign particle in liquid insulation [9]. Free electrons are emitted and accelerated in highly purified liquid with the applied uniform field till avalanche multiplication occurs. The foreign particles in liquid dielectric can enhance electric field strength and cause perturbations in the uniform field. Then, the impurities will align in a bridge which can lead to electrical breakdown in liquid dielectric. The occurrence of voids, cavities or gaseous bubbles as impurities in the insulating liquids, which may have lower breakdown strength, can also trigger electrical breakdown in liquids.

Suwarno [14] investigated PD mechanism in silicone oil (synthetic insulating oil) using needle-plane electrode system. The maximum value of PD charges concentrated at the peak of the sinusoidal applied voltage. Yi [15] experimentally showed that the PDIV

values for two different transformer fluids were about the same, namely synthetic ester (17.5 kV) and natural ester (18.3 kV). However, PD charges above the PDIV values were significantly different with the highest charges detected in synthetic ester and followed by natural ester.

2.1.1.3 Solid Discharges

There are always electron traps in solids due to the presence of impurities. Under high electric field stress, electrons can trap in solid materials prior to breakdown. Electrical breakdown in solid materials can also be due to thermal instability. Thermal breakdown occurs if heating continuously generated due to electron injection and multiplication in the insulating solids. Temperature increase within the dielectric solids causes increased number of ionic charges. As a result, chemical degradation or physical melting of the insulation leads to electrical breakdown in solid materials [9].

The presence of voids in epoxy resin as solid dielectric has been proved to be the source of PD generation. Hikita [16] explained theoretically that larger void size in epoxy resin caused higher PD charge level. This was supported experimentally where 2.4 mm diameter of void in epoxy resin produced higher PD charge amplitude than 1.0 mm diameter of void [17]. PDIV decreased with the increase of void diameters in solid dielectrics as described theoretically by Nosseir [18] and experimentally by Adhikari [19].

2.1.2 Types of Partial Discharges

Partial discharges are mostly produced at the degraded location of dielectric materials in combination with sufficiently high electric field. There are three main types of PDs based on their location and mechanism [20]. They are internal discharge, surface discharge and corona discharge.

Internal discharges occur in the small cavities of solid or liquid dielectric materials, as depicted in Figure 2.3 (a). The gas or oil inside the inclusions or voids will be ionised

with the presence of high and ground potential between them. Then, electrical discharges will be developed inside these voids and cause electrical breakdown in the dielectric materials.

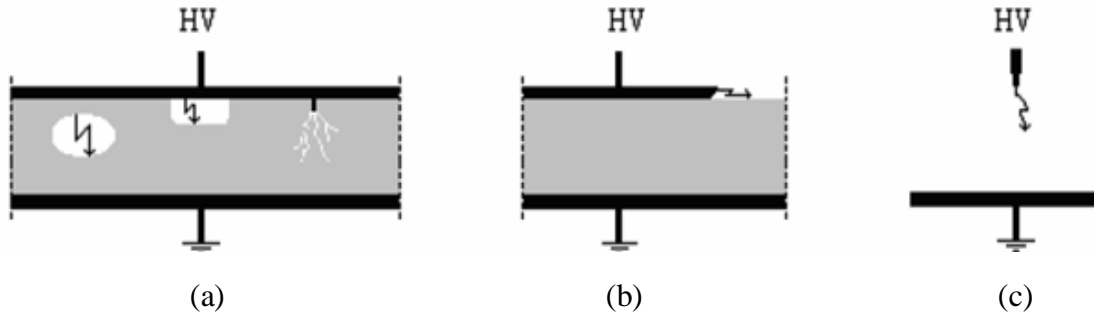


Figure 2.3: The classifications of partial discharge: (a) internal discharge (void, metal discharge and treeing), (b) surface discharge, and (c) corona discharge.

Surface discharge can occur when an electric field stress component is parallel to a dielectric surface, as shown in Figure 2.3 (b). For examples, the discharge can occur at the end of power cables, overhang of generator winding and metal casing of bushing that makes contact with the epoxy resin insulator.

Corona discharge is an electrical discharge that occurs at a sharp protrusion or edge of high electric field metallic contacts, as in Figure 2.3 (c). Small sharp particle or dust on the surface which acts as contamination in gas insulated system may initiate the discharge. Then, electrical discharge will develop at the tip of the particle and cause insulation failure. Corona discharges only occur in gas or liquid dielectrics.

2.2 Types of Partial Discharge Detection

The insulation condition of electrical equipment can be monitored and analysed by PD detection system. PD activities can generate electrical pulses and other effects such as chemical reaction of insulating materials, acoustic waves and electromagnetic waves. These signals can be detected by specific types of PD detection technologies.

2.2.1 Motivation for PD Detection

Condition-based maintenance (CBM) is carried out based on forecast studies which are obtained from periodic analyses that detect the onset of system deterioration. The diagnostic techniques of CBM require nondestructive testing techniques, advanced technologies, measureands, and diagnostic tools to measure, monitor and trending various equipment performance parameters [21]. Partial discharge measurement is one of the trending analyses used for measuring insulation deterioration of electrical machines which can be useful in proposing scheduled maintenance activities. If the measured PD level of high voltage equipment is low or at acceptable level, the scheduled maintenance for the machines can be postponed until PD level reaches the moderate level which may require planning for the maintenance in the next 6 months. There are two main techniques to measure PD signals which are explained by CIGRE [22], they are conventional and non-conventional techniques. Conventional or electrical PD measurement is based on the IEC 60270 guidelines [2] while non-conventional PD measurement includes chemical, acoustic and electromagnetic methods.

2.2.2 Conventional Partial Discharge Detection

Condition-based maintenance system requires an effective data-collection technology that can be analyzed to provide information on the probability of system failure. A variety of advanced technologies are applied to monitor the condition of assets in CBM activities, for example, conventional PD measurement.

Conventional PD measurement can measure apparent charge of partial discharges using basic circuit connection as shown in Figure 2.4 [2]. Apparent charge is the integrated current pulse generated by PD activities transmitting through the test circuit and measured by measuring instrument as charge in the order of picocoulombs (pC). From Figure 2.4, a noise blocking filter is required to suppress high frequency interference from the power source. Z_{mi} is the input impedance of measuring system. C_a is the virtual test object capacitance of the insulation system. C_k is the coupling capacitor which limits the power frequency charging current from the test object pass through Z_{mi} . The discharge current will be converted into equivalent voltage at Z_{mi} which will be an input to the measuring instrument.

One of the most widespread online applications of conventional PD measurement is detection of deterioration in rotating machines such as high voltage generators and motors. This electrical PD measurement can be applied to measure on-line PD activity in insulation system of stator windings, for motors and generators, by permanent installation of a coupling capacitor at each winding phase. A high voltage 80 pF coupling capacitor (6.9 kV, capable to measure PD in hundred megahertz (MHz) range) is connected to each stator winding lead of a motor [23]. The capacitor blocks low frequency voltage while passing high frequency voltage that accompanies PD. The PD signals were differentiated from noise signals by measuring their rise time. PD signals generated fast rise time (about 4 ns), and slow rise time (50 μ s) detected on the noise signals. However, PD-like noise from power system, such as arcing from switchgear, can also be detected by the capacitor. Stone [24] developed a system to differentiate the external noise using two 80 pF capacitors per phase (six capacitors for one machine). The two capacitors were separated by at least 2 m apart per phase. If the first signal detected at the capacitor nearest to the stator winding, then the signal is PD signal from stator winding. However, if the first signal measured at the capacitor closest to the power system, then the signal is noise signal. Figure 2.5 shows a commercial (IRIS) coupling capacitor where the high voltage end is connected to the winding busbar and PD signal is measured from the ground end of the capacitor.

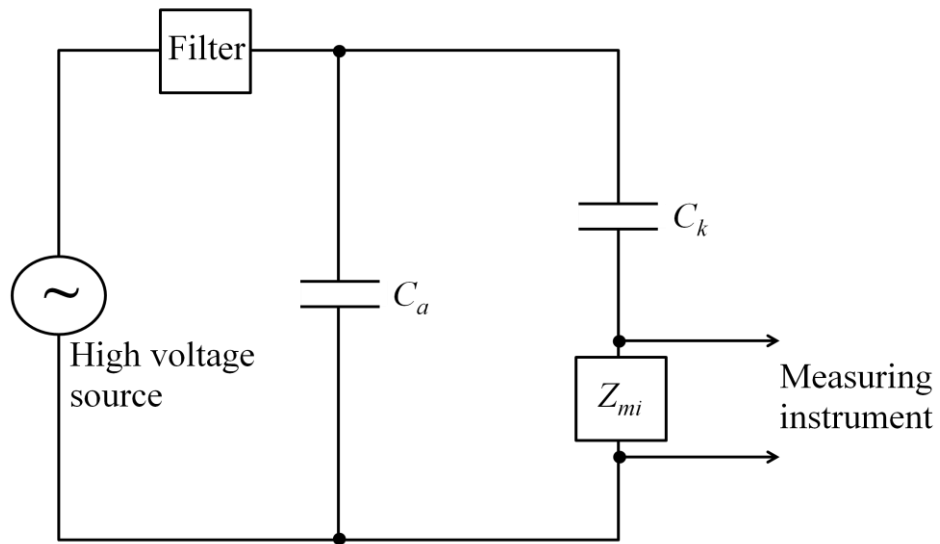


Figure 2.4: Basic circuit for partial discharge measurement.

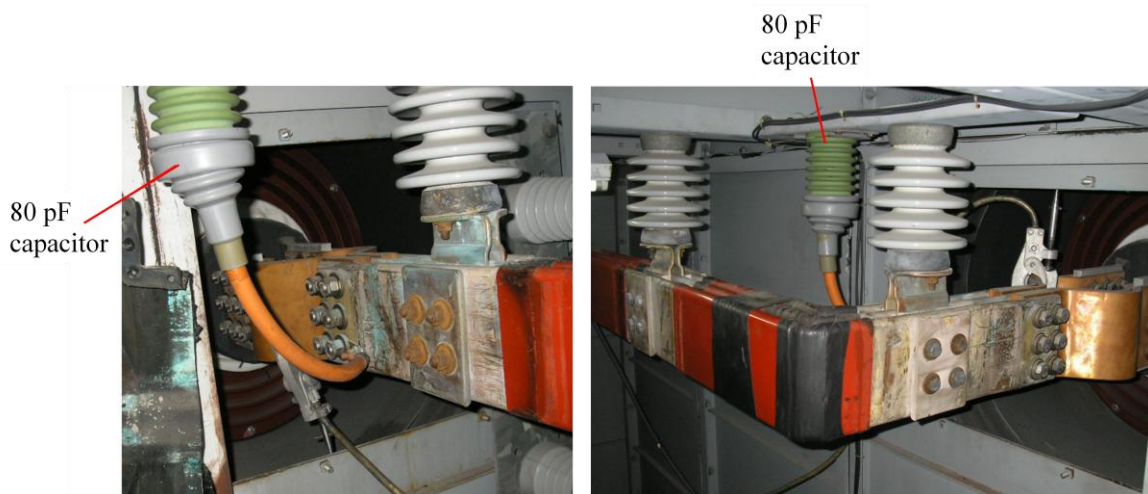


Figure 2.5: 16 kV IRIS Power Engineering coupling capacitor is mounted on the generator body. The terminal busbar of power generator is connected to the high voltage end of the capacitor (orange cable). PD signals are measured from the ground end of the capacitor [25].

2.2.3 Unconventional Partial Discharge Detection

The unconventional PD measurement can detect PD signals that occur in insulating materials of electrical equipment using specified sensors. The sensors are not electrically connected to the HV part of the equipment circuit hence the installation of the sensors is more safe and convenient. PD activities generate effects other than electrical pulses such as chemical decomposition of insulating materials, acoustic waves and electromagnetic waves [26]. These non-electrical physical phenomena can be detected by different diagnostic techniques with appropriate sensors. This section discusses unconventional PD measurement using chemical, acoustic and electromagnetic techniques.

2.2.3.1 Chemical Partial Discharge Detection

Chemical PD measurement is usually based on the analysis of gases produced because of oil or gas decomposition. Thermal and electrical disturbances can cause chemical decomposition of the insulating materials. Chemical detection can be applied in variety of electrical equipment, for example, oil-filled electrical equipment (power transformers) and gas-filled electrical equipment (gas insulated substation, GIS).

PD activities can occur in mineral oil of power transformers and even at winding insulation. Thermal stress or local hot spots on paper winding of the transformers can generate gas bubbles (PD sources) and then release into mineral oil. This defect can cause decomposition of the paper. The most common sources of PD in power transformers are tip electrode (corona), floating conductive particle and gas bubble (void) in the insulating medium [27]. The decomposition of cellulosic paper produces carbon monoxide (CO), carbon dioxide (CO₂), hydrogen (H₂) and methane (CH₄). Oil decomposition is complicated since mineral oils are composed of many different hydrocarbon molecules [28]. Common byproducts of the oil decomposition are hydrogen (H₂), methane (CH₄), acetylene (C₂H₂), ethylene (C₂H₄) and ethane (C₂H₆). These gases can be produced in oil transformers because of natural ageing and also due to faults. The type of incipient faults can be interpreted based on the concentration of these gases in oil-filled transformers. This interpretation is called dissolved gas analyses (DGA). DGA can be used to

determine the operating condition of the transformer. There are several DGA interpretation methods such as IEC 60599 method [29], IEEE Std C57.104TM-2008 method [28] and Duval triangle method [30].

PD is a subset of insulation defects in mineral oil that can be detected by DGA. The types of faults that may occur in oil-filled transformers, according to IEC 60599, are partial discharge with X-wax (solid material which is produced from mineral oil due to electrical discharge) formation on paper insulation; discharges of low energy evidenced by carbonization of paper insulation; discharges of high energy evidenced by extensive carbonization of paper insulation and tripping of the equipment, thermal fault of less than 300 °C, thermal fault between 300 and 700 °C, and thermal fault of more than 700 °C. Table 2.2 indicates the gas levels for normal operating condition of oil power transformers, reported by IEEE method [28]. Figure 2.6 provides the significant gases and proportions for partial discharge in transformer oil [28]. Low-energy electrical discharge, such as partial discharge, generates high concentration of hydrogen. Duval used the Triangle graphical method to visualize the types of faults in oil transformers, as indicated in Figure 2.7. The region labelled DT in the Triangle represents the mixtures of electrical and thermal faults. Duval coordinated three types of gases (one at each side of the Triangle) to represent the types of transformer faults. The gases are CH₄ (the weakest C-H bonds, 338 kJ/mole), C₂H₄ (C=C double bond, 720 kJ/mole), and C₂H₂ (C≡C triple bond, 960 kJ/mole). C₂H₄ and C₂H₂ gases require higher temperature to form as stable recombination products, which are 500 and 800 °C respectively [29]. From figure 2.6, if $x = 19 \mu\text{L/L}$, $y = 2 \mu\text{L/L}$ and $z = 1000 \mu\text{L/L}$, the percentages of the gases are 1.86% C₂H₂, 0.20% C₂H₄ and 97.94% CH₄. This indicates that the power transformer has PD activities. IEC and IEEE methods considered gas concentration of normal transformer operation was different but not very significant.

Table 2.2

Example of dissolved gas concentrations of power transformers at normal operating condition [28].

Dissolved gas concentration limits ($\mu\text{L/L}$)						
Hydrogen (H_2)	Methane (CH_4)	Acetylene (C_2H_2)	Ethylene (C_2H_4)	Ethane (C_2H_6)	Carbon monoxide (CO)	Carbon dioxide (CO_2)
≤ 100	≤ 120	≤ 1	≤ 50	≤ 65	≤ 350	$\leq 2,500$

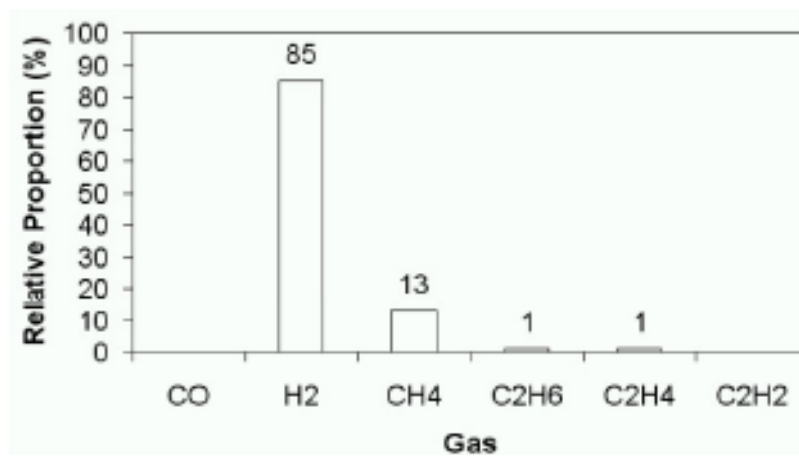
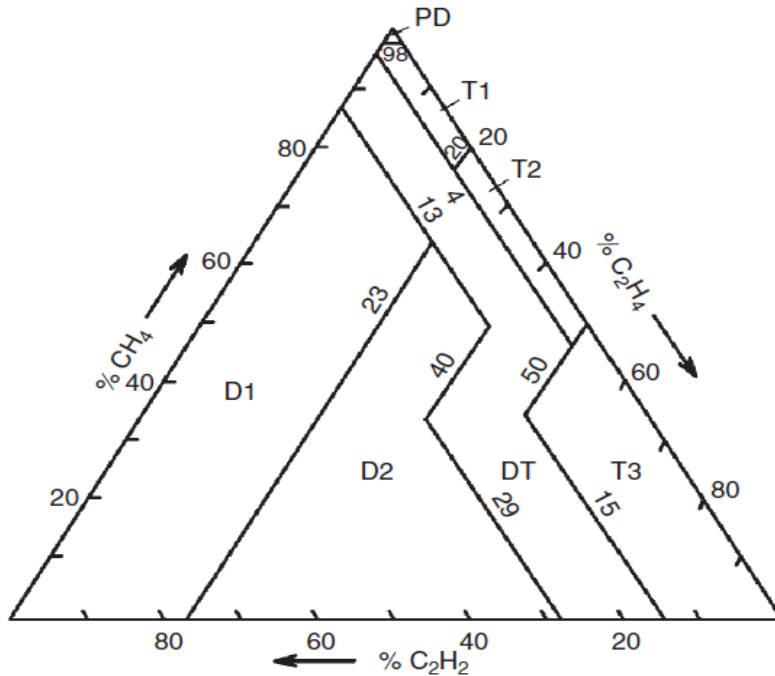


Figure 2.6: Principal gas (hydrogen) for partial discharge in transformer oil [28].



where PD = Partial discharge
D1 = Discharges of low energy
D2 = Discharges of high energy
T1 = Thermal fault, $t < 300\text{ }^{\circ}\text{C}$
T2 = Thermal fault, $300\text{ }^{\circ}\text{C} < t < 700\text{ }^{\circ}\text{C}$
T3 = Thermal fault, $t > 700\text{ }^{\circ}\text{C}$

$$\% \text{C}_2\text{H}_2 = \frac{x}{x+y+z} \times 100$$

$$\% \text{C}_2\text{H}_4 = \frac{y}{x+y+z} \times 100$$

$$\% \text{CH}_4 = \frac{z}{x+y+z} \times 100$$

x = Concentration of C_2H_2 in $\mu\text{L/L}$

y = Concentration of C_2H_4 in $\mu\text{L/L}$

z = Concentration of CH_4 in $\mu\text{L/L}$

Fault type	Limits of regions			
PD	98% CH_4			
D1	23% C_2H_4	13% C_2H_2		
D2	23% C_2H_4	13% C_2H_2	40% C_2H_4	29% C_2H_2
T1	4% C_2H_2	20% C_2H_4		
T2	4% C_2H_2	20% C_2H_4	50% C_2H_4	
T3	15% C_2H_2	50% C_2H_4		

Figure 2.7: Duval's triangle [30].

Nowadays, equipment operators can perform DGA testing in-house without the need to send transformer oil samples to various laboratories. This new technology can reduce maintenance costs and produce quicker testing results. For example, Kelman Transport X measures gas concentrations using photo-acoustic spectrometer, as shown in Figure 2.8. It can detect moisture and seven different gases which are H_2 , CO_2 , CO , C_2H_4 , C_2H_6 , CH_4 and C_2H_2 gases. The gas absorbs electromagnetic radiation from infrared light which will increase the gas temperature and then the pressure of the gas in a sealed bottle. The amplitude of the pressure waves will be detected by sensitive microphones.

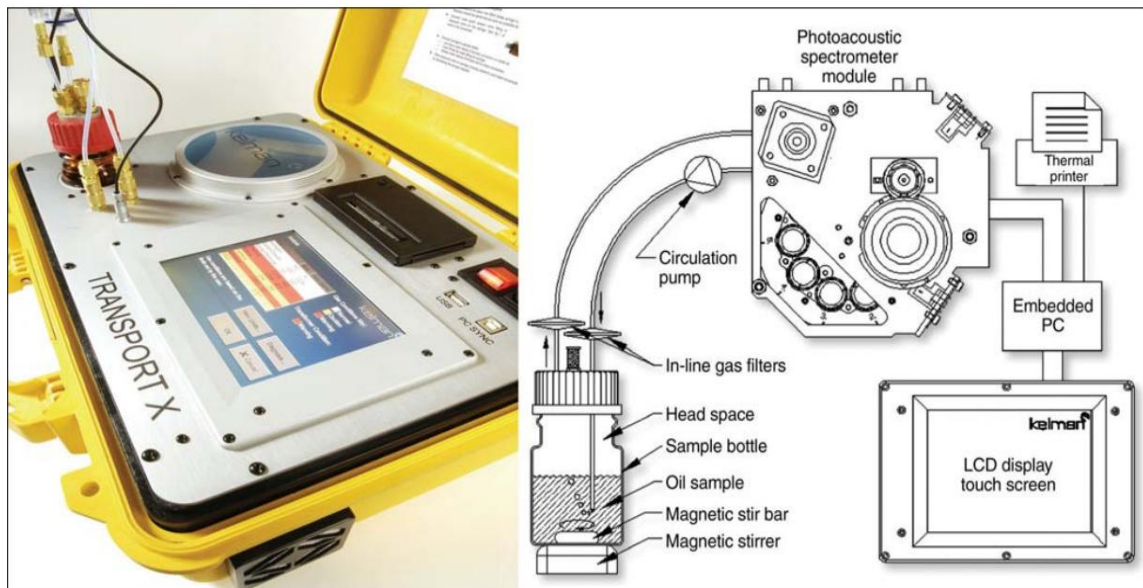


Figure 2.8: Kelman's portable DGA system (Transport X) [31].

Chemical gas analysis is also effective in detecting faults of sulfur hexafluoride (SF_6) gas equipment such as GIS. SF_6 is chemically inert and thermally stable at normal temperature [32] but when PD happens in SF_6 gas tank, SF_6 molecules will be decomposed into metal fluorides and sulfur fluorides (SF_4). If the reaction occurs on copper conductor [33], the byproducts are SF_4 and copper fluoride (CuF_2) as in (2.1). Furthermore, SF_4 is an unstable intermediate product which can react with moisture to form thionyl fluoride (SOF_2) and hydrogen fluoride (HF) as in (2.2); and with oxygen to

generate thionyl tetrafluoride (SOF₄) as in (2.3). Sulfuryl fluoride (SO₂F₂) can be generated when SOF₄ reacts with moisture, as shown in (2.4), and SOF₂ reacts with oxygen, as described in (2.5) [34] [35]. SOF₄ can hydrolyse easily to produce SO₂F₂ and HF. SOF₂ also reacts with moisture to yield SO₂ and HF but the reaction rate is too slow [39]. There are also other chemical byproducts of SF₆ gas such as aluminium fluoride (AlF₃), carbon tetrafluoride (CF₄), carbon dioxide (CO₂) and sulfur dioxide (SO₂) [36] [37] [38] [39]. The detection of PD activities is possible by analysis of these SF₆ decomposition products. The British Standard [40] recommends guidelines for the maximum acceptable gaseous decomposition product levels of SF₆ gas insulated equipment as defined in Table 2.3. The main stable byproducts of SF₆ are CF₄, CO₂, SO₂F₂, SOF₄, SOF₂, SO₂ and HF. HF is a highly acidic substance that can react readily with metal and dielectric material.

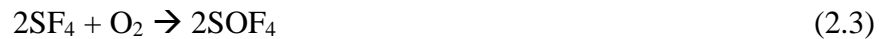


Table 2.3

Maximum acceptable gaseous decomposition products [40].

Impurity	Maximum acceptable levels (µL/L)
SO ₂ + SOF ₂	12
HF	25
Total gaseous decomposition products	50

Detection methods for SF₆ decomposition products include gas detection tube [41] [42], gas chromatography [39] and gas sensors [43] [44] [45]. The gas detection tube can be applied on-site for measuring gas concentrations in GIS. A chemical reaction causes discoloration of detecting element. However, the tube has low accuracy and cannot be used repeatedly, which is not suitable for continuous remote PD monitoring. Gas chromatography is a laboratory-based gas analysis technique, rather than continuous on-line monitoring, which separates the decomposition products in a tube. Each different product needs a different time to traverse the tube. Ju [39] explained the concentration measurement of decomposition products (SOF₂, SO₂F₂, CF₄ and CO₂) due to four different PD sources at GIS system using gas chromatography. The defect types are metallic protrusion, metallic particles on GIS tank, metallic particles on spacer, and loose connection between spacer and HV conductor, as shown in Figure 2.9. These defects were modelled in laboratory such as a needle-plane electrode, copper particles on a tank, copper particles on epoxy, and gap between epoxy and HV conductor, as indicated in Figure 2.10. From the experimental results, as in Figure 2.11, SOF₂ component has the highest concentration rate for all the defect types except for the loose connection defect. Metallic protrusion indicates the highest concentration rate for all the four decomposition products compared to the loose connection defect.

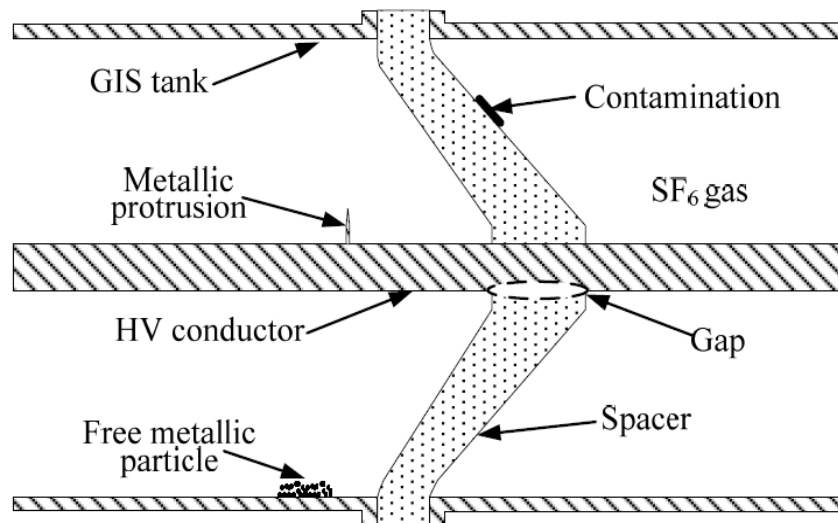


Figure 2.9: A selection of defect types in GIS [39].

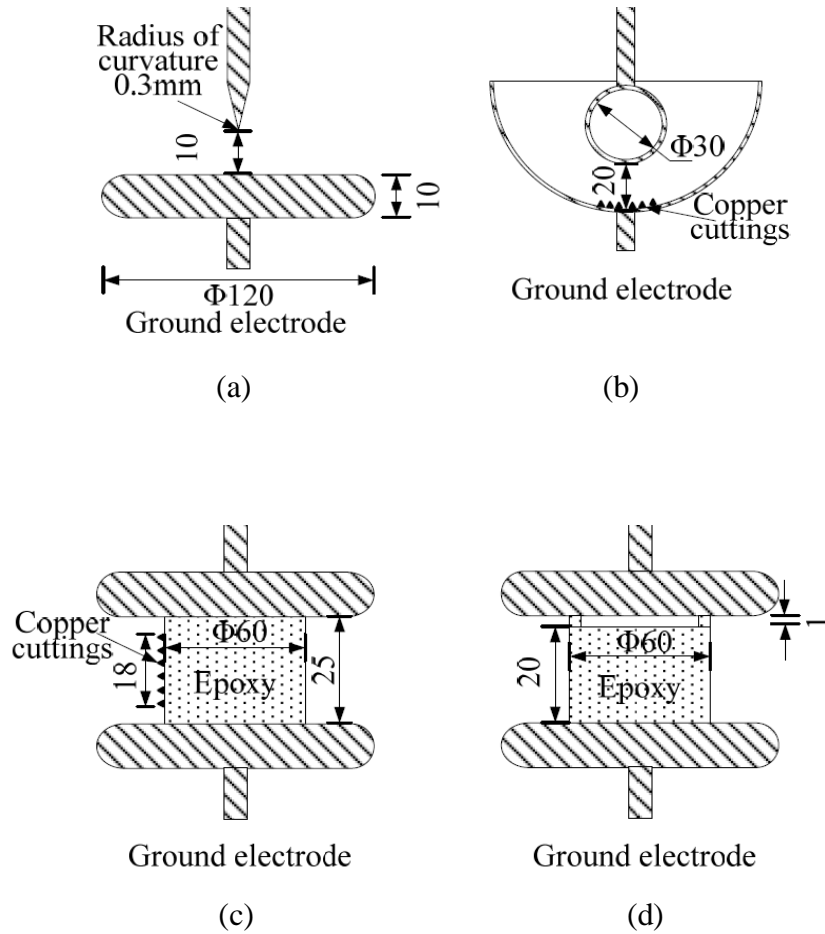


Figure 2.10: The modelled defect types in GIS during PD measurement: (a) needle-plane electrode system, (b) particles on tank, (c) particles on spacer, and (d) gap between spacer and HV conductor [39]. Note that all dimensions are in millimeter (mm).

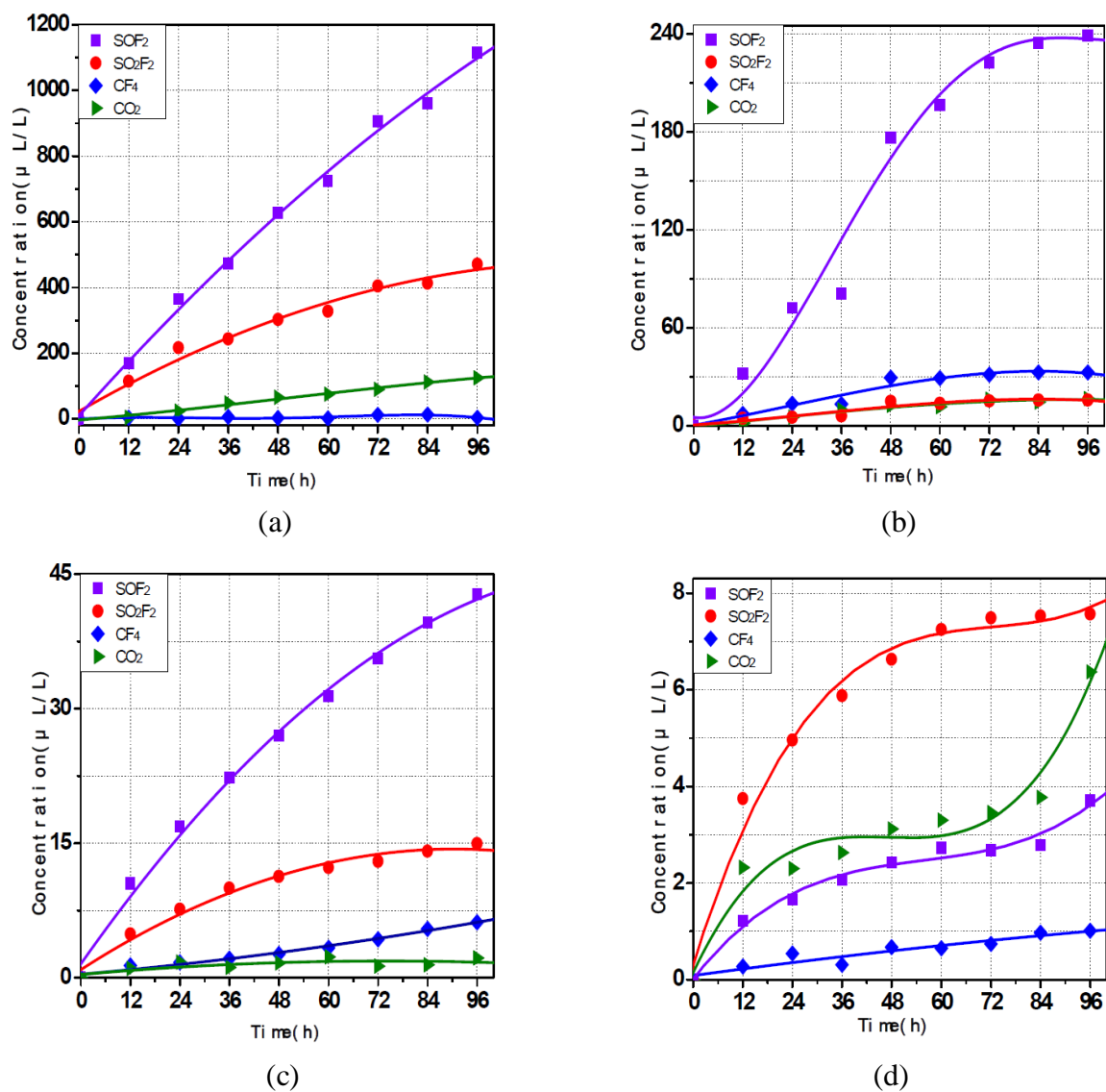


Figure 2.11: The concentration rate of four SF₆ decomposition products (SOF₂, SO₂F₂, CF₄, and CO₂) for the modelled defects in GIS: (a) metallic protrusion, (b) particles on tank, (c) particles on spacer, and (d) gap between spacer and HV conductor [39].

Gas sensor is easy to use on-site and able to monitor gas concentration which leads to PD. The main structure of gas sensor consists of two parallel electrodes and a solid electrolyte between the electrodes to measure decomposed gas through electrochemical reaction. Electrical signals will be generated when electrochemical reactions occur on the electrodes, as explained in Figure 2.12. The solid electrolytes that compose of silver ion (Ag^+) or copper ion (Cu^{++}) may produce silver fluoride (AgF) or copper fluoride (CuF_2) when react with SF_6 decomposition products. The produced compounds can reduce the effectiveness of ion conduction by preventing the movement of ions in the electrolytes. The electrical conductivity of the solid electrolytes can be affected by temperature, as temperature increases the conductivity increases [44].

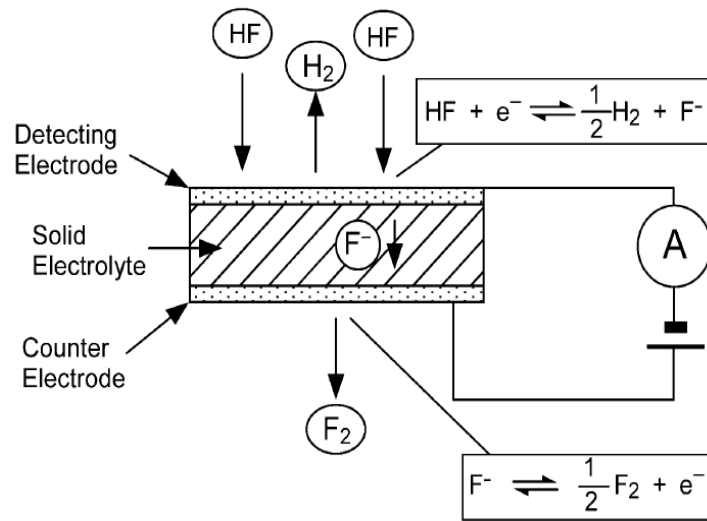


Figure 2.12: Current generation of electrochemical SF_6 decomposition gas sensor [45].

2.2.3.2 Acoustic Partial Discharge Detection

The ultrasonic waves generated by PD activities can propagate through dielectric materials which surround the PD sources inside electrical equipment and the propagated signals can be measured by acoustic sensors outside the wall of the electrical equipment. Since acoustic sensors are applied externally, they are suitable for online PD measurement without disturbing the normal operation of the equipment. The major advantage of acoustic PD measurement is the capability to locate PD sources in HV

electrical equipment. The location of PD sources can be calculated using time-of-flight measurements [26] [46] which required more than one sensors at different locations. PD signal propagates in all directions inside electrical equipment. The time difference between the arrival-time of the signal at different sensors can indicate the location of PD source. The velocity of acoustic waves that propagates through insulating media is required to calculate the location of PD sources. Table 2.4 summarises the velocity of acoustic waves for main insulating media used in high voltage application [47] [48].

Table 2.4

Acoustic velocity of insulating media [47] [48].

Medium	Velocity (m/s)
Air	343
SF ₆ gas	133
Transformer oil	1415

Researchers have proved that PD activities due to needle-plane, plane-plane and metallic floating configuration in transformer oil can be detected using acoustic sensor with detected frequency ranges between 50 – 300 kHz [49] [50] [51], as illustrated in Figure 2.13. Piezoelectric transducers which convert the acoustic waves to electrical signals (voltages) can be used to measure and locate PD sources in power transformers [52] [53] [54]. The sensors were attached to the transformer tank using magnetic transducer interface. Various materials inside the tank such as pressboard, solid insulation and metal structures can attenuate acoustic signals with each of these materials having different attenuation properties [55] [56] [47]. The location of PD sources in a tank using acoustic sensor can be difficult if (i) PD activities occur within the winding materials, (ii) thicker walls for large electrical machines where more attenuation of the PD signals, (iii) the presence of acoustic noises from surrounding environment, and (iv) acoustic waves propagate through different media with different acoustic velocities. Acoustic PD sensors can also externally mount on metal enclosure of GIS system [57]. Measuring PD activities that occur in power cables using acoustic sensors is not very useful because the

sensitivity of the sensors reduced largely with distance from PD source and the properties of cable materials reduce the sensitivity [58].

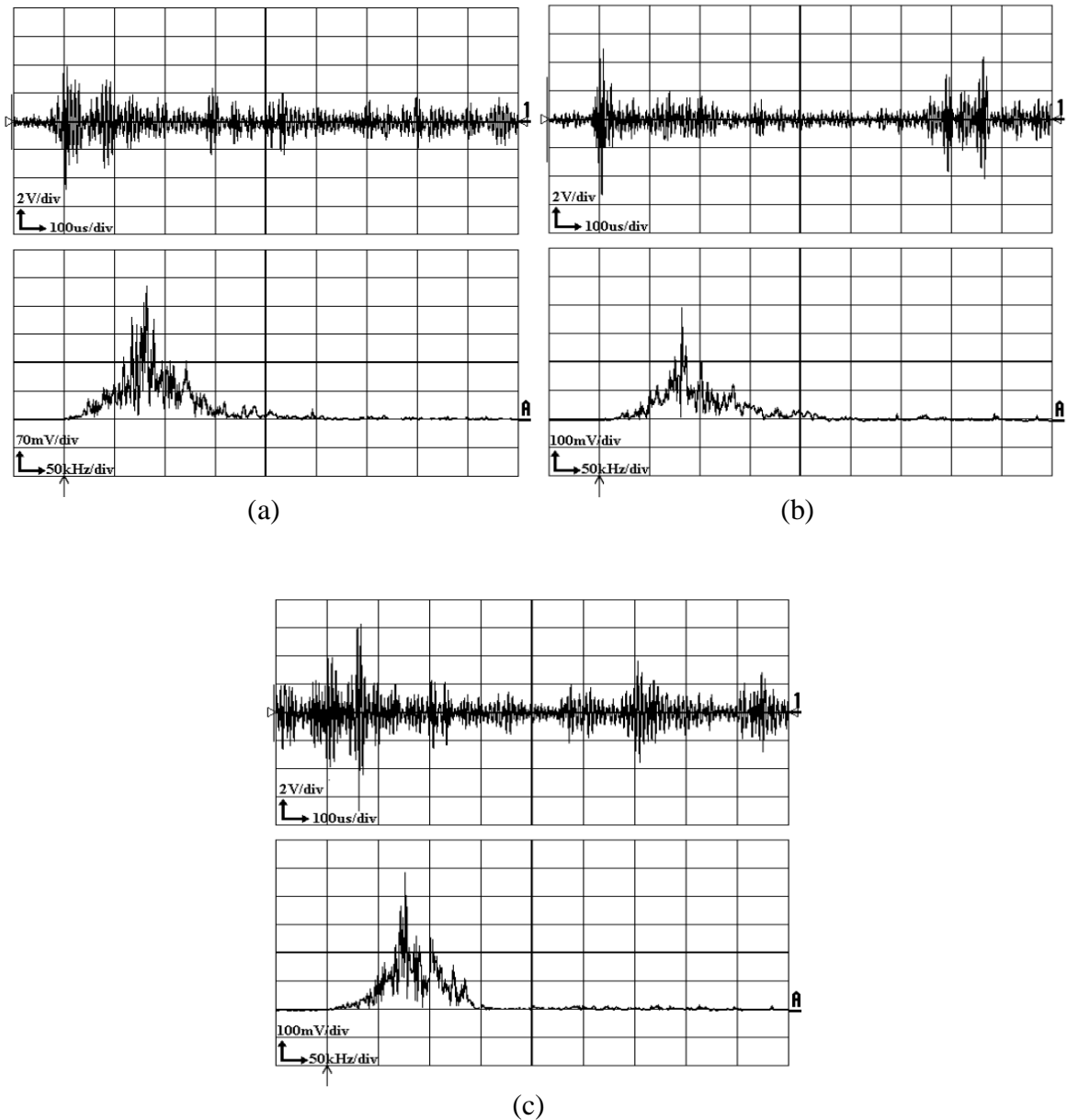


Figure 2.13: Examples of time domain and frequency domain partial discharge signals measured by acoustic sensor: (a) needle-plane, (b) plane-plane, and (c) metallic floating configuration [49].

2.2.3.3 Electromagnetic Partial Discharge Detection

PD activity also creates electromagnetic transients caused by rapid increase in current pulses. Electromagnetic PD measurement involves high frequency (HF), very high frequency (VHF) and ultra high frequency (UHF) ranges. The frequency ranges of HF, VHF, and UHF are 3 – 30 MHz, 30 – 300 MHz, and 300 – 3000 MHz, respectively [22]. This section explains HF and VHF PD detection systems, while UHF PD detection systems will be discussed in Chapter 3 because of their special relevance to this research.

In HF and VHF PD measurement, the sensors used are typically based on capacitive and inductive detection principles. The capacitive detection involves measuring electrical charge between two metal plates separated by dielectric. The inductive principle explains that an alternating current in a conductor can induce a current to flow in another conductor. PD signals in power cables can be measured using these measurements, as illustrated in Figure 2.14. Therefore, there are two types of electromagnetic sensors to measure PD signals in cables which are capacitive sensor (the sensor is connected as position 1 or position 2 as in Figure 2.14) and inductive sensor (the sensor is connected as position 3 or position 4 as in Figure 2.14). Capacitive PD detection for power cables involves measurement of electric field generated by PD source. Position 1 capacitive sensor in Figure 2.14 shows conventional PD detection of power cable. Coupling capacitor is electrically connected to cable termination, for example at 11 kV switchgear [59]. Conductive material of capacitive sensors, such as metallic tape, is attached to the semi-conducting screen of cable joints which represents position 2 capacitive sensor as in Figure 2.14. PD signal is measured using measurement unit that is connected to the conductive material of the sensor. The operating frequency of the tape-type sensor can reach about 200 MHz [60]. The installation of the sensors, for position 1 and position 2 of capacitive sensors, at the cable terminations or joints is done when the cables are out of service.

Inductive sensors are more practical and convenient for measuring PD signals in power cables. This is because they do not need any electrical connection to high voltage part of the cables and the measurement can be done even when the cable systems are in operation. High frequency current transformer (HFCT) is the inductive PD sensor widely

used to detect PD activities in power cables. It converts magnetic field, generated by PD source inside the power cables, to current and then output voltage. Ahmed [61] explained that the size of HFCTs will have different operating frequency ranges from 10 kHz to 200 MHz. The HFCT was placed around the outer side of 13 kV EPR (ethylene-propylene-rubber) insulated cable, as position 3 (inductive sensor) in Figure 2.14. High frequency components of PD spectrum are attenuated more than low frequency components. For example, 100 MHz components of PD spectrum attenuated to half value of 12 mV initial level (at the location of PD source) when the PD was detected by HFCT at about 35 m from the PD source, as shown in Figure 2.15. While 50 MHz components of PD spectrum attenuated to 6 mV (with the same initial value of 12 mV) at about 60 m from the PD source. PD spectrum with frequency more than 100 MHz, the signal can only be detected by HFCT within 2 m from the source.

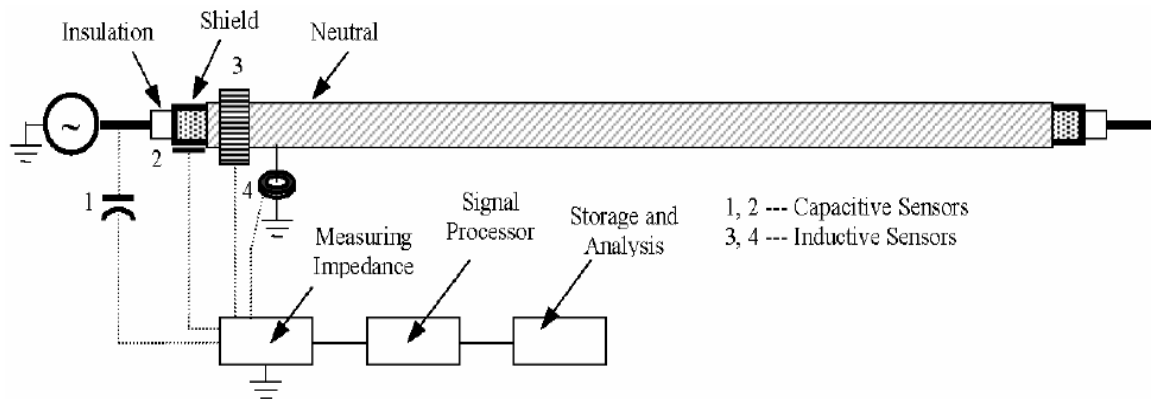
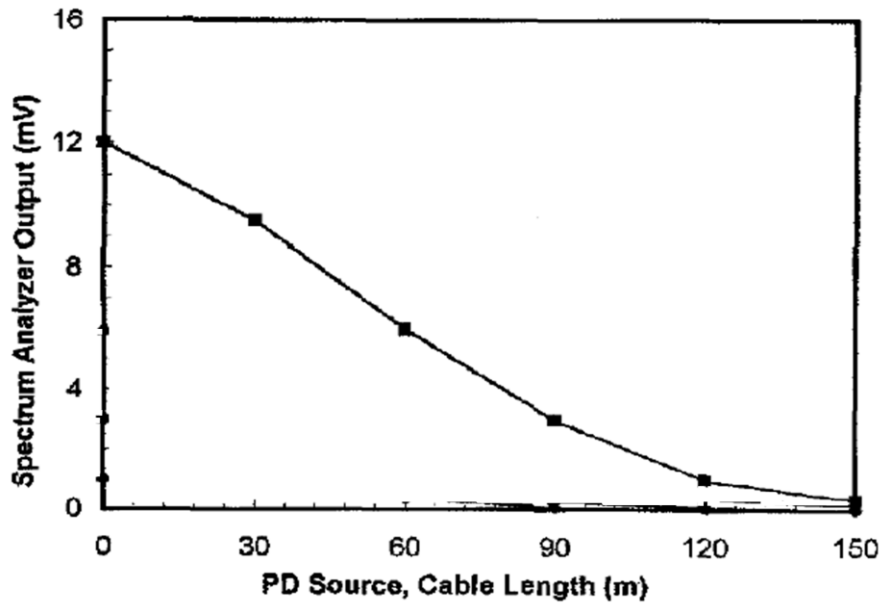
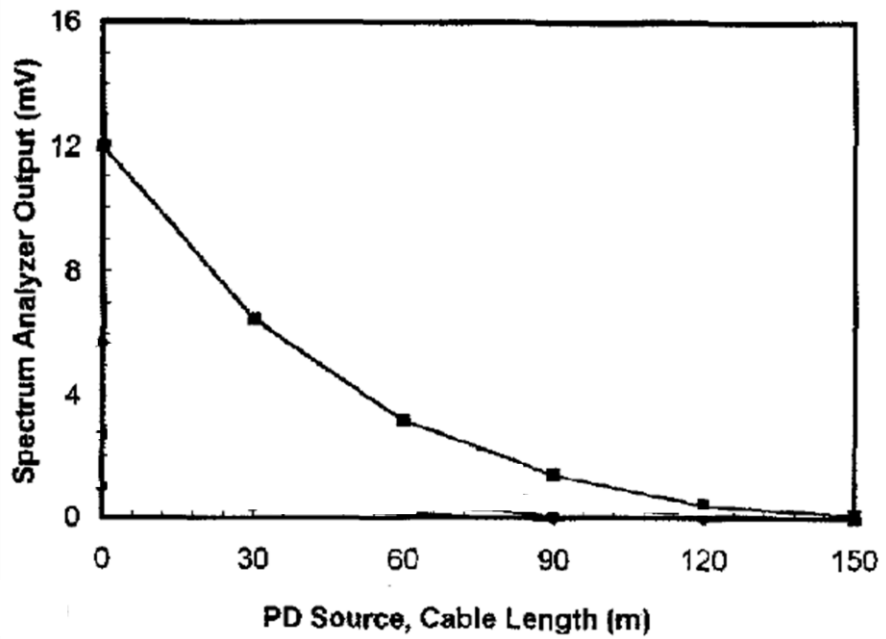


Figure 2.14: Typical arrangement of capacitive (position 1 and position 2) and inductive (position 3 and position 4) sensors for cable PD measurement [62].



(a)



(b)

Figure 2.15: The attenuation characteristics of 100 pC PD pulse in 13 kV EPR insulated cable: (a) 50 MHz components of PD spectrum and (b) 100 MHz components of PD spectrum [61].

PD activity in power cables can generate high frequency electromagnetic waves which can propagate through the earth screen of the cables. The waves will leak outside the cables and can be detected by inductive PD sensors at the ground system such as substation earth [63] [64], as illustrated as position 4 in Figure 2.14. Phung [65] used clip-on HFCTs with frequency response up to 50 MHz to detect PD activities in power cable. The HFCTs are clamped around the earth connection of the cable as shown in Figure 2.16. Just after PD ignition in power cable, two equal PD pulses are produced and travel away from PD source in different direction. The PD pulse that reaches cable termination will then travel in the reverse direction (same direction as the other pulse) towards the detection system, as explained in Figure 2.17. This is because impedance mismatch occurs at the load end where the characteristic impedance of the cable is not equal to load impedance. A Rogowski coil current transducer (RCCT) is also an inductive-type sensor which can measure current pulses that occurs due to PD activities in power cables [66]. The main difference between RCCT and HFCT is that the core of RCCT is made of non-magnetic material. The induced current (range of 1 A to 100 kA) in RCCT increases linearly with induced voltage (range of 0.1 V to 10 V) but the value of the induced voltage is very low [67]. Therefore, it has wide operating current range but low sensitivity. The magnetic core of HFCT causes it to saturate at high currents.

Electromagnetic waves produced by PD sources propagate in all direction inside electrical equipment. The waves can escape from the electrical machine through joints or insulating gasket of the machine and travel on the outer surface of the earthed enclosure. Transient earth voltage (TEV) sensor can be used to measure the pulse-like voltage of the escaped waves. The output signal of TEV detector can be voltage signal and the sensor is mounted magnetically on the external surface of switchboard enclosure [68]. Experimental results prove that the sensor can measure different kinds of discharges inside switchgear tank such as corona discharge, surface discharge, and internal discharge [69]. The frequency range and output voltage limit of the PD signals measured by the sensor are from 15 MHz to 30 MHz and under 50 mV, respectively. Reid [70] conducted on-site PD measurement on MV switchgear enclosure using TEV sensors. The sensitivity of the sensor is very low but still capable to locate PD sources in the substation.

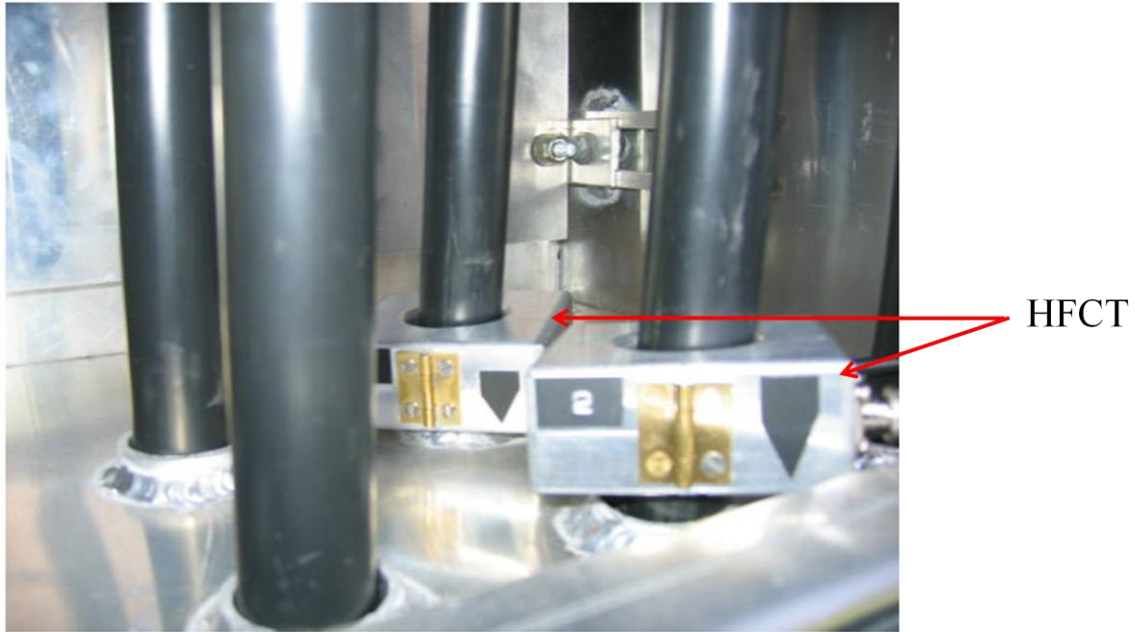


Figure 2.16: Two HFCTs are clamped around earth connections of 33 kV cable termination [65].

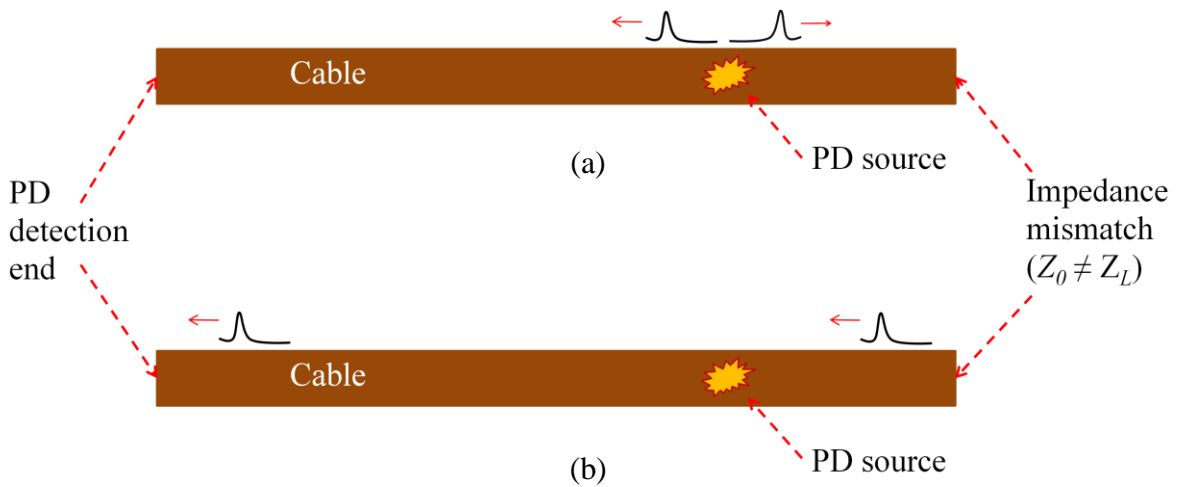


Figure 2.17: PD pulse propagation in power cables: (a) both pulses propagate in opposite direction just after PD generation, and (b) both pulses propagate in the same direction (towards detection system). The pulse that reaches an end will reverse direction and travel in the same direction as the other pulse. Impedance mismatch, when the characteristic impedance of the cable (Z_0) is not equal to load impedance (Z_L), generates a reflected pulse at the load end.

2.3 Conclusion

The apparent charge of PD can vary based on test cell arrangement and types of insulating materials. PD can occur in gas, liquid and solid dielectrics of high voltage equipment. The conventional PD measurement can measure apparent charge of partial discharges using a coupler that electrically connected to high voltage circuit of test object. PD sensors used in unconventional measurement are not physically connected to high voltage part of test object which is more safe and convenient to install. Chemical PD detection is difficult to locate the source of discharges because the system only measures the chemical concentrations of dielectrics that lead to PD activity. Acoustic PD measurement can be affected by various factors such as (i) signal attenuation due to the thickness of tank walls, (ii) environmental noises and (iii) the different characteristics of acoustic wave propagation that travels through different types of materials. Inductive electromagnetic PD measurement (below UHF range) is the best technique to measure PD activity in power cables. This is because HFCT is easily clamped around the cable even when the cable is on load.

Chapter 3: Ultra High Frequency (UHF) Partial Discharge Detection

The advantages of unconventional UHF approach, as compared to the conventional method are excellent sensitivity to partial discharge condition of the dielectric materials [71] and greater immunity to interference signals during on-site measurements [72]. The sensors are mounted on the high voltage equipment without direct connection to the HV circuit of the test objects and are able to monitor defects in large systems by using multiple sensors to cover the large area. By timing the arrival of PD signals at several UHF sensors on a transformer tank, the location of PD source can be estimated [73]. Although UHF PD measurement is valuable, it can be more useful if the data measurement is integrated with other types of PD measurement for example, UHF PD measurement of power transformers being integrated with chemical PD measurement (such as DGA) of the transformers. Chemical measurement can indicate PD activity occurs at the cellulosic paper of transformer winding and UHF measurement can locate the PD source.

In the early application of UHF partial discharge sensors, the sensors were installed on GIS tank to monitor electrical discharges from the tank. Then the application of UHF PD sensors has been evolved to monitor and even locate PD sources inside other high voltage equipment such as power transformers. Basically, there are two types of UHF sensors which are internal and external sensors. This chapter describes electromagnetic PD detection which covers the characteristic frequency range of ultra-high frequencies (300 – 3000 MHz). The different types of UHF PD sensors for different application of HV equipment systems will be explained, in particular the UHF PD detection in GIS and power transformers.

3.1 UHF Partial Discharge Sensors for GIS Application

PD pulses usually involve rise times of a nanosecond or less which will excite a signal in the UHF range [74]. Sub-nanosecond current pulse causes the radiation of wideband

transient electromagnetic field. This transient can be detected using UHF sensors. The original application of the sensors was in gas-insulated substation (GIS) to detect and locate PD sources [75] [76]. There are mainly two types of UHF PD sensors for GIS application which are internal sensor and external sensor.

Internal UHF PD sensors are mounted inside GIS during the construction of new GIS or during planned outage of in service GIS. UHF signals induced by PD sources in 154 kV GIS model can be detected in gigahertz (GHz) range, as described in [77]. Typical PD sources in GIS were modelled experimentally by Gao [78] such as floating metal, corona discharge, free metallic particle, void in spacer material and surface discharge. The discharges were detected by an internal UHF sensor that was mounted inside GIS enclosure as depicted in Figure 3.1. Flat metallic sensors of 10 cm diameter were used as internal disc antennas to detect UHF signals of PD activities inside GIS system [79]. The diameter of the internal disc sensor can be dictated by the diameter of GIS metal enclosures. There are also other designs of internal disc sensors to measure PD signals inside GIS, such as spiral sensor [80], conical sensor [81], dipole-type (two half-disc plates) sensor [82], and earthing switch sensor [83] [84], as depicted in Figure 3.2. The earthing switch sensor is a capacitive electrode that can be installed at disconnector/earthing switch (DES) of GIS tank. Significant PD levels caused by free moving particle in 362 kV GIS occur in the frequency region of 500 – 800 MHz, as demonstrated in Figure 3.3 which was taken from paper [79]. Prominent level of unwanted noises can occur in the low frequency region (less than 250 MHz region).

External UHF PD sensor is fitted to the inspection window of GIS tanks. An external UHF sensor (window-type sensor) can be used to measure PD signals generated inside GIS enclosure, as shown in Figure 3.4. The dielectric window where the external sensor is mounted on it during UHF PD measurement can increase the average frequency response of the external sensor, compared to internal sensor as shown in Figure 3.5. Measurement of the frequency responses of UHF PD sensors will be discussed in section 4.4. Microstrip patch antenna is also another type of external UHF sensors. This sensor can detect PD signals that leak from GIS disc insulators [85] [86]. The sensor was mounted on the insulation externally, as demonstrated in Figure 3.6. The sensor is

suitable for on-line PD measurement of GIS systems. It does not require window structure on the GIS wall to measure PD activity. The frequency bandwidth of the sensor is between 340 MHz and 440 MHz. The main structures of the sensor are rectangular metal patch (antenna patch), dielectric plate, metal floor and feeder where electromagnetic waves will be transmitted to measuring equipment. Kaneko [87] described that higher strength of PD signals can be detected at the midpoint between the bolts of GIS flange, as shown in Figure 3.7, compared to when the sensor was placed on the bolts. This is because the electromagnetic waves can propagate through the insulation spacer of GIS tank at the midpoint between the bolts. The strength of the waves is reduced at the metal bolts because they have the same grounding potential as GIS tank. The signals were measured using horn sensor mounted externally at the insulation spacer of GIS tank, as pictured in Figure 3.7.



Figure 3.1: Internal UHF PD sensor mounted inside experimental 220 kV GIS system [78].

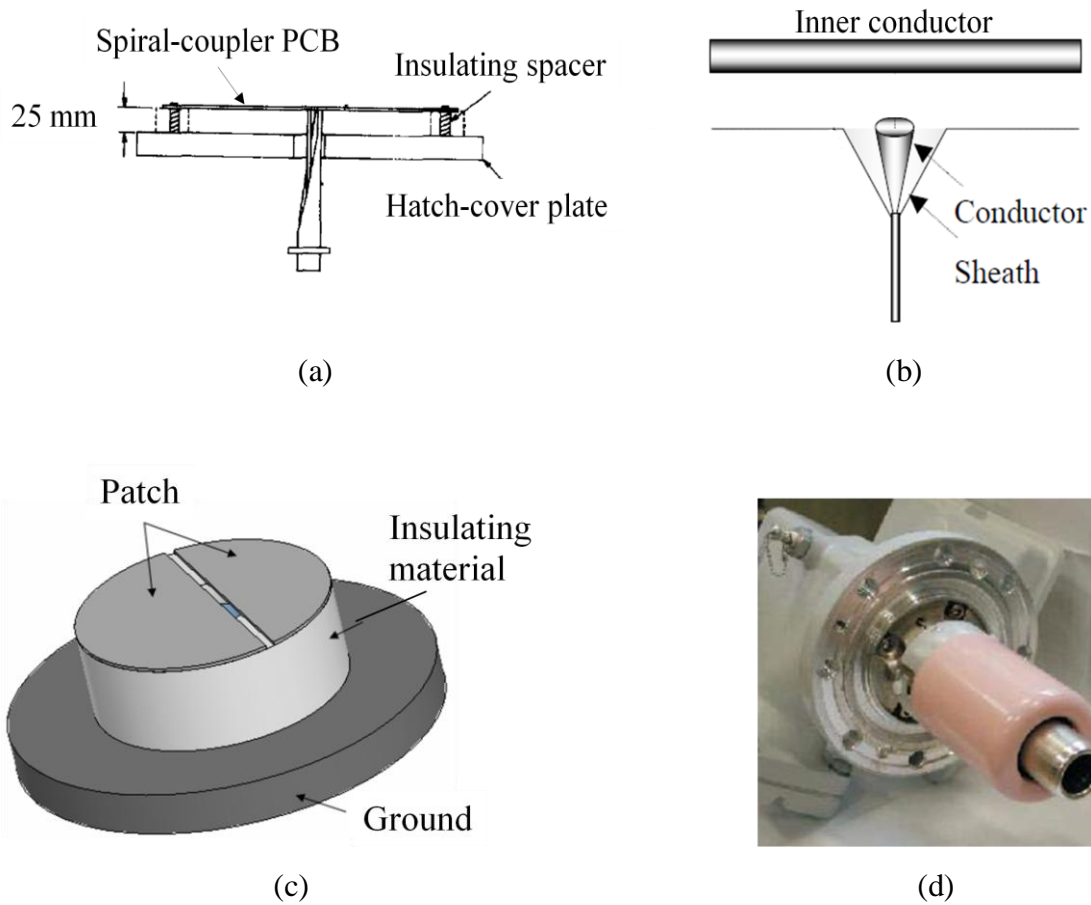


Figure 3.2: Examples of internal UHF PD sensors for GIS application: (a) spiral sensor [80], (b) conical sensor [81], (c) dipole sensor [82], and (d) conventional earthing switch adapted for use as a sensor [83]. PCB represents printed circuit board.

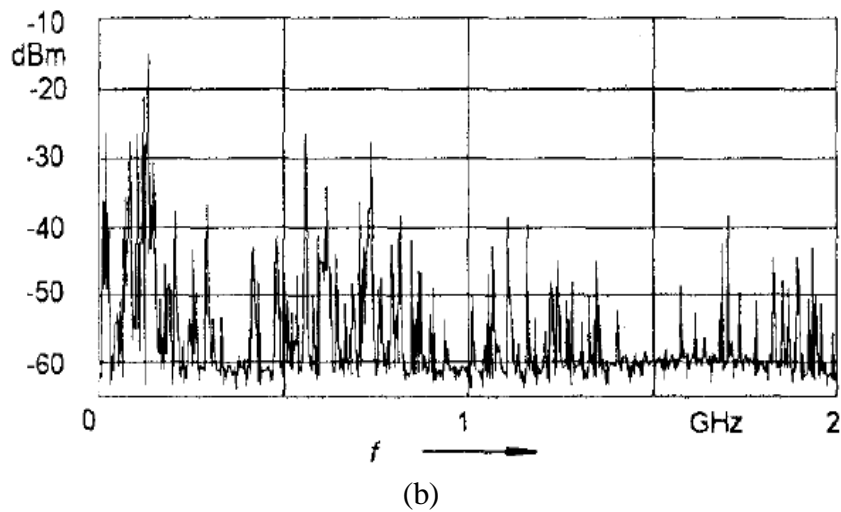
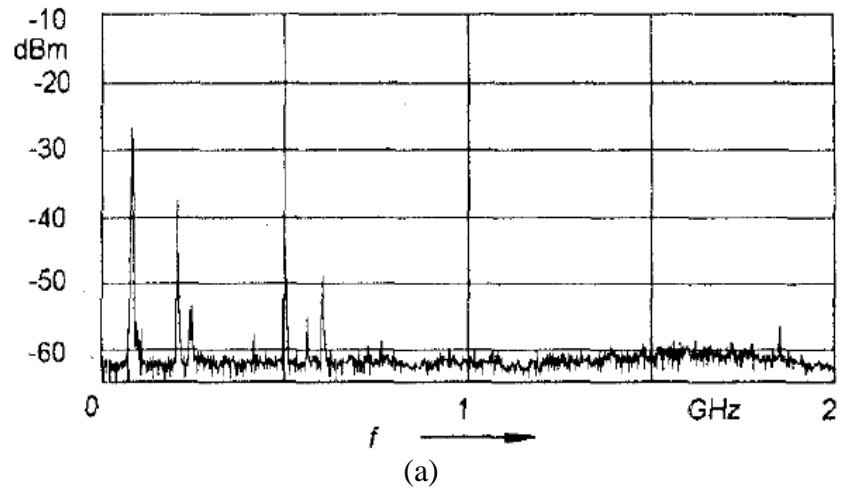


Figure 3.3: Signals detected by internal UHF disc sensor in GIS: (a) noise signal before PD signal is induced; and (b) measured signal when PD source due to free moving particle is generated [79]. The resonant response of the measured signal occurs due to the reflection of PD signal on GIS tank.



Figure 3.4: External UHF PD mounted on the inspection window of GIS tank. The sensor is connected to an amplifier with a passband between 300 MHz and 2 GHz [83].

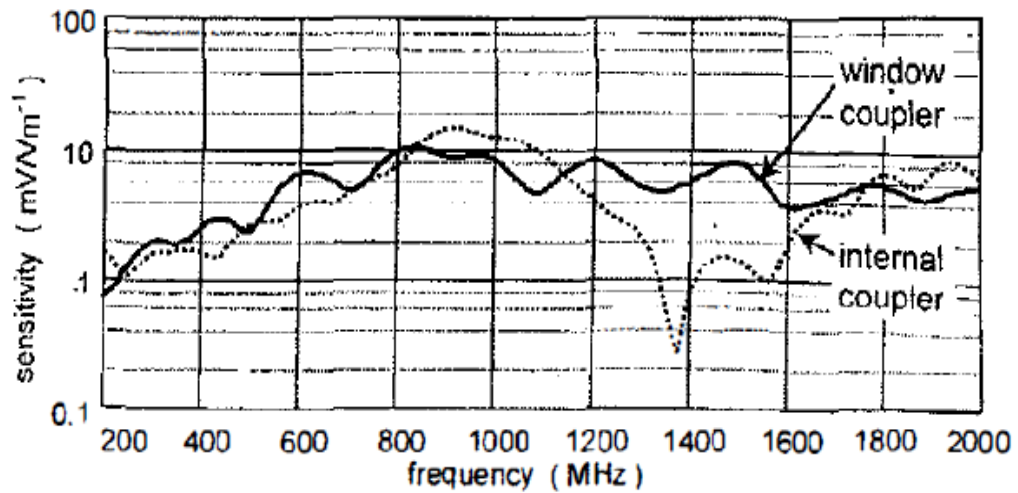


Figure 3.5: The frequency responses of internal and external (window-type) sensors for GIS tank [88].



Figure 3.6: Microstrip patch antenna mounted on GIS disc insulator [85].

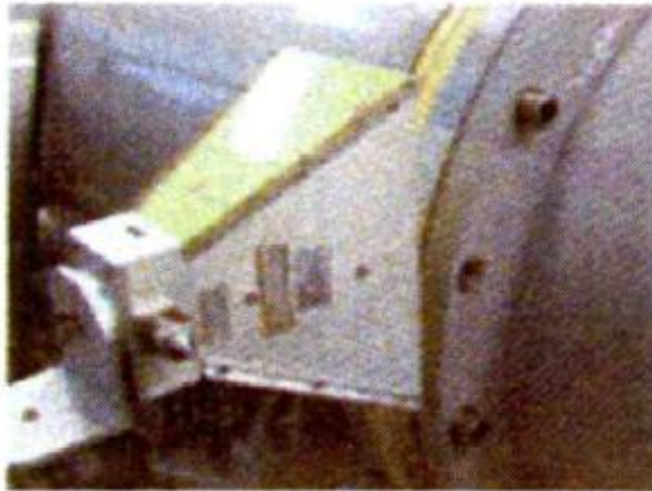


Figure 3.7: Horn sensor directed at the insulation spacer of GIS tank [87].

Three main components of UHF PD measurement system for GIS or other high voltage systems can include sensor, measuring unit, and control unit [89] [82]. Sensor technology is an important field since sensor can be installed at small space, can perform continuous monitoring, and it is very sensitive to small changes. Sensor component is the first component in the measurement system that detects and measures variables of PD signals. The selection of sensor technology can involve (i) types of UHF PD sensors (internal or external sensor) that can be easily installed with acceptable sensitivity level, and (ii)

location of sensors to be mounted which then affects the number of sensors used to cover most of the monitoring area. Measuring unit can consist of (i) a filter that transmits only the required frequency range of measured signals, (ii) an amplifier which increases signal amplitude to a useable level, and (iii) analogue-to-digital converter that ensures analogue signals detected by sensors are converted to digital signals. The control unit may have functions such as displaying PD signals, identification of PD types, generation of alarms for the system, and locating PD source. Azcarraga [83] used two different displaying techniques to diagnose PD signal in GIS which were time domain signal and phase resolved PD (PRPD) pattern. Time domain signal was analysed to assess the location of PD source using time-of-flight (TOF) method. Figure 3.8 shows a simple TOF method to locate PD source using two UHF PD sensors mounted on GIS tank. The location of PD sources can be calculated using (3.1), with reference to Figure 3.8.

$$D_1 = \frac{D_t - (D_2 - D_1)}{2} = \frac{D_t - (c \times \Delta t)}{2} \quad (3.1)$$

where D_1 = Distance between PD source and Sensor 1

D_2 = Distance between PD source and Sensor 2

D_t = Distance between Sensor 1 and Sensor 2

c = speed of light (0.3 m/ns)

Δt = time difference between arrival time of PD signals at Sensor 1 and Sensor 2

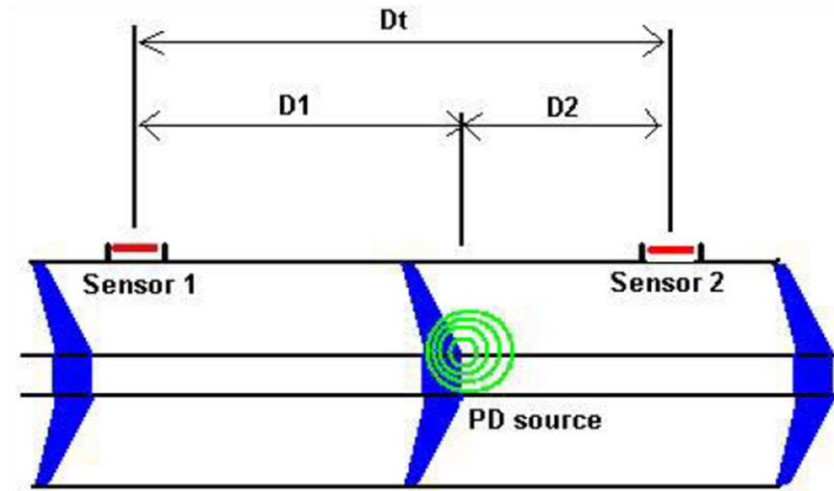
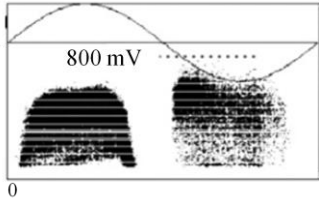
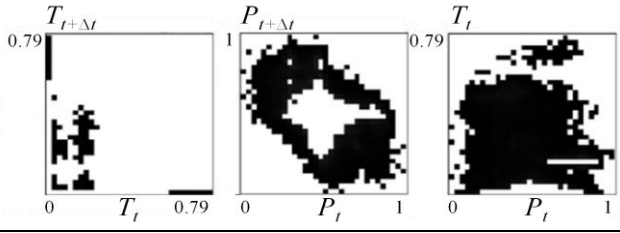
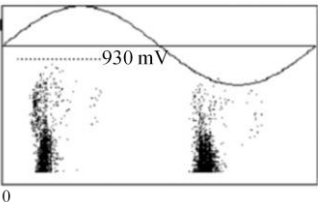
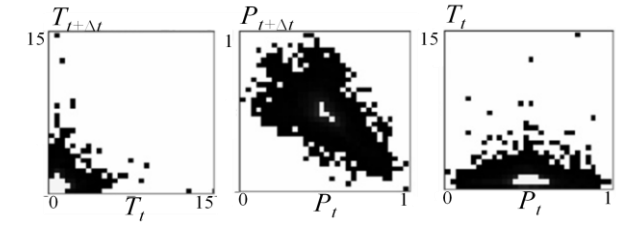
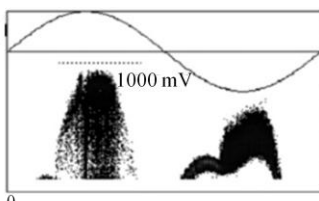
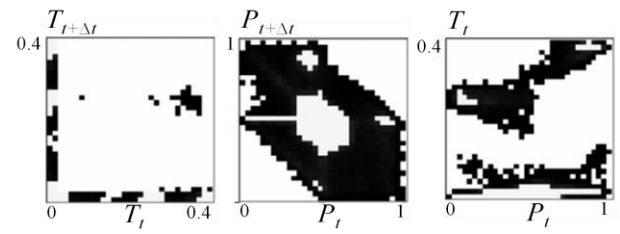
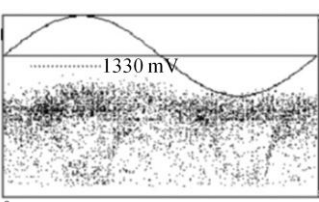
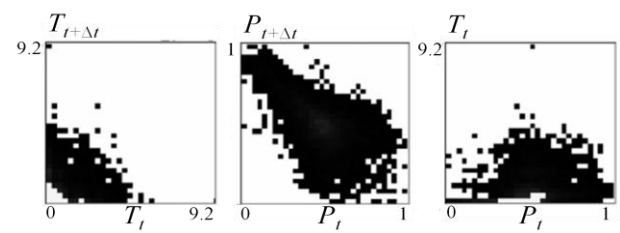
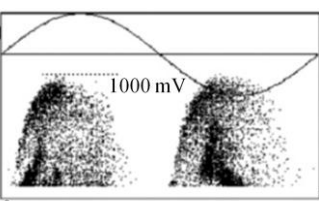
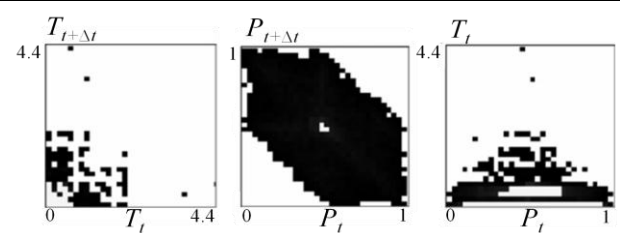


Figure 3.8: Time-of-flight method for PD source location using time domain signals to measure the time difference of PD signals at two UHF PD sensors [83].

Types of defects in GIS can be identified using PD pattern classifications such as PRPD pattern and clustering method. The PRPD pattern classifies PD types by applying phase information of the applied voltage, while clustering method does not [78] [90]. The PRPD analysis requires accumulating each PD pulse that occurs on several phase ranges into one phase cycle of the applied voltage, as illustrated in Table 3.1. The clustering method is effective when it is difficult to accurately determine the phase of the applied voltage. Clustering method involves calculating the difference between the amplitude of consecutive normalized PD magnitudes (P_i), the normalized difference of voltage amplitudes (V_i), and the normalized difference of onset times (T_i) [90]. The time is normalized using the interval time of one complete cycle of the applied voltage. The comparisons between PRPD pattern and clustering method for different types of PD sources in GIS are tabulated in Table 3.1.

Table 3.1

PRPD pattern and clustering method for different types of PD sources in GIS using internal UHF sensor (microstrip patch antenna) [90].

PD source	PRPD pattern	Clustering method
Needle-plane		
Metallic particle on conductor		
Floating electrode (bolt)		
Free moving particle on the bottom of enclosure		
Void in solid dielectric		

3.2 UHF Partial Discharge Sensors for High Voltage Transformer Application

Power transformers serve the important function of stepping up voltage at generation station and step-down voltage at distribution station. Transformer failures can increase the cost of operation drastically. The typical causes of transformer failures can be classified into two types which are internal and external causes [91]. The internal causes for oil-filled transformers can be tap changer failure, insulation deterioration, overheating, solid contamination in the mineral oil, and high level of moisture and oxygen. The contact mechanism of tap changer is the most common failure for power transformers followed by insulation deterioration of windings and mineral oil [92]. Lightning strikes and switching operations can be external causes of transformer failures. The insulation defects produce PD signals which can be detected by UHF sensors mounted on the transformer tanks. Monitoring the health of oil-immersed power transformers may involve detecting any defect in the insulation system such as corona discharge, void and poor contact or loose connection [93].

Installing UHF PD sensors on existing power transformers can be difficult since transformer tanks act as the Faraday cage. Judd [94] described three methods of installing the sensors on power transformers where different types of sensors were needed. The sensors involved were external window-type sensor, internal sensor, and inserted probe sensor.

The first method is by using window-type sensor where the sensor can be permanently installed or as portable sensor. The sensor is mounted externally on the dielectric window of the transformer tank where PD measurement can be done without interrupting the operation of the transformer. A blanking plate can be used to protect the window from environmental effect or external mechanical force when there is no sensor mounted on it, as shown in Figure 3.9. The steel plate is removed when measuring the PD activities using portable sensor. The plate is not required if window sensor is permanently installed on the transformer tank. This method has been applied on real power transformers by many researchers such as on 150 kV transformers [95] and 275 kV transformer [96], as described in Figure 3.10. Window-type UHF sensor can also detect PD signal in liquid nitrogen (LN_2) which has been proved experimentally by Truong [97]. The liquid has

been suggested as a dielectric medium for high temperature superconducting (HTS) transformer. The transformer uses liquid nitrogen (LN_2) instead of mineral oil as dielectric liquid [98]. The dielectric strength of the cryogenic liquid is 1100 kV/mm [99] whereas for mineral oil it is about 30 kV/mm [100].

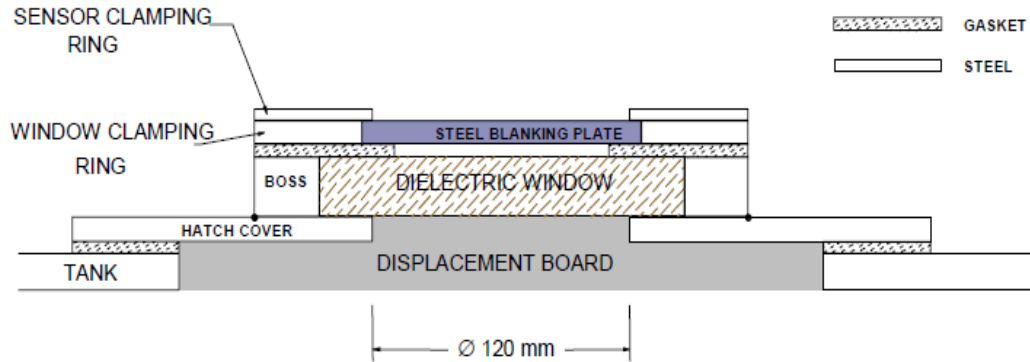


Figure 3.9: Dielectric window for UHF PD sensor mounting on transformer tank [94].

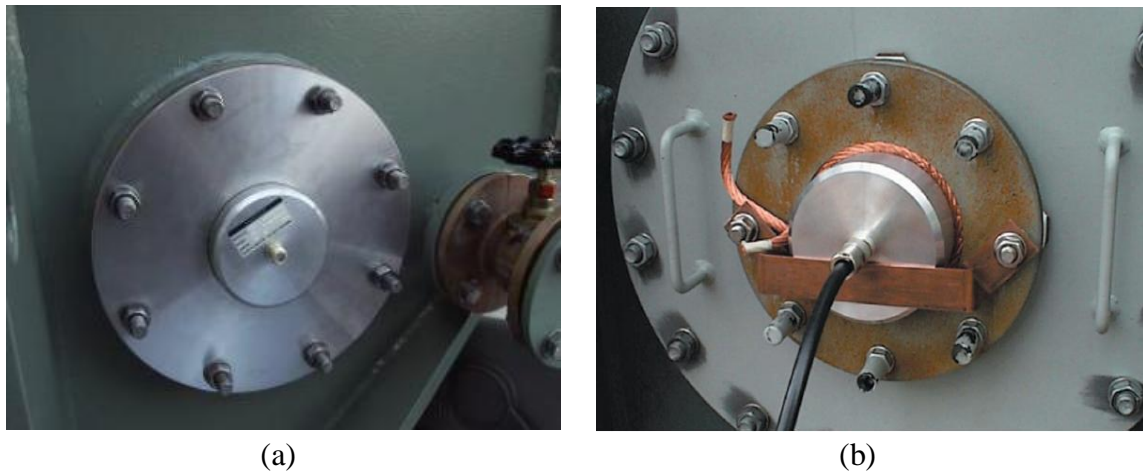


Figure 3.10: External window-type UHF PD sensor mounted on: (a) 150 kV [95] and (b) 275 kV [96] power transformers.

Permanent installation of internal sensors is the second method to detect PD activities inside the transformer tanks. The outer sleeve and inner sleeve are made of dielectric material and metallic material, respectively as shown in Figure 3.11. Spiral sensor is one of the UHF PD sensors used to detect PD signals in power transformers. Sinaga [101] used spiral sensors with the diameter of 10 cm, as shown in Figure 3.12, to measure and locate PD source experimentally in oil-filled tank. Mingjun [102] applied internal spiral sensor to measure PD activities inside 500 kV power transformer, as depicted in Figure 3.13. The internal sensor was encapsulated by epoxy resins which act as dielectric material, anti-corrosion coating and high-temperature tolerance. It operated in an effective frequency range of 500 – 1500 MHz. Installation of window-type and internal-type UHF sensors needs to be done during manufacturing or major overhaul of the transformers.

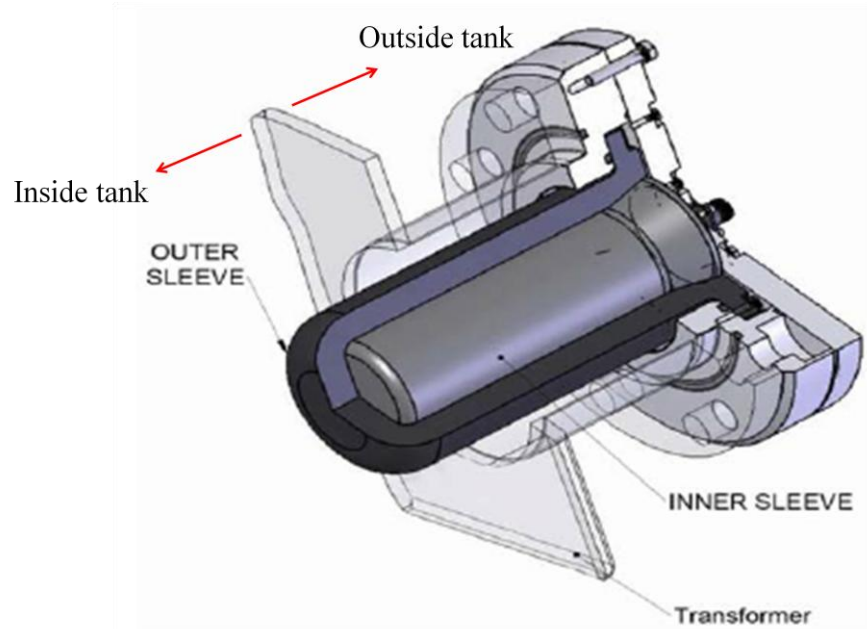


Figure 3.11: Internal UHF PD sensor for power transformers [94].



Figure 3.12 : Experimental spiral UHF PD sensor that was immersed in an oil-filled tank [101].

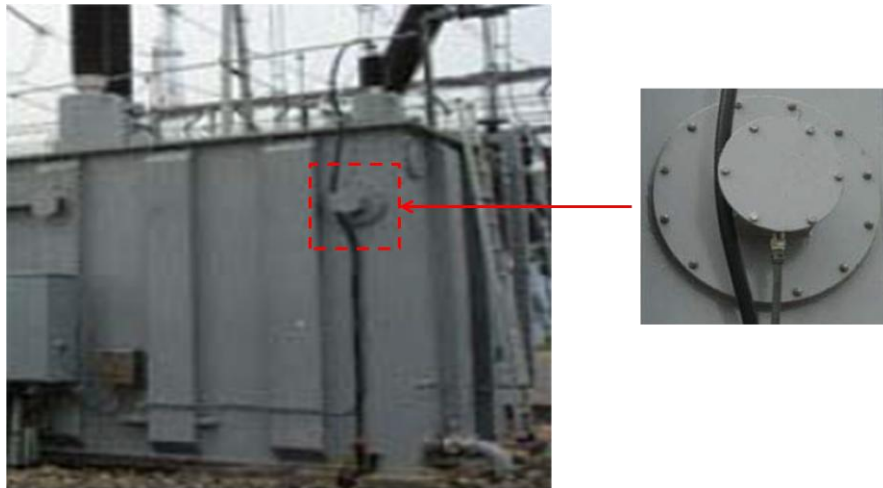


Figure 3.13: Internal spiral UHF PD sensor mounted on oil-filled transformer [102].

The third method of installing UHF PD sensors on power transformers is by insertion of probe sensor, as shown in Figure 3.14. The probe sensor is deployed through oil valve of the transformers [103], as described in Figure 3.15. This method is convenient because no extra structure is required on the transformer tank such as window; and PD measurement can be done while the transformer is in operation. However, the access to the oil valve is limited as it depends on how many are available and not in use. The oil valve must also be of a design that can allow a probe to be inserted when open such as gate valve. Therefore, locating PD source using this method alone is not effective where more than one UHF sensors are required. However, the combination of all the three types of UHF PD sensors (external window-type sensor, internal sensor and inserted probe sensor) for PD location in transformer tank can be possible.

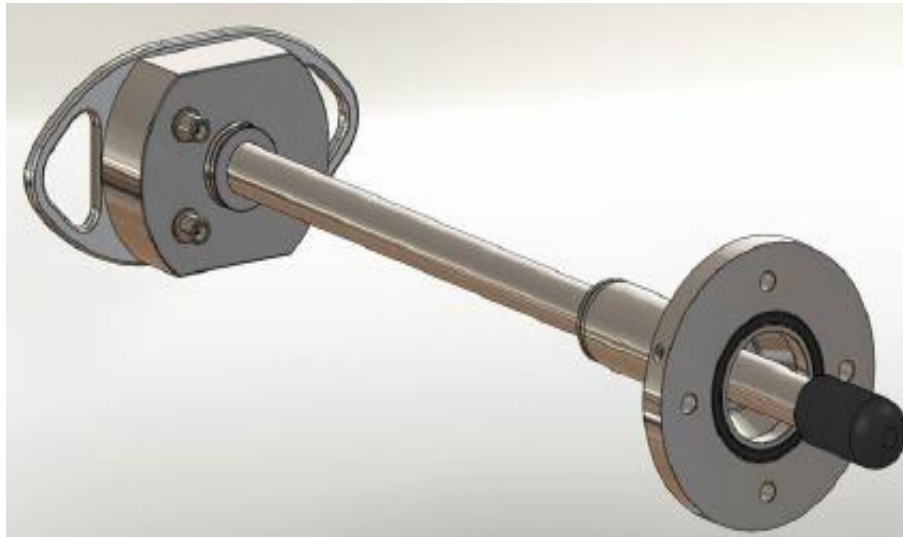
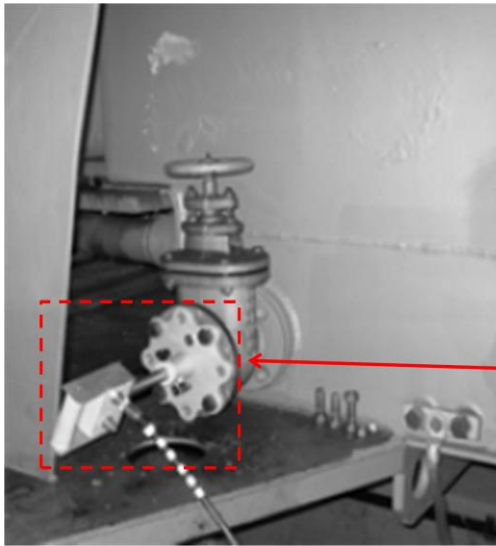


Figure 3.14: Probe UHF PD sensor for insertion through oil valve of power transformers [94].



(a)



(b)

Figure 3.15: UHF probe sensor installed at the drain valve of: (a) 380 kV [103] and (b) 110 kV [104] oil-filled transformers for on-line PD measurement.

Locating PD sources inside power transformers is possible by using more than one UHF PD sensor mounted on the transformer tanks. The differential arrival times of PD signals at three or four UHF sensors can be applied as the basis to predict the location of PD sources [94] [95]. PD-type signal in oil-filled transformers can be generated by using an artificial PD pulse that be injected externally to one of the sensors [105] [106]. The sensor can be any type of UHF PD sensors which is accessible to measure PD signal generated inside the power transformers. Pulse injection can test the operation of UHF PD location system for power transformers. For example, if there are four UHF PD sensors installed on the transformer tank, one of the sensors can be used as PD pulse injection point. The PD location should be at the area near to the location of the injected pulse sensor.

3.3 Conclusion

Installing UHF PD sensors on HV equipment can help to (i) monitor and trend the state of equipment insulation, and (ii) schedule maintenance activity and plan risk assessment of the equipment. Time domain signal from the sensor can be used to assess the location of PD source using time-of-flight method. The response of external UHF PD sensors can give better result compared to the response of internal sensors. Different designs and types of UHF PD sensors have different responses in measuring PD signals. Therefore, a method is needed to evaluate which sensor is the effective one. Sensor calibration system can be used to measure the responses of UHF PD sensors and a standard level of sensor responses can be applied to differentiate which sensors with the best responses. This technology will assist in selection of the most optimal UHF PD sensors to be installed on the equipment. The next chapter will elaborate the calibration systems of UHF PD sensors that been used to measure sensor responses.

Chapter 4: UHF Partial Discharge Sensor Calibration

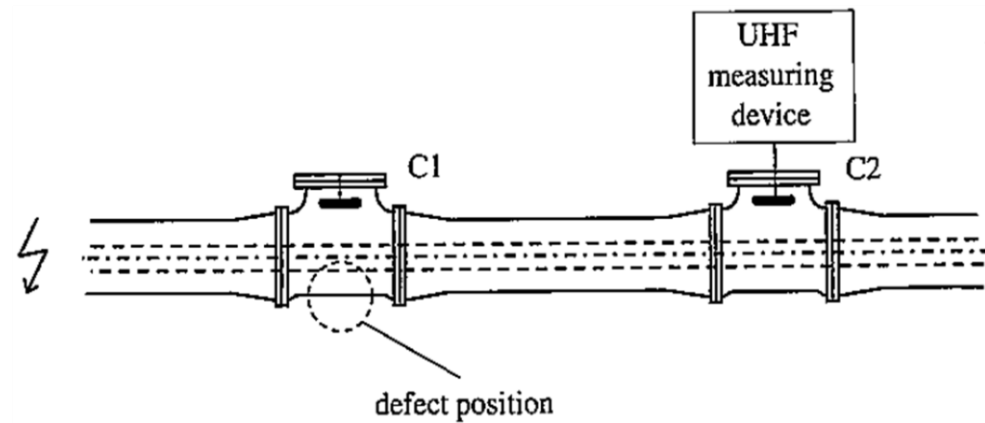
Generating a consistent PD signal from real defect in HV equipment can be difficult since the production of PD pulses can be influenced by (i) the types of defects such as metallic protrusion, free metallic particle and others, and (ii) the levels of applied voltages. Assessing the sensitivity of UHF sensors is possible by using a constant artificial pulse that represents the real defect of PD activities. Measuring the performance of UHF sensors using a standard artificial PD pulse as an input to a calibration system can establish the range of sensor responses. With the standard sensor response, the sensor manufacturers can fabricate UHF PD sensors within the standard requirement. This chapter discusses three types of UHF sensor calibration systems, which are double cone GIS system, cone calibration system, and transverse electromagnetic (TEM) calibration system.

4.1 Assessing the Sensitivity of UHF Sensors

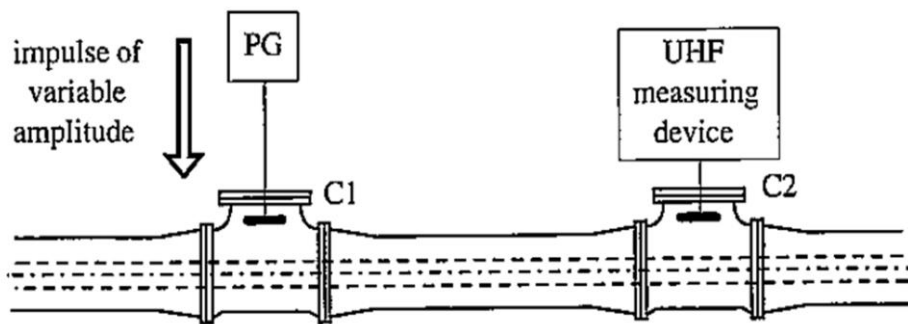
The designs and sensitivities of UHF PD sensors are different based on the application and specific requirements. The output of UHF sensors is a voltage signal. All these sensors have been designed based on accessibility of the sensors to be installed or mounted on high voltage equipment. The location and arrangement of sensor mounting on high voltage equipment may result in different sensitivity of the sensor.

The sensitivity of UHF PD sensors in GIS is aimed at ensuring they can detect a minimum level of PD apparent charge of about 5 pC [107] [108]. Internal UHF disc-type sensor was tested for sensitivity in GIS application, as shown in Figure 4.1. Two types of PD pulses were used which represent PD apparent charge of about 5 pC. They were real defect of free conducting particle inside GIS; and artificial low voltage pulse with an amplitude of 7 V that when applied to a UHF sensor emits UHF signals [107]. The real defect was placed near to sensor 1 (C1) as shown in Figure 4.1. The artificial pulse was applied to the first sensor (C1) and UHF signal similar to the electromagnetic wave of the

real defect was measured at the second sensor (C2). The amplitude of the artificial PD pulse was varied until the magnitude of the measured UHF signal was about the same magnitude as the measured UHF signal acquired from the real defect. Figure 4.2 shows the UHF signals detected by disc sensors for the real defect and varied artificial pulse with some amplitude differences at certain frequency ranges especially at frequency of 600, 1000 and 1300 MHz.

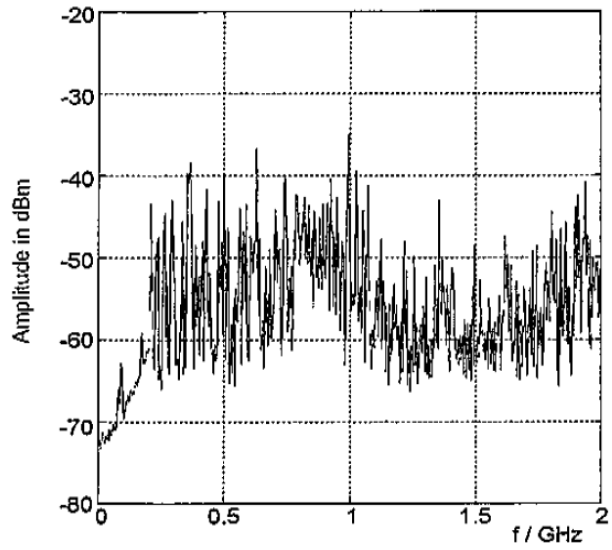


(a)

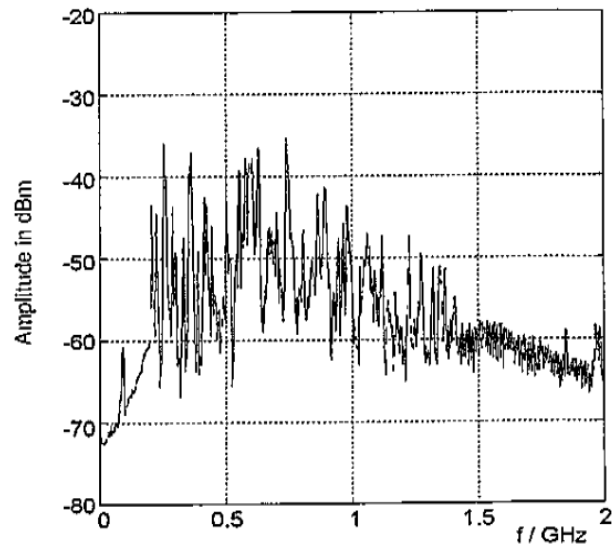


(b)

Figure 4.1: Experimental measurement of assessing the sensitivity of internal UHF PD sensor for GIS application using: (a) real defect and (b) artificial PD pulse. Note that PG, C1 and C2 stand for pulse generator, coupler 1 and coupler 2, respectively [107].



(a)



(b)

Figure 4.2: The frequency responses of UHF PD signals for: (a) real defect of free particles and (b) artificial PD pulse of electromagnetic waves with applied amplitude of 7 V [107].

The same method of sensitivity verification has been applied to a UHF PD sensor of a power transformer [109]. A spark plug, as a real defect, was mounted on the top cover of transformer tank near to one of the external window-type sensors (Sensor 1), as shown in Figure 4.3. The sensor response was measured at another sensor (Sensor 2). The artificial pulse of 14.2 V that represented as spark plug defect was applied to Sensor 1. The comparison of UHF signals measured by window-type sensors for spark plug defect and artificial pulse is depicted in Figure 4.4, with more amplitude differences especially in the frequency range above 500 MHz. Therefore, a standard sensitivity check for UHF PD sensors is important where all UHF sensors can be tested using a standard test procedure. It also helps sensor manufacturers to evaluate and improve their sensor design based on customer requirement. The next sections discuss some standard procedures for calibration system of UHF PD sensors.

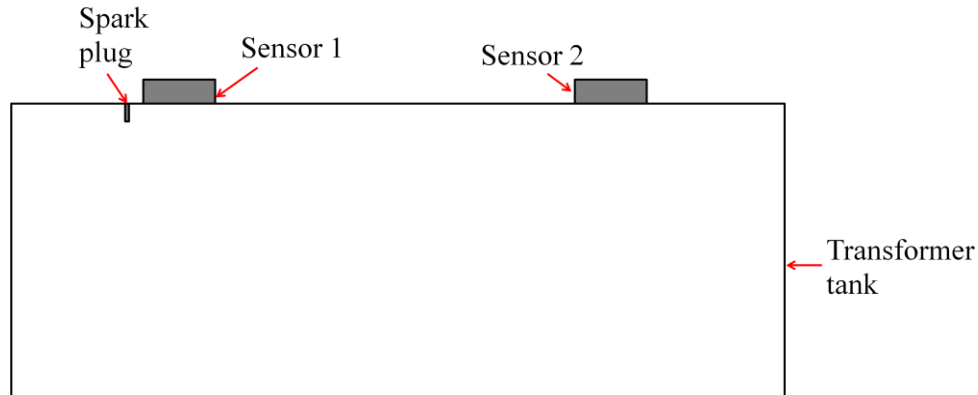


Figure 4.3: Illustration of laboratory setup used to perform a sensitivity check for UHF PD detection on power transformer.

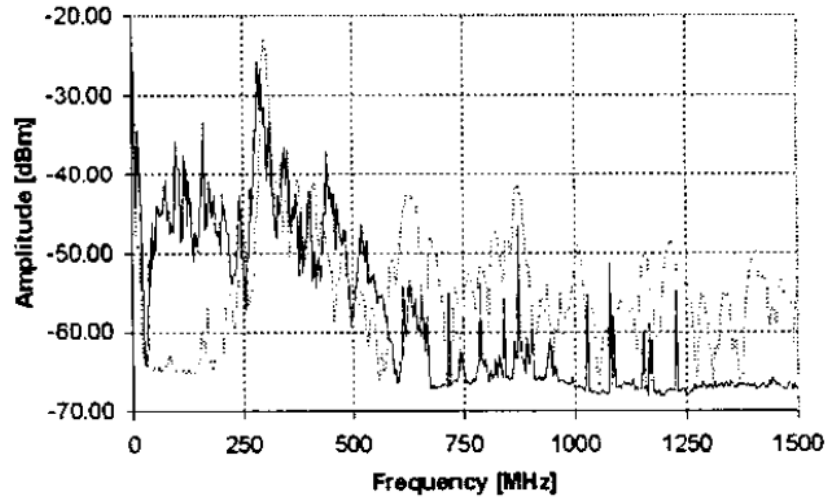


Figure 4.4: The responses of UHF PD signals generated by spark plug (solid line) and artificial pulse of electromagnetic waves with applied amplitude of 14.2 V (dotted line) [109].

4.2 Double Cone GIS System

UHF sensors are widely used for detecting and locating PD sources in GIS system. The frequency responses of the sensors can be measured using double cone GIS chamber. The cone is as a tapered coaxial transmission line enables that the large GIS to be connected to standard 50 Ω RF connectors. Neuhold [110] examined the difference of the internal sensor responses measured by (i) CIGRE method [107] with real PD source (needle electrode on GIS conductor) and (ii) double cone GIS chamber. The GIS test chamber, as described in Figure 4.5, was used to measure the sensor response using CIGRE method. The real defect was placed on HV conductor near the internal sensor. Figure 4.6(a) shows the schematic diagram of the double cone GIS test chamber used to measure the frequency response of UHF sensor. The input and output terminals are connected to applied voltage source and 50 Ω load, respectively. The input power level of -60 dBm, corresponds to power (P) of 1 nW ($\text{dBm} = 10 \log_{10}(1000P)$) and 0.224 mV on 50 Ω load, from HP 8591E spectrum analyser was applied to the input terminal. The measuring system consists of a GIS section, as shown in Figure 4.6(b), with conical coaxial lines as the transmission lines. The UHF PD sensor is mounted at the middle of the double cone

test chamber. Figure 4.7 compares the internal sensor responses measured using CIGRE method and double cone GIS system. The differences in the responses of both methods can be due to (i) the internal sensor on double cone GIS system captured some reflected signals (because of impedance mismatch at the output terminal) as the cone length is too short to differentiate reflected signal from required signal, and (ii) the signal of injected input power does not represent PD signal with fast rise time.

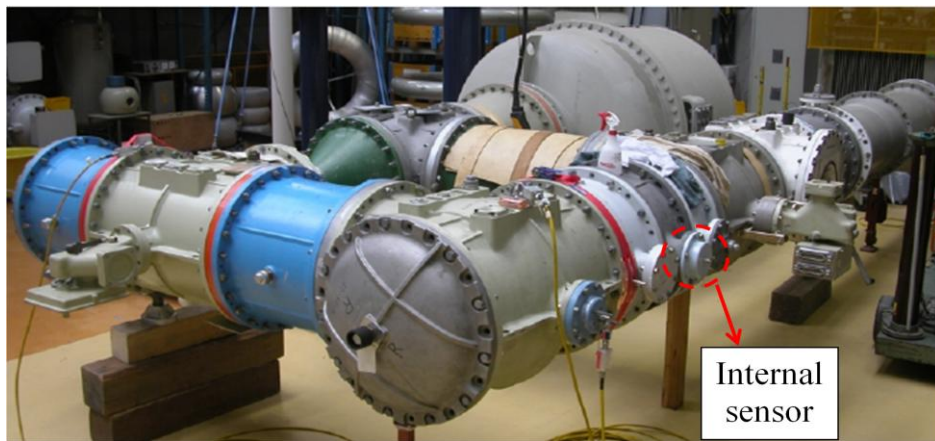
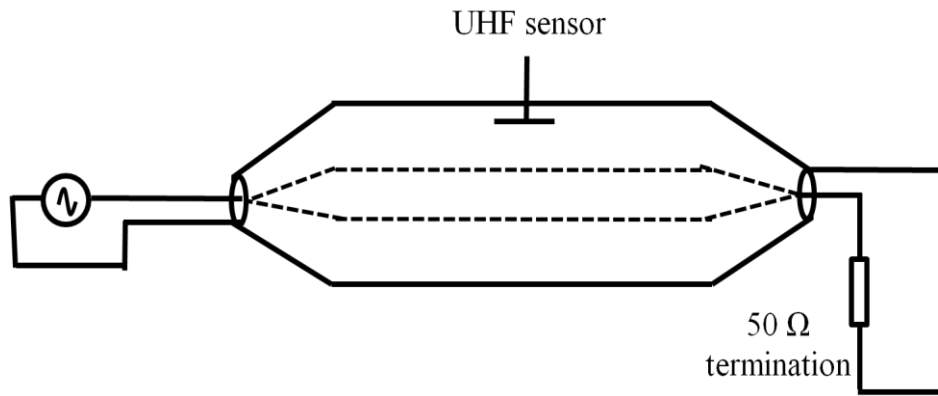


Figure 4.5: GIS test chamber used to measure internal sensor response using CIGRE method [110].



(a)



(b)

Figure 4.6: Double cone GIS test chamber: (a) schematic diagram and (b) fabricated chamber [110].

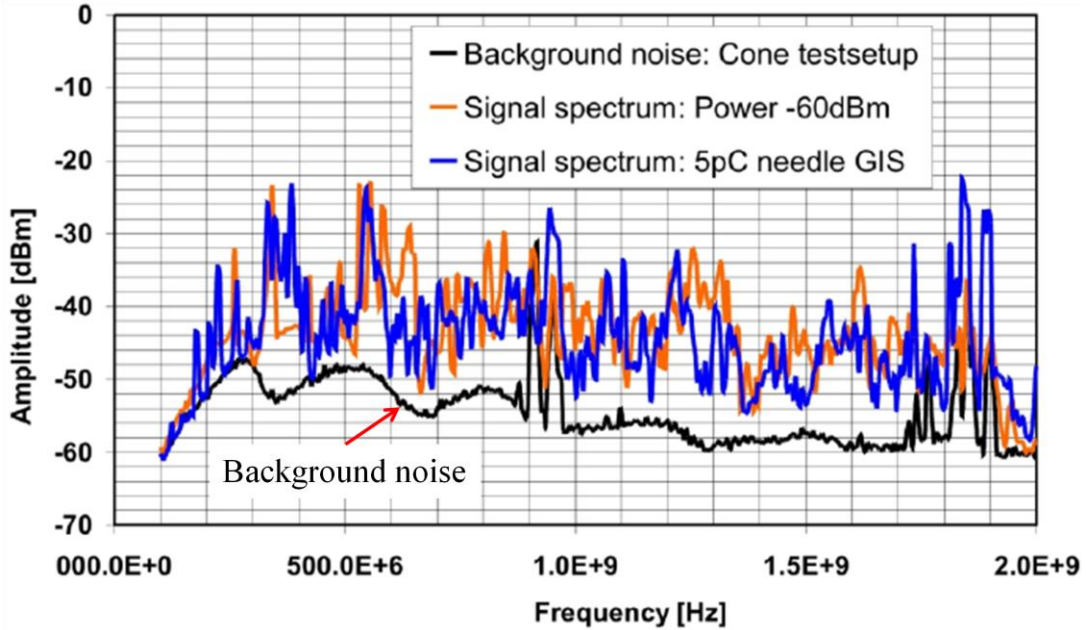


Figure 4.7: Frequency responses of internal UHF PD sensor using CIGRE method (blue line) and double cone GIS system (orange line). The background noise (black line) was measured when the input power of double cone GIS system was disconnected [110].

4.2.1 The Model of UHF PD Sensor as a Capacitor

Kurrer [111] explained that UHF PD sensor is behaving like an antenna at high frequency range. The calculated frequency responses of internal disc sensor, as a capacitive divider and the antenna impedance, are compared with the measured frequency response using double cone test chamber. The equivalent circuit that represents internal disc sensor as capacitive sensor in GIS tank is shown in Figure 4.8. C_1 and C_2 represent the capacitance between inner conductor of the GIS and disc sensor, and the capacitance between the disc sensor and GIS enclosure. R_L is defined as the resistance of measuring equipment. U_0 and U_2 are symbolised as the excited voltage source at the sensor plate and voltage difference at R_L , respectively. The calculated frequency response of the disc sensor is shown in Figure 4.9. The response is calculated by inserting (4.1) into (4.2). Z_1 is the parallel impedance of R_L and reactance of C_2 capacitance (X_{C_2}).

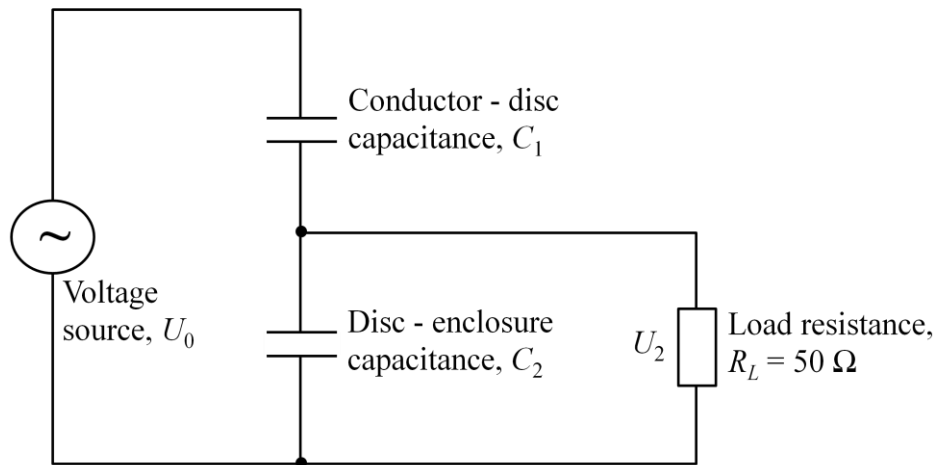


Figure 4.8: Circuit diagram for internal disc sensor as a capacitive sensor inside GIS tank [111].

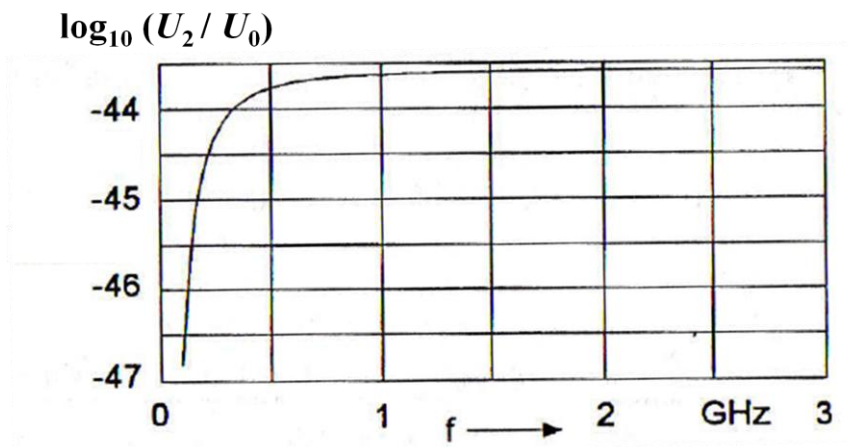


Figure 4.9: Calculated frequency response of a disc sensor modelled as a capacitive sensor where R_L equals to 50Ω , C_1 is 0.2 pF for a 420 kV commercial GIS tank and C_2 is 30 pF for the disc sensor [111].

$$Z_1 = \frac{1}{\frac{1}{R_L} + \frac{1}{X_{C_2}}} = \frac{1}{\frac{1}{R_L} + \omega C_2} \quad (4.1)$$

$$\frac{U_2}{U_0} = \frac{Z_1}{Z_1 + \frac{1}{\omega C_1}} = \frac{C_1}{C_1 + C_2 + \frac{1}{\omega R_L}} \quad (4.2)$$

4.2.2 The Model of UHF PD Sensor as an Antenna

In UHF range, the internal disc sensor in GIS tank was represented as disc antenna, as defined in circuit diagram of Figure 4.10. The antenna impedance Z_a consists of real part (R_a resistance) and imaginary part (X_a reactance with C_a capacitance), as in (4.3). The conductance and susceptance of the disc impedance represent as Y_a and Y_b , respectively, are given in (4.4). The feeding line is the transmission line between the disc plate and sensor output terminal with the length of L . The characteristic impedance of the feeding line (Z_0) equals to 210Ω . The input impedance of the feeding line (Z_{in}) at the feeding line end is given in (4.5) where β , λ , f and c are phase constant, wavelength, frequency and speed of light, respectively.

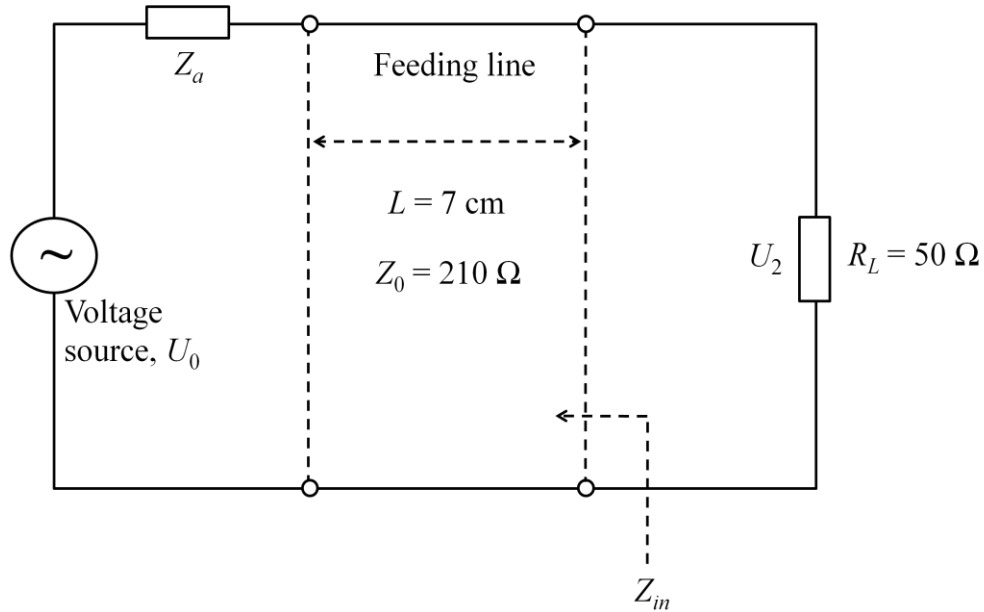


Figure 4.10: Equivalent circuit of internal disc antenna in UHF range inside GIS tank [111].

$$Z_a = R_a - j X_a = R_a - j \frac{1}{\omega C_a} \quad (4.3)$$

$$Z_a = \frac{1}{Y_a - j Y_b} = \frac{1}{\frac{R_a}{R_a^2 + X_a^2} - j \left(-\frac{X_a}{R_a^2 + X_a^2} \right)} \quad (4.4)$$

$$Z_{in} = Z_0 \left(\frac{Z_a + j Z_0 \tan(\beta L)}{Z_0 + j Z_a \tan(\beta L)} \right), \quad \beta = \frac{2\pi}{\lambda}, \quad \lambda = \frac{c}{f} \quad (4.5)$$

The calculated frequency response of the disc antenna is shown in Figure 4.11. The response is calculated by substituting (4.6) and (4.7) into (4.8) where R_{in} is the source impedance (50Ω) at the input terminal of GIS and U'_0 is the applied voltage at the input terminal of GIS section, as described in Figure 4.12.

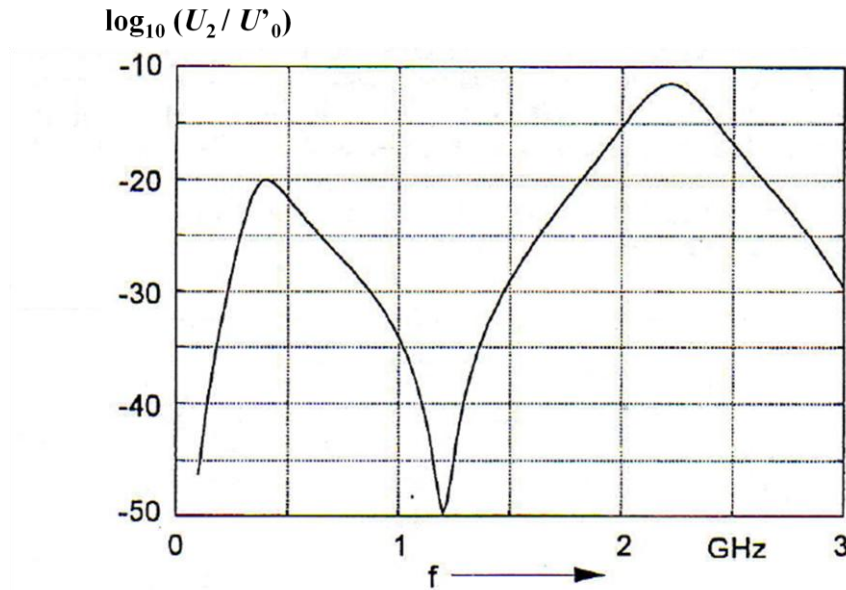


Figure 4.11: Calculated frequency response of a disc antenna where R_a resistance is 11Ω and C_a is 3.3 pF [111].

$$\frac{U_0}{U'_0} = \sqrt{\frac{Y_a R_{in}}{2}} \quad (4.6)$$

$$\frac{U_2}{U_0} = \frac{R_L}{R_L + Z_{in}} \quad (4.7)$$

$$\frac{U_2}{U'_0} = \frac{U_0}{U'_0} \cdot \frac{U_2}{U_0} \quad (4.8)$$

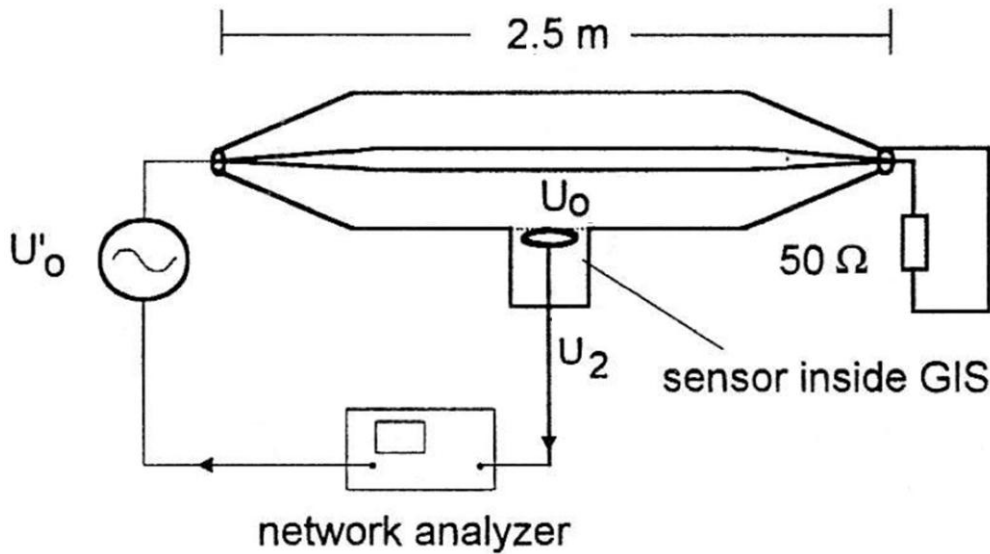


Figure 4.12: The measurement of the frequency response of disc sensor using the double cone calibration system [111].

The frequency response of internal disc antenna, shown in Figure 4.13, was measured using the double cone GIS system. The disc sensor is better represented as disc antenna than capacitive sensor. This is because the calculated frequency response of disc antenna (Figure 4.11) demonstrates better response characteristic than capacitive sensor (Figure 4.9) when compared with measured frequency response (Figure 4.13) at high frequency range.

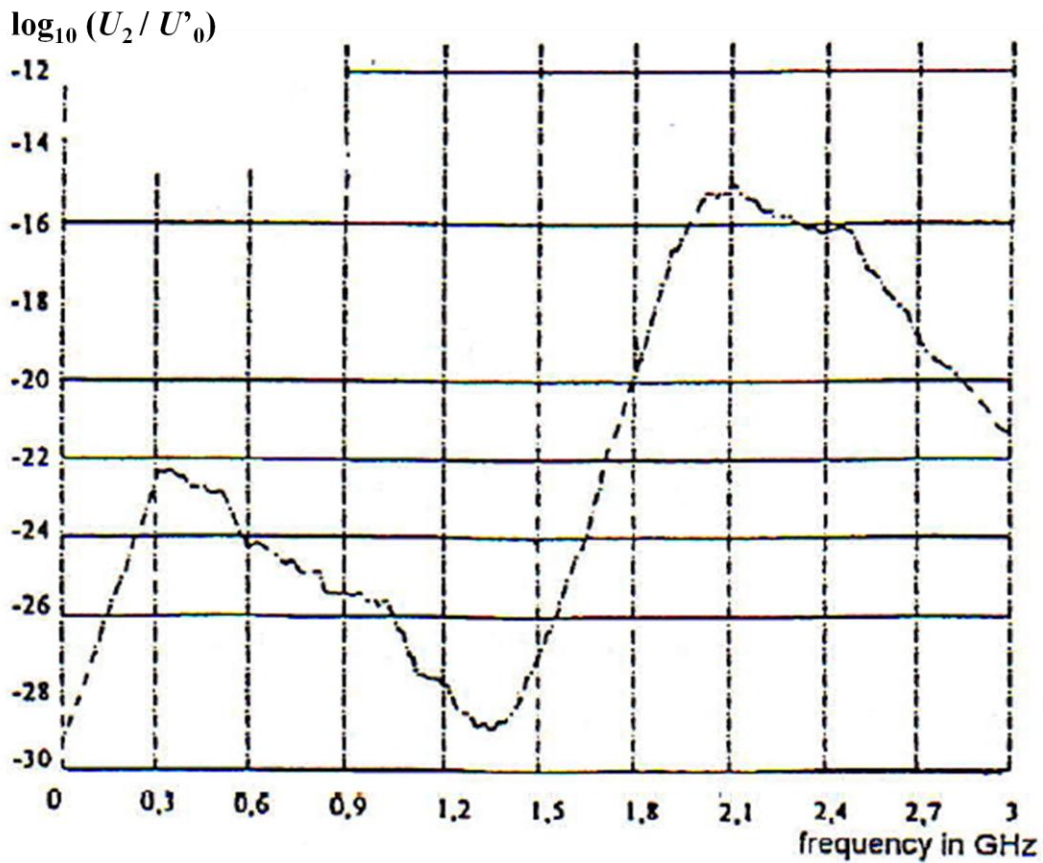


Figure 4.13: Measured frequency response of an internal disc sensor using the double cone GIS system [111].

4.3 Monopole Cone Calibration System

A new calibration system for UHF sensors has recently been proposed which basically consists of a large monopole cone antenna, metallic ground plane, and signal generator [112]. The signal generator was connected to the cone antenna where electromagnetic wave was transmitted to the sensor location, as pictured in Figure 4.14. The cone calibration system was performed in an anechoic chamber, as illustrated in Figure 4.15, to reduce any disturbance from the surrounding environment since the calibration system is an open transmission line.

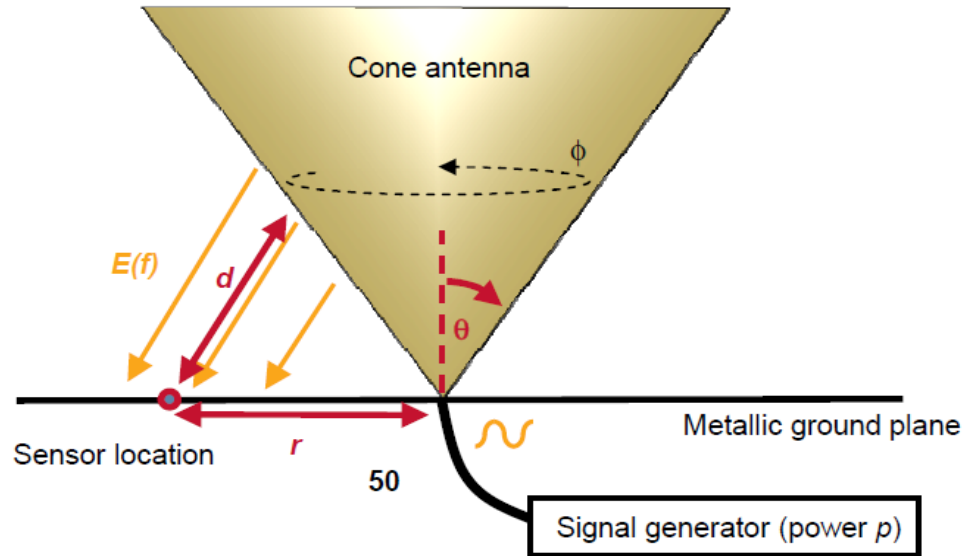


Figure 4.14: Basic representation of monopole cone calibration system [112].

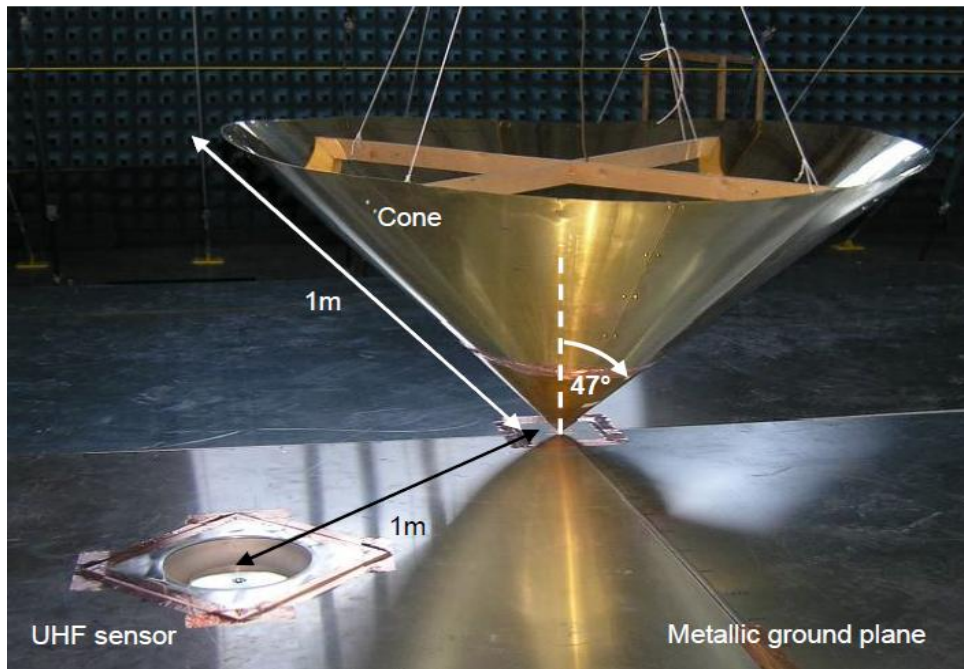


Figure 4.15: Monopole cone calibration system was installed in an anechoic chamber with UHF sensor located 1 m away from the antenna feed point [112].

The electric fields on a ground plane of the cone calibration cell were measured using monopole sensor, as shown in Figure 4.13. The size of the square ground plane is $4\text{ m} \times 4\text{ m}$. The measurements were done at 16 different locations of the sensor in a square area of $15\text{ cm} \times 15\text{ cm}$ (one measurement at every 5 cm). The variations of the electric fields for 16 different locations of the sensor is within a range of $\pm 1.5\text{ dB}$. The result shows that the measurement may have low uncertainty of the electric fields. However, more studies need to be done on this system to measure the sensor response such as the effects of (i) different lengths and opening angles of the cone antenna, (ii) reflections at the end of the cone antenna, and (iii) the distance of sensor location from the cone antenna on the responses of UHF sensors.

4.4 TEM Calibration of UHF Partial Discharge Sensors

The previous calibration systems, double cone GIS system and monopole cone calibration system, use a network analyser to inject a swept frequency signal into the transmission line. The injected signal generates electromagnetic wave with sinusoidal form which, due to reflections and standing waves, could reach the sensor under test when the field strength at the maximum, minimum or in between. The measured output from the sensor which is in frequency domain can be influenced by both the input signal and reflected signal.

The transverse electromagnetic (TEM) calibration system reported by M. Judd in paper [113] was designed to inject a step signal into the system which generated a uniform electromagnetic wave. Instead of trying to eliminate reflected signals at the end of transmission line, the required response to the incident signal is obtained using time-domain gating. The acquisition of the signal is limited to times before the reflection occurs.

This section describes the origins of a (TEM) calibration system that was used to measure the frequency responses of UHF PD sensors, as explained by M. Judd in paper [113]. TEM wave is a characteristic when electric field and magnetic fields are perpendicular to each other, and both fields are perpendicular to the direction of wave

propagation, as explained by F. T. Ulaby [114]. The electromagnetic waves generated by PD activities are transmitted through the dielectric material which surrounds the PD source and can be measured by UHF sensors. An artificial pulse of known intensity can be used to represent the electromagnetic wave and measure the performance of UHF sensors. A pulse generator can generate an artificial step electric field with a short rise time similar to PD signal in TEM calibration cell. The cell supports a plane wave that propagates in TEM mode. The calibration system can be used to measure the responses of UHF PD sensors for any application without building actual high voltage equipment such as GIS tank or transformer tank.

The frequency responses of UHF PD sensors are calculated by dividing the output voltage of the sensors (mV) in frequency domain over the input electric field of reference monopole probe (V/m) in frequency domain giving sensitivity in units of mm. The input electric field of the sensor under test is determined by using the output voltage of a reference monopole probe placed at the location of the tested sensor. The Fast Fourier Transform (FFT) and equivalent circuit formula (equation (5.1) which will be explained in section 5.3) are applied to calculate the input electric field in frequency domain.

A monopole probe was used as a reference to measure the incident electric field of the sensors in TEM calibration cell, as shown in Figure 4.16. 25 mm probe was chosen because the effective height (h_e) and input impedance (Z) of the probe can be calculated, as described in [115] [116], and the size of the probe is small where the response can be assumed as the response to the electric field at a point. The equivalent circuit of the probe as an electric field sensor is presented in Figure 4.17 and the transfer function of the circuit can be represented as in (4.9).

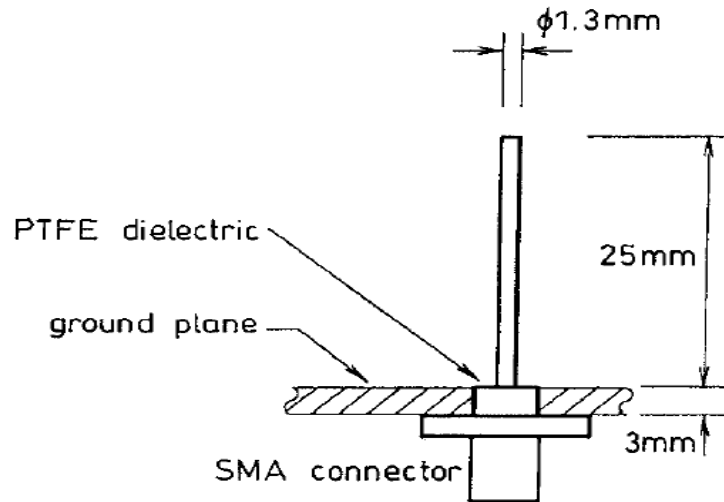


Figure 4.16: Reference monopole probe used to measure electric field normal to UHF sensor [113].

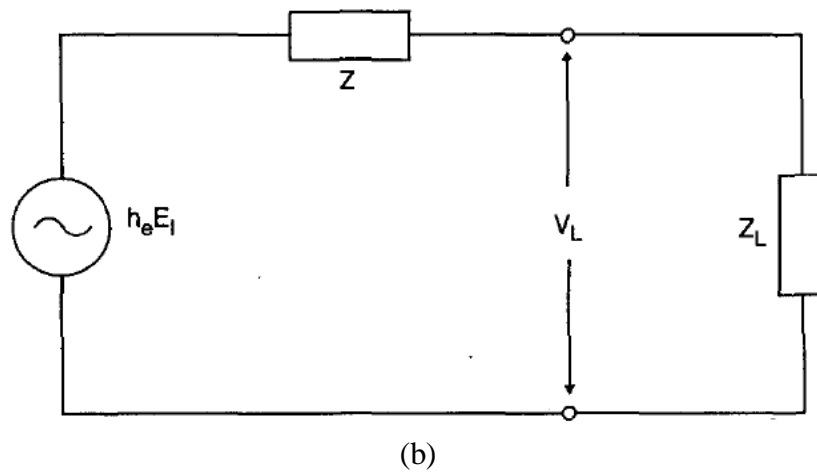
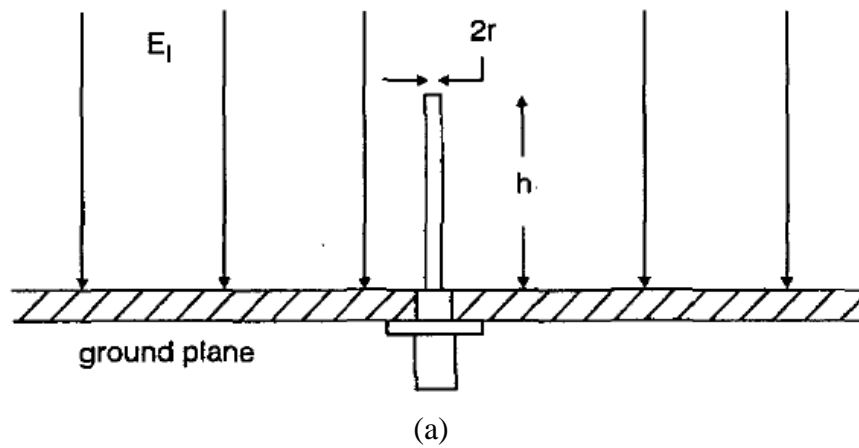


Figure 4.17: Reference monopole probe: (a) configuration; and (b) equivalent circuit [116].

$$H = \frac{V_L}{E_I} = \frac{h_e Z_L}{Z + Z_L} \quad (4.9)$$

where V_L = output voltage (mV)

E_I = incident electric field that normal to ground plane (V/m)

h_e = effective height of the probe (mm)

Z_L = load impedance (50 Ω)

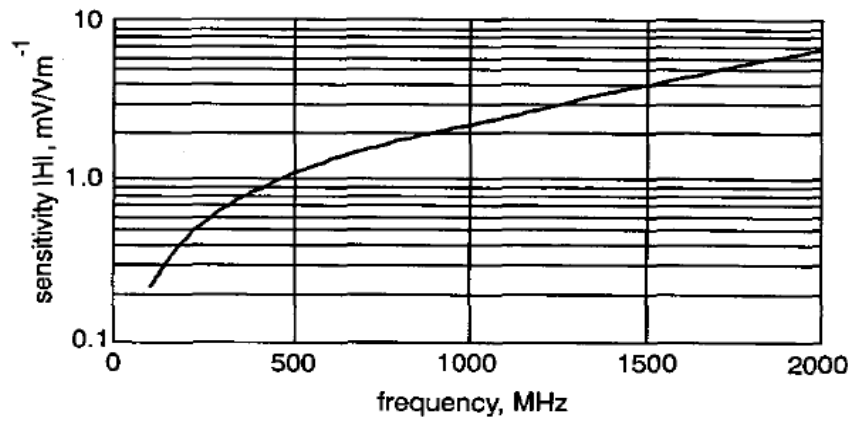
Z = input impedance (Ω)

Parameters that define the theoretical transfer function of the 25 mm monopole probe are tabulated in Table 4.1. The theoretical and measured responses of the reference probe using the cell are compared in Figure 4.18 with minimal errors. The probe was also measured at the National Physical Laboratory (NPL) for validation.

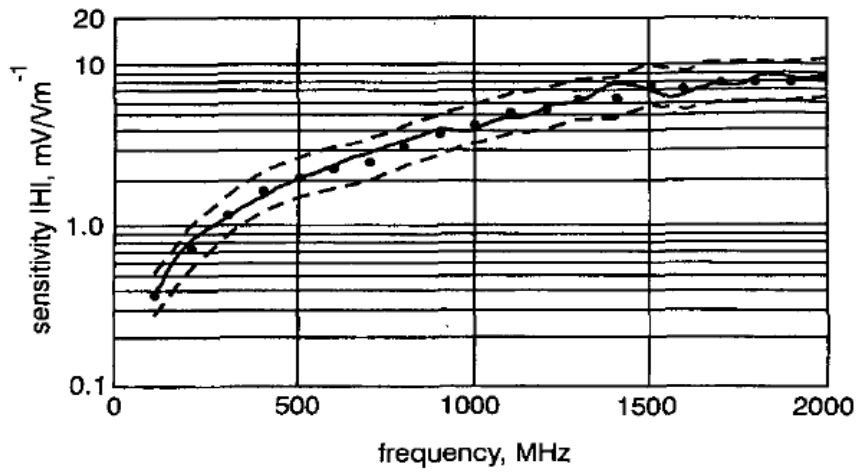
Table 4.1

Calculated transfer function of the 25 mm reference monopole probe [116].

Frequency (MHz)	Effective height, h_e (mm)		Input impedance, Z (Ω)		Sensitivity, $ H $ (mm)
	Real part	Imaginary part	Real part	Imaginary part	
954	11.6	0.0	2.5	- 280.0	2.0
1336	12.0	- 0.1	5.2	- 179.7	3.2
1718	12.6	- 0.1	9.2	- 115.5	4.9
2099	13.3	- 0.2	15.2	- 68.5	7.0



(a)



(b)

Figure 4.18: Frequency responses of the 25 mm reference monopole probe: (a) theoretical response; (b) laboratorial measurements, note that \bullet , — and - - - represent NPL measurement, transient measurement and calibration uncertainty limits, respectively [116].

The open TEM calibration cell consists of a ground metal plane (bottom plane) and a conductor plane (top plane) supported by insulating rods, as illustrated in Figure 4.19. A parallel plate transmission line was created in which the artificial electric field is perpendicular to the UHF sensor, as explained in Figure 4.20. The signal generator is connected at the input side of the conductor plane; and 50Ω load is terminated at the output side. The load impedance Z_L must be matched to the characteristic impedance of the transmission plane Z_0 to minimize the wave reflection coefficient, Γ that is related through (4.10) [114].

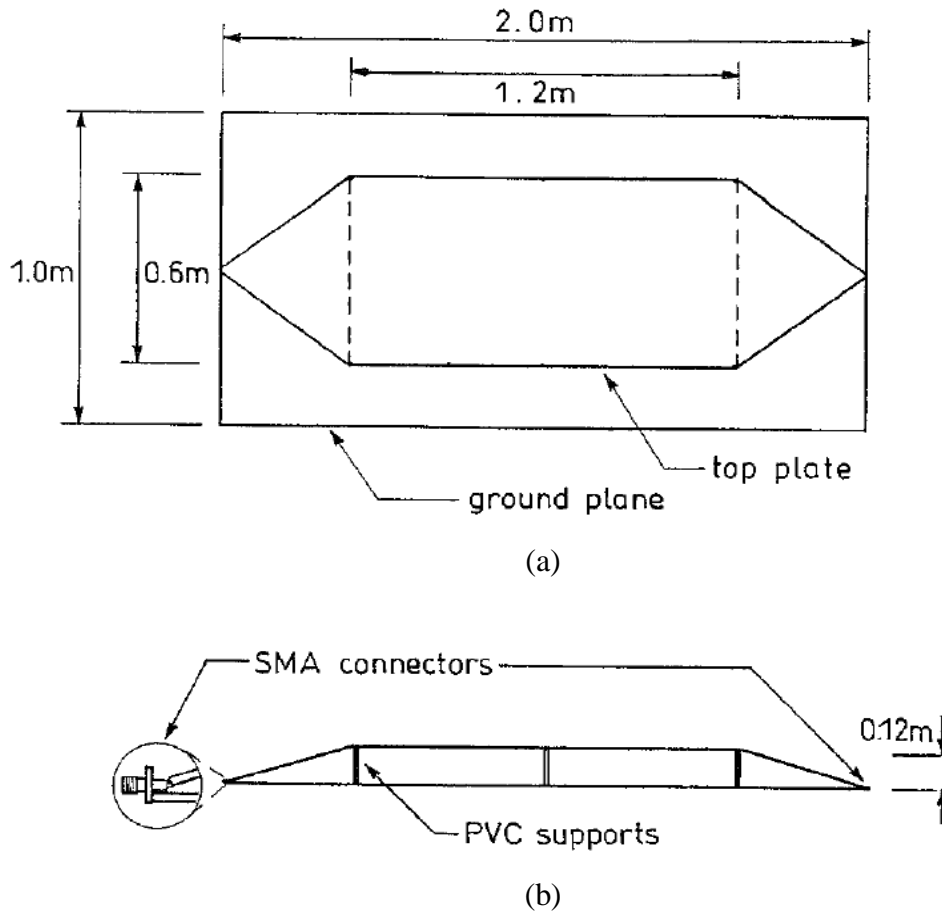


Figure 4.19: The structure of open TEM calibration cell (a) top view; and side view [113].

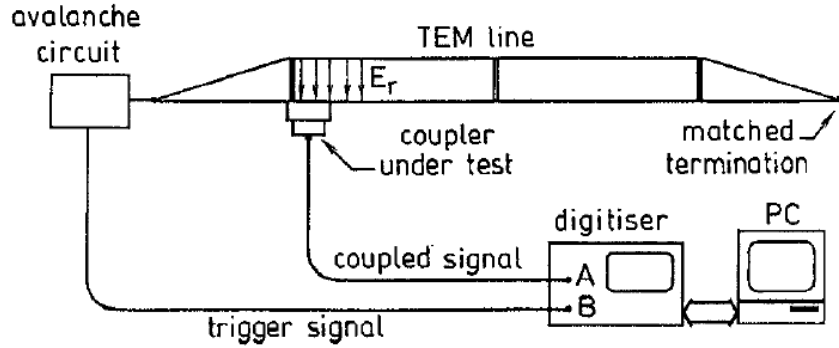


Figure 4.20: Test configuration for response measurement of UHF sensors using TEM calibration cell [113].

$$\Gamma = \frac{Z_L - Z_0}{Z_L + Z_0} \quad (4.10)$$

The sensor sensitivity was specified by dividing the output voltage of the sensor in frequency domain by the incident electric field normal to the sensor in frequency domain. The frequency range of 200 – 1800 MHz was defined as operational frequency range for the calibration system [113]. However, the calibration system required an amplifier to overcome the radiation loss due to its open structure. This enables the generated electromagnetic waves radiate to the outside environment. The corners at the conductor plane also introduce electric field distortion that affects electric field uniformity inside the TEM cell.

4.5 Conclusion

The sensitivity of UHF PD sensors is measured using a standard calibration cell instead of using a representative structure of high voltage equipment such as GIS tank and power transformer tank, as explained by Neuhold in paper [110] and Kurrer in paper [111] using double cone GIS test chamber; Gautschi in paper [112] using monopole cone calibration system; and Judd in paper [113] using TEM calibration system. It was found that an artificial pulse is applied to represent the electromagnetic wave generated by PD source,

as described by CIGRE in paper [107] tested in GIS tank and Meijer in paper [109] experimented in a transformer tank. Therefore, applying the same pulse as an input signal, the sensitivity of UHF PD sensors with different designs can be obtained and compared. It has been proved that the UHF PD sensor is better represented as an antenna rather than as a capacitive sensor. The response of UHF PD sensors is affected by antenna impedance and characteristic impedance of the sensor feeding line. UHF PD sensor was firstly used in GIS system to detect PD activity and then the sensor was applied in power transformer. Therefore, many studies to assess the sensitivity of the sensors were done in GIS system. The disadvantage of double cone GIS calibration system is shorter transmission line which causes signal reflection at the end of the line. Monopole cone and TEM calibration systems use open calibration cells where noise signals from surrounding environment could affect the sensor sensitivity.

Chapter 5: GTEM Calibration of UHF Partial Discharge Sensors

A completely enclosed TEM calibration cell was developed to reduce the radiation losses. The structure of the cell also avoids the corners to maintain the uniformity of the electric field inside the cell. The cell measures the frequency response of UHF sensors and it is known as GTEM (gigahertz transverse electromagnetic) calibration cell [116]. The GTEM cell provides shielded environment, it does not require internal support for the septum (inner conductor), and the cell length allows the sensor response to be measured before unwanted reflection reaches the sensor.

Partial discharge signals generate electromagnetic waves that are capable of propagating through free space and dielectrics. The wave can be detected by UHF PD sensors with an acceptable sensitivity. National Grid Company requires that the average sensitivity of UHF PD sensors for the frequency range 500 to 1500 MHz must be larger than 6.0 mV/Vm^{-1} where the output voltage of the sensors is 6 mV rms for an incident UHF electric field of 1 Vm^{-1} rms [117]. The minimum sensitivity shall not be less than 2.0 mm over at least 80% of the frequency range, as defined in Table 5.1. The requirements are applied to both internal and external UHF sensors for GIS application. Typically, PD peak signals in GIS occur in the frequency range of 500 to 1500 MHz [118] [75] [119]. This standard has been used by UHF sensor manufacturers as a guidance to design their sensors even for other application, such as in power transformer. PD peak signals that generated in oil power transformer also take place in the same frequency range [120].

Calibration is a special form of testing and quality assurance whose objective is to make sure measurement and control instruments are within specified limits. A standard calibration system can be used to calibrate the sensitivity of the sensors in a laboratory [121]. In the calibration system, there are two important elements, which are the structures of calibration cell and the parameters of incident step excitation. This system can be used as a standard test condition to compare different types of UHF PD sensors and optimize the design of new sensors.

Table 5.1

UHF sensor specification for GIS application [117].

Frequency range (MHz)	Mean effective height, H_e (mm)	Minimum effective height, $H_{e\ min}$ (mm)
500 – 1500	6.0	2.0

5.1 The Structures of Calibration Cell

Electromagnetic wave propagates in free space at the velocity of light and consists of oscillating electric and magnetic field intensities. Calibration cell is a fundamental tool in evaluating the performance of UHF PD sensors that permits the simulated effects of TEM plane wave incident on sensor under test.

The pulsed GTEM test cell described in [121] can be used to calibrate the UHF sensor experimentally. It has been designed to measure frequency response of UHF sensors at high-frequency range. The length of the cell, depicted in Figure 5.1, is 3 m with an output aperture of 1 m × 1 m. The septum of the GTEM cell is formed by 9 separate wires in a plane halfway between the upper and lower faces of the cell. A 10 V pulse generator is connected to the input of the wires which excites a propagating electric field step. The wires are terminated at steel rod that provides mechanical support. Figure 5.2 shows the GTEM calibration cell which was used to measure the frequency responses of UHF PD sensors in laboratory. Table 5.2 describes the specifications of test equipment used to calibrate UHF PD sensors in laboratory. The cell benefits from the Faraday Cage principle where the electric field within a closed surface is zero. All the external disturbances, for example mobile phone signals, can be eliminated. The sensor under test is mounted at measurement aperture which is halfway between the input conductors and output terminated conductors. The sensor is subjected to an incident TEM wave of known intensity. TEM transmission lines are used to generate an electric field similar to that experienced by the sensors when monitoring PD activities.

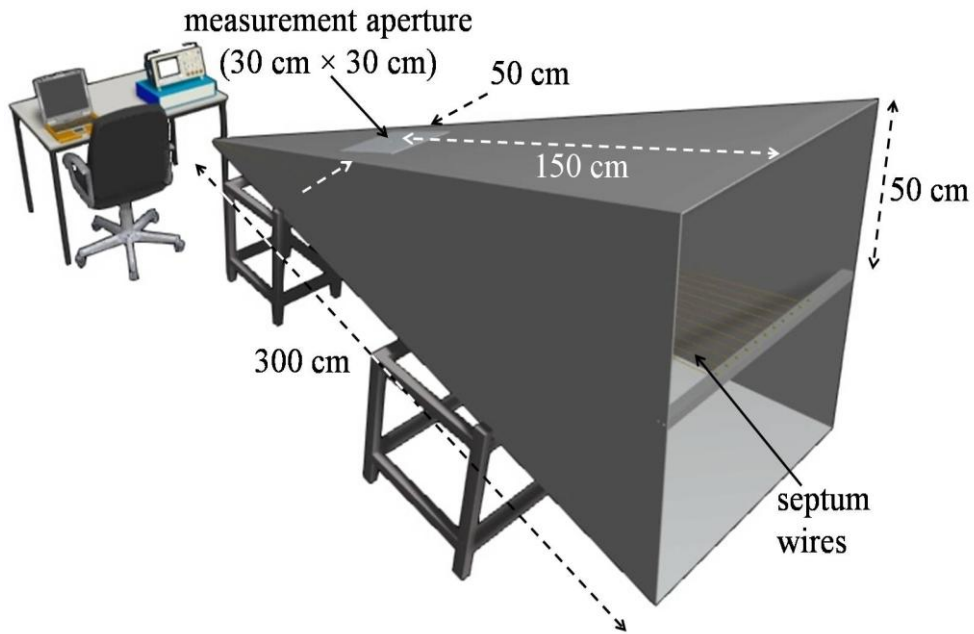


Figure 5.1: Illustration of the GTEM cell. UHF PD sensors to be tested are mounted at the measurement aperture.

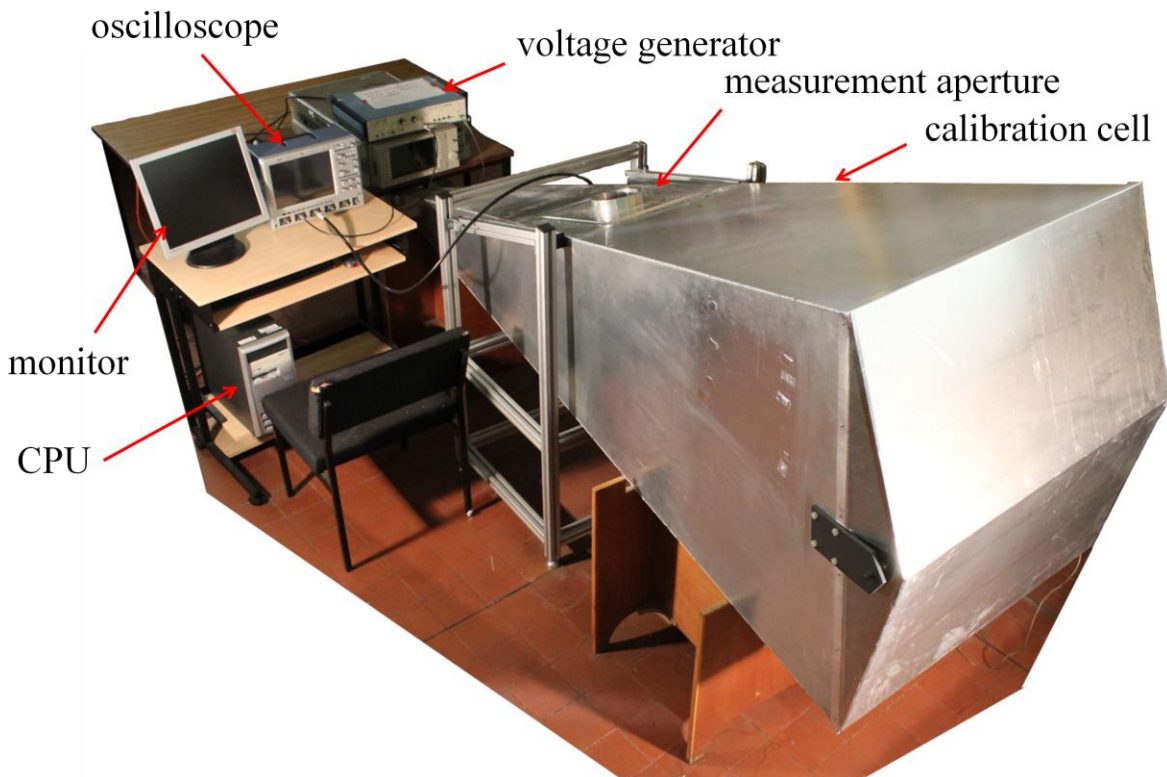


Figure 5.2: The GTEM cell to measure frequency responses of UHF PD sensors in the laboratory.

Table 5.2

Specifications of test equipment for UHF PD calibration system.

Equipment	Specification
Pulse generator	Manufacturer: Picosecond Pulse Labs (PSPL) Model: 4050 Rise time: 45 ps (transition duration from 10% to 90% of 10V) Positive pulse amplitude: 10 V Pulse duration: 10 ns (transition duration at 50% of amplitude level between rise time and fall time)
Oscilloscope	Manufacturer: LeCroy Model: WaveRunner 104Xi Bandwidth: 1 GHz Sampling rate: 10 GSamples/s Channels: 4

5.2 The Parameters of Incident Step Excitation

The step excitation of electric fields can be easily generated using a simple electrical circuit compared to pulsed excitation. Figure 5.3 shows the generated voltage from the 10 V step generator that been injected to the septum wires of the GTEM cell. The rise time is a measure of the upper frequency limit for electromagnetic waves emitted from PD signals. The 10% - 90% rise time of the step voltage is 350 ps measured using a digitiser with an analogue bandwidth of 1 GHz. During the measurement of sensor responses, the signals are measured using a 1 GHz bandwidth digitiser (LeCroy oscilloscope).

For laboratory calibration, a monopole probe is used as a standard to measure the incident uniform field at the location of measurement aperture, as described in section 4.4. The sensitivities of UHF PD sensors are obtained as a frequency response in post-processing using a fast Fourier transform (FFT) algorithm. This involves dividing the output voltage of the sensors in frequency domain (mV) by the input electric field in frequency domain (V/m) to give the sensitivity as an *effective height* in mm.

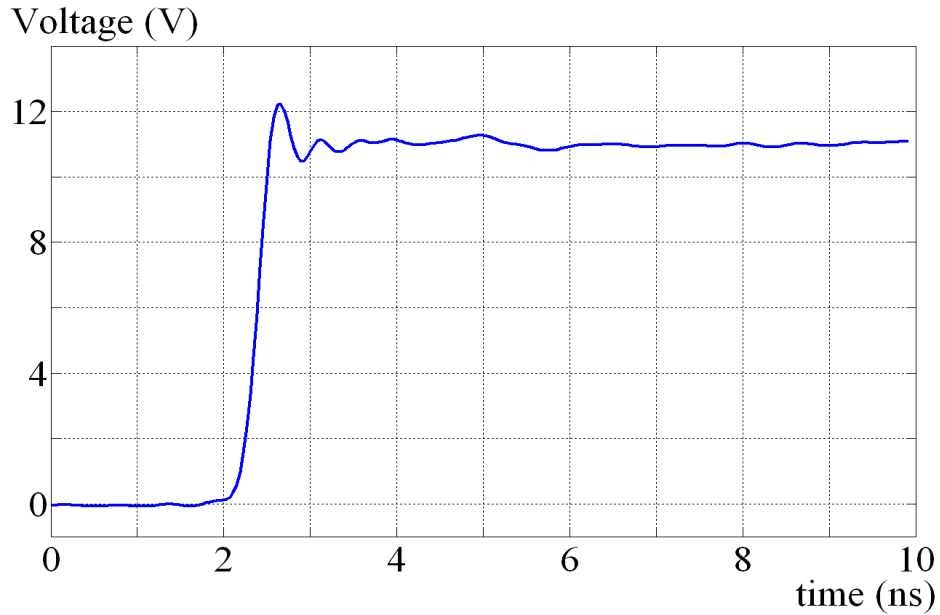


Figure 5.3: The step voltage from voltage generator circuit [121]. The pulse was injected to the calibration cell until the unwanted reflected wave was detected by the tested sensor. The sensor response was measured using the incident signal only where the reflected signal was cut off by time-domain gating.

5.3 Laboratory Calibration of UHF Partial Discharge Sensors using GTEM cell

The frequency responses of existing UHF PD sensors were measured experimentally by the author using GTEM calibration cell. They are monopole probe of the kind used as a reference sensor in the GTEM calibration system; experimental disc-type sensor; large monopole-type PD sensor developed for use on an experimental model transformer tank; and conventional disc-type sensor model that is representative of the type used in GIS. These devices are shown in Figure 5.4 to Figure 5.7, respectively.

The accuracy of the digital representation and reconstituted original signal are dependent on the Nyquist sampling theorem. The theorem stated that a continuous signal can be represented and then reconstituted back from a set of samples if the number of samples per second is at least twice the maximum frequency in the signal [122]. Therefore if the maximum frequency in the signal is 1 GHz, the sampling frequency must at least 2×10^9 samples per second. The sensitivity of the sensors is measured using a 1 GHz bandwidth

digitiser with an effective sampling rate of 25.6×10^9 samples/s (256 sample points over 10 ns).

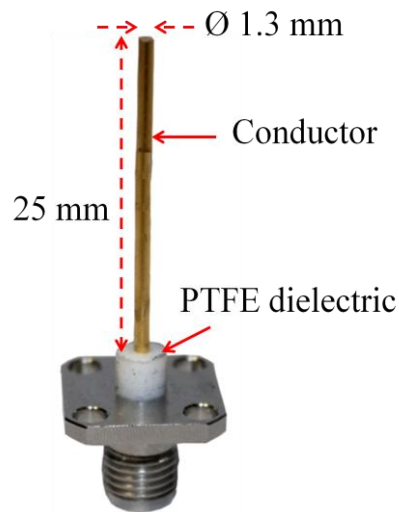


Figure 5.4: 25 mm reference monopole probe.



Figure 5.5: Experimental disc-type UHF PD sensor.



Figure 5.6: Experimental monopole-type UHF PD sensor.

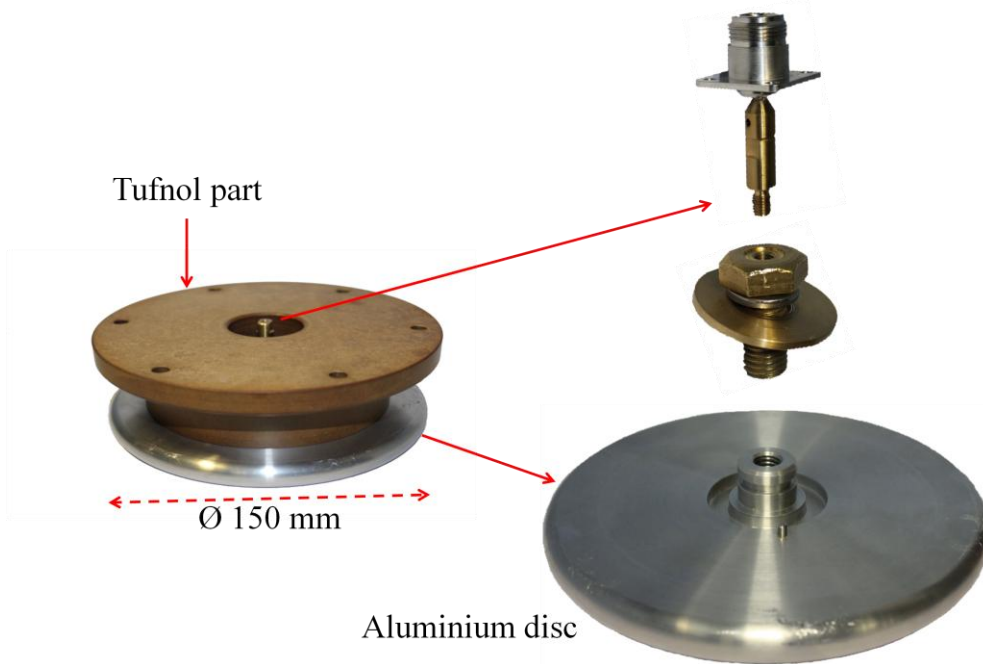


Figure 5.7: Conventional disc-type UHF PD sensor. The thickness of the disc is 10 mm.

The same reference monopole probe for TEM calibration cell, as described in Section 4.4, is used in GTEM calibration cell. The rise time of the electric field step is 350 ps and it is calculated as the time required for the electric field to rise from 10 % to 90 % of its maximum value.

The measured step electric field at the centre of the sensor test aperture which is measured using the reference monopole probe, as shown in Figure 5.8, is used as the input electric field of the sensor under test [123]. The step electric field is generated by injecting step voltage, as shown in Figure 5.3, into the GTEM calibration cell. The input electric field in frequency domain, $E(\omega)$ is calculated using (5.1). The measured output voltage (V_L) in time domain from the probe is converted to frequency domain using fast Fourier transform (FFT) algorithm. The effective height (h_e) and input impedance (Z) of the probe, as in Table 4.1, is interpolated based on the sampling rate of the probe output voltage (39.06 ps). Then, $E(\omega)$ is transformed to time domain $E(t)$ using inverse FFT

method. The calculated $E(\omega)$ is used to calculate the response of the unknown sensor $H(\omega)$ using (5.2) where $V_S(\omega)$ is the output voltage of the sensor in frequency domain.

$$E(\omega) = \frac{V_L(\omega)}{h_e(\omega)} \times \left(\frac{50 + Z(\omega)}{50} \right) \quad (5.1)$$

$$H(\omega) = \frac{V_S(\omega)}{E(\omega)} \quad (5.2)$$

The calibration arrangement of the sensors is illustrated in Figure 5.9 to Figure 5.12 each of which illustrates the sensor mounting arrangement on high voltage equipment system. The average sensitivities of the sensors were measured using the GTEM calibration system and the results are shown in Figure 5.13. The experimental disc sensor with disc diameter of 125 mm has a flat response compared to other sensors. The measured sensitivities of the sensors are then compared with finite-difference time-domain (FDTD) technique in section 6.3.

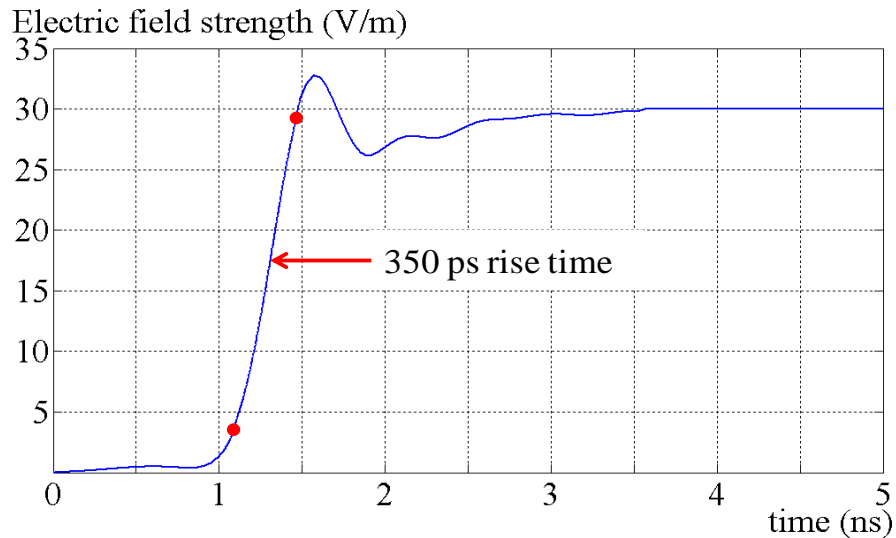


Figure 5.8: The step electric field applied to UHF PD sensors under test for laboratory calibration.

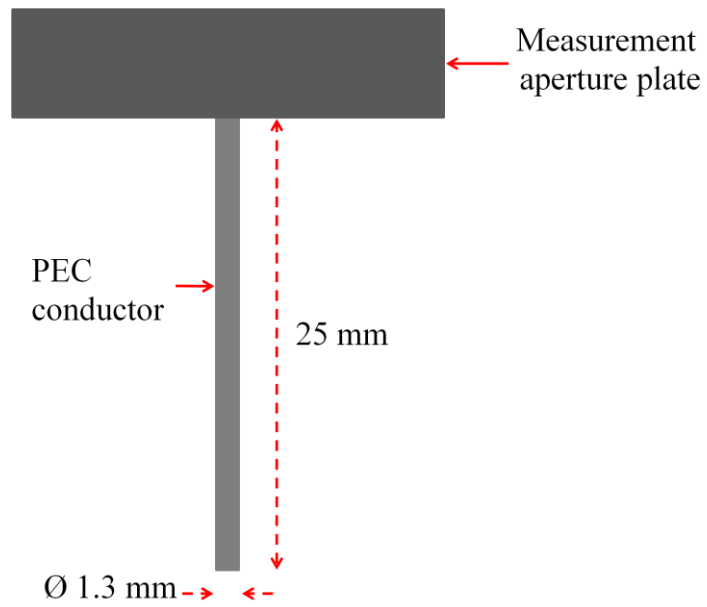
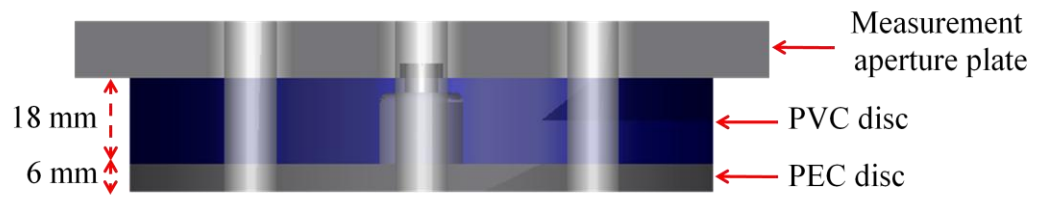
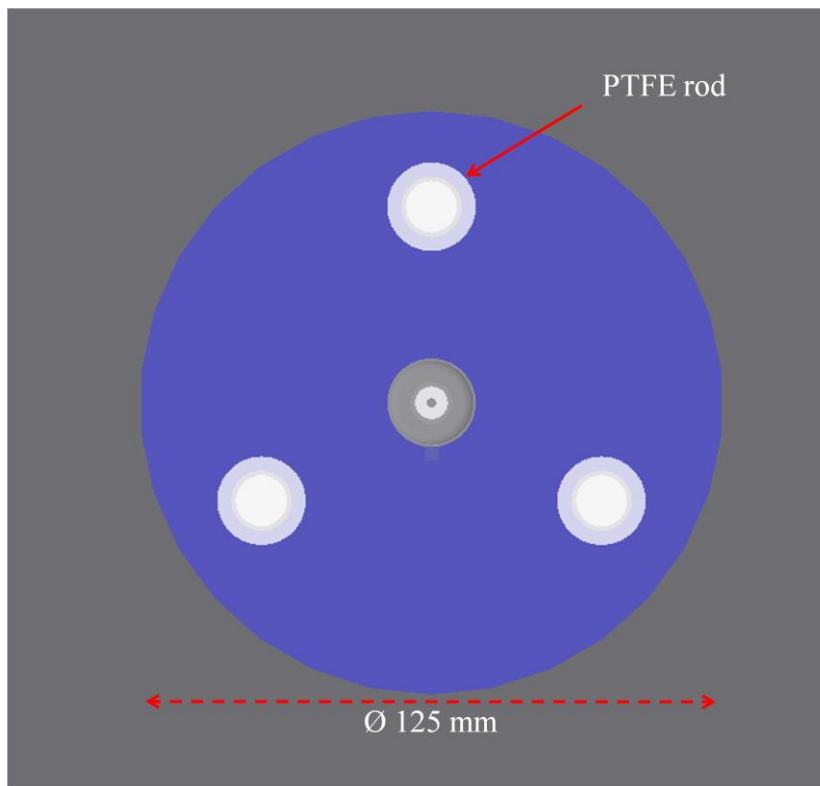


Figure 5.9: 25 mm reference monopole probe at the measurement aperture of GTEM cell.



(a)



(b)

Figure 5.10: Experimental disc-type UHF PD sensor as an internal sensor. Simplified modelling views: (a) side view and (b) top view.

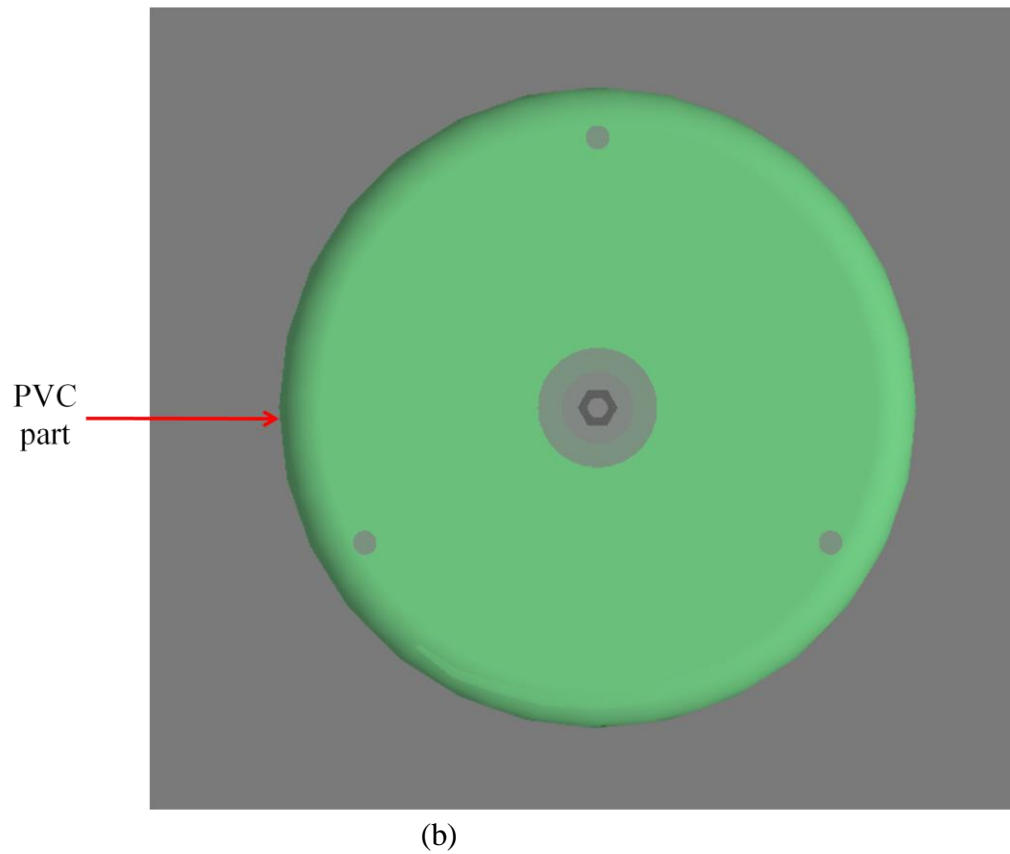
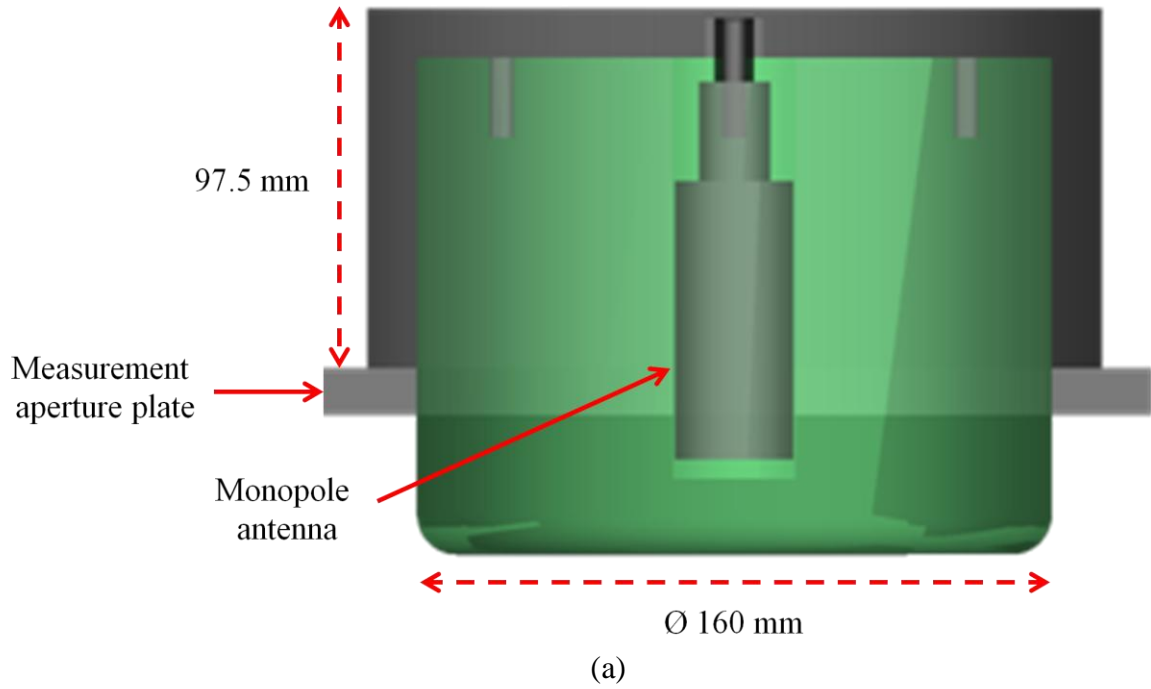
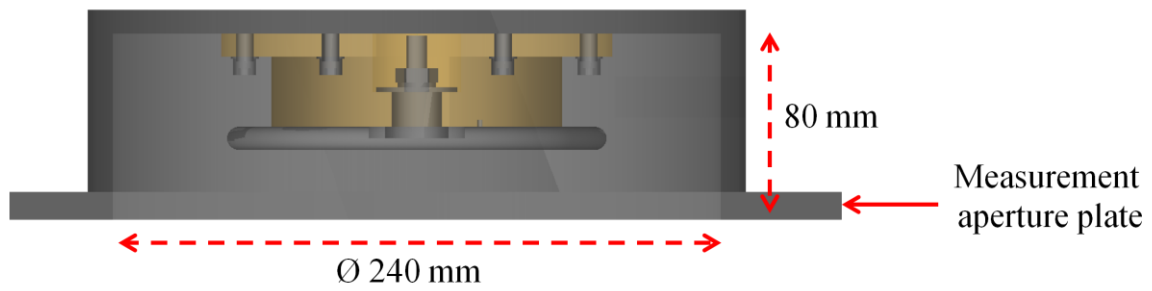
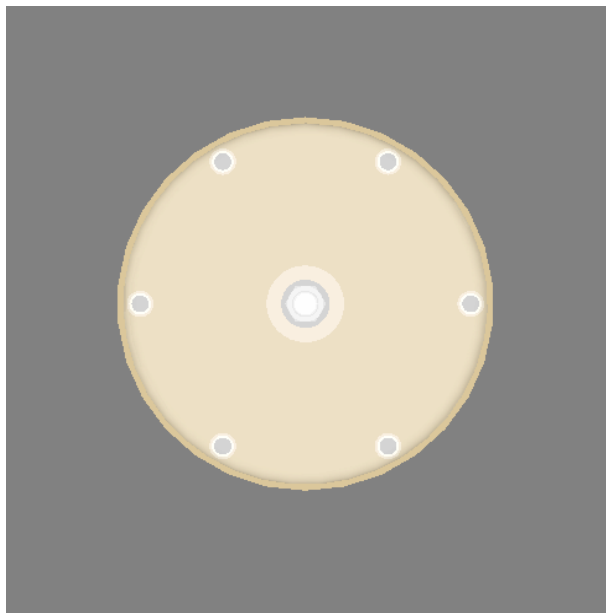


Figure 5.11: Experimental monopole-type UHF PD sensor for power transformer application as an internal sensor. Graphical modelling views: (a) side view and (b) top view.



(a)



(b)

Figure 5.12: Conventional disc-type UHF PD sensor for GIS application as an internal sensor. The designed views: (a) side view and (b) top view.

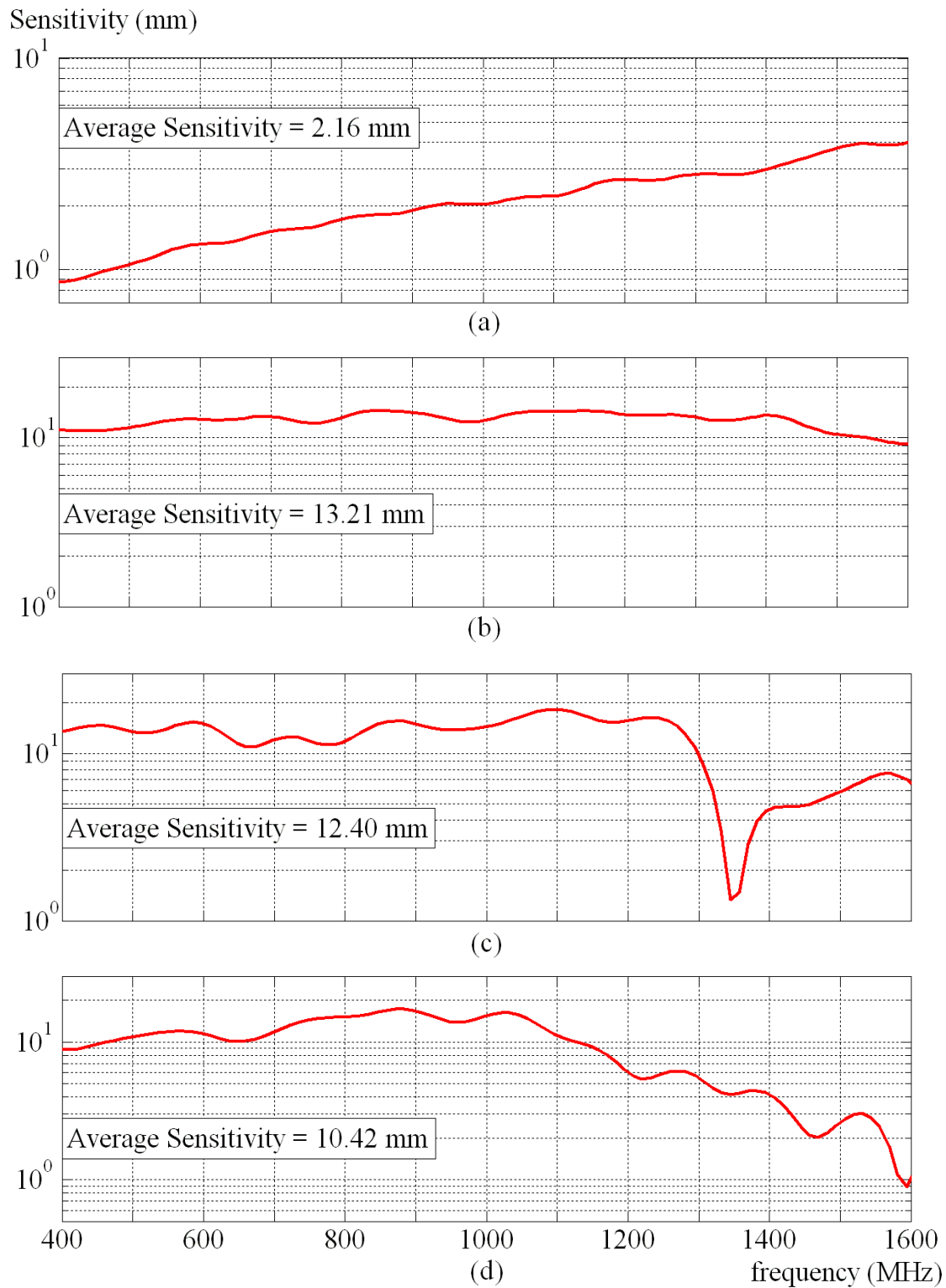


Figure 5.13: The measured average sensitivities of PD sensors: (a) 25 mm reference probe, (b) experimental disc sensor, (c) monopole sensor, and (d) conventional disc sensor.

5.4 Conclusion

The GTEM calibration system is used to measure the responses of UHF PD sensors. The GTEM cell generates uniform plane wave propagation and is able to distinguish the unwanted reflected signal using time-domain gating. The average sensitivity of the sensors for the frequency range 500 to 1500 MHz must be larger than 6.0 mV/Vm^{-1} , as recommended by National Grid Company. In this chapter, the responses of the four existing sensors were measured experimentally by the author using the GTEM calibration system. The existing sensors are 25 mm reference probe, experimental disc sensor, monopole sensor and conventional disc sensor. The experimental disc sensor has a flat response compared to other sensors. All the sensors have average sensitivities more than 6.0 mV/Vm^{-1} except for the reference probe. The reference probe was used to measure the input electric field for all the tested sensors.

Chapter 6: Finite-Difference Time-Domain (FDTD) Modelling of Electromagnetic Waves

Finite-difference time-domain (FDTD) is a method to model electromagnetic wave propagation and interactions with the structure of materials [124] [25]. It employs vector partial differential equations in computational electromagnetics. The computational electromagnetic methods by applying Maxwell's equations have emerged as an important technology due to the computation power and memory of high performance computers.

This chapter introduces Maxwell's equations in the form used to model electromagnetic phenomena in PD propagation in power transformer and UHF PD calibration system using XFDTD software. The software package is a three-dimensional full wave electromagnetic analyser. FDTD method by implementing Maxwell's equations is then proved to be reliable in predicting frequency responses of UHF PD sensors using simulated calibration system. Some factors that affect the response of UHF PD sensors are then examined without changing the material types and sizes of the sensors physically. The changes are made through changing the relative permittivities of dielectric materials and varying sensor sizes in the FDTD simulation.

6.1 Introduction of FDTD Method

The FDTD method for electromagnetic waves was introduced by Kane Yee [125] [126] in 1966 who described a numerical technique for solving Maxwell's curl equations directly in the time-domain on a space grid. The orthogonal Yee cell, shown in Figure 6.1, is the building block of the FDTD method, where the electric and magnetic fields are defined at discrete points interleaved around a cell. Each electric field component is located a half-cell width from the origin in the direction of its orientation and each magnetic field component is offset to the centre of three faces of the cell.

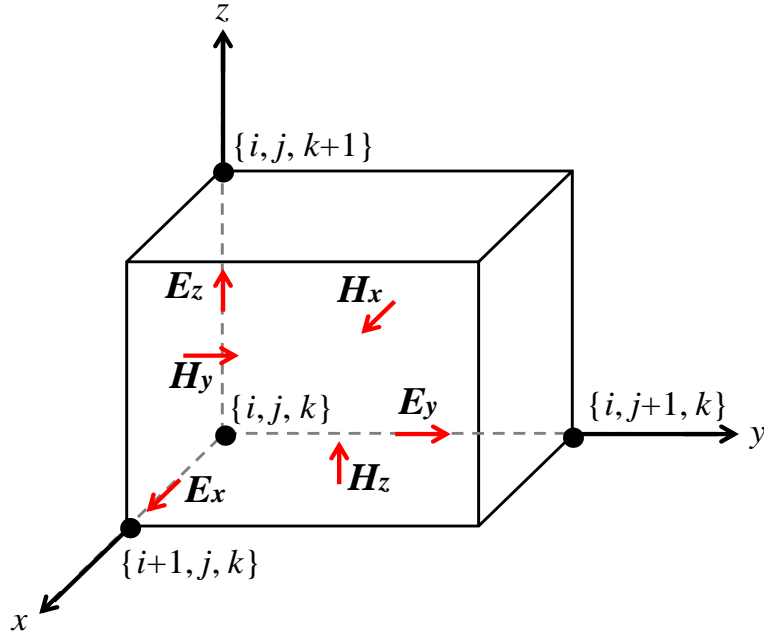


Figure 6.1: The Yee cell. Electric field components are at the centres of the cell edges and the magnetic field components are in the centres of the cell faces. The variables i , j , and k are indices for the spatial mesh in the orthogonal x , y , and z -directions, respectively.

A time-varying magnetic field produces an electric field (Faraday's law) and a time-varying electric field gives rise to a magnetic field (Ampere's law). Therefore, the time-dependent Maxwell's equations are used to calculate the electromagnetic wave propagation in FDTD method. The equations are [114]:

$$\nabla \times \mathbf{H} = \sigma \mathbf{E} + \frac{\partial \mathbf{D}}{\partial t} \quad (6.1)$$

$$\nabla \times \mathbf{E} = - \frac{\partial \mathbf{B}}{\partial t} \quad (6.2)$$

where \mathbf{D} = 3-dimensional vectors of electric flux density (C/m^2)
 \mathbf{E} = 3-dimensional vectors of electric field intensity (V/m)

- t = Time (s)
 \mathbf{B} = 3-dimensional vectors of magnetic flux density (T)
 \mathbf{H} = 3-dimensional vectors of magnetic field intensity (A/m)
 σ = constant electric conductivity (S/m)

Six scalar equations to represent the orthogonal field components can be derived from Maxwell's equations by applying $\mathbf{D} = \varepsilon\mathbf{E}$ and $\mathbf{B} = \mu\mathbf{H}$ to equations 6.1 and 6.2, respectively, and rearranging the equations to give:

$$\frac{\partial E_x}{\partial t} = \frac{1}{\varepsilon} \left(\frac{\partial H_z}{\partial y} - \frac{\partial H_y}{\partial z} - \sigma E_x \right) \quad (6.3)$$

$$\frac{\partial E_y}{\partial t} = \frac{1}{\varepsilon} \left(\frac{\partial H_x}{\partial z} - \frac{\partial H_z}{\partial x} - \sigma E_y \right) \quad (6.4)$$

$$\frac{\partial E_z}{\partial t} = \frac{1}{\varepsilon} \left(\frac{\partial H_y}{\partial x} - \frac{\partial H_x}{\partial y} - \sigma E_z \right) \quad (6.5)$$

$$\frac{\partial H_x}{\partial t} = \frac{1}{\mu} \left(\frac{\partial E_y}{\partial z} - \frac{\partial E_z}{\partial y} \right) \quad (6.6)$$

$$\frac{\partial H_y}{\partial t} = \frac{1}{\mu} \left(\frac{\partial E_z}{\partial x} - \frac{\partial E_x}{\partial z} \right) \quad (6.7)$$

$$\frac{\partial H_z}{\partial t} = \frac{1}{\mu} \left(\frac{\partial E_x}{\partial y} - \frac{\partial E_y}{\partial x} \right) \quad (6.8)$$

where ε = permittivity of a material

μ = permeability of a material

In the FDTD method, the electromagnetic fields and structural materials of interest are made discrete in space and time. The space is segmented into box-shaped cells, as in Figure 6.1, and time is quantised into steps (also known as time step). Therefore, the electric and magnetic fields in Maxwell's equations are divided into many grid units along three axes with the space steps of grids and time step. The difference calculations in space and time based on ∂x , ∂y , ∂z , and ∂t can be replaced by Yee's notation of space steps and time step as defined as Δx , Δy , Δz , and Δt respectively. Then, the Maxwell's equations can be expressed as the form in (6.9), where n is the time index. The final Yee equations in the central difference form for both the temporal and spatial derivatives are shown in (6.10) until (6.15) [127].

$$F^n(i, j, k) = F(i\Delta x, j\Delta y, k\Delta z, n\Delta t) \quad (6.9)$$

$$\begin{aligned} \frac{E_x^{n+1/2}(i+1/2, j, k) - E_x^{n-1/2}(i+1/2, j, k)}{\Delta t} &= \frac{1}{\epsilon} \left(\frac{H_z^n(i+1/2, j+1/2, k) - H_z^n(i+1/2, j-1/2, k)}{\Delta y} - \right. \\ &\left. \frac{H_y^n(i+1/2, j, k+1/2) - H_y^n(i+1/2, j, k-1/2)}{\Delta z} - \sigma \frac{E_x^{n+1/2}(i+1/2, j, k) + E_x^{n-1/2}(i+1/2, j, k)}{2} \right) \end{aligned} \quad (6.10)$$

$$\begin{aligned} \frac{E_y^{n+1/2}(i, j+1/2, k) - E_y^{n-1/2}(i, j+1/2, k)}{\Delta t} &= \frac{1}{\epsilon} \left(\frac{H_x^n(i, j+1/2, k+1/2) - H_x^n(i, j+1/2, k-1/2)}{\Delta z} - \right. \\ &\left. \frac{H_z^n(i+1/2, j+1/2, k) - H_z^n(i-1/2, j+1/2, k)}{\Delta x} - \sigma \frac{E_y^{n+1/2}(i, j+1/2, k) + E_y^{n-1/2}(i, j+1/2, k)}{2} \right) \end{aligned} \quad (6.11)$$

$$\begin{aligned} \frac{E_z^{n+1/2}(i, j, k+1/2) - E_z^{n-1/2}(i, j, k+1/2)}{\Delta t} &= \frac{1}{\epsilon} \left(\frac{H_y^n(i+1/2, j, k+1/2) - H_y^n(i-1/2, j, k+1/2)}{\Delta x} - \right. \\ &\left. \frac{H_x^n(i, j+1/2, k+1/2) - H_x^n(i, j-1/2, k+1/2)}{\Delta y} - \sigma \frac{E_z^{n+1/2}(i, j, k+1/2) + E_z^{n-1/2}(i, j, k+1/2)}{2} \right) \end{aligned} \quad (6.12)$$

$$\begin{aligned} \frac{H_x^{n+1}(i, j + 1/2, k + 1/2) - H_x^n(i, j + 1/2, k + 1/2)}{\Delta t} = \\ \frac{1}{\mu} \left(\frac{E_y^{n+1/2}(i, j+1/2, k+1) - E_y^{n+1/2}(i, j+1/2, k)}{\Delta z} - \frac{E_z^{n+1/2}(i, j+1, k+1/2) - E_z^{n+1/2}(i, j, k+1/2)}{\Delta y} \right) \end{aligned} \quad (6.13)$$

$$\begin{aligned} \frac{H_y^{n+1}(i + 1/2, j, k + 1/2) - H_y^n(i + 1/2, j, k + 1/2)}{\Delta t} = \\ \frac{1}{\mu} \left(\frac{E_z^{n+1/2}(i+1, j, k+1/2) - E_z^{n+1/2}(i, j, k+1/2)}{\Delta x} - \frac{E_x^{n+1/2}(i+1/2, j, k+1) - E_x^{n+1/2}(i+1/2, j, k)}{\Delta z} \right) \end{aligned} \quad (6.14)$$

$$\begin{aligned} \frac{H_z^{n+1}(i + 1/2, j + 1/2, k) - H_z^n(i + 1/2, j + 1/2, k)}{\Delta t} = \\ \frac{1}{\mu} \left(\frac{E_x^{n+1/2}(i+1/2, j+1, k) - E_x^{n+1/2}(i+1/2, j, k)}{\Delta y} - \frac{E_y^{n+1/2}(i+1, j+1/2, k) - E_y^{n+1/2}(i, j+1/2, k)}{\Delta x} \right) \end{aligned} \quad (6.15)$$

The time step is defined as the time needed for the field to propagate from one cell to another cell. The time step and the size of the cells are related as shown below to ensure numerical stability of the calculation [128]:

$$\Delta t = \frac{\Delta s}{\sqrt{3}c} \quad (6.16)$$

where Δt = time step

Δs = the smallest length of the cells

c = the speed of light

A perfectly matched layer (PML) is used to absorb radiated fields using finite numbers of FDTD layers instead of extending the grid cell indefinitely. This method also can save computational memory usage during simulation. PML act as a lossy layer where permittivity (ϵ) and permeability (μ) are complex numbers. If electromagnetic wave propagates from medium 1 to medium 2, which is the PML medium, the reflection coefficient, Γ of the wave can be represented as in (6.17) [114]:

$$\Gamma = \frac{\eta_2 - \eta_1}{\eta_2 + \eta_1} \quad (6.17)$$

η_1 and η_2 are the intrinsic impedances of medium 1 and medium 2, respectively. In the PML algorithm, equations (6.18) and (6.19) below are introduced [127] where σ_e and σ_m are the electric conductivity and magnetic conductivity; μ_1 and μ_2 are the permeability of medium 1 and medium 2; and ϵ_1 and ϵ_2 are the permittivity of medium 1 and medium 2.

$$\frac{\mu_1}{\epsilon_1} = \frac{\mu_2}{\epsilon_2} \quad (6.18)$$

$$\frac{\sigma_e}{\epsilon_2} = \frac{\sigma_m}{\mu_2} \quad (6.19)$$

By substituting equations (6.18) and (6.19) into the intrinsic impedance, $\eta = \sqrt{\frac{\mu}{\epsilon}}$, the impedances for both media are equal, as shown in (6.20). Therefore, when η_1 and η_2 are equal, the reflection coefficient, Γ in (6.17) must be zero and the electromagnetic wave is absorbed at the PML region.

$$\eta_1 = \sqrt{\frac{\mu_1 \left(1 - j \frac{\sigma_m}{\omega \mu_1}\right)}{\varepsilon_1 \left(1 - j \frac{\sigma_e}{\omega \varepsilon_1}\right)}} = \sqrt{\frac{\mu_2 \left(1 - j \frac{\sigma_e}{\omega \varepsilon_1}\right)}{\varepsilon_2 \left(1 - j \frac{\sigma_e}{\omega \varepsilon_1}\right)}} = \sqrt{\frac{\mu_2}{\varepsilon_2}} = \eta_2 \quad (6.20)$$

Modelling of PD phenomena in a cylindrical tank using the FDTD method was outlined in [129]. The PD signal was simulated by applying a current source in free space inside the cylindrical cavity. A monopole probe was used to measure the PD signal. The simulated result was compared with the experimental result where it demonstrated good agreement. The experimental PD source inside the chamber was generated by needle-plane electrode. The intensity of electric fields generated by PD sources in dielectric materials was investigated using FDTD modelling in [130]. Gaussian current source was used to generate PD source in a cavity of the dielectrics. The amplitude of the radiated electric fields generated by the PD source is higher for polymer (relative permittivity $\varepsilon_r = 2.984$) and epoxy resin ($\varepsilon_r = 3.772$) insulators than ceramic ($\varepsilon_r = 11.840$) insulator. The amplitude of the field radiation also increases with increasing radius of the dielectric cavities.

FDTD simulation has also been applied to study the propagation characteristics of electromagnetic wave caused by PD source in GIS [131]. The electric fields generated by PD sources (Gaussian pulse injected on the inner surface of GIS enclosure, outer surface of inner conductor and on the surface of spacer insulator) were measured at point coordinate located on the surface of internal disc sensors. The electric field reduces in amplitude as it propagates through the insulator.

When a broadband transient excitation signal source is used, this technique is capable of predicting the response of a system over a wide range of frequencies with a single simulation run. For example, a single execution of the simulation to determine the transient time-domain response of a sensor can be used to obtain its frequency response by applying a Fourier transform algorithm to the time-domain data at the post-processing stage.

There are other computational methods that can be used to analyze PD characteristics and electromagnetic waves for examples, finite element method (FEM) [87] and finite integration technique (FIT) [132] that have been demonstrated to investigate electromagnetic wave propagation through insulating spacer in GIS.

6.2 Partial Discharge Propagation in Transformer using FDTD Method

Modelling PD phenomena by using the FDTD method is much safer than attempting it with high voltage experiments. Furthermore, it is much easier to change parameters in the model and study their influence on the PD detection. A three-dimensional geometry has been created using FDTD software to represent a transformer tank containing a PD current source, UHF sensors, transformer tank, cores and copper windings. The general instruction to model the geometry using XFDTD software [133] is explained in Appendix 2. The transformer model, shown in Figure 6.2, represents a HV transformer tank in the HV Laboratory at University of Strathclyde, as shown in Figure 6.3.

The tank and cores are modelled as perfect electric conductor (PEC) material and the windings with copper material. The UHF disc sensors, as modelled in Figure 6.4, have the thickness and diameter of 14 mm and 200 mm, respectively. The passive load is connected between the mid-point of the PEC disc sensor and tank wall. The material properties of the modelled geometries are described in Table 6.1. The relative permeability for all geometries is equal to 1. Figure 6.5 shows the location of PD current source, which is winding-to-winding discharge, inside the simulated transformer. The coordinates of the four sensors are based on the positions of the 50 Ω loads which is 0.4 cm tangential from the tank wall. The coordinates of S1, S2, S3, and S4 sensors are {130.0, 0.4, 40.0}, {270.0, 0.4, 200.0}, {270.0, 199.6, 40.0}, and {40.0, 199.6, 210.0} cm, respectively. The coordinates of PD source is from {60.8, 57.9, 47.0} to {60.8, 57.9, 47.4} cm which is 0.4 cm height in z -direction. The thickness of the copper winding is 0.4 cm.

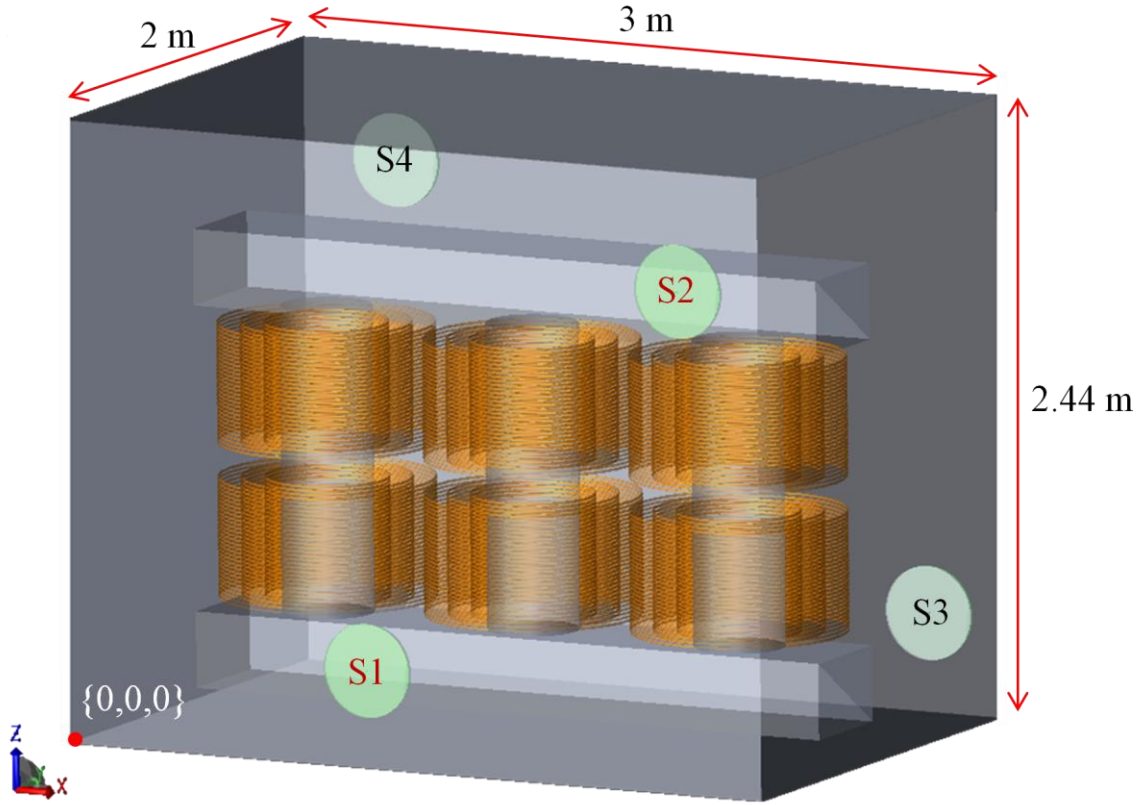


Figure 6.2: The FDTD model representation of transformer tank with four UHF disc sensors (S1, S2, S3, and S4).

The simulation time for the simulation is 1 hour and 45 minutes with mesh size and time step of 0.4 cm (for all directions) and 7.7 ps, respectively. The 0.4 cm mesh size was chosen because the smallest structure of the modelled transformer tank was the thickness of the winding which was 0.4 cm. The pulse width of Gaussian PD current source is 0.21 ns, as presented in Figure 6.6, with the amplitude of 1 A which corresponds to a charge of about 200 pC. The pulse width is measured by calculating the time interval between the ascending edge and descending edge of the pulse at 50 % amplitude of the peak value [134]. The charge, Q is calculated using (6.21). The typical apparent charge of PD due to surface discharge on oil-pressboard interface in transformers is about 200 pC [135] [136].

$$Q = \int_{t_1}^{t_2} i(t) dt \quad (6.21)$$

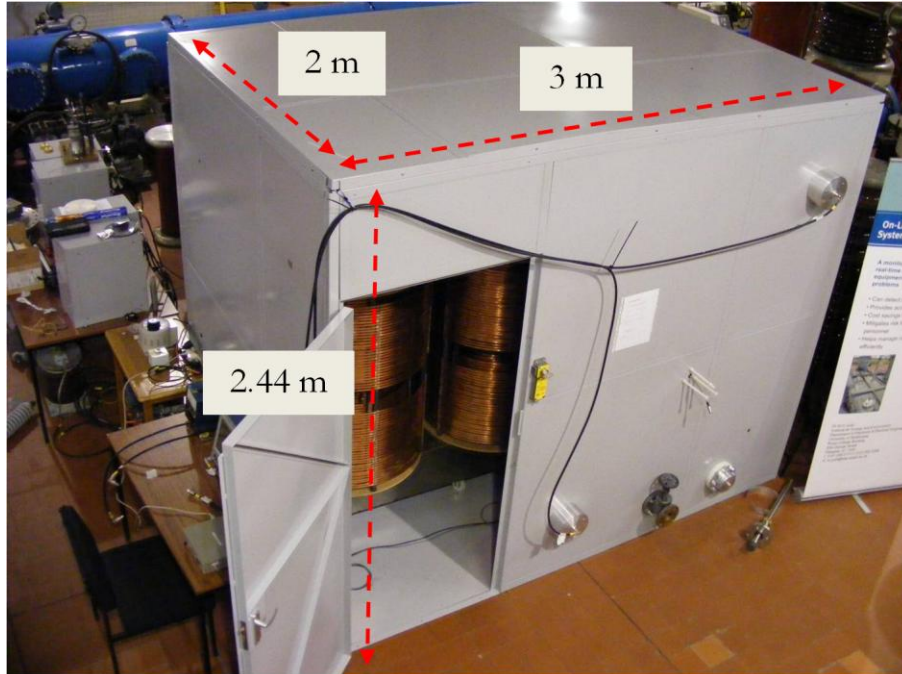


Figure 6.3: The power transformer in HV laboratory with four UHF monopole sensors mounted on the wall tank. Note that two sensors are mounted at the front side of the tank and another two sensors are at the back side of the tank.

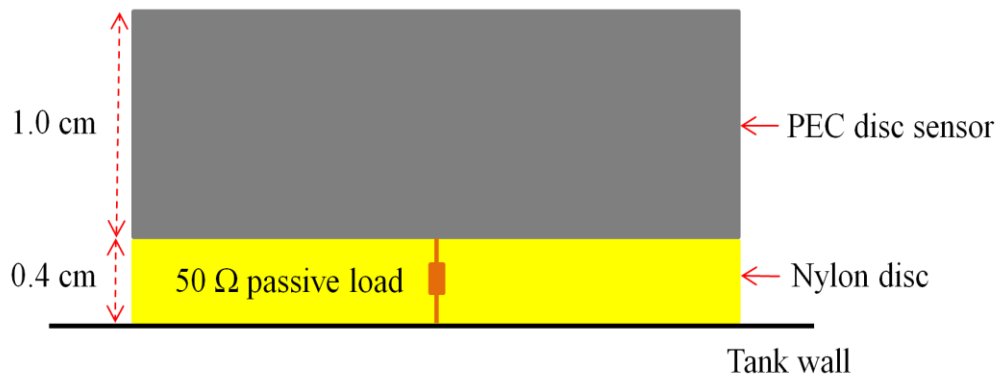


Figure 6.4: The modelled UHF disc sensor that been mounted on the transformer wall.

Table 6.1

The material properties of the modelled transformer tank [137] [138].

Geometry	Relative permittivity	Conductivity (S/m)
Copper winding	1.0	5.85×10^7
Nylon disc	3.4	0

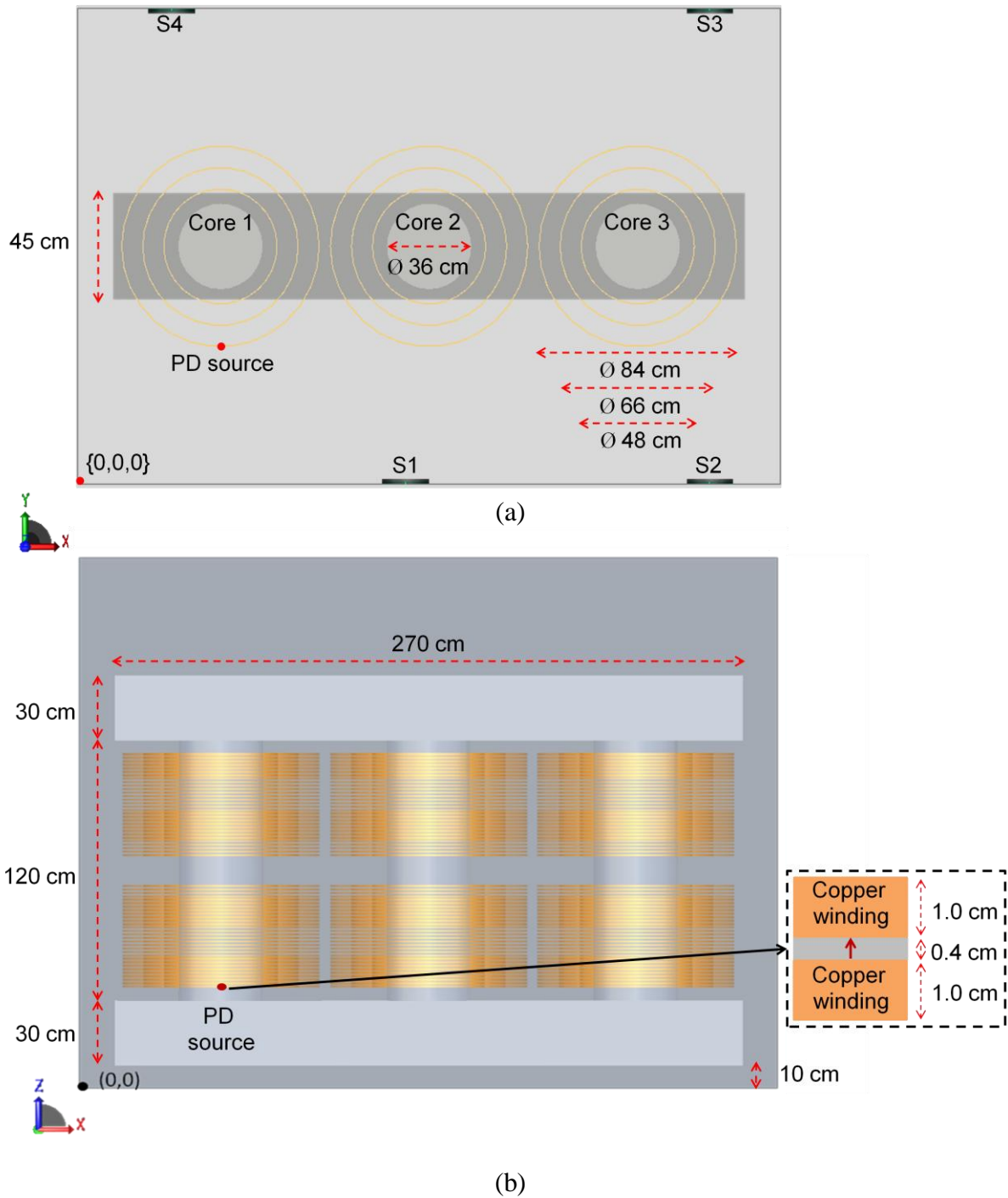


Figure 6.5: The location of PD current source in modelled power transformer without mineral oil: (a) top view and (b) side view.

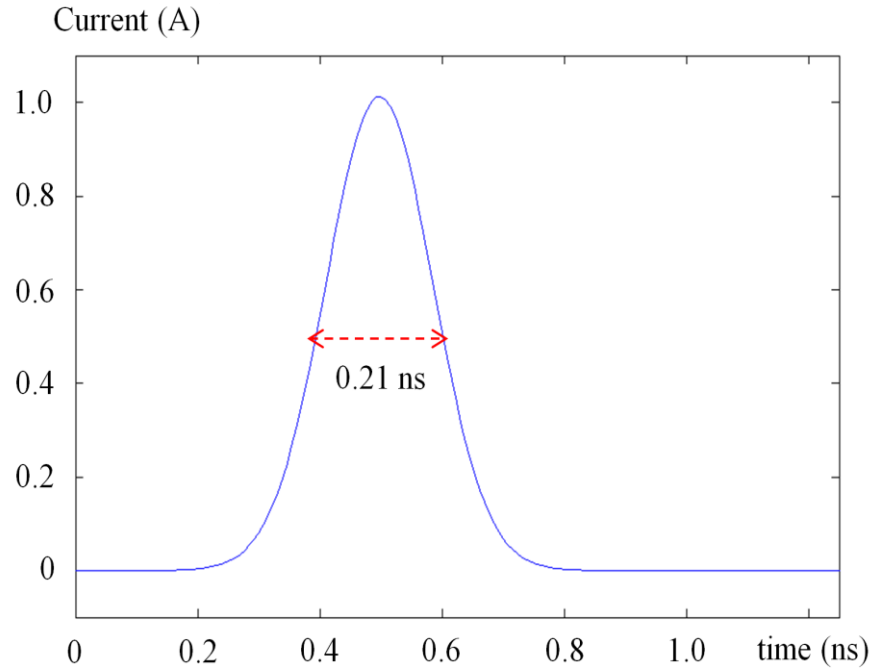


Figure 6.6: PD pulse waveform with 0.21 ns pulse width.

Accurate onset time determination for UHF signals is important for locating PD sources in power transformers. The PD location can be estimated by timing the arrival of UHF signals at several sensors on a transformer tank. The arrival time of UHF PD signal at each sensor can be measured using threshold method which is 2 % of the maximum amplitude of squared voltage [139]. Figure 6.7 shows squared output voltages of UHF PD signals at four sensors during FDTD simulation. S1 sensor detected the PD signal first as it was near to the PD source location, followed by S4, S2 and S3 sensors. The estimated distance between PD source and UHF sensors is compared with the shortest propagation path of UHF signals using a numerical procedure based on [140] and 2 % threshold of maximum squared voltage, as described in Table 6.2.

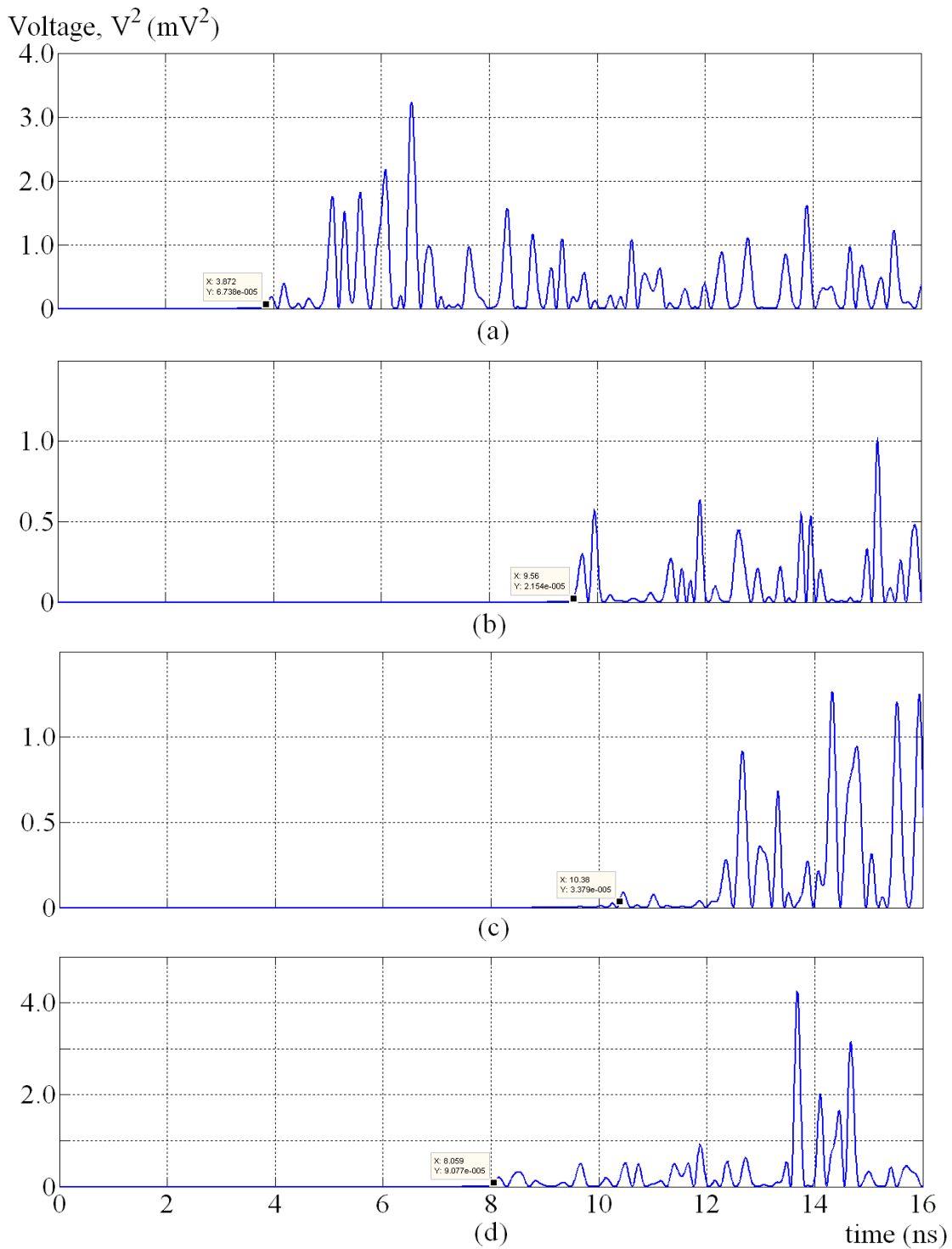


Figure 6.7: The squared output waveforms of four UHF sensors for the modelled transformer: (a) Sensor 1, (b) Sensor 2, (c) Sensor 3, and (d) Sensor 4. The measured arrival time of the PD signal for S1, S2, S3, and S4 sensors are 3.87 ns, 9.56 ns, 10.38 ns, and 8.06 ns, respectively.

Figure 6.8 and Figure 6.9 show the shortest path of electromagnetic wave propagation generated by PD source in two-dimensional view. The geometrical calculations of propagation distances between PD source in the simulated transformer tank and S3 sensor; and between PD source and S4 sensor are calculated based on Figure 6.8 and Figure 6.9, respectively.

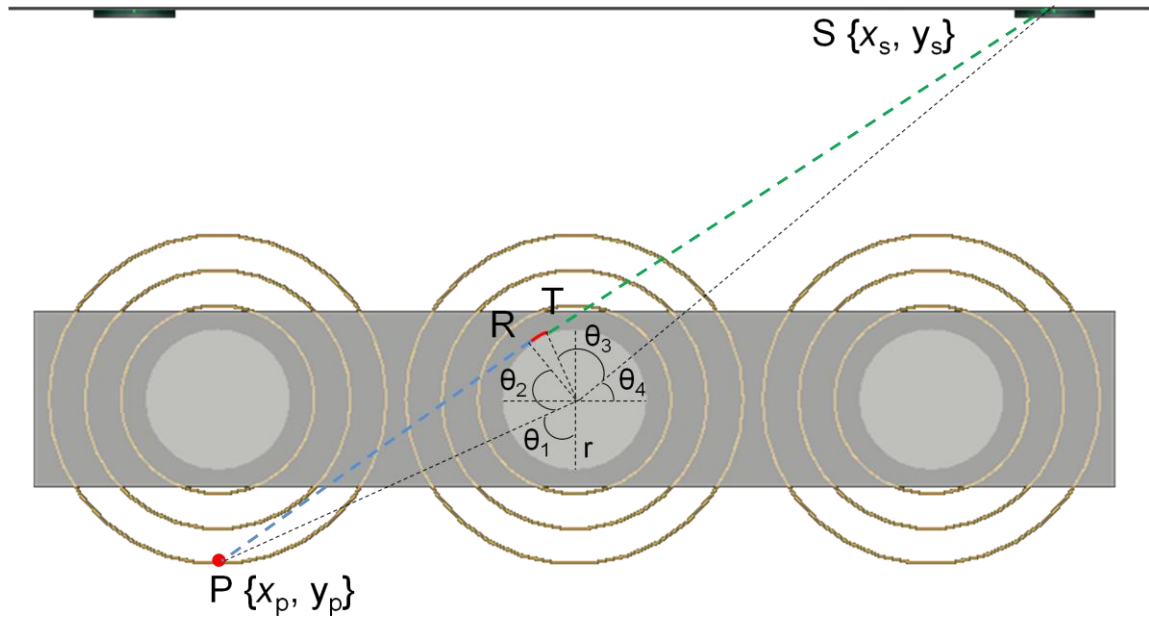


Figure 6.8: The shortest propagation path of electromagnetic wave in two-dimensional (x - y) view between PD source and Sensor 3 (S3).

$\{a,b\}$ = central coordinates of Core 2 in x - y view = $\{150,100\}$ cm

$$l_{ST} = \sqrt{(x_s - a)^2 + (y_s - b)^2 - r^2} = 154.91 \text{ cm}$$

$$l_{RP} = \sqrt{(x_p - a)^2 + (y_p - b)^2 - r^2} = 96.98 \text{ cm}$$

$$\theta_1 = \tan^{-1} \left(\frac{a - x_p}{b - y_p} \right) = 1.13 \text{ rad,}$$

$$\theta_2 = \tan^{-1} \left(\frac{l_{RP}}{r} \right) = 1.39 \text{ rad}$$

$$\theta_3 = \tan^{-1} \left(\frac{l_{ST}}{r} \right) = 1.46 \text{ rad,}$$

$$\theta_4 = \tan^{-1} \left(\frac{y_s - b}{x_s - a} \right) = 0.69 \text{ rad}$$

$$l_{TR} = r (1.5 \Pi - \theta_1 - \theta_2 - \theta_3 - \theta_4) = 0.76 \text{ cm}$$

$$l_{SP} = l_{ST} + l_{TR} + l_{RP} = 252.65 \text{ cm}$$

$$L_{SP} = \sqrt{l_{SP}^2 + (z_p - z_s)^2} = 252.75 \text{ cm}, \quad z_p = 47 \text{ cm}, \quad z_s = 40 \text{ cm}$$

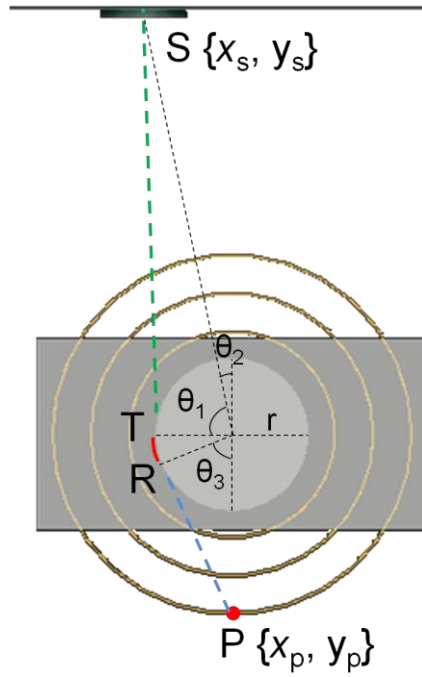


Figure 6.9: The electromagnetic wave propagation path between PD source in the simulated transformer tank and Sensor 4 (S4).

$$\{c,d\} = \text{central coordinates of Core 1 in } x\text{-}y \text{ view} = \{60.8,100\} \text{ cm}$$

$$l_{ST} = \sqrt{(x_s - c)^2 + (y_s - d)^2 - r^2} = 100.14 \text{ cm}$$

$$l_{RP} = \sqrt{(x_p - c)^2 + (y_p - d)^2 - r^2} = 38.06 \text{ cm}$$

$$\theta_1 = \tan^{-1} \left(\frac{l_{ST}}{r} \right) = 1.39 \text{ rad}, \quad \theta_2 = \tan^{-1} \left(\frac{c - x_s}{y_s - d} \right) = 0.21 \text{ rad}$$

$$\theta_3 = \tan^{-1} \left(\frac{l_{RP}}{r} \right) = 1.13 \text{ rad}, \quad l_{TR} = r (\Pi - \theta_1 - \theta_2 - \theta_3) = 7.41 \text{ cm}$$

$$l_{SP} = l_{ST} + l_{TR} + l_{RP} = 145.61 \text{ cm}$$

$$L_{SP} = \sqrt{l_{SP}^2 + (z_p - z_s)^2} = 218.57 \text{ cm}, \quad z_p = 47 \text{ cm}, \quad z_s = 210 \text{ cm}$$

Table 6.2

The percentage differences between measured and theoretical distances.

Sensor	Arrival time ^a (ns)	Distance (cm)		Difference (%)
		Measured ^b	Theoretical	
S1	3.87	116.10	90.24 ^c	28.66
S2	9.56	286.80	265.48 ^c	8.03
S3	10.38	311.40	252.75 ^d	23.20
S4	8.06	241.80	218.57 ^d	10.63

Note: a = The arrival time is calculated based on 2 % threshold of maximum squared voltage

b = The measured distance is calculated using speed of light equals to 3×10^8 m/s

c = The distance is calculated using $\sqrt{(x_1 - x_2)^2 + (y_1 - y_2)^2 + (z_1 - z_2)^2}$

d = The distance is calculated based on [140]

Table 6.2 shows that the FDTD method can be used to study the propagation characteristics of PD signal in power transformer. The percentage difference of the distance for FDTD measurement and theoretical method can be due to (i) PD signal can propagate along the PEC disc surface before reaching the 50Ω load, and (ii) the effect of copper winding is ignored in calculating the theoretical values. The results also show that the simplified UHF disc sensors are reasonable to represent the UHF sensors inside the transformer at HV laboratory.

The next section demonstrates that it is possible to predict the sensitivity of UHF sensors using FDTD simulation with reasonable accuracy. Then Chapter 7 discusses the

possibility of designing and optimizing new UHF sensor using FDTD method to a large extent before fabricating the physical device.

6.3 Predicting Frequency Responses of UHF PD Sensors using FDTD Method

In this section the FDTD method is used to apply the same transient electric field waveform that is used in the UHF sensor calibration system within a model space that represents a subset of the GTEM test cell structure.

A calibration system is needed to prevent equipment or sensor inaccuracy due to drifting effect; and meet the required standard of sensitivity. A three-dimensional geometry of the calibration cell, as shown in Figure 6.10, has been created to represent the GTEM cell in the laboratory (as in Figure 5.2) using XFDTD software. For the purpose of FDTD simulation, several simplifications were made to the geometry of the calibration cell. Firstly, on the basis of symmetry, only the upper half of the GTEM cell was modelled, being represented as a tapered pair of planar conductors with a 1:6 gradient. In this step, the individual septum wires were also replaced by a planar conductor, since leaving them as thin wires would have necessitated very large regions of fine sub-meshing in the model and would then require extension of the volume. Secondly, the side walls of the GTEM were not included, since they would prevent the launching of a vertically polarized uniform electric field plane wave into the structure. Thirdly, the modelled cell was reduced in length to 2 m by removing the 1 m of tapered section towards the input of the cell. This was done to avoid the need for representing fine mechanical detail at the input, where there is a transition from an N-type coaxial connector to the GTEM septum. A consequence of this simplification is that, instead of using a voltage source input within the model, a corresponding vertically polarized electric field plane wave was launched between the plates (from the left in Figure 6.10). The same step electric field was applied, as in Figure 5.8, at the input side. Lateral tapering of the cell was also not included in the model, which used a fixed width of 50 cm, equal to the width of the GTEM at its mid-point where the measurement aperture is located. These simplifications resulted in a representative model of the physical test cell and the region of interest while avoiding

structural complexity and excessive simulation run times. Conductors forming the test cell were represented as perfect electric conductor (PEC) regions in the FDTD model. Overall, the translation of the physical structure of the GTEM into the FDTD model domain produces a structure that is much closer to the ideal test configuration, which would consist of two infinite, parallel planar conductors with a perpendicularly polarized plane wave propagating between them. The level of agreement between measured and simulated results presented later in this section for four different sensors suggests that the simplifications within the FDTD model are sufficiently valid for it to serve as a useful tool for design purposes.

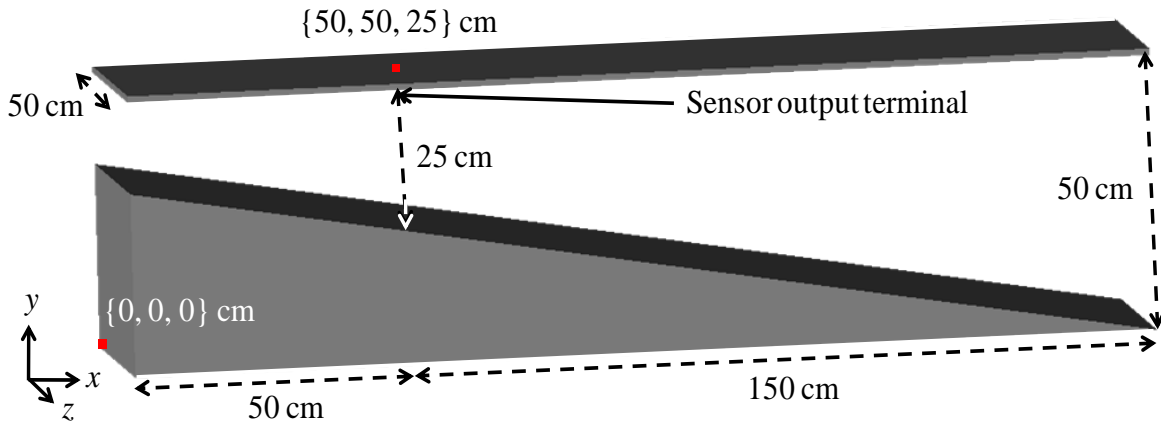


Figure 6.10: The simulated calibration cell using FDTD software. The simulated plane wave propagates in positive x -direction.

The sensors shown in Figures 5.4, 5.5, 5.6 and 5.7 were modelled in the FDTD software using the dimensions and material properties of the physical sensors. The corresponding sensor models are shown in Figures 6.11 until 6.14 and the properties of the materials are listed in Table 6.3. Polytetrafluoroethylene (PTFE), polyvinyl chloride (PVC) and a filled epoxy resin (Tufnol) were the dielectric materials used. Relative permeability and electrical conductivity values used for all dielectrics were 1.0 and 0, respectively. UHF sensor models were positioned between the two conductors in Figure 6.10, with their

output terminals at coordinates $\{50, 50, 25\}$ cm, where there is 25 cm between the top plate and the bottom sloping conductor (which represents the septum).

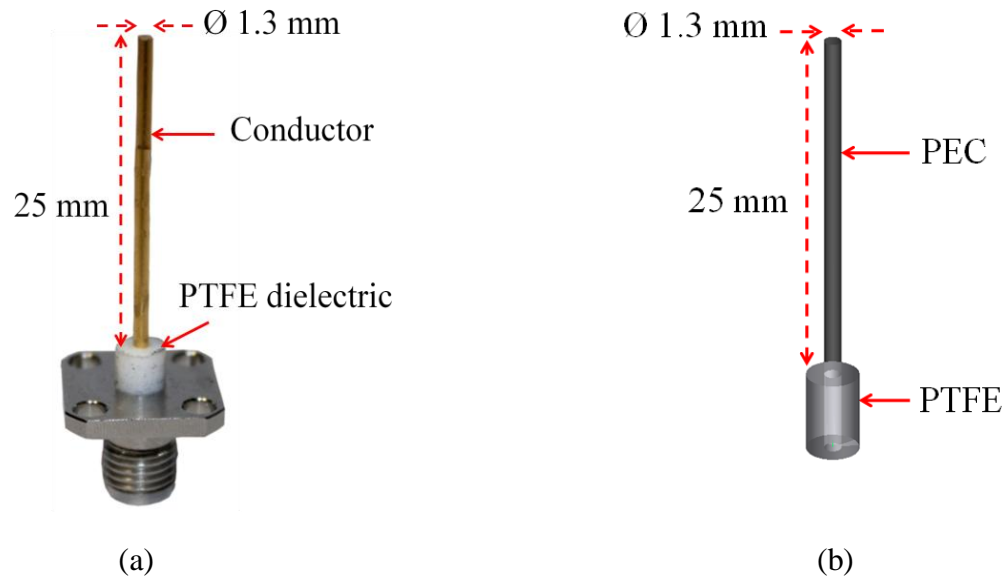


Figure 6.11: 25 mm reference monopole probe: (a) physical sensor and (b) modelled sensor.

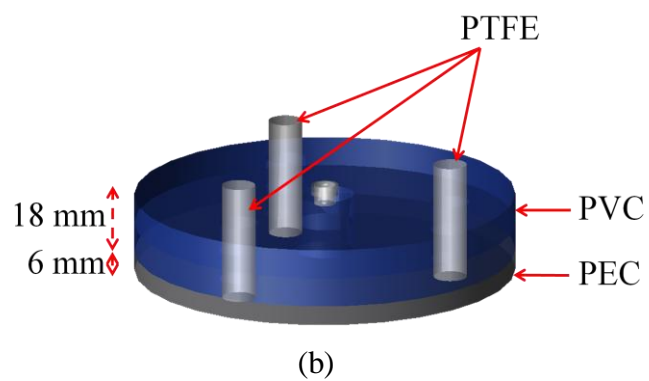
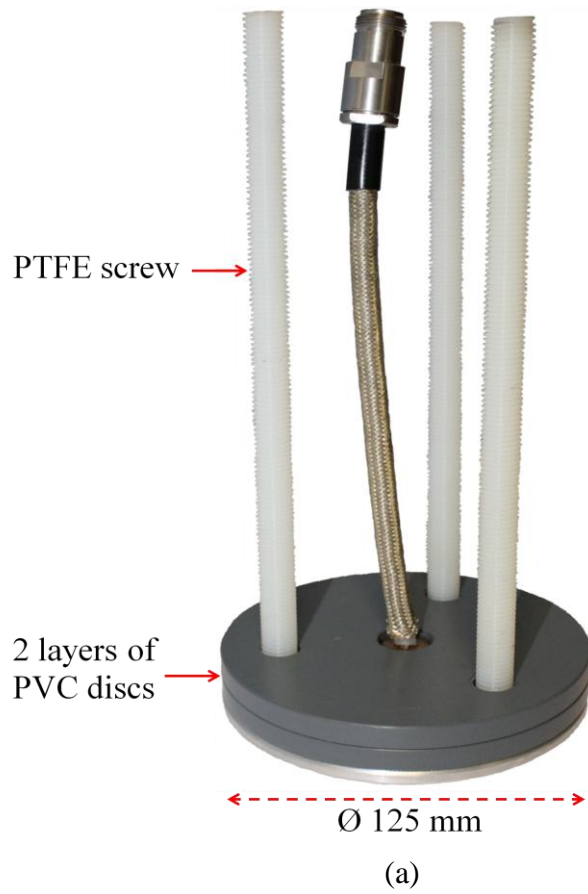


Figure 6.12: Experimental disc-type PD sensor: (a) physical sensor and (b) modelled sensor.

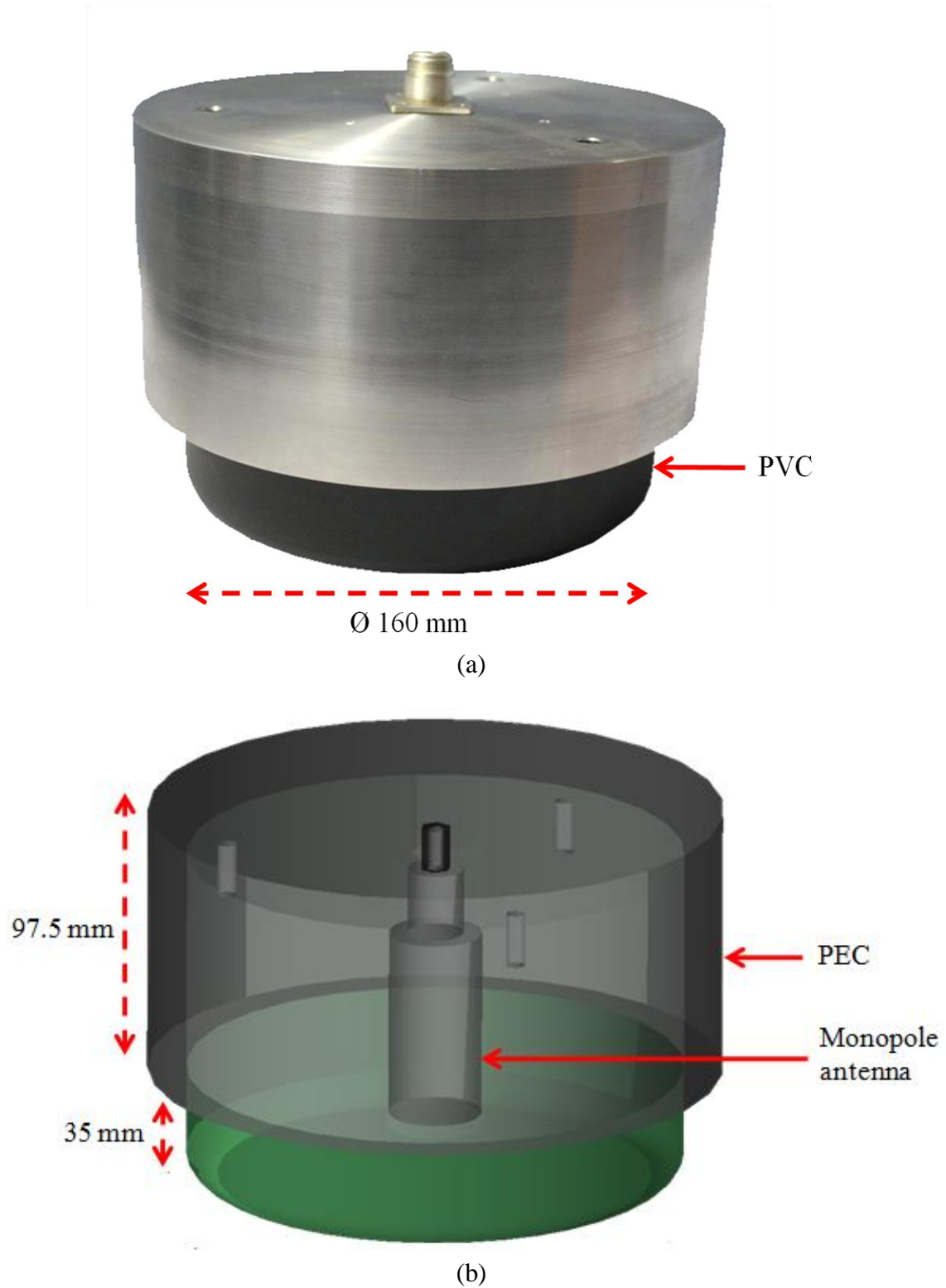
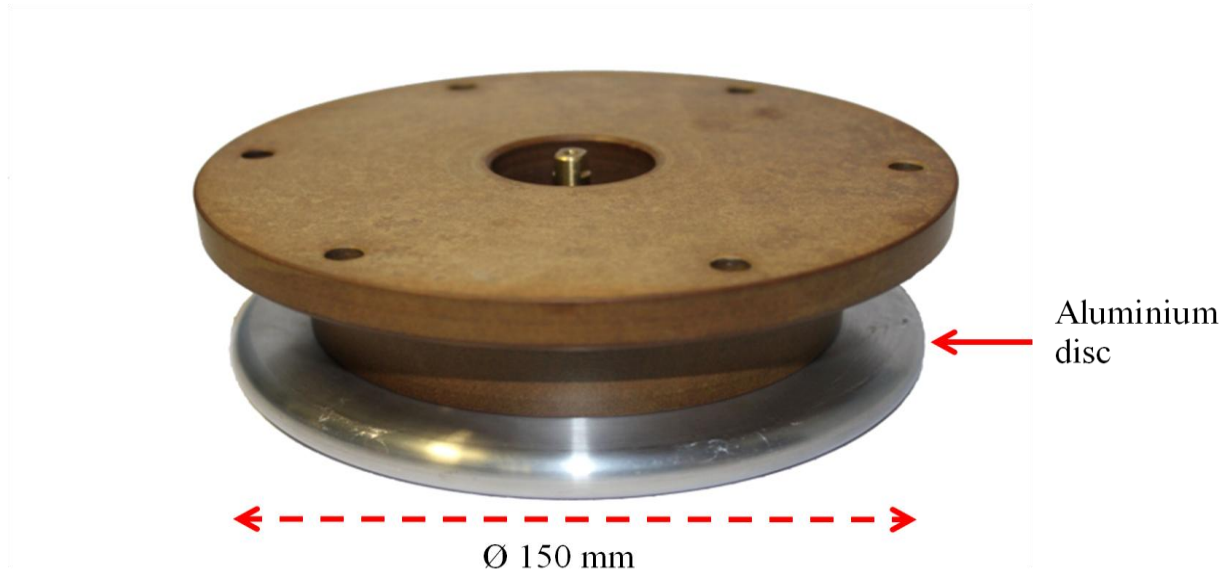
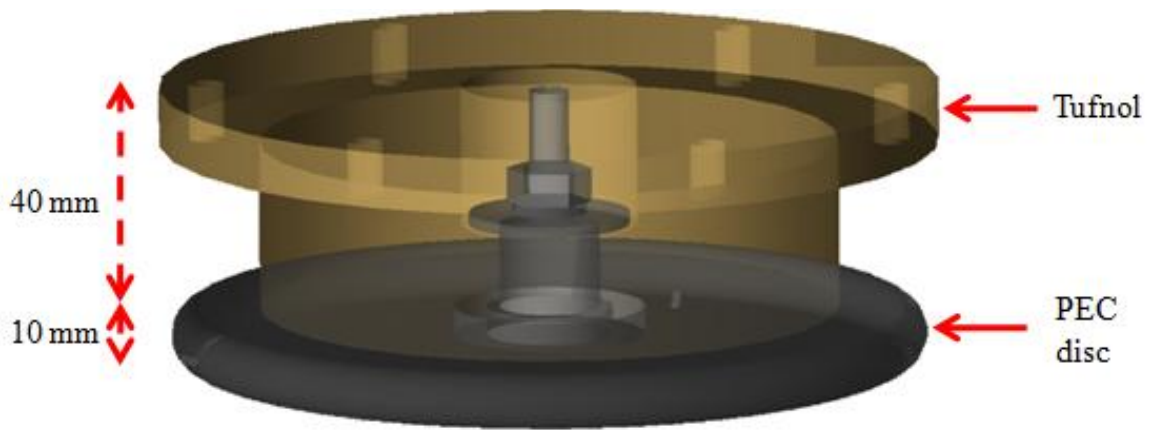


Figure 6.13: Experimental monopole-type PD sensor: (a) physical sensor and (b) modelled sensor.



(a)



(b)

Figure 6.14: The diagram of conventional disc-type PD sensor: (a) physical sensor and (b) modelled sensor.

Table 6.3

Dielectric materials of the modelled sensors [138].

Material	Relative permittivity
PTFE	2.0
PVC	2.6
Tufnol	3.4

During simulation, the region around the sensor was modelled with finer meshing than other regions so that small mechanical details could be represented with greater accuracy. Localising the sub-meshing in this way helps to minimize the extra computational burden of representing smaller components within the sensors. The simulated parameters are summarised in Table 6.4, where the run times quoted are for a PC with an Intel Xeon X5550 (2.67 GHz) processor and 12 GB RAM. A perfectly matched layer (PML) boundary condition was applied to all faces of the simulation volume as the termination of FDTD grids. Since there are no walls on the left and right sides of the simulated GTEM (x - y plane faces in Figure 6.10), this artificial absorbing layer will absorb incident waves that reach all faces (minimising distortion of the signals due to unwanted reflections).

Table 6.4

Simulation parameters of the modelled sensors.

Sensor	Cell size (cm)		Time step (ps)	Simulation run time
25 mm probe	0.05	x: 49.0 – 51.0 y: 46.0 – 51.0 z: 24.0 – 26.0	0.963	37 min.
	1.00	other regions		
Experimental disc sensor	0.10	x: 43.5 – 56.5 y: 47.1 – 51.0 z: 18.5 – 31.5	1.926	42 min.
	1.00	other regions		
Monopole sensor	0.10	x: 40.7 – 59.3 y: 46.2 – 62.2 z: 15.7 – 34.3	1.926	2 hrs, 13 min.
	1.00	other regions		
Conventional disc sensor	0.10	x: 37.0 – 63.0 y: 49.0 – 62.0 z: 12.0 – 38.0	1.926	2 hrs, 17 min.
	1.00	other regions		

A 50 Ω lumped-element load was connected between the output terminal of the UHF sensor and the ground plane (which is the top plate of the simulated GTEM cell). The simulated output voltage of the UHF sensor was recorded across this 50 Ω load, which represents the normal cable and measurement impedance used in UHF PD detection systems. The frequency response of the modelled sensors is obtained using a Fast Fourier transform (FFT) algorithm, as is described in Appendix 3. The output voltages and frequency responses of the sensors are compared between the laboratory experimental results and FDTD simulations in Figure 6.15 and Figure 6.16. The overall figure-of-merit sensitivity is calculated for each sensor based on the average sensitivity over the frequency range 500 – 1500 MHz. Figure 6.15 and Figure 6.16 illustrate that the simulation and laboratory results are comparable and demonstrate that the FDTD approach is capable of analyzing and predicting the output of UHF PD sensors in the time-domain and the frequency-domain.

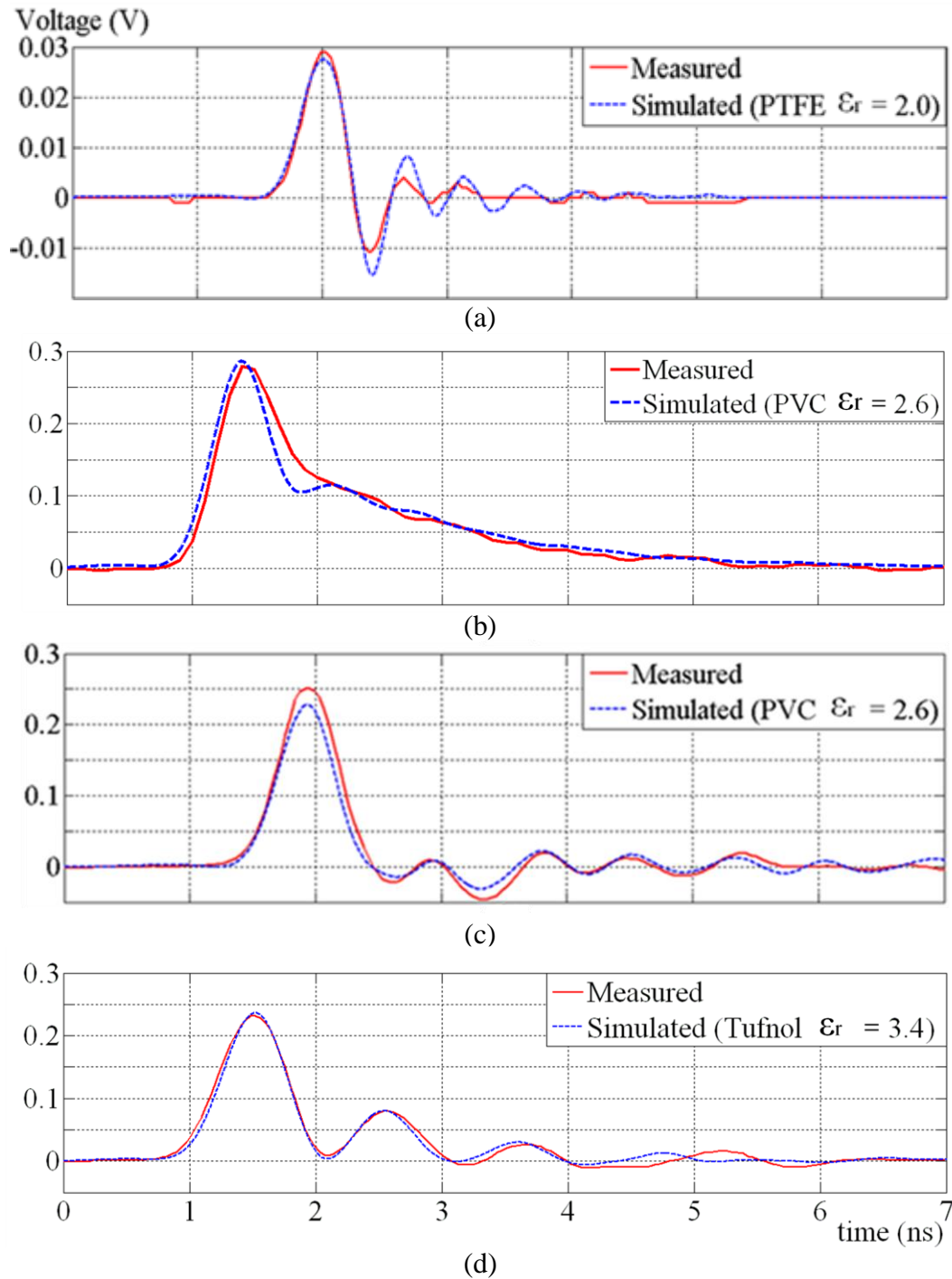


Figure 6.15: Comparison of measured and simulated output voltages: (a) 25 mm probe, (b) experimental disc sensor, (c) monopole sensor, and (d) conventional disc sensor.

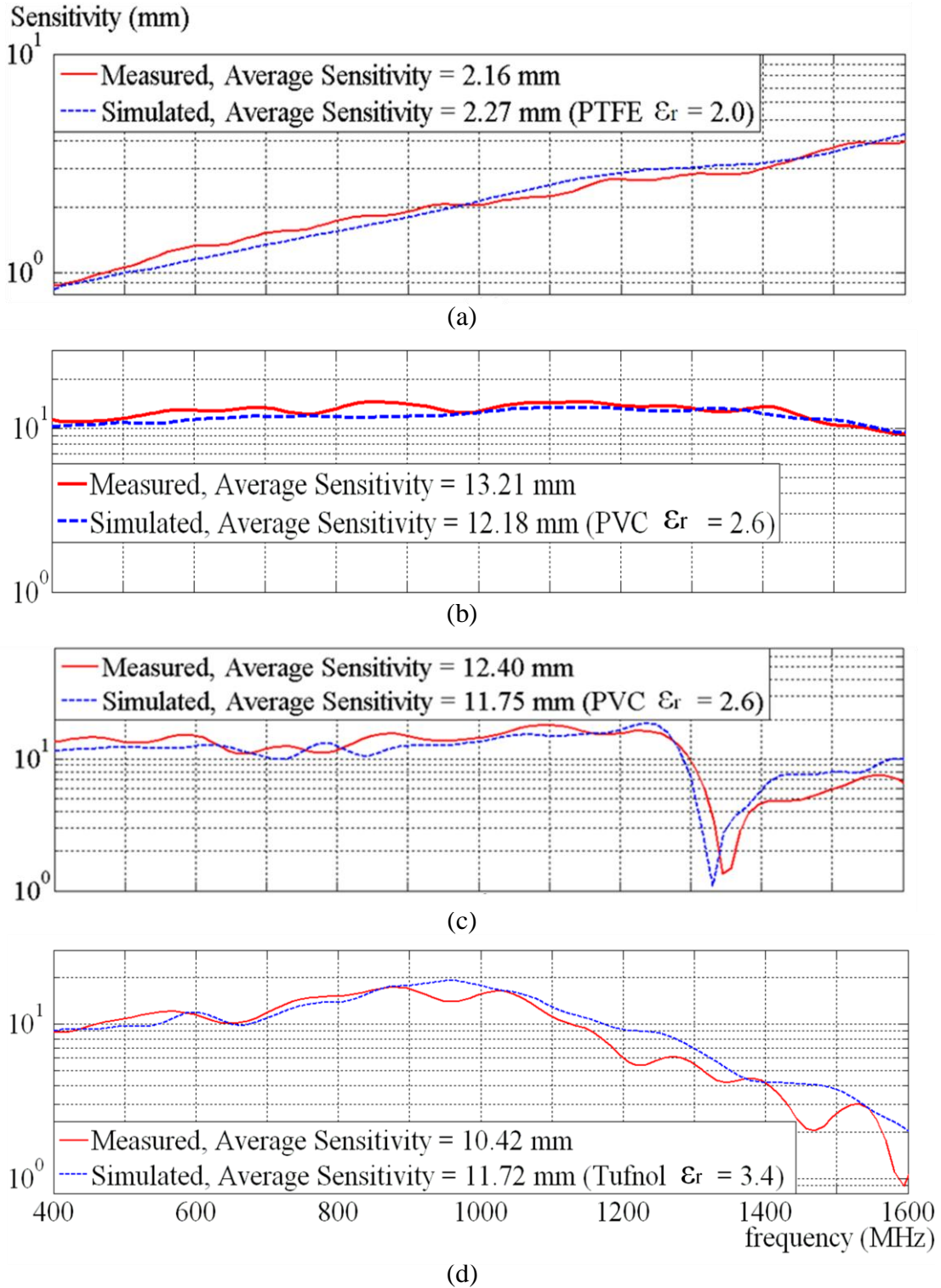


Figure 6.16: Comparison of measured and simulated frequency responses: (a) 25 mm probe, (b) experimental disc sensor, (c) monopole sensor, and (d) conventional disc sensor.

In the FDTD simulation, all metals are assumed to be perfect electric conductor (PEC) with relative permittivity and electrical conductivity equal to 1 and infinity, respectively. To investigate the effect of using real metals such as aluminium and brass materials on the sensor response, the conventional disc sensor, as in Figure 6.14, was simulated using the material properties as in Table 6.5. The aluminium material was defined for the disc and six washer-screw structures that hold the sensor structure on the hatch as shown in Figure 5.12. The washer-screw structure that holds the disc on Tufnol part, as shown in Figure 5.7, was set as brass material. The hatch and simplified calibration cell are assigned as PEC material in the simulation. The simulated grid size remained the same as in Table 6.4 for conventional disc sensor.

Table 6.5

Material properties for the conventional UHF disc sensor during simulation [137].

Material	Relative permittivity	Electrical conductivity (S/m)
Aluminium	1	3.69×10^7
Brass		1.59×10^7
Tufnol	3.4	0

The simulation time for the sensor properties (in Table 6.5) was the same as using PEC material for the sensor metal structures which is 2 hours and 17 minutes. Figure 6.17 shows the comparisons of simulated output voltages and frequency responses of the conventional disc sensor using (i) all sensor metals as PEC and (ii) aluminium and brass materials for the disc and washer-screw geometries. The fact that the results appear identical indicates that aluminium and brass structures of the sensor can be represented as PEC in the simulation.

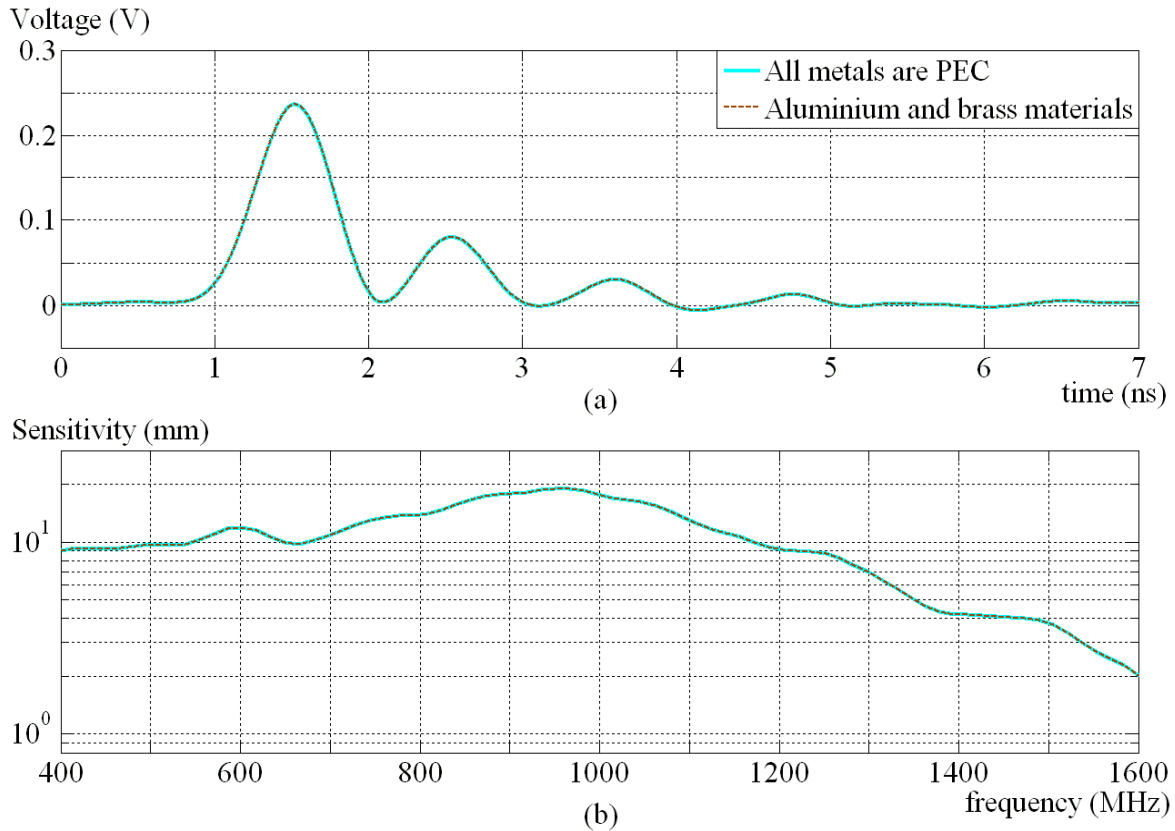


Figure 6.17: The simulated results: (a) output voltages and (b) frequency responses of conventional UHF disc sensor using (i) all sensor metals as PEC materials and (ii) aluminium and brass materials for the sensor metals, showing that the results are identical.

6.4 Study of Factors that Affect the Sensitivity of UHF PD Sensors

The FDTD method is useful for investigating the influence of material properties and sensor structure. To demonstrate this capability on the monopole sensor and conventional disc sensor, as in Figures 6.13 and 6.14 respectively, two parameters were varied to investigate their effect on sensitivity, namely, the relative permittivity of the dielectrics and the geometry of the sensors.

6.4.1 Relative Permittivity of Dielectric Materials

The incident electric field, cell size, time step, and sensor dimensions were kept the same when simulating different values of relative permittivity of the insulating materials. The simulation results presented in Table 6.6 show that, as the relative permittivity of the insulating materials increases, the output voltage decreases slightly. This agrees with (6.22) where V , E , d , ρ_s , and ε are voltage difference, electric field strength, distance, surface charge density, and the permittivity of the dielectric medium, respectively [114]. ε is expressed in (6.23), where ε_r is the relative permittivity or dielectric constant of the materials and ε_0 is the electric permittivity of free space (8.854×10^{-12} F/m).

$$V = Ed = (\rho_s/\varepsilon) d \quad (6.22)$$

$$\varepsilon = \varepsilon_r \varepsilon_0 \quad (6.23)$$

Table 6.6

Simulated output voltages of UHF PD sensors with varying relative permittivity.

Sensor component	Relative permittivity	Simulated V_{pk-pk} (V)	Percentage difference of simulated V_{pk-pk} (%)
Monopole dielectric part	1.6	0.2670	2.77
	2.6	0.2598	Reference value
	3.6	0.2525	-2.81
	4.6	0.2511	-3.35
	5.6	0.2462	-5.23
Conventional disc dielectric part	1.4	0.2774	5.60
	2.4	0.2749	4.64
	3.4	0.2627	Reference value
	4.4	0.2536	-3.46
	5.4	0.2531	-3.65

Figure 6.18 shows the averaged sensitivity of the two PD sensors over 500 - 1500 MHz as a function of relative permittivity of their structural insulating components. The monopole and conventional disc sensors show different responses to permittivity changes. However, compared with the overall sensitivity, these results indicate that permittivity is not a particularly critical parameter and both sensors would have a satisfactory response with any insulation having a dielectric constant within the typical range of 2.0 to 5.0.

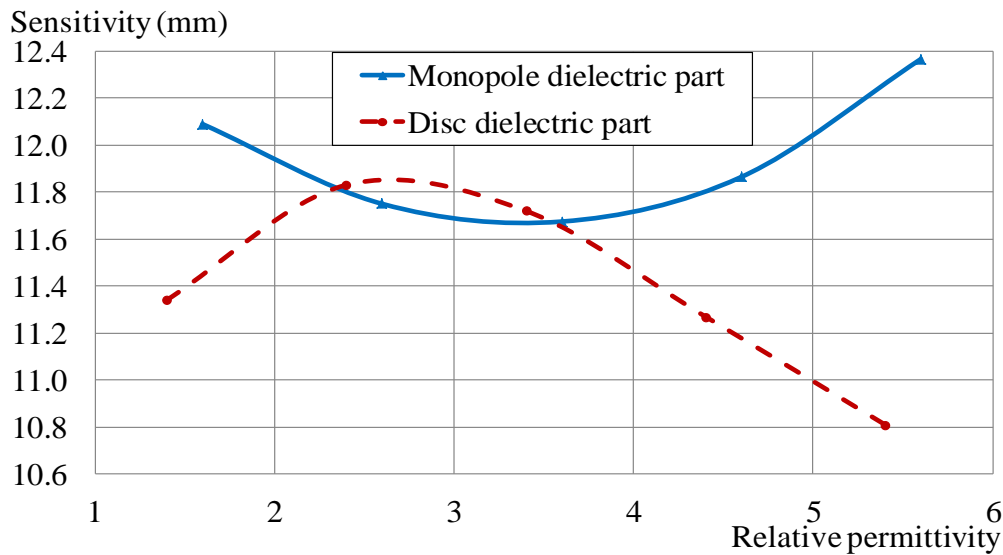


Figure 6.18: Simulated sensitivities of the monopole sensor and conventional disc sensor over 500 – 1500 MHz as a function of relative permittivity of their insulating structural components.

6.4.2 Geometry of the Sensors

Since UHF PD sensors respond through their interaction with electromagnetic waves, sensor geometry greatly influences the output voltage and frequency response. To study these effects, simulations were carried out to assess the effects of (i) decreasing the diameter of PVC materials of UHF monopole sensor while keeping the relative permittivity of PVC materials fixed at 2.6, and (ii) increasing the diameter of PEC conventional disc sensor while keeping the relative permittivity of Tufnol fixed at 3.4.

Figure 6.19 presents the simulated frequency responses for the original and a range of modified sensor component diameters. For the monopole sensor, the first dip in the curve (at 1330 MHz) for average sensitivity of the 16 cm diameter PVC part shifts to higher frequencies as PVC diameter decreases. In contrast, for each conventional disc sensor diameter the frequency response curve stays broadly the same, as does the position of the least sensitive frequency, at around 1700 MHz. The sensitivity simulation results, summarized in Table 6.7 and Figure 6.20, indicate that the output voltage and average sensitivity will decline when decreasing the diameter of the PVC body of the monopole sensor or increasing the diameter of PEC disc sensor.

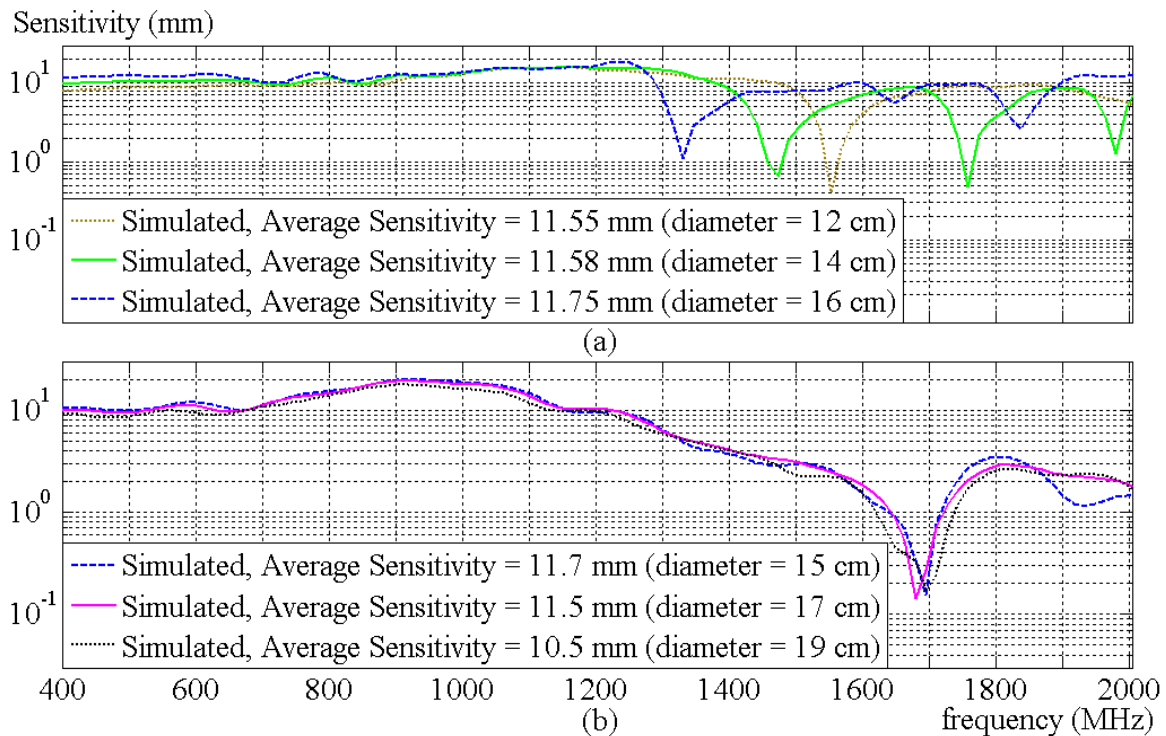


Figure 6.19: Simulated frequency responses when: (a) varying diameter of PVC body of the monopole sensor, and (b) varying diameter of the PEC disc of the conventional disc sensor.

Table 6.7

Simulated output voltage for various diameters of PVC body (monopole sensor) and PEC disc (conventional disc sensor).

Sensor component	Diameter (cm)	Simulated V_{pk-pk} (V)	Percentage difference of simulated V_{pk-pk} (%)
PVC body ($\epsilon_r = 2.6$)	12	0.2072	-20.25
	14	0.2354	-9.39
	16	0.2598	Reference value
PEC disc	15	0.2627	Reference value
	17	0.2547	-3.05
	19	0.2401	-8.60

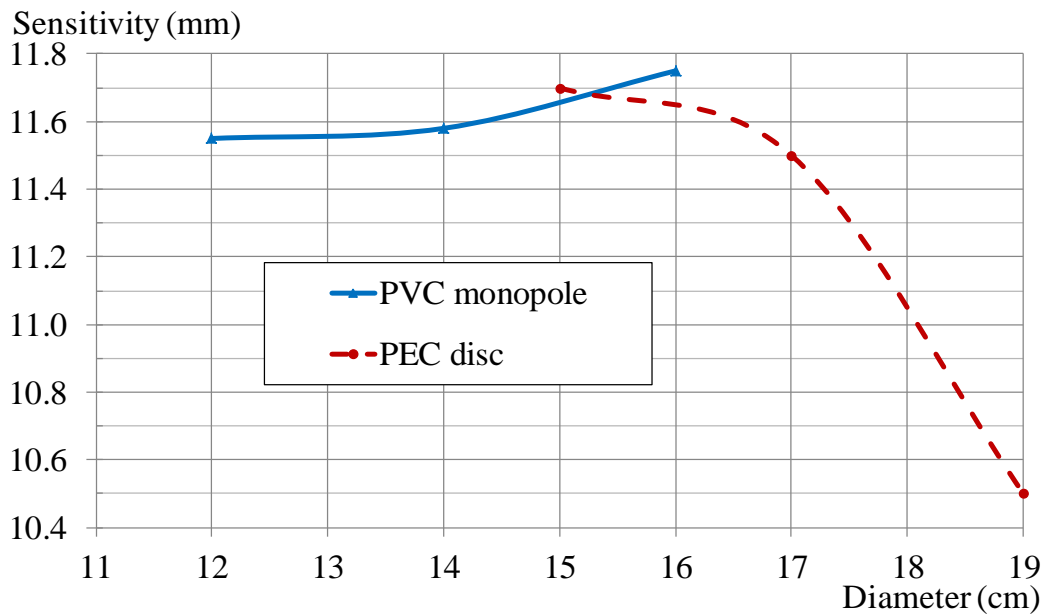


Figure 6.20: Average sensitivity simulation results for varying diameters of the PVC body of the monopole sensor and the PEC disc of the conventional disc sensor.

6.5 Conclusion

Partial discharge propagation in power transformer tank is modelled using FDTD technique. This help in analysing the arrival time of PD signals which is used to locate PD source in transformer tank. Modelling electromagnetic wave propagation in a tank is easier and not expensive compared to building a physical tank with cores, windings, sensors and mineral oil. The responses of the existing UHF sensors are predicted using the simulated calibration cell in FDTD software with minor error of 7.65%. Localising the sub-meshing helps to improve the accuracy of the models and reduce simulation time. The accuracy is improved by defining finer meshing around the small mechanical details of the modelled sensors. The sensor metal models are expressed as PEC in the simulation. This demonstrates that the modelling of UHF sensors is much easier because different types of metal materials can be combined and represented as PEC material. The author has proved that relative permittivity of dielectric materials and geometry of the sensors affect the average sensitivity. The average percentage change of the sensitivity for the relative permittivity of modelled monopole sensor and disc sensor is 32.5% for each 1.0 relative permittivity change. The average percentage change of the sensitivity for the geometry of both sensors is 35 % for 2 cm change in diameter. Next chapter describes the development of a novel disc-type sensor using the FDTD method.

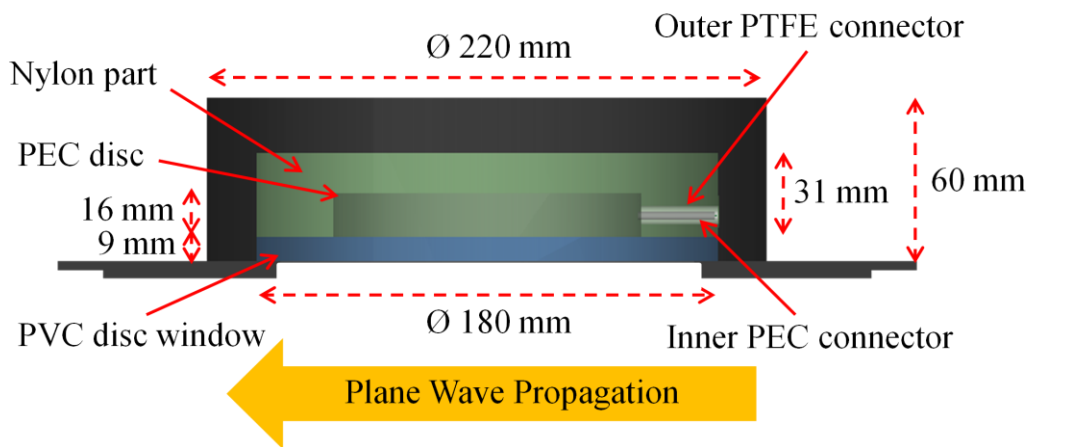
Chapter 7: Development of a Novel UHF PD Sensor using FDTD Simulation

The level of agreement between measured and simulated results presented in section 6.3 for four different sensors suggests that the simplifications within the FDTD model are sufficiently valid for it to serve as a useful tool for design purposes. The simplified calibration system represented in FDTD simulation can be used to predict frequency responses of UHF PD sensors. Localised meshing in the simulation can be applied to reduce memory space requirement and simulation time. The simulated PEC properties for the sensor metals can represent the real metals of the sensor such as aluminium and brass metals. The work presented in this chapter demonstrates the use of FDTD simulation to predict the frequency response of a novel disc-type UHF PD sensor design. The novel sensor could be mounted on a GIS or power transformer tank as an external PD sensor. The sensor was designed with the output connector located at the side of the disc sensor, which is mechanically preferable for routing of the UHF signal cable. Then the sensor was fabricated based on the modelled design. The experimental and simulated results of the calibrated novel sensor agreed with minor differences. Next, the same sensor was improved in term of the frequency response by optimising some mechanical structures of the modelled sensor. The improved sensor with highest sensitivity and easily manufactured structures was built and tested successfully. FDTD method has proved as a beneficial technique to design and predict the responses of UHF PD sensors.

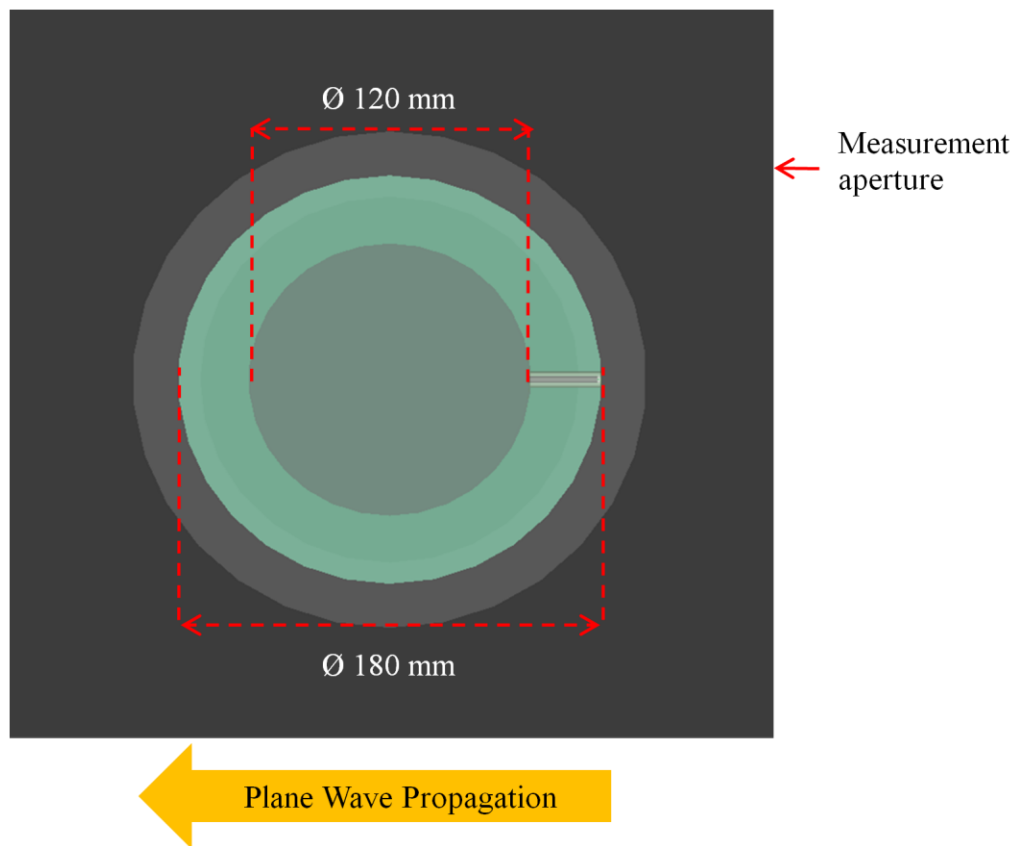
7.1 Modelling a Novel External Disc-Type UHF PD Sensor

A novel external disc-type UHF PD sensor was modelled using XFDTD software, as shown in Figure 7.1. This type of sensor could be applied externally to monitor PD levels for GIS and power transformers. The sensor was designed such that it did not protrude into the tank, nor require separate dielectric ‘window’, disc-type sensor because it could

be made mechanically robust, simple construction and could be permanently bolted on like a hatch cover.



(a)



(b)

Figure 7.1: The model of novel external disc-type UHF PD sensor with the output voltage measurement at the side of the disc sensor: (a) side view and (b) top view.

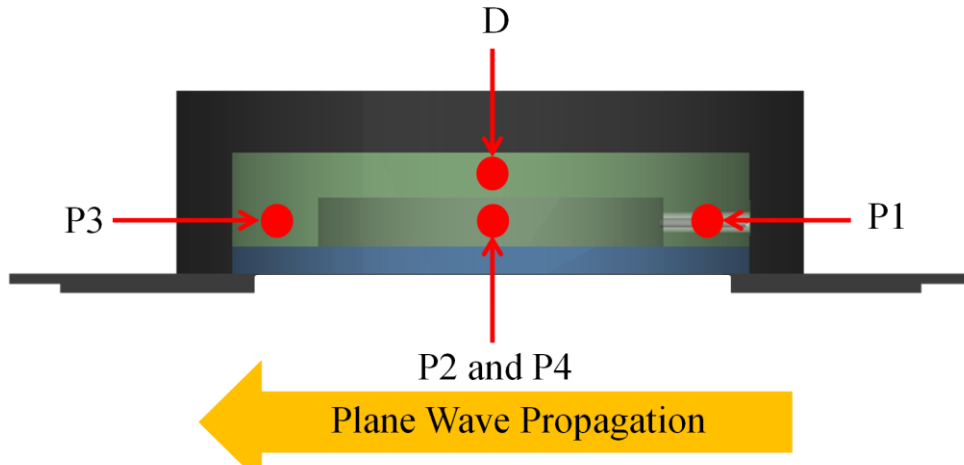
Three dielectric materials were used to model the sensor, described in Table 7.1, with relative permeability and conductivity equal to 1.0 and 0, respectively. The relative permittivities are based on [141]. The applied step electric field for the simulation of the sensor response was the same as in Figure 5.8. The output voltage of the sensor was simulated at five different positions with respect to the incident plane wave in the calibration system, as depicted in Figure 7.2. The output connector was located centre vertically to represent D location, and the other four locations of connectors (P1, P2, P3 and P4) were positioned horizontally with 90° apart. The simulated parameters of the modelled sensor are listed in Table 7.2.

The frequency response of the novel sensor was simulated using the calibration procedure introduced in section 6.3. The different locations of the voltage connections were simulated one at a time. The output voltages and the frequency responses of the sensor with different locations of voltage connections are shown in Figure 7.3. P1 and P3 locations of the output voltages have the higher average sensitivity and the first peak of response is at lower frequency (650 MHz). The vertical position of the output connection (D location) shows reduced response compared to P1 and P3 locations. The responses of the sensor for P2 and P4 locations are the same and they also have the lowest responses.

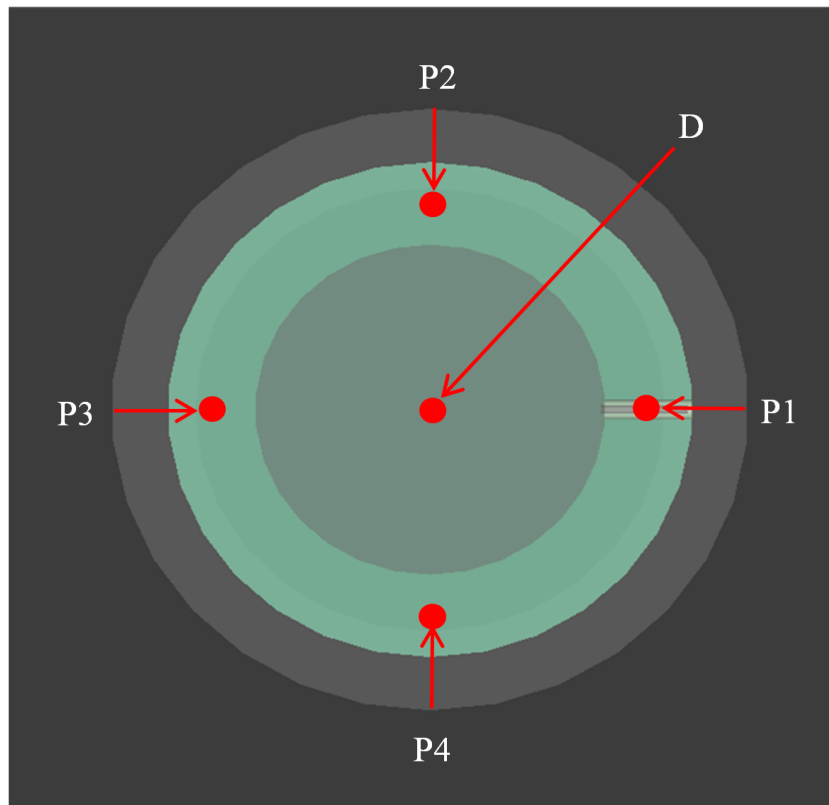
Table 7.1

Dielectric materials of the modelled sensor [141].

Material part	Relative permittivity
PTFE connector	2.1
PVC disc	2.8
Nylon part	3.0



(a)



(b)

Figure 7.2: The different positions of 50Ω loads (D, P1, P2, P3 and P4 positions) where the output voltages of the novel external disc-type UHF PD sensor are measured: (a) side view and (b) top view.

Table 7.2

Simulation parameters of the modelled sensor.

Cell size (cm)		Time step (ps)	Simulation run time
0.10	x: 39.0 – 61.0 y: 49.5 – 57.0 z: 14.0 – 36.0	1.926	1 hr, 44 min.
1.00	other regions		

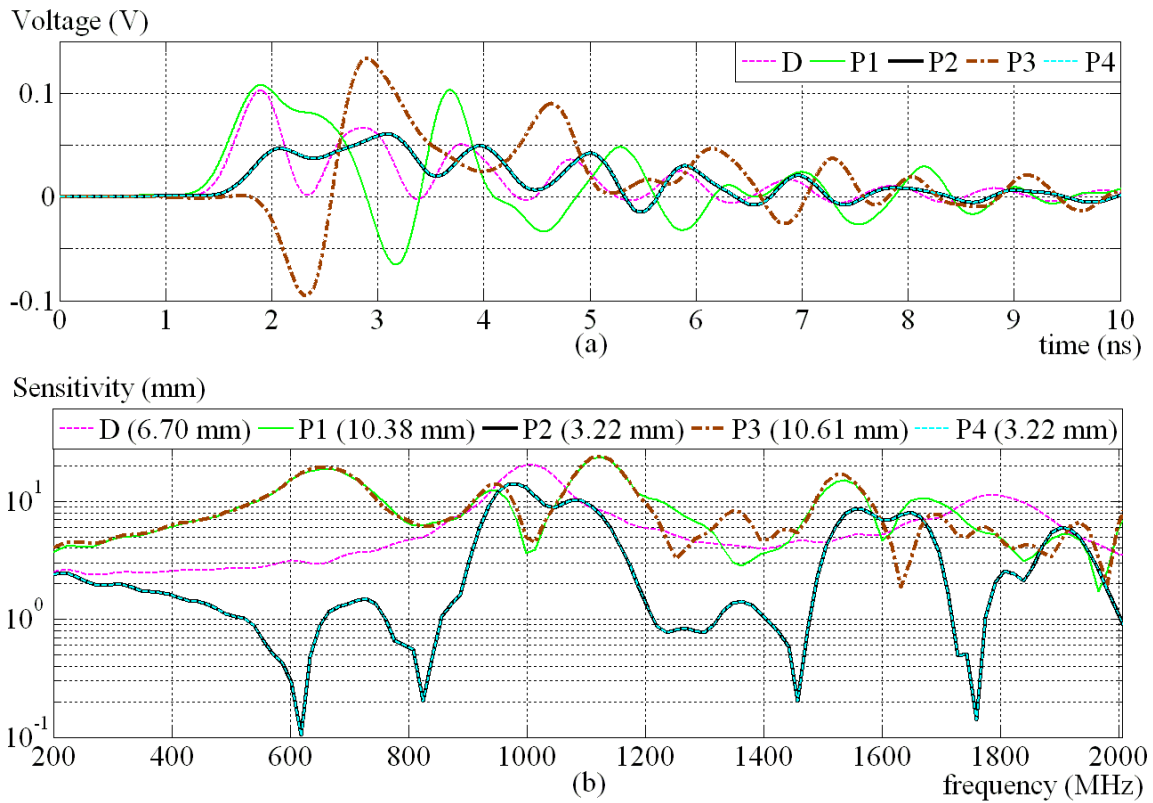


Figure 7.3: The simulated output voltages (a) and the frequency responses (b) of the sensor with different locations of voltage connections. Note that D, P1, P2, P3 and P4 refer to the different locations of output voltages as described in Figure 7.2.

The electric field distribution on the disc sensor can be explained using plane-wave equation. The electric field components (E_y) perpendicular to the disc surface, as shown in Figure 7.4, are expressed as [142] [80]:

$$E_y = E_0 J_n(kr) \cos n\theta \quad (7.1)$$

where E_0 is a constant, J_n is the n th-order Bessel function, the wavenumber (k) = $\omega\sqrt{\mu\epsilon}$ and r is the radius of the disc. From (7.1), the electric field strength will not be optimum and have the same value when θ is equal to 90° and 270° , because of the cosine function. This explains why the output voltages at P2 and P4 location (as in Figure 7.2) are the same and the values are low, as in the simulation results of Figure 7.3 (a).

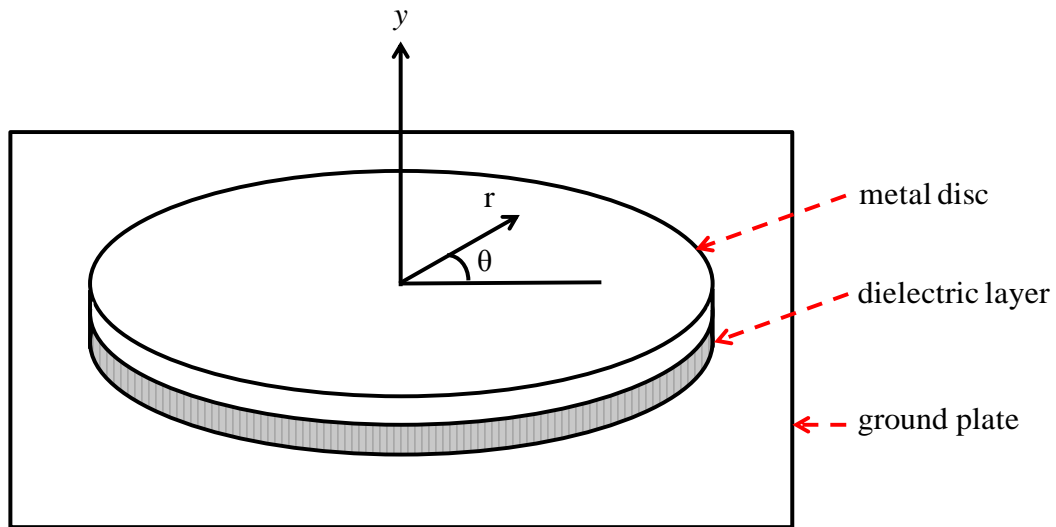


Figure 7.4: The coordinate configuration of the disc coupler.

7.2 Fabricating a Novel Disc-Type UHF PD Sensor

After modelling the new disc sensor using XFDTD software and predicting the average sensitivities, the sensor was fabricated in the laboratory with the output voltage connection in horizontal direction, as shown in Figure 7.5. The horizontal connection of output voltage was selected because the average sensitivities of the sensor are higher for P1 and P3 positions of the voltage connection compared to vertical position (D), as in Figure 7.3.

Using the same disc sensor, the output voltages and frequency responses were measured in the laboratory for four different positions of voltage connection (P1, P2, P3 and P4 positions), as defined in Figure 7.2. The voltage connection of the sensor was aligned toward the input terminal of the calibration cell to represent P1 position. P2, P3 and P4 positions of the voltage connection were arranged by rotating the sensor 90°, 180 ° and 270 °, respectively. The experimental and simulated results are compared as shown in Figures 7.6 and 7.7. The comparison shows that there are minor differences in the amplitude and shape of the output voltages and average sensitivities of the measured and simulated external disc-type UHF PD sensor.

Further investigation was done to study the effect of the nylon part, as in Figure 7.5 (b), on the average sensitivity of the disc sensor. In the simulation, the nylon part was deleted and replaced with free space region. During experiment, the nylon part was removed and replaced with five blocks of dielectric material, four blocks at the side and one block on the bottom of PEC disc as shown in Figure 7.8. The block is made of high-performance Rohacell foam with very low relative permittivity about the same as relative permittivity of air. The blocks were used to support and make sure PEC disc was at the same position as measuring the sensor with the nylon part.

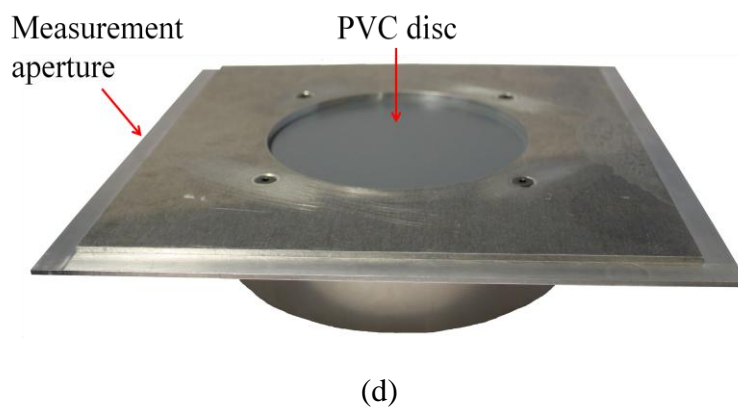
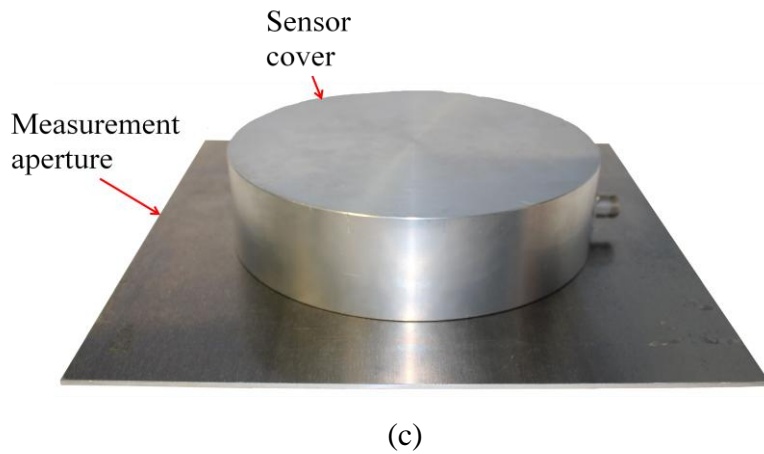
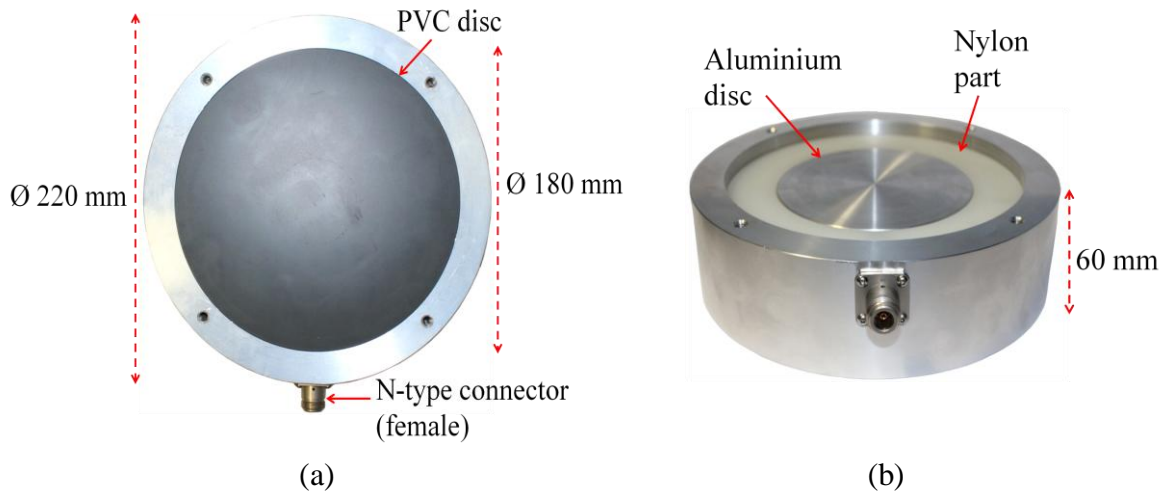


Figure 7.5: The fabricated novel disc-type UHF PD sensor: (a) top view, (b) side view with the PVC disc removed from the front face, (c) bottom view with attached measurement aperture, and (d) top view with the measurement aperture.

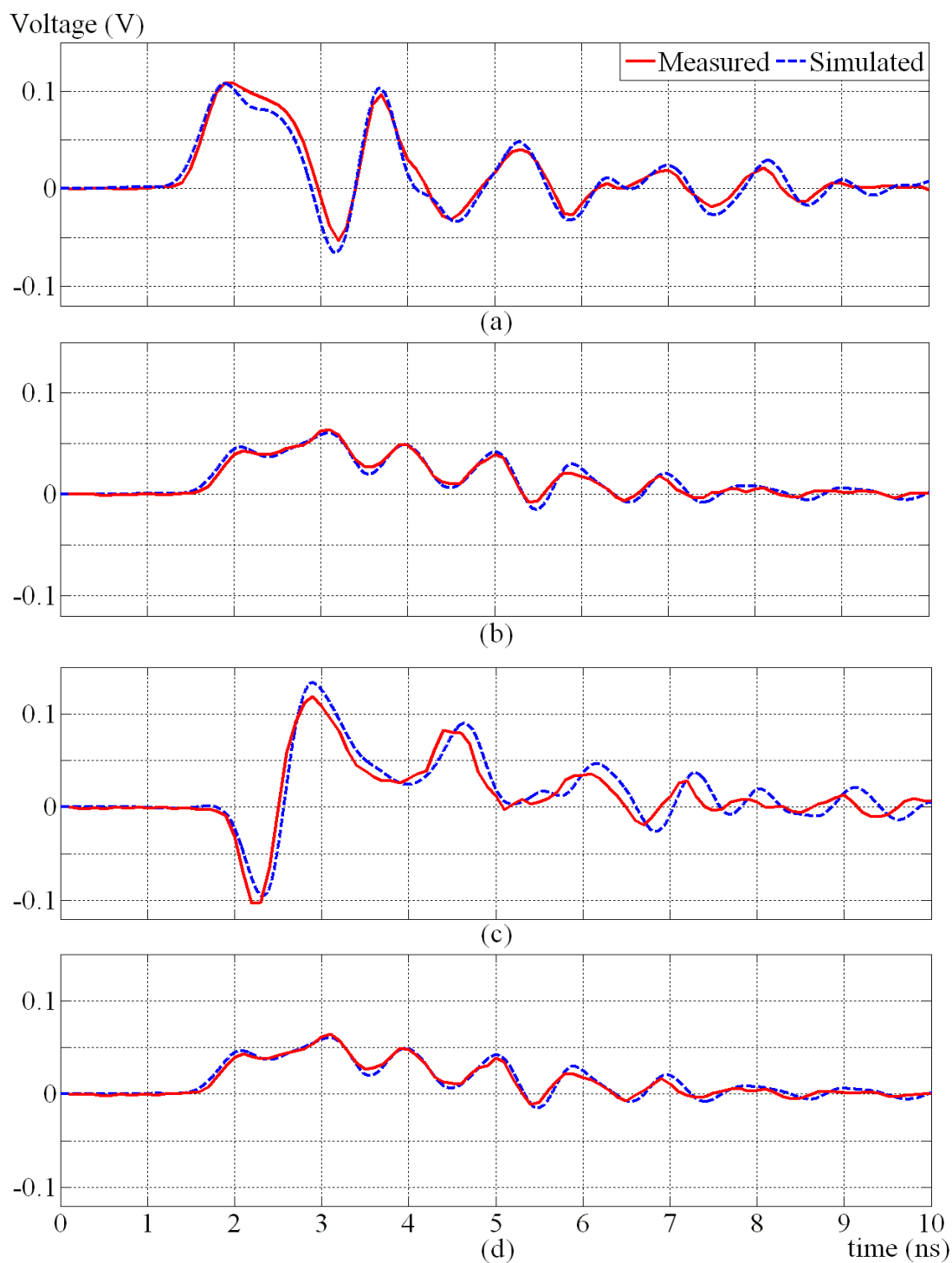
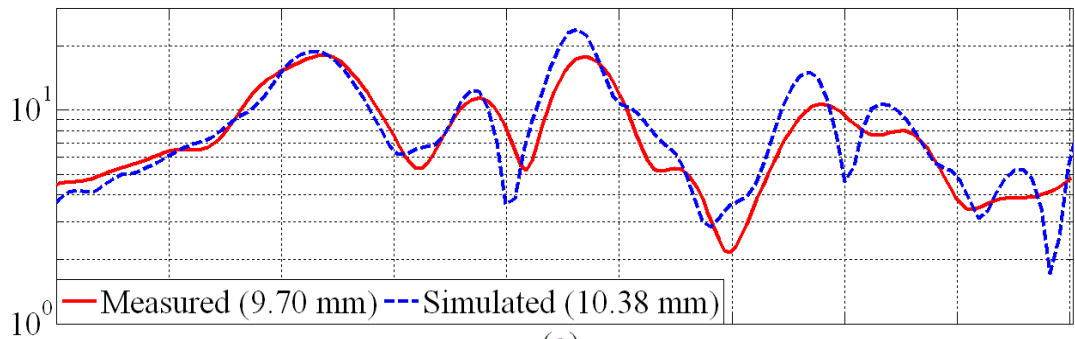
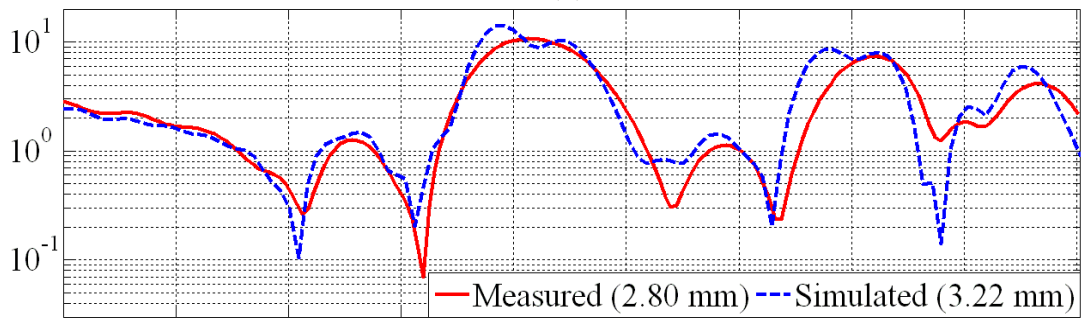


Figure 7.6: The measured and simulated output voltages for four different positions of voltage connector: (a) P1 position, (b) P2 position, (c) P3 position, and (d) P4 position.

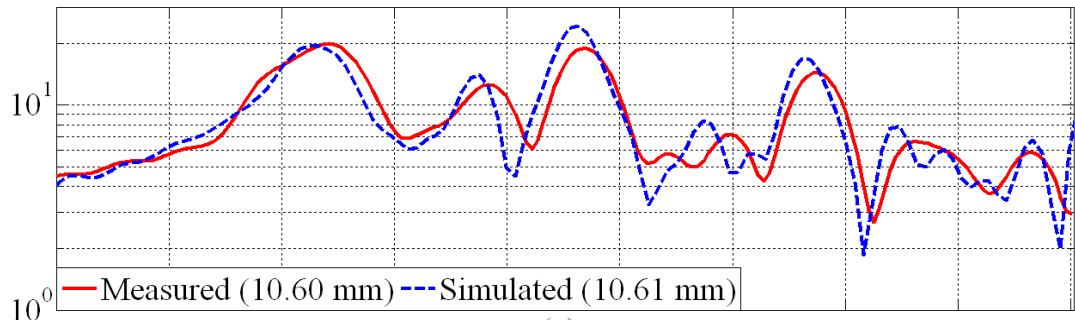
Sensitivity (mm)



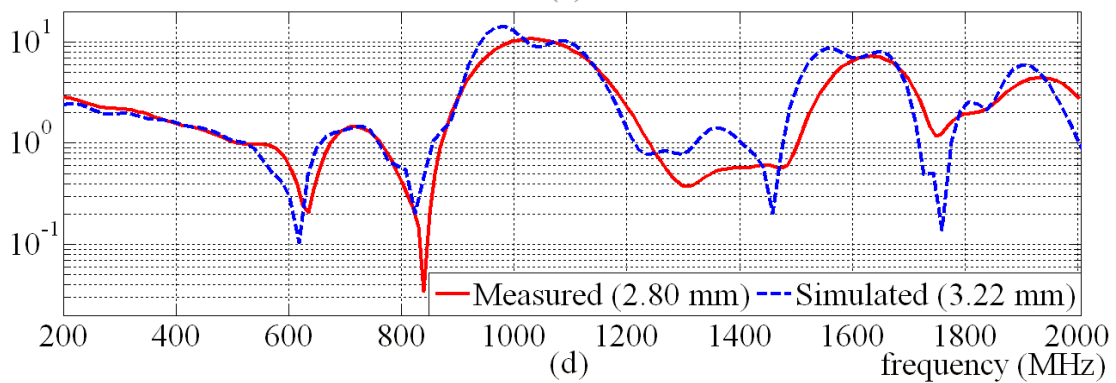
(a)



(b)



(c)



(d)

Figure 7.7: The measured and simulated frequency responses for four different positions of voltage connector: (a) P1 position, (b) P2 position, (c) P3 position, and (d) P4 position.

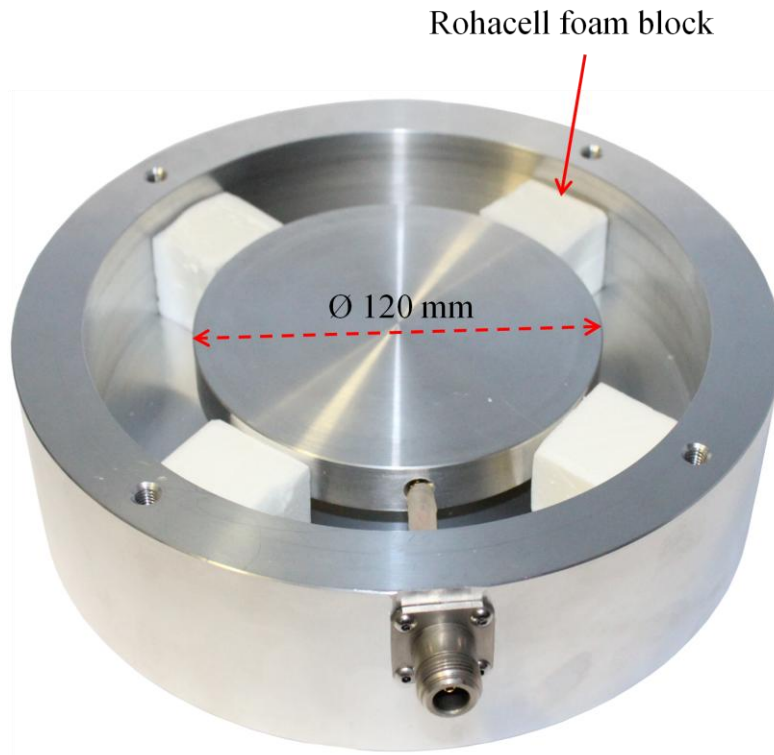


Figure 7.8: The disc-type UHF PD sensor without nylon part and replaced with foam blocks.

The output voltages and frequency responses of the sensor without the nylon part are described in Figures 7.9 and 7.10, respectively. The figures compare the experimental and simulated results for four different positions of voltage connection. The output voltages of the sensor without nylon part (as in Figure 7.9), for all positions of voltage connection, have quite similar shapes and larger amplitudes as compared to the output voltages of the sensor with nylon part (in Figure 7.6). In Figures 7.7, (i) the first peaks of the sensor responses for P1 and P3 output positions occur at about 650 MHz; and (ii) the first dips of the sensor responses for P2 and P4 output positions are observed at frequency of 620 MHz. In contrast to Figure 7.10, there is no dominant peak (at 650 MHz for P1 and P3 positions) or dip (at 620 MHz for P2 and P4 positions). This can be caused by the absence of nylon part in the sensor.

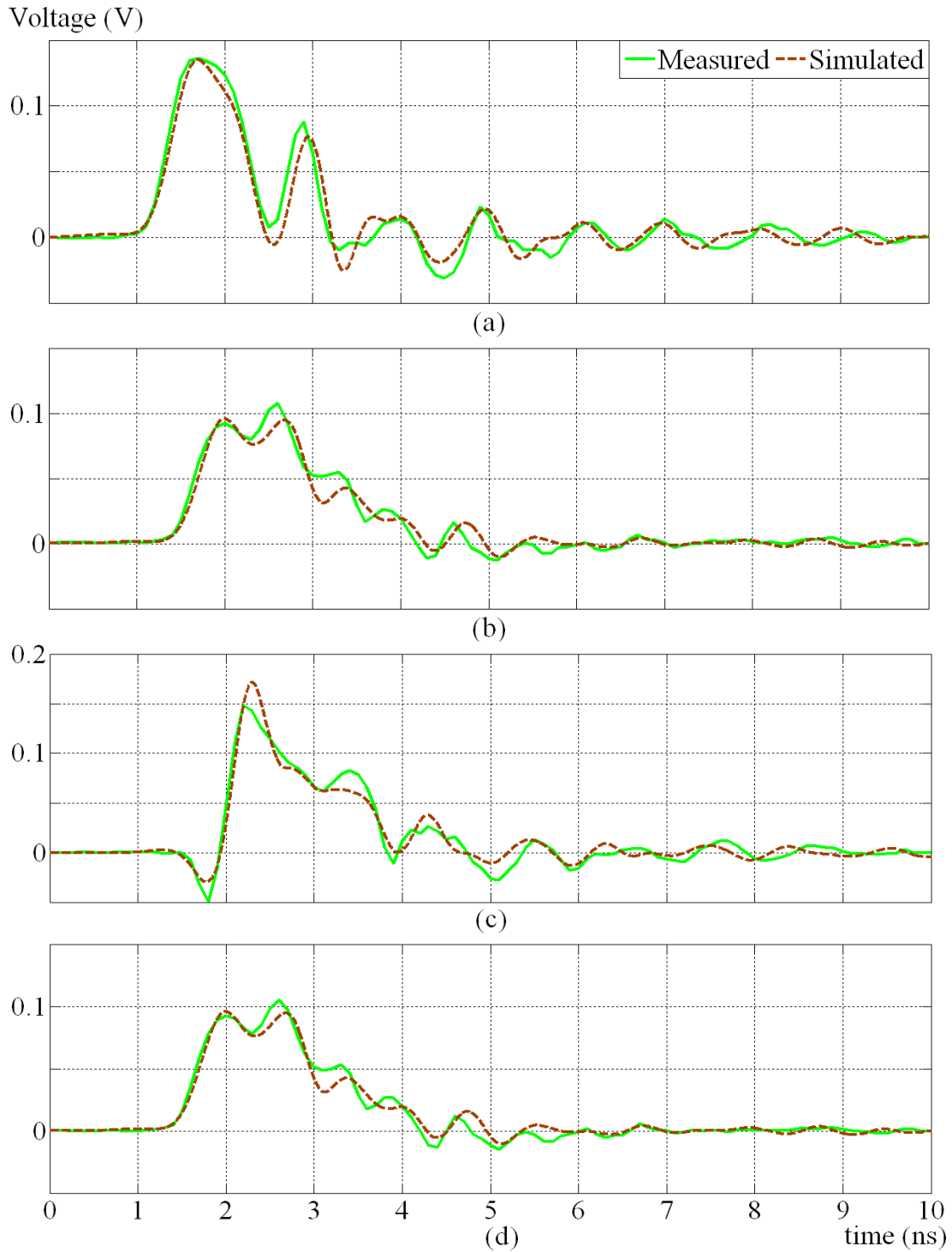


Figure 7.9: The measured and simulated output voltages for four different positions of voltage connector without nylon part: (a) P1 position, (b) P2 position, (c) P3 position, and (d) P4 position.

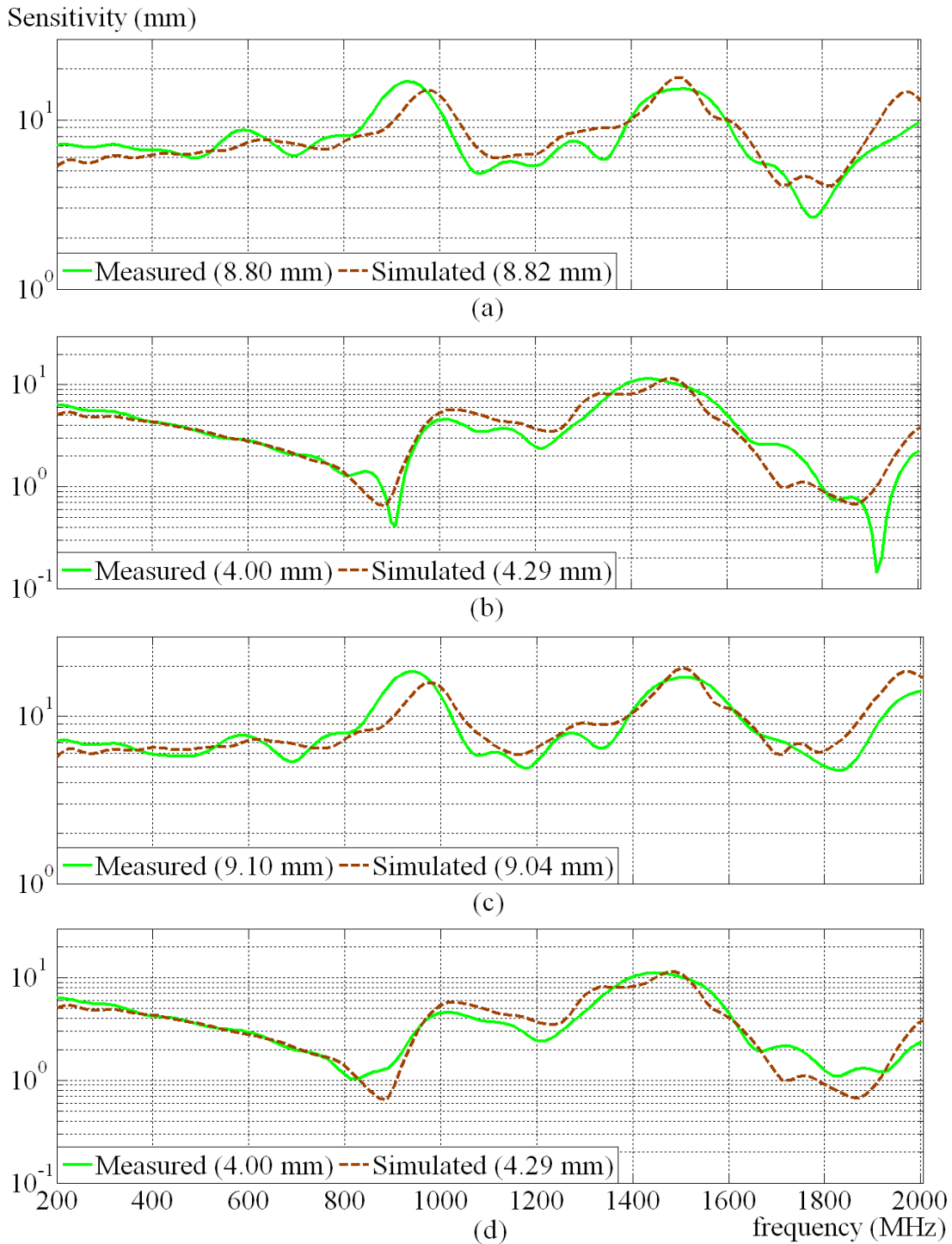


Figure 7.10: The measured and simulated frequency responses for four different positions of voltage connector without nylon part: (a) P1 position, (b) P2 position, (c) P3 position, and (d) P4 position. The different outputs of the measured responses for P2 and P4 positions of the connector can be due to experimental mounting error of the sensor.

7.3 Improving the Novel External Disc-Type UHF PD Sensor

This section explains further optimisation of the new sensor design to improve the response of the novel external disc-type sensor. The response of the sensor varies with sensor mounting angle. The response is higher when the output position of the sensor is rotated at P1 and P3 positions (as in Figure 7.2) compared to P2 and P4 positions. Therefore, the sensor design was modified so that the 90° rotational symmetry of the sensor breaks up, as described in next section. There are two promising designs of the external disc-type UHF PD sensor which show improvement of the sensor response and small variations in the response with different angle of sensor mounting. The first design is changing the relative permittivity of half-nylon part and the second design is inserting four earth rods between PEC disc and the sensor cover. The half-nylon part was assigned with different relative permittivities that broken up the rotational symmetry of the sensor. Adding the earth rods between the disc and sensor cover also disturbed the rotational symmetry and it was easier to physically fabricate compared to the half-nylon model.

7.3.1 Different Relative Permittivity of Half-Nylon Part

The nylon part as in Figure 7.1 is separated 45° horizontally into two parts which are Dielectric 1 and Dielectric 2, as described in Figure 7.11. The PVC disc remained complete as in Figure 7.1 with relative permittivity of 2.8. The two dielectric parts were simulated with different relative permittivities as in Configuration 1 and Configuration 2 in Table 7.3. The simulated relative permittivities were 2.1, 2.8 and 5.5 that represented PTFE, PVC and filled Tufnol materials. Configuration 2 was simulated with higher difference of the relative permittivities between Dielectric 1 and Dielectric 2 as compared to Configuration 1. This is to disturb the symmetrical distribution of the electric fields around the disc sensor.

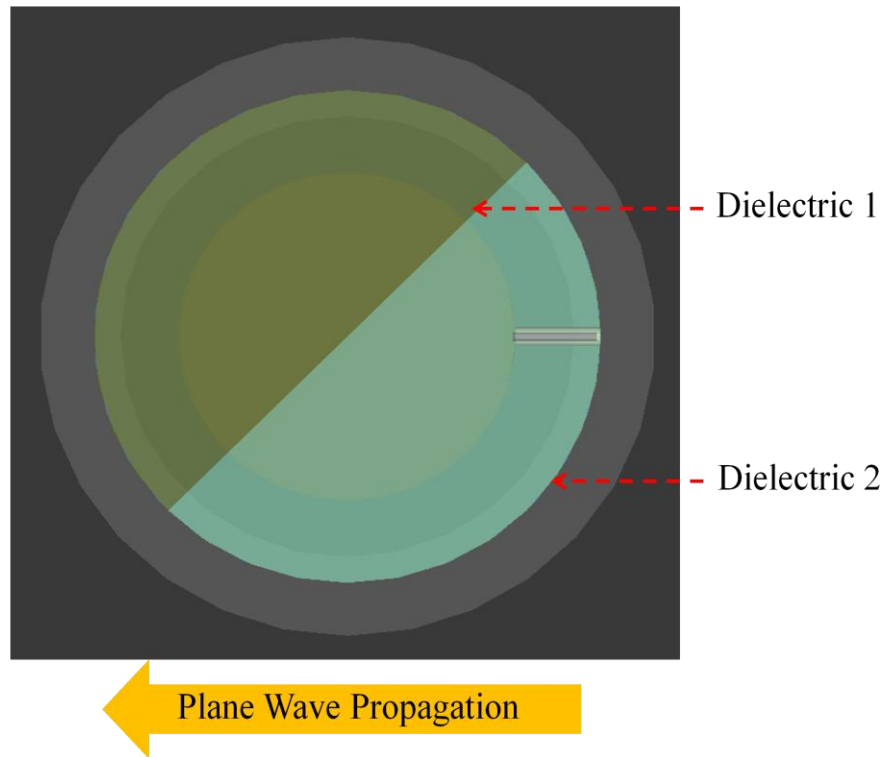
Figure 7.12 shows the simulated frequency responses of the disc sensor with both configurations. Both configurations improve the average sensitivity of the sensor, by comparing with Figure 7.7. However, Configuration 2 improves the average sensitivity of the sensor more than Configuration 1 with higher relative permittivity of dielectric 2 part.

The sensitivity differences between P1, P2, P3 and P4 output positions of Configuration 2 are also reduced where the electric fields around the disc sensor distributed more evenly. This was proved by the simulated responses of the four different positions of the connector with an average of 1.93 mm sensitivity change between the connector positions compared to 4.89 mm sensitivity change for the original novel model of the sensor. Therefore, the half-nylon model distributes the electric fields around the disc sensor more evenly with low sensitivity change between the connector positions compared to the original model of the sensor.

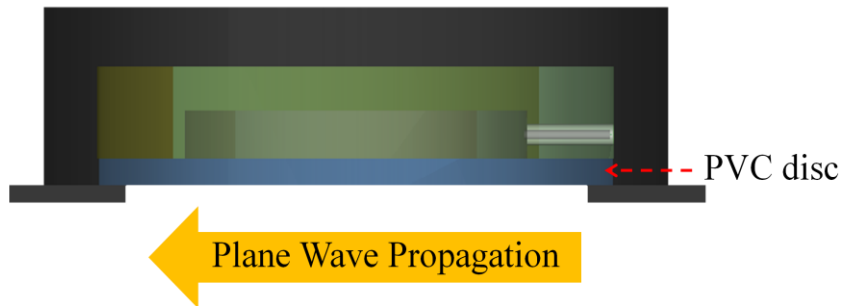
Table 7.3

The configurations of different relative permittivity materials.

Configuration	Relative permittivity	
	Dielectric 1	Dielectric 2
1	2.1	2.8
2	2.1	5.5



(a)



(b)

Figure 7.11: The position of output voltage connector (P1 position) with two halves of the former nylon part replaced with different relative permittivity materials (Dielectric 1 and Dielectric 2): (a) top view and (b) side view. The sensor is rotated 90° counter clockwise to represent P2 position of output voltage connector, 180° clockwise (P3 position of output voltage connector) and 270° counter clockwise (P4 position of output voltage connector).

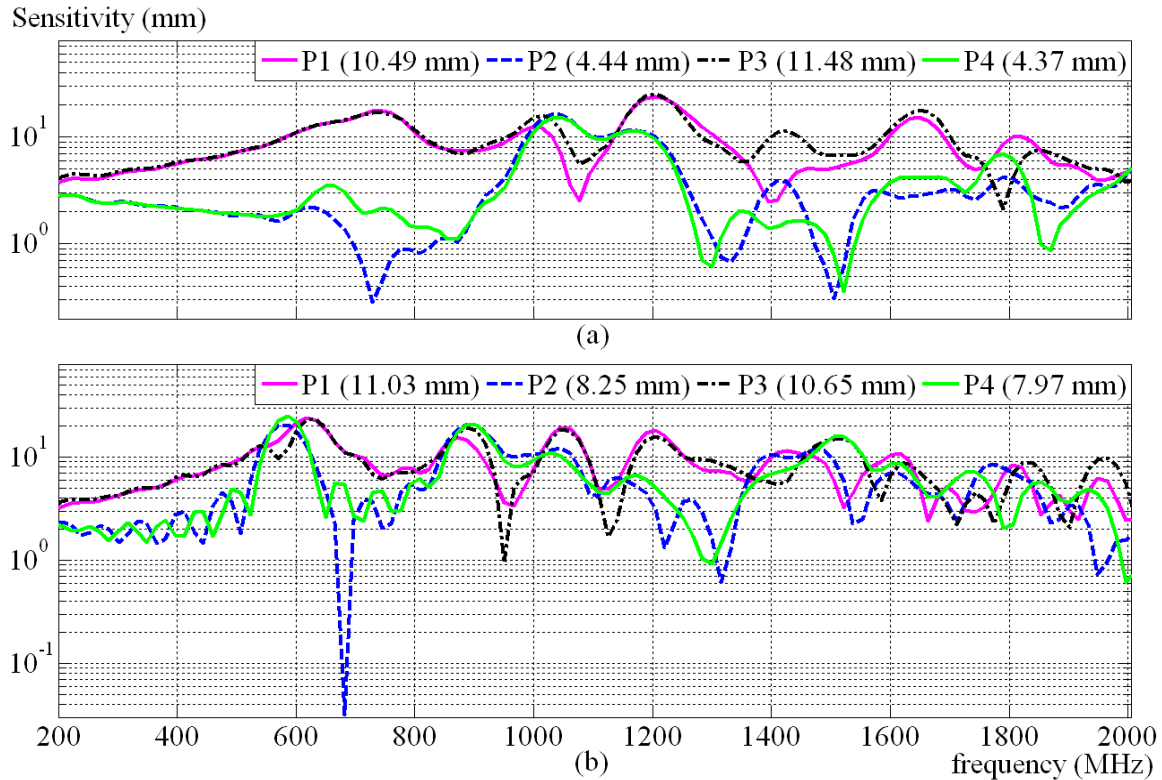


Figure 7.12: The simulated frequency responses of the disc-type sensor with four different positions of voltage connection for: (a) Configuration 1 and (b) Configuration 2 (as described in Table 7.3).

7.3.2 Four Earth Rods

The second alternative design of the disc-type sensor is by adding four earth rods on the disc sensor. This model was applied to break up the rotational symmetry of the sensor. The PVC disc and nylon part, as in Figure 7.1, retained the same structure with relative permittivity of 2.8 and 3.0, respectively. The earth rods were modelled between PEC disc and sensor cover, as shown in Figure 7.13. Four holes were made at the nylon part to locate the four earth rods. The sensor design was simulated with three different diameters of the rods which were 2.0 cm, 2.5 cm and 3.0 cm.

Figure 7.14 shows the frequency responses of the sensor for four earth rods of varying diameters. The rods with 2.5 cm in diameter result in slightly higher average sensitivity

than the other two diameters. The sensitivity at frequencies below 600 MHz for all three diameter rods is decreased especially for P2 and P4 positions of voltage connection, as compared to the sensor responses of the original disc sensor in Figure 7.7. The sensor sensitivity at the frequency of about 650 MHz increases for all positions of output connection especially P2 and P4 position, relative to Figure 7.7. The responses of the improved design for P1 and P3 output locations are about the same. Although the rods earth the sensor at low frequencies, the sensor can have a non-zero response which means that the sensor response has a value at the low frequency region even after adding the earth rods. The advantages of the rods are excellent mechanical strength and no possibility of capacitively coupled high voltage at the sensor output. The response of the sensor is higher for 2.5 cm diameter of the earth rods. The average increase of the responses for four positions of the connector is 2.50 mm (for 2.5 cm diameter of the rods) while 2.0 and 3.0 diameters of the rods are 2.37 mm and 2.41 mm, respectively. Therefore, 2.5 cm diameter of the rod was further investigated to improve the response of the novel sensor.

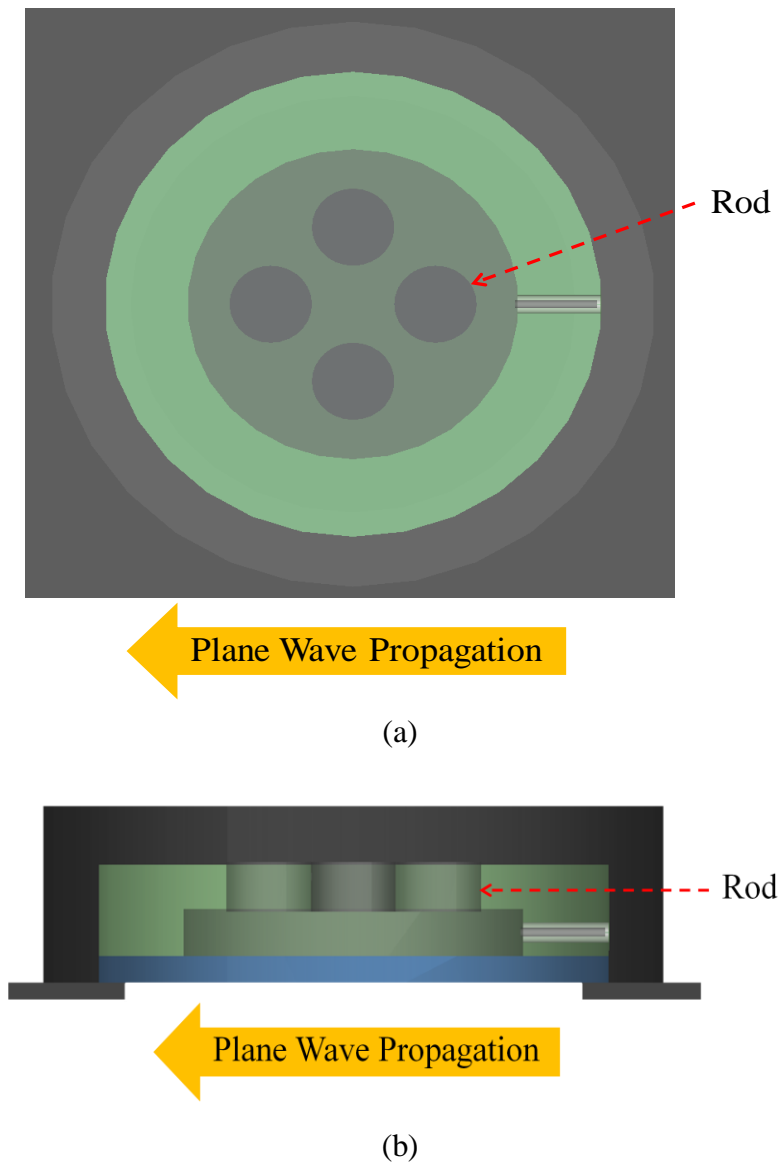


Figure 7.13: The position of output voltage connector (P1 position) with four earth rods: (a) top view and (b) side view. The diameter of the rods is 3.0 cm.

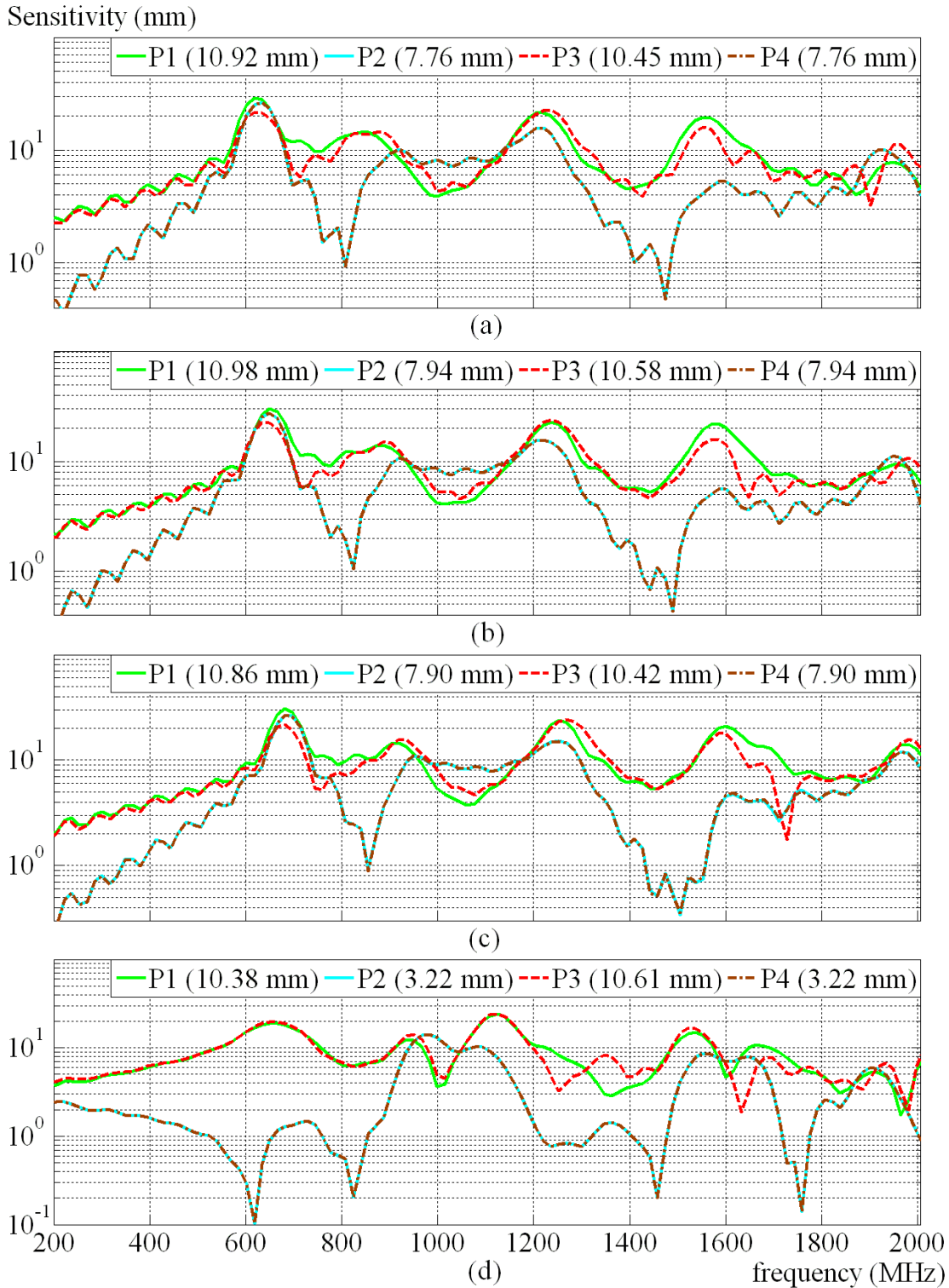


Figure 7.14: The simulated frequency responses of the improved sensor for different positions of voltage connection with four earth rods: the diameters of the rods are (a) 2.0 cm, (b) 2.5 cm, and (c) 3.0 cm. The original simulated responses are shown in (d), from Figure 7.7.

The sensor design was further simulated with 2.5 cm diameter of four earth rods with the rods are rotated 45° from the axis of the output connection, as shown in Figure 7.15. This design slightly increases the average sensitivity of the sensor for output voltage connectors at P1 and P3 positions in Figure 7.16, compared with Figure 7.14 (b). However, the responses of the sensor for P2 and P4 positions slightly reduce.

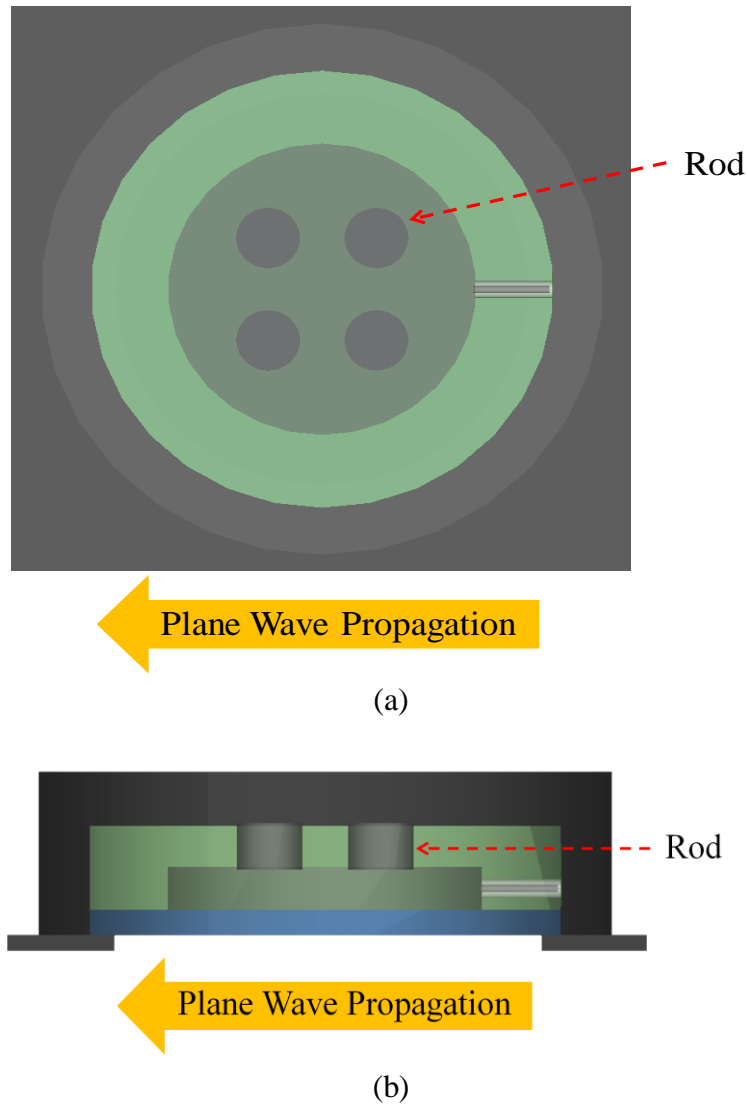


Figure 7.15: The position of output voltage connector (P1 position) with four earth rods that have been rotated 45° where Figure 7.13 as the reference configuration: (a) top view and (b) side view.

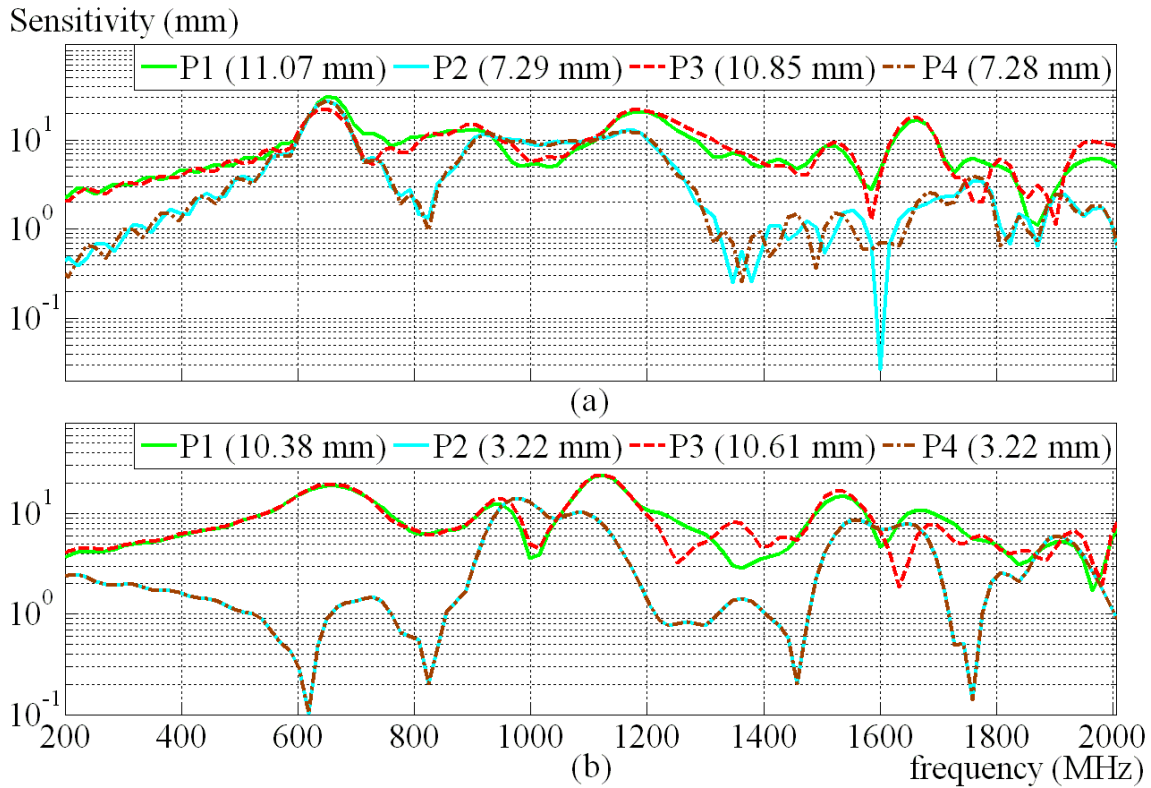
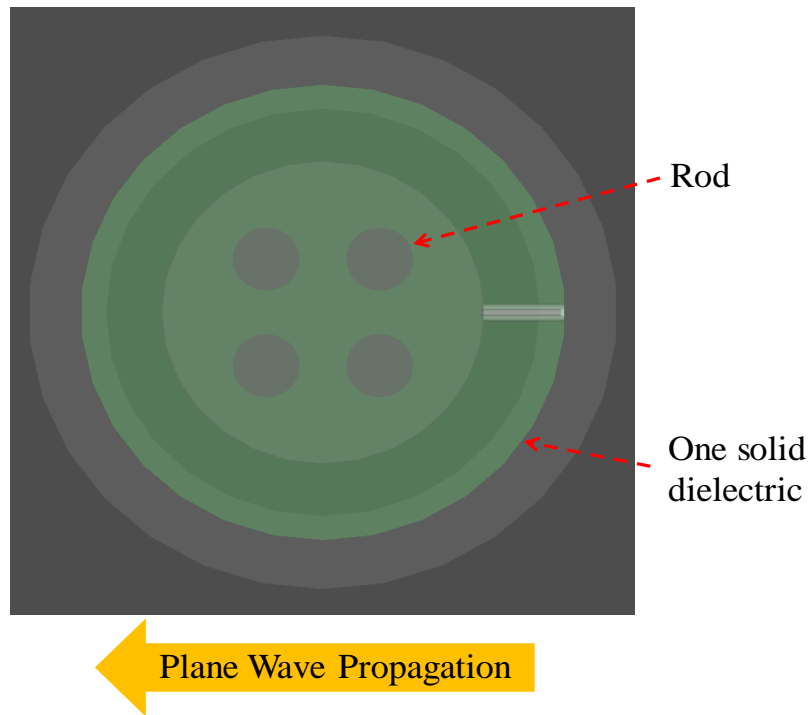
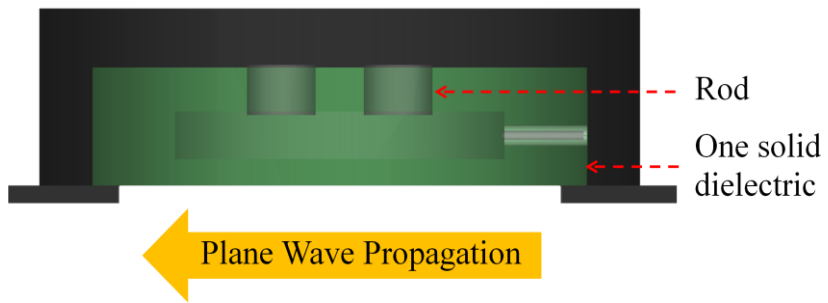


Figure 7.16: The simulated frequency responses of the sensor for different positions of voltage connection with four rotated earth rods (the diameter of the rods is 2.5 cm) are shown in (a). The original simulated responses are shown in (b), from Figure 7.7.

Then, the rotated earth rods were simulated by combining the nylon part and PVC disc as one solid dielectric, as depicted in Figure 7.17. The use of a single material would simplify the design and also allow the device to be made by ‘potting’ the sensor in a resin-based compound. Three different relative permittivities of the dielectric were simulated which were 2.8, 3.0 and 5.5 that represent as PVC, nylon and filled Tufnol materials, respectively. The average sensitivities of the combined dielectrics with different relative permittivities are listed in Table 7.4. PVC material with relative permittivity of 2.8 as the combined dielectrics for the sensor suggests the best material with highest average sensitivity for all positions of the voltage connection.



(a)



(b)

Figure 7.17: The combined dielectric parts for P1 position of output voltage connector with four rotated earth rods (the diameter of the rods is 2.5 cm): (a) top view and (b) side view.

Table 7.4

The average sensitivity of the sensor for combined dielectrics.

Relative permittivity of the combined dielectrics	Output voltage position	Average sensitivity (mm)
2.8	P1	11.12
	P2	7.58
	P3	10.88
	P4	7.58
3.0	P1	11.01
	P2	7.25
	P3	10.31
	P4	7.25
5.5	P1	9.31
	P2	4.31
	P3	9.23
	P4	4.32

7.4 Frequency Response Analysis of the Improved Design Sensor

From Table 7.4, the modelled structure of the sensor with rotated earth rods and uniform dielectric (relative permittivity equals to 2.8) gives the best response compared to other designs of the sensor. It is also easy to fabricate compared to the design with half nylon parts as in Figure 7.11. Therefore, the sensor with rotated earth rods and PVC dielectric material was manufactured. The internal parts of the fabricated sensor are shown in Figure 7.18. The top of the four earth rods are connected to the sensor cover using “banana” connectors and the bottom parts are screwed to the aluminium disc of the sensor. This is to ensure the earth rods are placed at the exact positions and also make sure a firm contact between the earth rods and the sensor cover; and between the rods and aluminium disc. Figure 7.19 shows the improved disc sensor where PVC disc is placed on top of the aluminium disc.

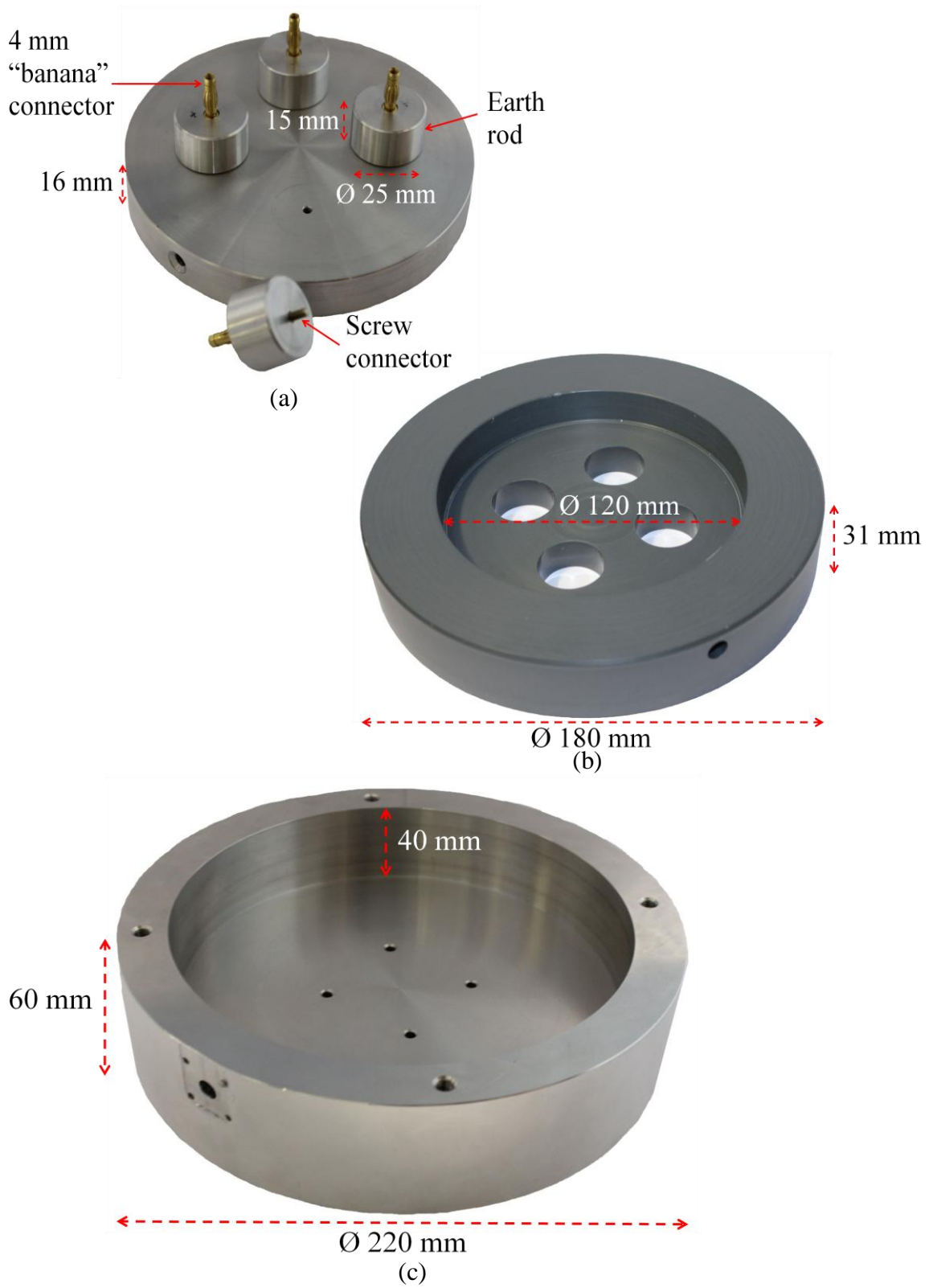


Figure 7.18: The internal parts of the improved novel external disc-type UHF PD sensor: (a) aluminium disc with earth rods, (b) PVC part, and (c) sensor cover.

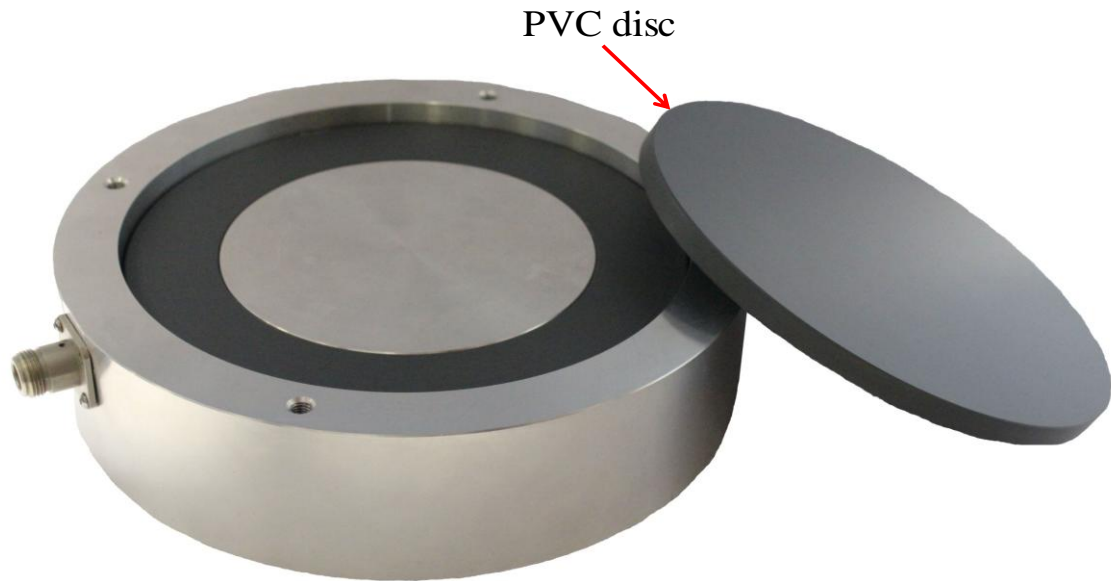


Figure 7.19: The improved external disc-type UHF PD sensor.

The measured frequency responses of the improved external disc-type sensor are compared with the simulated design of combined dielectric with relative permittivity of 2.8 as in Table 7.4. The measured and simulated results in Figure 7.20 show that they are almost the same in shape and amplitude. The response results, especially for P2 and P4 voltage locations, indicate that the improved sensor is a more effective design compared to the original sensor responses in Figure 7.7.

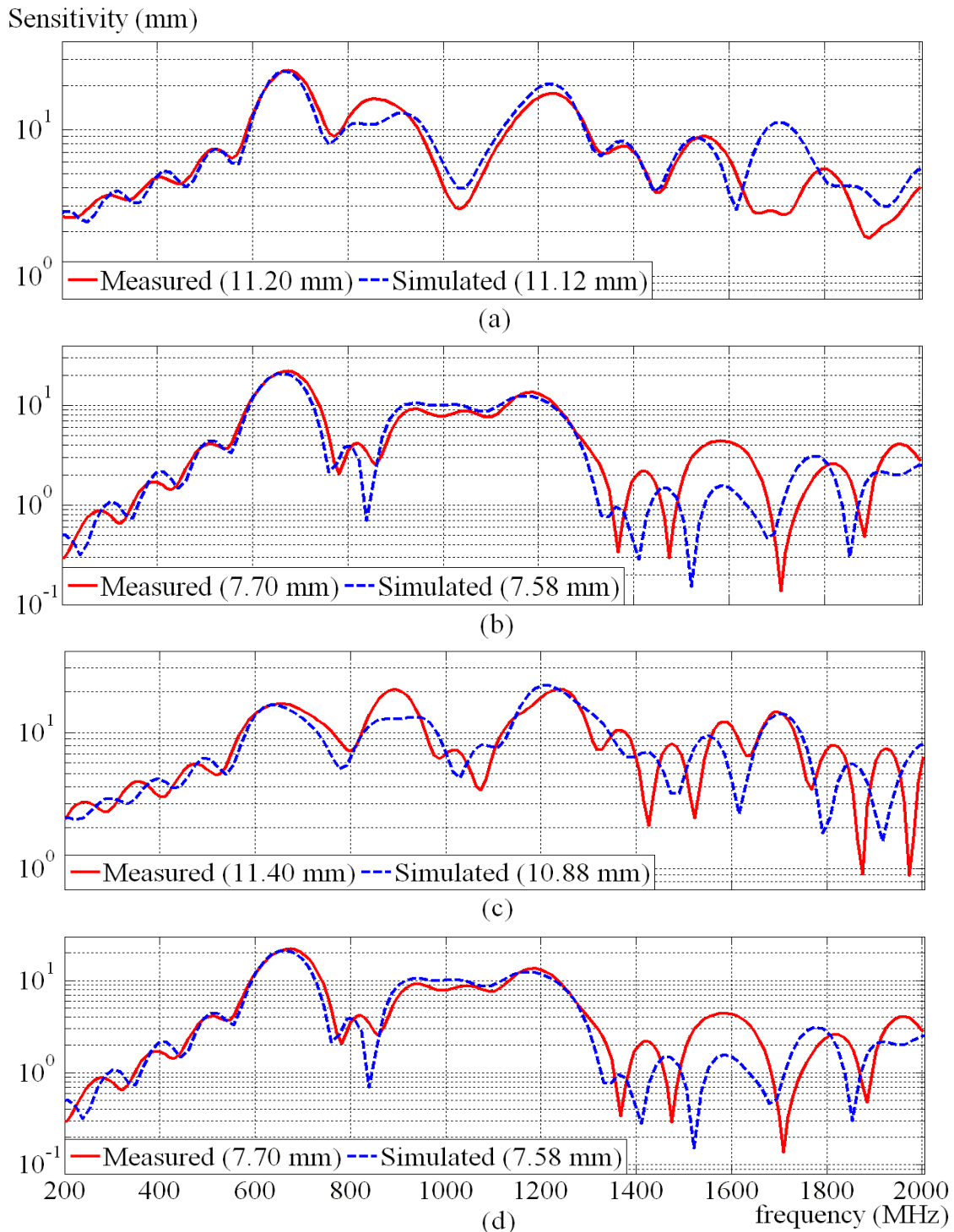


Figure 7.20: The measured and simulated frequency responses for four different positions of improved disc-type UHF PD sensor with four voltage connector positions: (a) P1 position, (b) P2 position, (c) P3 position, and (d) P4 position.

7.5 Simulated Calibration System and Parallel Plates Application

This section discusses the different structure of calibration system by applying parallel plates instead of sloped calibration model as in Figure 6.10. The sloped calibration model represents the GTEM calibration cell where electromagnetic waves uniformly distribute from one point of the injected signal to large area of the cell. The parallel plates calibration system could conform better to the Yee cell mesh and potentially reduce the total simulation volume by making the plate length shorter. The length and width of the parallel plates are 100 cm and 50 cm, respectively. The gap distance between the parallel plates is 25 cm. The modelled sensors are located at the middle of the top plate as demonstrated in Figure 7.21. The simulation involved all the modelled sensors, namely, the 25 mm reference probe, experimental disc-type sensor, monopole sensor, conventional disc sensor, original external disc-type sensor and improved external disc-type sensor. The same technique for localised meshing was used for all the modelled sensors as in sloped calibration system.

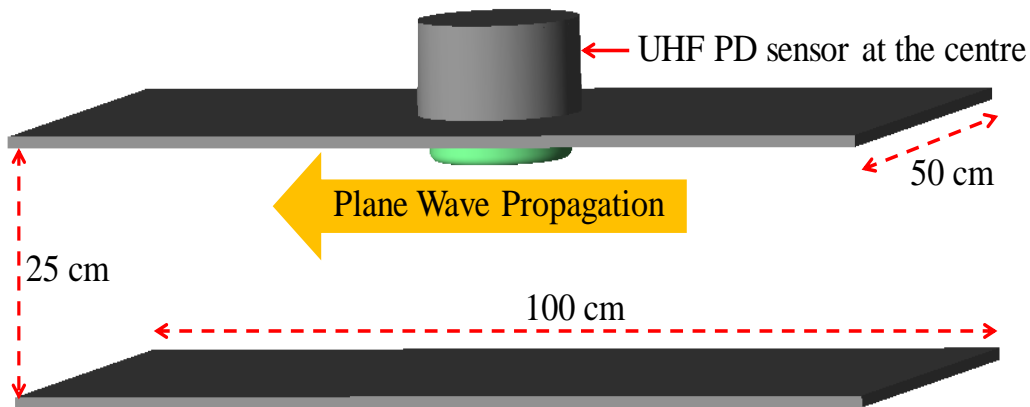


Figure 7.21: The parallel plates calibration system to simulate the frequency responses of UHF PD sensors.

The frequency responses of all the sensors simulated using the parallel plates calibration system are compared with the experimental results and simulated results using sloped calibration system, as shown in Figure 7.22 until 7.24. The results describe the sensor responses simulated using parallel plates calibration system give higher error as compared to sloped calibration system. Table 7.5 presents the percentage differences of the responses for all the sensors using both calibration systems. These results prove that parallel plates calibration system cannot be used to represent GTEM cell in FDTD simulation. This is because the characteristic of electromagnetic wave propagation in GTEM cell is best represented by the sloped model of the calibration cell with average percentage error of 6.34 % for all the tested sensors, compared to parallel plates calibration system with 20.02 % error. The percentage differences of the responses are calculated by comparing the differences between simulated results and measured results. The percentage errors of the parallel plates application are too high compared to the simulated responses for sloped calibration system. The computational time for parallel plates application is less because the number of mesh cells is lower than the sloped calibration system as the size of the parallel plates calibration cell is smaller.

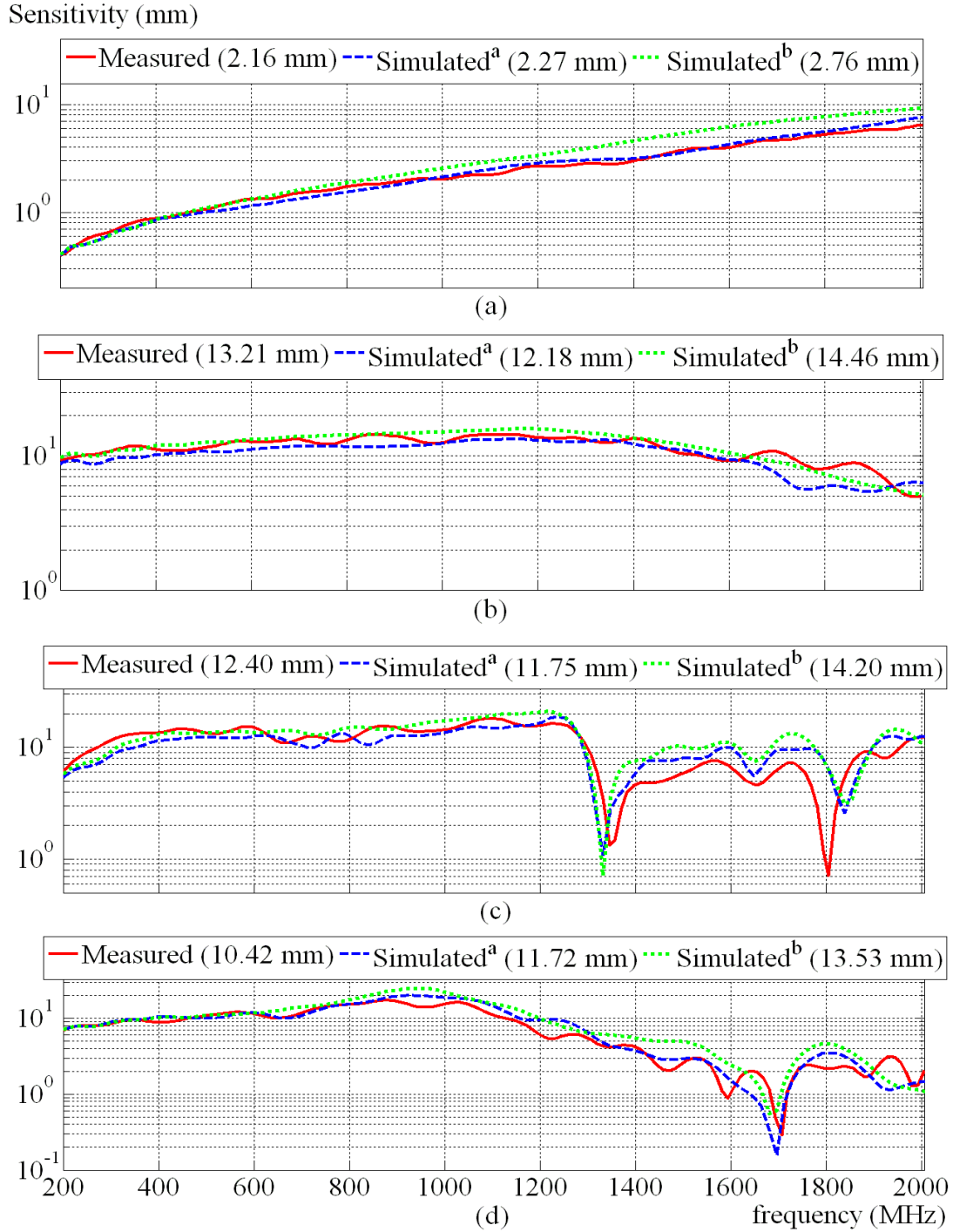


Figure 7.22: Frequency responses of existing PD sensors: (a) 25 mm reference probe, (b) experimental disc sensor, (c) monopole sensor, and (d) conventional disc sensor for measured results and simulated results using sloped calibration system (Simulated^a) and parallel plates calibration system (Simulated^b).

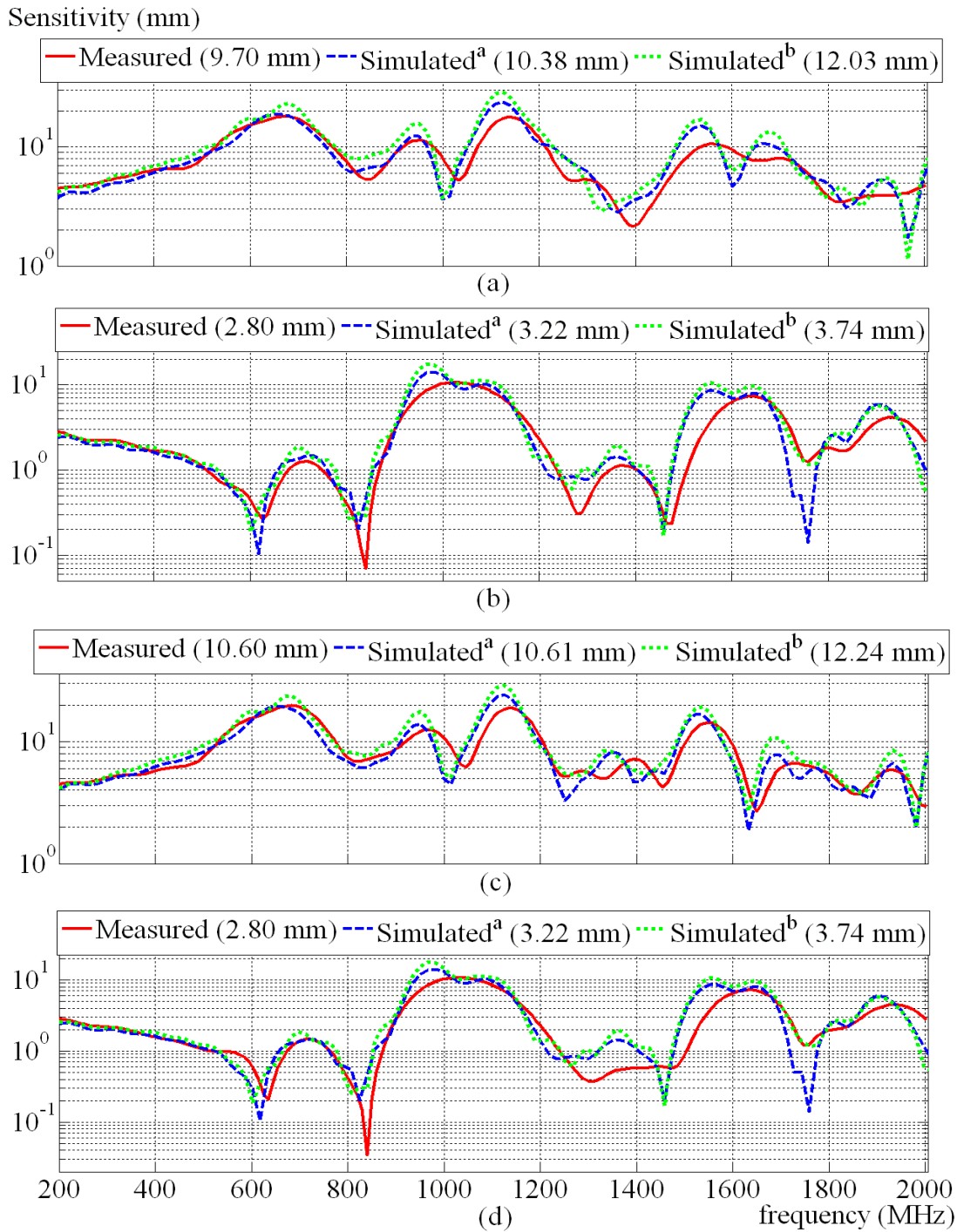


Figure 7.23: The responses of the new external disc sensor for different positions of voltage connectors: (a) P1 position, (b) P2 position, (c) P3 position, and (d) P4 position. The results are compared between the experimental data and simulated data.

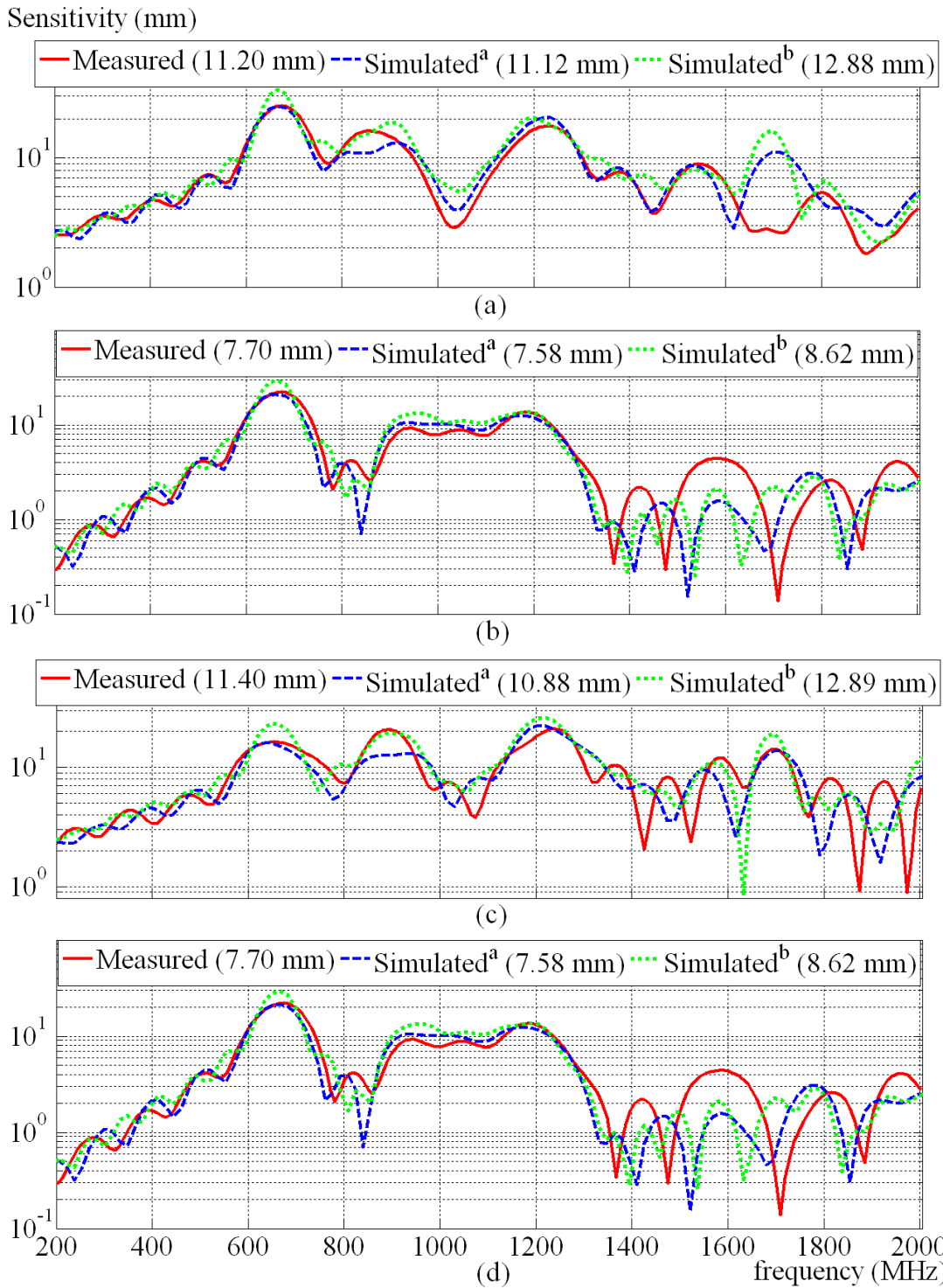


Figure 7.24: The improved external disc sensor for different positions of voltage connectors: (a) P1 position, (b) P2 position, (c) P3 position, and (d) P4 position.

Table 7.5

The comparison of frequency responses between sloped calibration system and parallel plates calibration system.

Sensor	Frequency response (mm)			Percentage difference between simulated and measured responses (%)		Simulation run time		
	Measured	Simulated ^a	Simulated ^b	Simulated ^a	Simulated ^b	Simulated ^a	Simulated ^b	
25 mm probe	2.16	2.27	2.76	5.09	27.78	37min	12min	
Experimental disc	13.21	12.18	14.46	-7.80	9.46	42 min	27 min	
Monopole	12.40	11.75	14.20	-5.24	14.52	2hrs,13min	1hr,31min	
Conventional disc	10.42	11.72	13.53	12.48	29.85	2hrs,17min	1hr,42min	
External disc	P1	9.70	10.38	12.03	7.01	24.02	1hr,44min	1hr,7min
	P2	2.80	3.22	3.74	15.00	33.57		
	P3	10.60	10.61	12.24	0.09	15.47		
	P4	2.80	3.22	3.74	15.00	33.57		
Improved external disc ^c	P1	11.20	11.12	12.88	-0.71	15.00	1hr,39min	1hr,6min
	P2	7.70	7.58	8.62	-1.56	11.95		
	P3	11.40	10.88	12.89	-4.56	13.07		
	P4	7.70	7.58	8.62	-1.56	11.95		

Note: ^a = Calibration system as in Figure 6.10

^b = Parallel plates calibration as in Figure 7.21

^c = Rotated earth rods with combined dielectric (PVC material)

7.6 Conclusion

The FDTD technique has demonstrated that it can optimise sensor design and predict the responses of UHF PD sensors. The horizontal output connector of the disc sensor gives higher response (average response of the connector positions is 6.86 mm) compared to the vertical output connector with response of 6.70 mm. The symmetrical effect of the sensor responses is disturbed by adding earth rods between the aluminium disc and sensor cover. The rods also provide excellent mechanical strength and prevent the sensor from capacitively coupled with high voltage circuit of the electrical equipment. The parallel plates calibration system has higher percentage difference between the simulated and measured responses of the sensors. The absolute average difference between the simulated and measured responses, for all the sensors in Table 7.5, using the parallel

plates calibration system is 20.02 % and by applying the sloped calibration system is 6.34 %.

8. Conclusions

Partial discharge occurs in gas, liquid and solid materials of high voltage equipment. The measured apparent charge of PD is affected by the test cell arrangement and types of dielectrics. The apparent charge is measured using the conventional PD technique where a sensor is physically connected to high voltage circuit of test object. UHF PD measurement is one of the unconventional PD measurements that a sensor is not electrically connected to high voltage part of the test object.

Locating PD sources in high voltage equipment is an increasingly important maintenance activity especially when the equipment is been scheduled for a short duration of overhaul period. Installing several UHF PD sensors on the equipment can help maintenance engineers to locate the defects by using time-of-flight methods. There are mainly two types of UHF PD sensors which are internal-type and external-type. The external sensor can give better response compared to internal sensor.

For better understanding the characteristics of UHF PD sensors, knowledge of the sensor response is important. The response is measured using a calibration cell instead of using a representative model of high voltage equipment. From the studies, an artificial pulse is used to represent PD signal. With the same pulse, the response of UHF PD sensors is obtained and compared for different types of sensors. UHF PD sensor behaves as an antenna rather than a capacitive sensor. A GTEM calibration cell can be used to measure the response of UHF PD sensors. The average sensitivity of the sensors must be higher than 6.0 mm, as recommended by National Grid Company. The responses of the four existing sensors have been experimentally measured by the author using the GTEM calibration system.

The sensor will be designed, fabricated and then calibrated with the hope that the design will meet the minimum standard required for the sensor average sensitivity. The computational FDTD electromagnetic modelling for parametric simulation and predicting the response of UHF PD sensors using a representation of a GTEM calibration cell has

demonstrated benefits in UHF PD sensor design. The response of the sensor can be predicted using FDTD method with minor errors. This method can reduce or eliminate repetitive process of fabricating and calibrating the sensor till it meets the minimum sensitivity standard. The characteristic of electromagnetic wave propagation generated by PD source in power transformer tank is also modelled using FDTD technique.

The responses of the existing sensors are predicted by the author using the FDTD method with 7.65 % error. The sensor metal is model as PEC in the simulation which makes the modelling easier. Comparison of simulated and laboratory experimental results show that there are relatively minor differences in the amplitude and shape of the time-domain output voltages and frequency responses of the measured and simulated UHF PD sensors. These differences are most likely to have arisen from the simplified representation of the GTEM cell structure within the FDTD model. For example, only the upper half of the cell was simulated; a solid septum was used instead of thin wires; and the metal sides of the cell were replaced with absorbing boundaries in the model. Nevertheless, measured and simulated results indicate that the FDTD method is an effective tool for designing and predicting the response of UHF PD sensors.

The relative permittivity of insulating materials and the geometry of UHF PD sensors play a significant role in determining their sensitivities and this has been illustrated by means of parametric studies using FDTD models. The FDTD method has potential to accelerate the effective design process for UHF PD sensors, reducing development costs and helping to optimize their performance. A novel external disc-type UHF PD sensor has been designed entirely within the domain of FDTD model and then validating its performance by constructing and testing a corresponding physical device. The vertical output connector of the disc sensor has lower response compared to the horizontal connector. The earth rods between the aluminium disc and sensor cover have improved the response and broken up the symmetrical effect of the disc sensor. The sensors can be used externally to monitor and locate PD sources in power transformer or even GIS system.

Parallel plates calibration system cannot represent the physical GTEM calibration system. This has been proved by the higher percentage error (20.02 %) of the average responses for all the tested sensors using the parallel plates model of calibration system, compared to the sloped model which is 6.34 %.

9. Future Works

A lot of future works can be done using the FDTD method since the simulated calibration system can represent the measured one. The research works can involve:

- Modelling a new UHF PD sensor with an effective size of the sensor that could reduce production cost but still maintaining the average sensitivity above the minimum standard or improving the sensitivity. A new gap-type UHF sensor can be designed to measure partial discharge signals that could propagate through gasket at the hatch plate of transformer or GIS system. Simulating the cheapest dielectric materials by changing the relative permittivity properties that will result in effective sensor response can also improving the modelling of a new sensor.
- Optimising the efficiency of using the FDTD technique in simulating the calibration system by (i) minimizing the volume of the simulated calibration system especially at the output side of the system, and (ii) increasing the mesh size which could speed up the simulation period if it is not increasing the percentage difference between simulated and measured results.
- It will also good to compare other numerical methods (such as FIT and FEM) in simulating a same system, for example calibration system of UHF sensors, in order to understand the differences in complexity to solve the equations, percentage errors between measured and simulated results, the effects of simulation time, and the requirement of computational memory spaces. The Yee cell, as a cuboid shape, does not conform well to circular or triangular structures.

Appendices

Copy of Paper: A. M. Ishak, P. C. Baker, W. H. Siew, and M. D. Judd, “Characterizing the Sensitivity of UHF Partial Discharge Sensors using FDTD Modeling”, *IEEE Sensors Journal*, vol. 13, pp. 3025 – 3031, Aug. 2013.

Characterizing the Sensitivity of UHF Partial Discharge Sensors using FDTD Modeling

A. M. Ishak, P. C. Baker, W. H. Siew, and M. D. Judd

Abstract—Ultra high frequency (UHF) partial discharge sensors are widely used for condition monitoring and defect location in the insulation systems of high voltage equipment. Designing sensors for specific applications often requires an iterative process of manufacture, test, and mechanical modifications. This paper demonstrates the use of finite-difference time-domain (FDTD) simulation as a tool to predict the frequency response of a UHF sensor design. Using this approach, the design process can be simplified and parametric studies can be conducted in order to assess the influence of component dimensions and material properties on the sensor response. The modeling approach is validated using a broadband UHF sensor calibration system, which uses the step response of the sensor to determine its frequency-domain transfer function. The use of a transient excitation source is particularly suitable for modeling using FDTD, which is able to simulate the step response output voltage of the sensor, from which the frequency response is obtained using the same post-processing applied to the physical measurement. Comparisons between simulation and measurement are made for three different sensors, demonstrating sensitivity agreement to within about 10%. Some examples of simple parametric studies carried out using the FDTD model are also presented.

Index Terms—Calibration, FDTD simulation, partial discharges, UHF sensor

Manuscript received August 27, 2012. This work was supported by the Universiti Pertahanan Nasional Malaysia (UPNM).

A. M. Ishak is a PhD student in the Department of Electronic & Electrical Engineering, University of Strathclyde and employed as an academic staff at the UPNM (e-mail: asnor.ishak@strath.ac.uk).

M. D. Judd, W. H. Siew, and P. C. Baker are with the Department of Electronic & Electrical Engineering, University of Strathclyde, Glasgow, UK (e-mail: m.judd@strath.ac.uk, wh.siew@strath.ac.uk, and peter.baker@eee.strath.ac.uk).

I. INTRODUCTION

Measurement and monitoring of partial discharge (PD) activity is an important method to assess the insulation condition of high voltage equipment. One of the techniques used to detect and locate PD sources is by using ultra high frequency (UHF) sensors. The first application of UHF sensors in this context was to locate defects causing PD in gas insulated substations (GIS) [1], [2]. Now well established in GIS applications, UHF sensors are increasingly being used to detect PD in power transformers [3], [4], [5], [6].

There are many types of UHF sensors that can detect electromagnetic waves that radiate from PD sources. The general types of UHF PD sensors are disc and spiral [7], monopole [8], and conical [9] types.

UHF PD sensors are continuously being developed to improve their sensitivity and range of applications for detecting and locating PD sources in power transformers. For example, the use of window-mounted UHF sensors can improve detection sensitivity [10] and offers a means of retrofitting during an outage [11]. UHF sensors have also been shown to be capable of detecting PD in transformer oil under DC voltage conditions [12] and locating PD sources inside transformer windings [13].

The electrical sensitivities of UHF sensors can be calibrated using a pulsed GTEM (gigahertz transverse electromagnetic) test cell [14]. For calibration, the sensors are mounted at an aperture on the GTEM cell and subjected to a sub-nanosecond electric field step. The sensitivities are obtained as a frequency response in post-processing using a fast Fourier transform (FFT) algorithm. This involves dividing the output voltage of the sensors in frequency domain (mV) by the input electric field in frequency domain (V/m) to give the sensitivity as an *effective height* in mm [15].

Finite-difference time-domain (FDTD) simulation is a computational modeling technique that is particularly suited to modeling the propagation of electromagnetic transients

and their interactions with different materials and structures. For example, modeling of PD phenomena is outlined in [16], while the modeling of a UHF spiral sensor using the FDTD method was reported in [17]. The intensity of electric fields generated by PD sources in dielectric materials was investigated using FDTD modeling in [18]. FDTD simulation has also been applied to study the propagation characteristics of electromagnetic wave caused by PD power cables [19] and GIS [20] [21]. There are other computational methods that can be used to analyze PD characteristics and electromagnetic waves for examples, finite element method (FEM) [22] and finite integration technique (FIT) [23] that have been demonstrated to investigate electromagnetic wave propagation through insulating spacer in GIS.

The study reported here demonstrates that it is possible to predict the sensitivity of UHF sensors using FDTD simulation with reasonable accuracy, offering the possibility of designing and optimizing new sensors to a large extent before manufacturing the physical device. The sensors considered in this paper are shown in Fig. 1 and comprise (a) a monopole probe of the kind used as a reference sensor in the GTEM calibration system; (b) a large monopole-type PD sensor developed for use on an experimental model transformer tank; and (c) a conventional disc-type sensor model that is representative of the type used in GIS. In each case, the sensor response is simulated and then compared with experimental measurements.

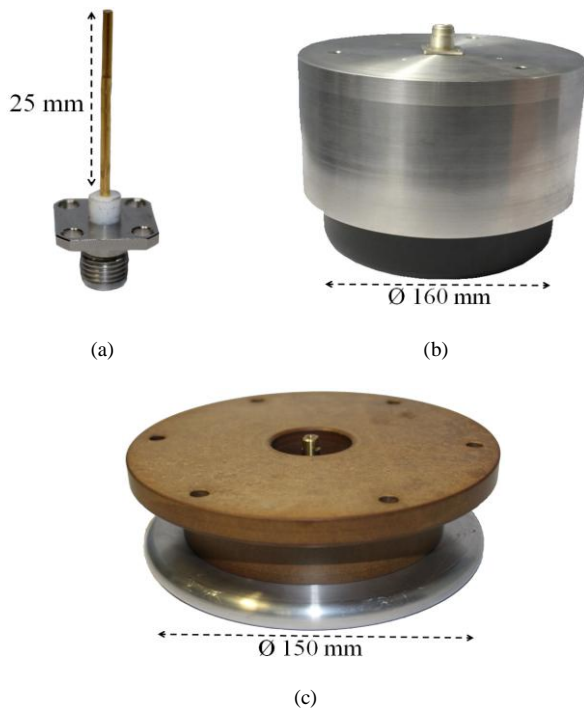


Fig. 1. UHF sensors investigated in this paper: (a) 25 mm reference probe, (b) experimental monopole-type PD sensor, and (c) disc-type sensor.

II. ELECTROMAGNETIC FINITE-DIFFERENCE TIME-DOMAIN (FDTD) MODELING

FDTD is a computational method to model electromagnetic wave propagation and interactions with the properties of materials [24]. When a broadband transient excitation signal source is used, this technique is capable of predicting the response of a system over a wide range of frequencies with a single simulation run. For example, a single execution of the simulation to determine the transient time-domain response of a sensor can be used to obtain its frequency response by applying a Fourier transform algorithm to the time-domain data at the post-processing stage.

The FDTD method was introduced by Yee in 1966 [25] who described a numerical technique for solving Maxwell's curl equations directly in the time-domain on a space grid. The orthogonal Yee cell, shown in Fig. 2, is the primary component of the FDTD method, where the electric and magnetic fields are defined at discrete points interleaved around a cell. Each electric field component is located a half-cell width from the origin in the direction of its orientation and each magnetic field component is offset to the centre of three faces of the cell.

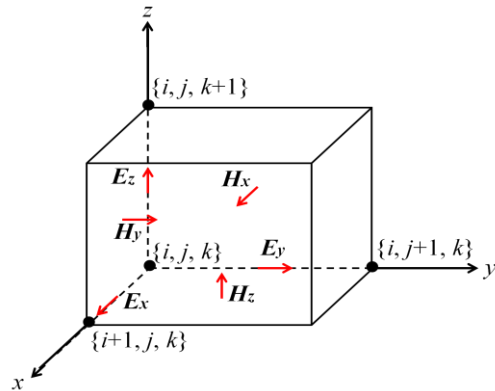


Fig. 2. The Yee cell [20]. Electric field components are at the centers of the cell edges and the magnetic field components are in the centers of the cell faces. The variables i , j , and k are indices for the spatial mesh in the orthogonal x , y , and z -directions, respectively.

Computational methods for applying Maxwell's equations have matured recently as consequence of the availability of high performance computational power in desktop workstations. The software package XFDTD 7.0 [26] was used for the simulations reported here.

III. SENSOR DESIGNS

The FDTD method was used to apply the same transient electric field waveform that is used in the calibration system within a model space that represents a subset of the GTEM

test cell structure. The sensors shown in Fig. 1 were modeled in the FDTD software using the dimensions and material properties of the physical sensors. The corresponding sensor models are shown in Fig. 3 and the properties of the materials are listed in Table I. Polytetrafluoroethylene (PTFE), polyvinyl chloride (PVC), and a filled epoxy resin (Tufnol) were the dielectric materials used. Relative magnetic permeability and electrical conductivity values used for all dielectrics were 1.0 and 0, respectively.

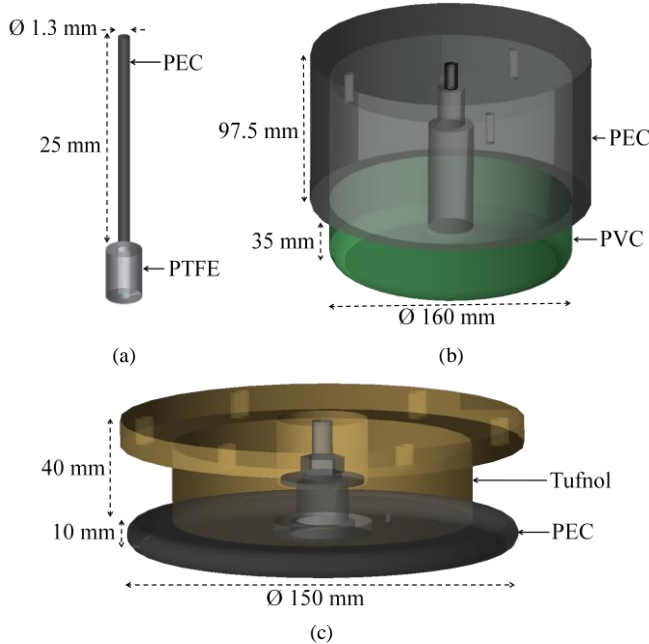


Fig. 3. Diagrams of the modeled sensors as represented within the FDTD software: (a) 25 mm reference probe, (b) experimental monopole-type PD sensor, and (c) disc-type sensor. Note that PEC refers to parts modeled as perfect electric conductors.

TABLE I

DIELECTRIC MATERIALS OF THE MODELED SENSORS

Material/Sensor	Relative Permittivity
PTFE Probe	2.0
PVC Monopole	2.6
Tufnol Disc	3.4

A 50 Ω lumped-element load was connected between the output terminal of the UHF sensor and the ground plane (which is the top plate of the simulated GTEM cell). The simulated output voltage of the UHF sensor was recorded across this 50 Ω load, which represents the normal cable and measurement impedance used in UHF PD detection systems.

IV. SENSOR CALIBRATIONS

The GTEM cell system described in [14] was used to calibrate the UHF sensor experimentally. The length of the

cell, depicted in Fig. 4, is 3 m with an output aperture of 1 m \times 1 m. The septum (inner conductor) of the GTEM cell is formed by 9 separate wires in a plane halfway between the upper and lower faces of the cell. A 10 V step generator connected to the input of the cell excites a propagating electric field step with a 10%-90% rise time of 350 ps, as shown in Fig. 5. This risetime was measured using a digitizer with an analogue bandwidth of 5 GHz. However, in the normal operation of the calibration system (which includes the measurements presented later in this paper), signals are measured using a 1 GHz bandwidth digitizer with an effective sampling rate of 25.6×10^9 samples/s (256 sample points over 10 ns).

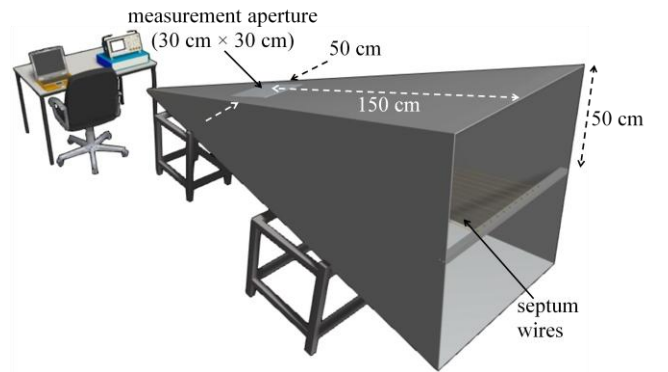


Fig. 4. Illustration of the GTEM cell. UHF PD sensors to be tested are mounted at the measurement aperture.

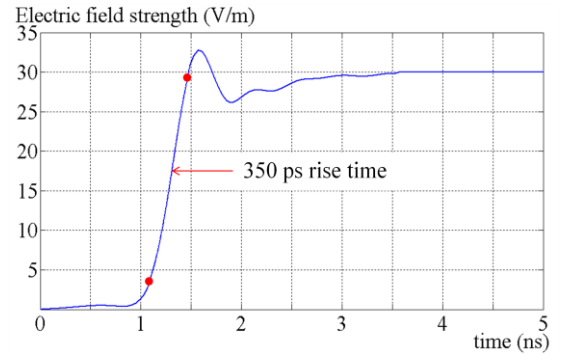


Fig. 5. The measured electric field step at the center of the sensor test aperture, which is applied to UHF PD sensors for both laboratory calibration and FDTD simulations. The direction of the electric field vector is upwards, and perpendicular to the upper conducting plate of the GTEM cell.

For the purpose of FDTD simulation, several simplifications were made to the geometry. Firstly, on the basis of symmetry, only the upper half of the GTEM cell was modeled, being represented as a tapered pair of planar conductors with a 1:6 gradient, as shown in Fig. 6. In this step, the individual septum wires were also replaced by a planar conductor, since leaving them as thin wires would

have necessitated very large regions of fine sub-meshing in the model and would then require extension of the volume to beyond the wires to incorporate an absorbing boundary. Secondly, the side walls of the GTEM were not included, since they would prevent the launching of a vertically polarized uniform electric field plane wave into the structure. Thirdly, the modeled cell was reduced in length to 2 m by removing the 1 m of tapered section towards the input of the cell. This was done to avoid the need for representing fine mechanical detail at the input, where there is a transition from an N-type coaxial connector to the GTEM septum. A consequence of this simplification is that, instead of using a voltage source input within the model, a corresponding vertically polarized electric field plane wave was launched between the plates (from the left in Fig. 6). Lateral tapering of the cell was also not included in the model, which used a fixed width of 50 cm, equal to the width of the GTEM at its mid-point where the measurement aperture is located. These simplifications resulted in a representative model of the physical test cell and the region of interest while avoiding structural complexity and excessive simulation run times. Further reductions in the simulated volume are likely to be possible in future to improve computational efficiency. UHF sensor models were positioned between the two conductors in Fig. 6, with their output terminals at coordinates $\{50, 50, 25\}$ cm, where there is 25 cm between the top plate and the bottom sloping conductor (which represents the septum). Conductors forming the test cell were represented as perfect electric conductor (PEC) regions in the FDTD model. Overall, the translation of the physical structure of the GTEM into the FDTD model domain produces a structure that is much closer to the ideal test configuration, which would consist of two infinite, parallel planar conductors with a perpendicularly polarized plane wave propagating between them. In fact, it is the approximations to this ideal necessitated by the practical system design that are being ‘undone’ to produce a much simpler representation within the FDTD model. The level of agreement between measured and simulated results presented later in this paper for three different sensors suggests that the simplifications within the FDTD model are sufficiently valid for it to serve as a useful tool for design purposes.

During simulation, the region around the sensor was modeled with finer meshing than other regions so that small mechanical details could be represented with greater accuracy. Localizing the sub-meshing in this way helps to minimize the extra computational burden of representing smaller components within the sensors. The simulated parameters are summarized in Table II, where the run times quoted are for a PC with an Intel Xeon X5550 (2.67 GHz)

processor with 12 GB RAM. A perfectly matched layer (PML) boundary condition was applied to all faces of the simulation volume. Since there are no walls on the left and right sides of the simulated GTEM (x - y plane faces in Fig. 6), this artificial absorbing layer will absorb incident waves that reach all faces (minimizing distortion of the signals due to unwanted reflections).

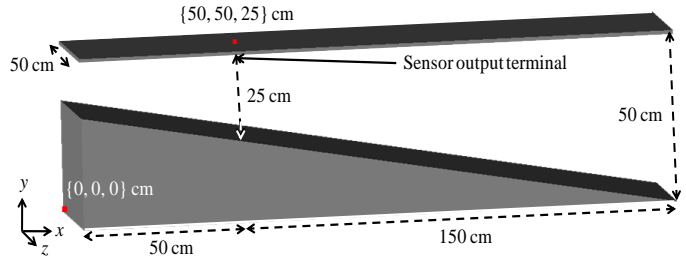


Fig. 6. Simplified representation of the GTEM cell used in the FDTD model. The simulated plane wave step propagates in the positive x -direction.

TABLE II
SIMULATION PARAMETERS OF THE MODELED SENSORS

Sensor	Cell size (cm)		Time step (ps)	Simulation run time
25 mm probe	0.05	x: 49.0 – 51.0 y: 46.0 – 51.0 z: 24.0 – 26.0	0.963	37 min.
	1.00	other directions		
Monopole sensor	0.10	x: 40.7 – 59.3 y: 46.2 – 62.2 z: 15.7 – 34.3	1.926	2 hrs, 13 min.
	1.00	other directions		
Disc sensor	0.10	x: 37.0 – 63.0 y: 49.0 – 62.0 z: 12.0 – 38.0	1.926	2 hrs, 17 min.
	1.00	other directions		

The output voltages and frequency responses of the sensors are compared between the laboratory experimental results and FDTD simulations in Fig. 7 and Fig. 8. The overall figure-of-merit sensitivity is calculated for each sensor based on the average sensitivity over the frequency range 500 – 1500 MHz [27]. This broadband averaging of the of the sensor response has been adopted due to the specific requirements of UHF PD sensors, in which the spectral content of the signal to be detected can vary over a considerable range [28]. Fig. 7 and Fig. 8 illustrate that the simulation and laboratory results are comparable and demonstrate that the FDTD approach is capable of analyzing and predicting the output of UHF PD sensors in the time-domain and the frequency-domain.

V. SENSITIVITY FACTORS

The FDTD method is useful for investigating the influence of material properties and sensor structure. To demonstrate this capability, two parameters were varied to investigate their effect on sensitivity, namely, the relative permittivity of the dielectric and the geometry of the sensors.

A. Relative Permittivity of Dielectric Materials

The incident electric field, cell size, time step, and sensor dimensions were kept the same when simulating different values of relative permittivity of the insulating material. The simulation results presented in Table III show that, as the relative permittivity of the insulating material increases, the output voltage decreases slightly.

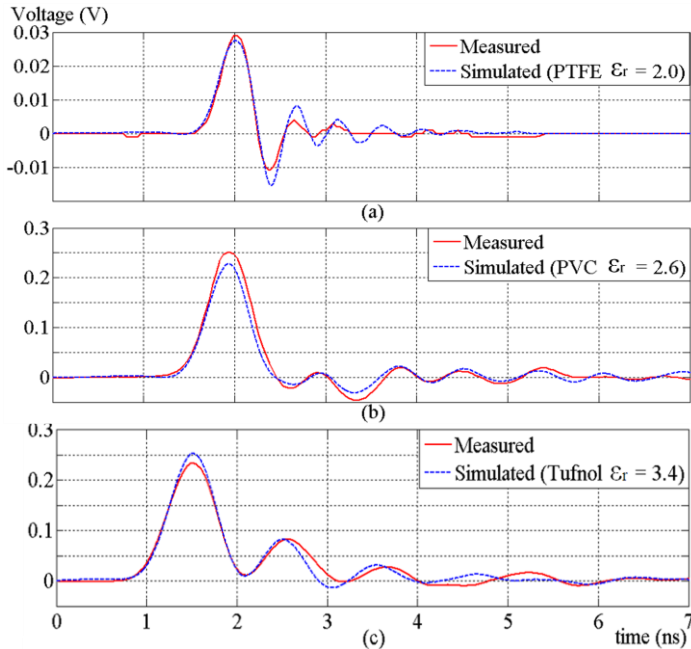


Fig. 7. Comparison of measured and simulated output voltages: (a) 25 mm probe, (b) monopole sensor, and (c) disc sensor.

Fig. 9 shows the average sensitivity of the two PD sensors over 500 - 1500 MHz as a function of relative permittivity of their structural insulating components. The monopole and disc sensors show different responses to permittivity changes. However, compared with the overall sensitivity, these results indicate that permittivity is not a particularly critical parameter and both sensors would have a satisfactory response with any insulation having a dielectric constant within the typical range of 2.2 to 5.0.

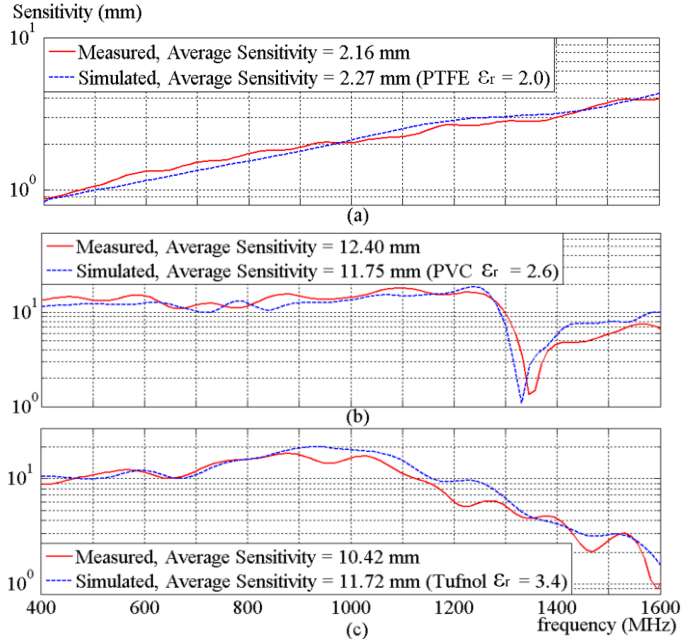


Fig. 8. Comparison of measured and simulated frequency responses: (a) 25 mm probe, (b) monopole sensor, and (c) disc sensor.

TABLE III
SIMULATED OUTPUT VOLTAGE OF UHF PD SENSORS WITH VARYING RELATIVE PERMITTIVITY

Sensor Component	Relative Permittivity	Simulated V_{pk-pk} (V)	Percentage Difference of Simulated V_{pk-pk} (%)
Monopole Dielectric Part	1.6	0.2670	2.77
	2.6	0.2598	Referenced Value
	3.6	0.2525	-2.81
	4.6	0.2511	-3.35
	5.6	0.2462	-5.23
Disc Dielectric Part	1.4	0.2774	5.60
	2.4	0.2749	4.64
	3.4	0.2627	Referenced Value
	4.4	0.2536	-3.46
	5.4	0.2531	-3.65

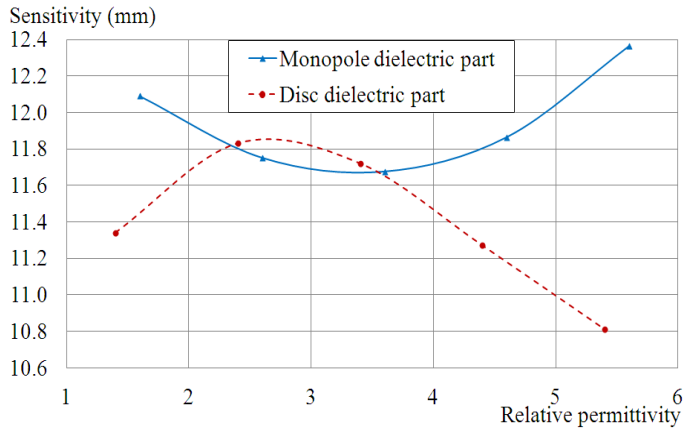


Fig. 9. Simulated sensitivities of the monopole sensor and disc sensor over 500 - 1500 MHz as a function of relative permittivity of their insulating structural components.

B. Geometry of the Sensors

Since UHF PD sensors respond through their interaction with electromagnetic waves, sensor geometry greatly influences the output voltage and frequency response. To study these effects, simulations were carried out to assess the effects of (i) decreasing the diameter of PVC materials of UHF monopole sensor while keeping the relative permittivity of PVC materials fixed at 2.6, and (ii) increasing the diameter of PEC disc sensor while keeping the relative permittivity of Tufnol fixed at 3.4.

Fig. 10 shows the simulated frequency responses for the original and some modified sensor component diameters. For the monopole sensor, the first dip in the curve for average sensitivity of the 16 cm diameter PVC part (at 1330 MHz) shifts to higher frequencies as PVC diameter decreases. In contrast, for each disc sensor diameter the frequency response curve stays broadly the same, as does the position of the least sensitive frequency, at around 1700 MHz. The sensitivity simulation results, summarized in Table IV and Fig. 11, indicate that the output voltage and average sensitivity will decline when decreasing the diameter of the PVC body of the monopole sensor or increasing the diameter of PEC disc sensor.

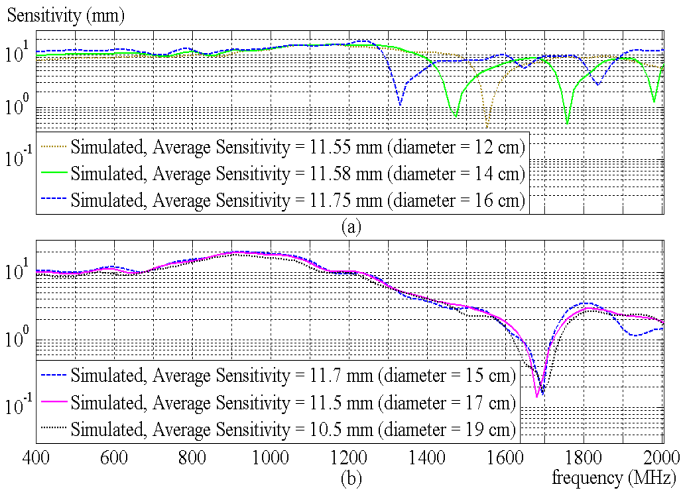


Fig. 10. Simulated frequency responses when (a) varying diameter of PVC body of the monopole sensor, and (b) varying diameter of the PEC disc of the disc sensor.

TABLE IV
SIMULATED OUTPUT VOLTAGE FOR VARIOUS DIAMETERS OF PVC BODY (MONOPOLE SENSOR) AND PEC DISC (DISC SENSOR)

Sensor Component	Diameter (cm)	Simulated V_{pk-pk} (V)	Percentage Difference of Simulated V_{pk-pk} (%)
PVC Body ($\epsilon_r = 2.6$)	12	0.2072	-20.25
	14	0.2354	-9.39
	16	0.2598	Referenced Value
PEC Disc	15	0.2627	Referenced Value
	17	0.2547	-3.05
	19	0.2401	-8.60

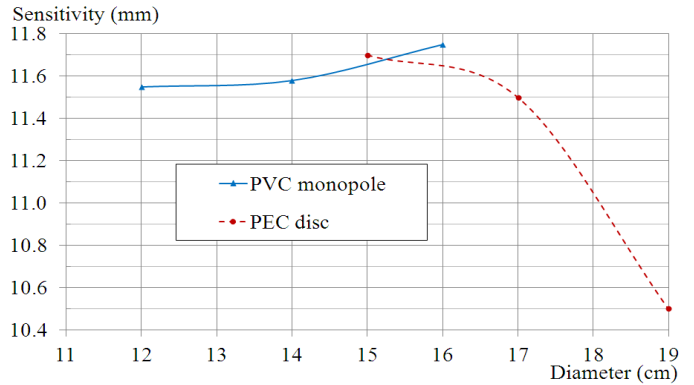


Fig. 11. Average sensitivity simulation results for varying diameters of the PVC body of the monopole sensor and the PEC disc of the disc sensor.

VI. CONCLUSION

This paper has demonstrated the use of computational FDTD electromagnetic modeling for parametric simulation and calibration of UHF PD sensors using a representation of a GTEM calibration cell. Comparison of simulated and laboratory experimental results show that there are relatively minor differences in the amplitude and shape of the time-domain output voltages and frequency responses of the measured and simulated UHF PD sensors. These differences are most likely to have arisen from the simplified representation of the GTEM cell structure within the FDTD model. For example, only the upper half of the cell was simulated; a solid septum was used instead of thin wires; and the metal sides of the cell were replaced with absorbing boundaries in the model. Nevertheless, measured and simulated results indicate that the FDTD method is an effective tool for designing and calibrating UHF PD sensors, with agreement to an accuracy of better than 10% for averaged sensitivity values over the frequency range 500 – 1500 MHz.

The relative permittivity of insulating materials and the geometry of the sensors play a significant role in determining their sensitivities and this has been illustrated by means of parametric studies using FDTD models. The FDTD method

has potential to accelerate the design process for UHF PD sensors, reducing development costs and helping to optimize their performance. In future work, the authors intend to demonstrate this by designing a novel sensor entirely within the domain of the FDTD model and then validating its performance by constructing and testing the corresponding physical device. In addition, the influence of mechanical manufacturing tolerances could be explored through simulation and measurement, while there remains considerable scope for refinements to the simulation process to quantify the trade-offs between mesh size, simulation accuracy and computation time.

REFERENCES

- [1] B. F. Hampton and R. J. Meats, "Diagnostic measurements at UHF in gas insulated substations", in *IEE Proc. Generation, Transmission and Distribution*, Vol. 135, pt. C, No. 2, pp. 137-144, Mar. 1988.
- [2] J. S. Pearson, O. Farish, B. F. Hampton, M. D. Judd, D. Templeton, B. M. Pryor and I. M. Welch, "Partial discharge diagnostics for gas insulated substations", *IEEE Trans. Dielectrics and Electrical Insulation*, Vol. 2, No. 5, pp. 893-905, Oct. 1995.
- [3] S. Coenen, S. Tenbohlen, S. M. Markalous and T. Strehl, "Sensitivity of UHF PD measurements in power transformers", *IEEE Trans. Dielectrics and Electrical Insulation*, Vol. 15, No. 6, pp. 1553-1558, 2008.
- [4] S. M. Markalous and A. Wilson, "Techniques for detection and location of partial discharge in power transformers", in *Proc. 11th INSUCON Int. Electrical Insulation Conf.*, Birmingham, UK, May 26-28, 2009.
- [5] Zhiguo Tang, Chengrong Li, Xu Cheng, Wei Wang, Jinzhong Li and Jun Li, "Partial discharge location in power transformers using wideband RF detection", *IEEE Trans. Dielectrics and Electrical Insulation*, Vol. 13, No. 6, pp. 1193-1199, 2006.
- [6] K. R. Hwang, E. T. Ryu, J. R. Jung, M. S. Kim, and H. J. Yang, "Development of UHF sensor for partial discharge diagnosis of power transformer", *XVII Int. Symp. High Voltage Engineering (ISH)*, Hannover, Germany, Aug. 2011.
- [7] M. D. Judd, O. Farish, and B. F. Hampton, "Broadband couplers for UHF detection of partial discharge in gas insulated substations", *IEE Proc. Science, Measurement and Technology*, Vol. 142, No. 3, pp. 237-243, May 1995.
- [8] A. J. Reid, I. Dick, and M. D. Judd, "UHF monitoring of partial discharge in substation equipment using a novel multi-sensor cable loop", *20th Int. Conf. Electricity Distribution*, CIRED, Prague, Jun. 8-11, 2009.
- [9] T. Hoshino, K. Nojima, and M. Hanai, "Real-time PD identification in diagnosis of GIS using symmetric and asymmetric UHF sensors", *IEEE Trans. Power Delivery*, Vol. 19, No. 3, Jul. 2004.
- [10] M. D. Judd, O. Farish, J. S. Pearson, and B. F. Hampton, "Dielectric windows for UHF partial discharge detection", *IEEE Trans. Dielectrics and Electrical Insulation*, Vol. 8, No. 6, Dec. 2001.
- [11] M. D. Judd, L. Yang, and I. B. B. Hunter, "Partial discharge monitoring for power transformers using UHF sensors Part 1: Sensors and Signal Interpretation", *IEEE Electrical Insulation Magazine*, Vol. 21, No. 2, Mar./Apr. 2005, pp. 5-14.
- [12] R. Sarathi, A. J. Reid, and M. D. Judd, "Partial discharge study in transformer oil due to particle movement under DC voltage using the UHF technique", *Electric Power Systems Research*, Vol. 78, Issue 11, pp. 1819-1825, Nov. 2008.
- [13] S. Coenen, S. Tenbohlen, S. Markalous, and T. Strehl, "Sensitivity limits of UHF PD measurements on power transformers", *Int. Symp. High Voltage Engineering (ISH)*, Cape Town, South Africa, Aug. 2009.
- [14] M. D. Judd and O. Farish, "A pulsed GTEM system for UHF sensor calibration", *IEEE Trans. Instrumentation and Measurement*, Vol. 47, No. 4, Aug. 1998.
- [15] M. D. Judd "Transient calibration of electric field sensors", *IEE Proc. Science, Measurement and Technology*, Vol. 146, No. 3, pp. 113-116, May 1999.
- [16] M. D. Judd "Using finite-difference time-domain techniques to model electrical discharge phenomena", *Annual Report Conf. Electrical Insulation and Dielectric Phenomena*, Vol. 2, pp. 518-521, Oct. 2000.
- [17] A. J. Reid, M. Stewart and M. D. Judd, "FDTD Modeling of UHF partial discharge sensor response", *Proc. 1st Int. Conf. SUPERGEN*, Nanjing, China, Apr. 2009.
- [18] A. Bojovschi, W. S. T. Rowe and K. L. Wong, "Electromagnetic field intensity generated by partial discharge in high voltage insulating materials", *Progress In Electromagnetics Research (PIER)*, Vol. 104, pp. 167-182, 2010.
- [19] D. Pommerenke, R. Jobava and R. Heinrich, "Numerical Simulation of Partial Discharge Propagation in Cable Joints using the Finite Difference Time Domain Method", *IEEE Electrical Insulation Magazine*, Vol. 18, No. 6, pp. 6-11, Nov. 2002.
- [20] T. Hoshino, S. Maruyama, and T. Sakakibara, "Simulation of Propagating Electromagnetic Wave due to Partial Discharge in GIS using FDTD", *IEEE Trans. Power Delivery*, Vol. 24, No. 1, Jan. 2009.
- [21] M. Hikita, S. Ohtsuka, J. Wada, S. Okabe, T. Hoshino and S. Maruyama, "Study of partial discharge radiated electromagnetic wave propagation characteristics in an actual 154 kV model GIS", *IEEE Trans. Dielectrics and Electrical Insulation*, Vol. 19, No. 1, pp. 8-17, Feb. 2012.
- [22] S. Kaneko, S. Okabe, M. Yoshimura, H. Muto, C. Nishida, and M. Kamei, "Detecting Characteristics of Various Type Antennas on Partial Discharge Electromagnetic Wave Radiating through Insulating Spacer in Gas Insulated Switchgear", *IEEE Trans. Dielectrics and Electrical Insulation*, Vol. 16, No. 5, pp. 1462-1472, Oct. 2005.
- [23] A. Tacchini, D. Grossi, L. Vincetti, M. Maini, S. Serra, M. Fattori, and L. Sandrolini, "Electromagnetic analysis of PD detection in GIS system", *Asia-Pacific Symp. Electromagnetic Compatibility (APEMC)*, Singapore, pp. 889-892, May 2012.
- [24] A. Taflov, *Advances in Computational Electrodynamics: The Finite-Difference Time-Domain Method*, USA: Artech House, 1998, pp. 11-17.
- [25] K. S. Yee, "Numerical solution of initial boundary value problems involving Maxwell's equations in isotropic media", *IEEE Trans. Antennas and Propagation*, Vol. 14, No. 3, pp. 302-307, May 1966.
- [26] *Full-wave, 3D, Electromagnetic Analysis Software*, Reference Manual, REMCOM Inc., 2009, pp. 1-12.
- [27] National Grid Company plc, "Capacitive couplers for UHF partial discharge monitoring", Technical Guidance Note: TGN(T)121, Issue 1, January 1997.
- [28] M. D. Judd, O. Farish, J. S. Pearson, and B. F. Hampton, "Dielectric windows for UHF partial discharge detection", *IEEE Trans. Dielectrics and Electrical Insulation*, Vol. 8, No. 6, pp. 953-958, Dec. 2001.

Asnor M. Ishak was born in Kuala Lumpur, Malaysia, in 1979. He is currently on the academic staff at the Universiti Pertahanan Nasional Malaysia (UPNM) and a PhD student in the Department of Electronic & Electrical Engineering, University of Strathclyde, Glasgow, UK. He graduated from the Universiti Tenaga Nasional (UNITEN), Malaysia with BSc (Hons) degree in Electrical and Electronic Engineering. Then he started his career as an electrical diagnostic engineer in TNB REMACO, Malaysia. Later, he received an MSc in Electrical Power Engineering with Business from University of Strathclyde, Glasgow, UK.

Pete C. Baker (M'2006) was a Research Associate within the Institute for Energy and Environment at the University of Strathclyde. He received his BEng (Hons) Degree and PhD from the University of Strathclyde in 2004 and 2010 respectively. His research interests include substation condition monitoring, wireless sensor networks, machine learning, energy harvesting and multi-agent systems. Dr Baker is now an Advanced Projects Engineer with Sentient Energy, based in Burlingame, CA, USA.

W. H. Siew is a Reader in the Department of Electronic & Electrical Engineering, University of Strathclyde, Glasgow, Scotland. He is a triple alumnus of the University of Strathclyde with degrees in B.Sc. (Hons) in Electronic & Electrical Engineering; PhD in Electronic & Electrical Engineering; and Master of Business Administration. His areas of research interest include large systems electromagnetic compatibility; cable diagnostics; lightning protection; and

wireless sensing systems. He is Convener of the CIGRE WG C4.2.08 and a member of the Technical Advisory Panel for the IET Professional Network on Electromagnetics. He is a Chartered Engineer and is an MIEEE and an MIEE.

Martin D. Judd (M'2002–SM'2004) was born in Salford, England, in 1963. He graduated from the University of Hull in 1985 with a BSc (Hons) degree in Electronic Engineering. His employment experience includes 4 years working for Marconi Electronic Devices Ltd followed by 4 years with EEV Ltd, both in Lincoln, England. Martin received his PhD from the University of Strathclyde in

1996 for research into the excitation of UHF signals by partial discharges in gas insulated switchgear. From 1999 to 2004 he held an EPSRC Advanced Research Fellowship concerned with electrodynamic of electrical discharge phenomena. His fields of interest include high frequency electromagnetics, generation and measurement of fast transients, partial discharges and energy harvesting. Professor Judd is now Manager of the High Voltage Technologies Research Laboratory within the Institute for Energy and Environment at the University of Strathclyde. He is a Chartered Engineer, a Member of the IET and Senior Member of the IEEE.

The General Simulation Procedures using XFDTD Software, Release 7.1.2.1, Remcom Inc.

1. Designing Geometry

A 2-dimensional (2-D) cross section is modelled by right-clicking on Parts, inside the Project Tree (left side of the main window) and choose *Create New > Extrude*. The 2-D shape can be created by using *Straight Edge*, *Polyline Edge*, *Rectangular* or *Circle Center, Radius* functions in Edit Cross Section tab (as shown in Figure A2.1).

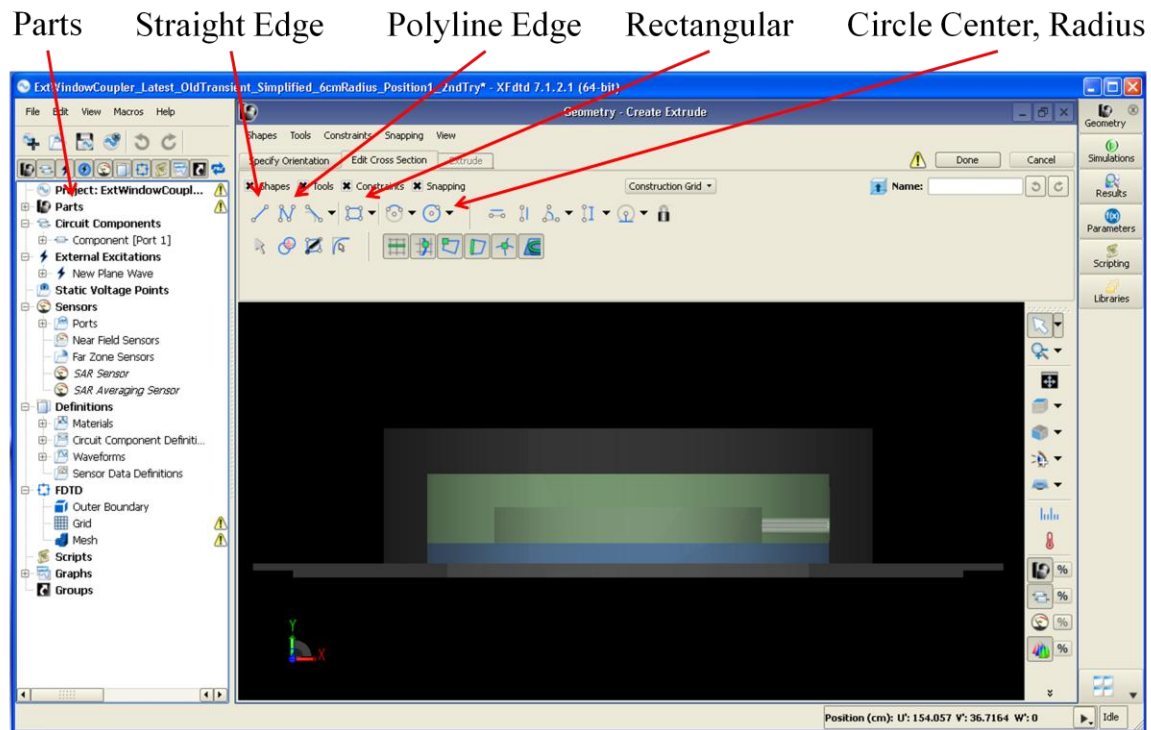


Figure A2.1: The Geometry – Create Extrude Window

Then the Extrude tab is used to extrude the 2-D drawing to 3-D object. A name can be assigned for each object using the *Name* space on top-right of the window shown in Figure A2.1. For example, Name: Box1. Click *Done* and the new Geometry window will

appear as in Figure A2.2 where the name of the object (Box1) is appear under subheading Parts.

The next object can be modelled using Create New tab and the object can be edited using Modify and Boolean operations. *Standard Views*, as in Figure A2.2, are used to view the object in different angles. To view the object freely at any angle, right-click on the object and keep holding the right button while moving the mouse. The *Toggle Parts Visibility* buttons control the view of object parts especially when to view the internal part of the completed object. To zoom in or zoom out the geometry, position the cursor on the geometry and then scroll up or scroll down the mouse, respectively. The background colour of the Geometry window can be changed to white or other colours by selecting *Edit > Application Preferences > Modeling > View Options > Background > Preset > White* (or any other colours).

2. Adding New Material

Once the geometrical objects are designed, material properties are assigned to the objects by creating material definition object. Right-click on the Materials tab under the subheading Definitions on the left of the Geometry window and then select *New Material Definition*. After completing the properties of the material, a material object with specific name of the material will be added under the subheading Materials. Drag the material object and drop it on the required geometry under the subheading Parts.

3. Defining Grid and Saving Output Voltage

After designing the geometries and specifying the materials for each of them, the grid system is set up by defining the FDTD cell size. The length of the cells cannot be larger than the smallest length in the geometry designs [133]. To assign the grid within the workspace window, double-click on Grid under subheading FDTD (left side of the Geometry window). In this simulation, localised grid system is applied where Size tab and Grid Regions tab are used. *Toggle Mesh Viewing Controls*, as shown in Figure A2.2, are used to view the mesh.

The output voltage of the UHF PD sensors is simulated by connecting 50 Ω load between the output terminal of the sensors and the ground geometry with one cell gap, as shown in Figure A2.3. The 50 Ω load is created by right-clicking Circuit Component Definitions (left side of the Geometry window) and then selecting *New Circuit Component Definition*. At the Feed Type, choose *Passive Load*. To locate the passive load on the geometry, right-click Circuit Components and then select *New Circuit Component with > New Passive Load Definition*. Choose the circuit component definitions that have been created before under Properties tab.

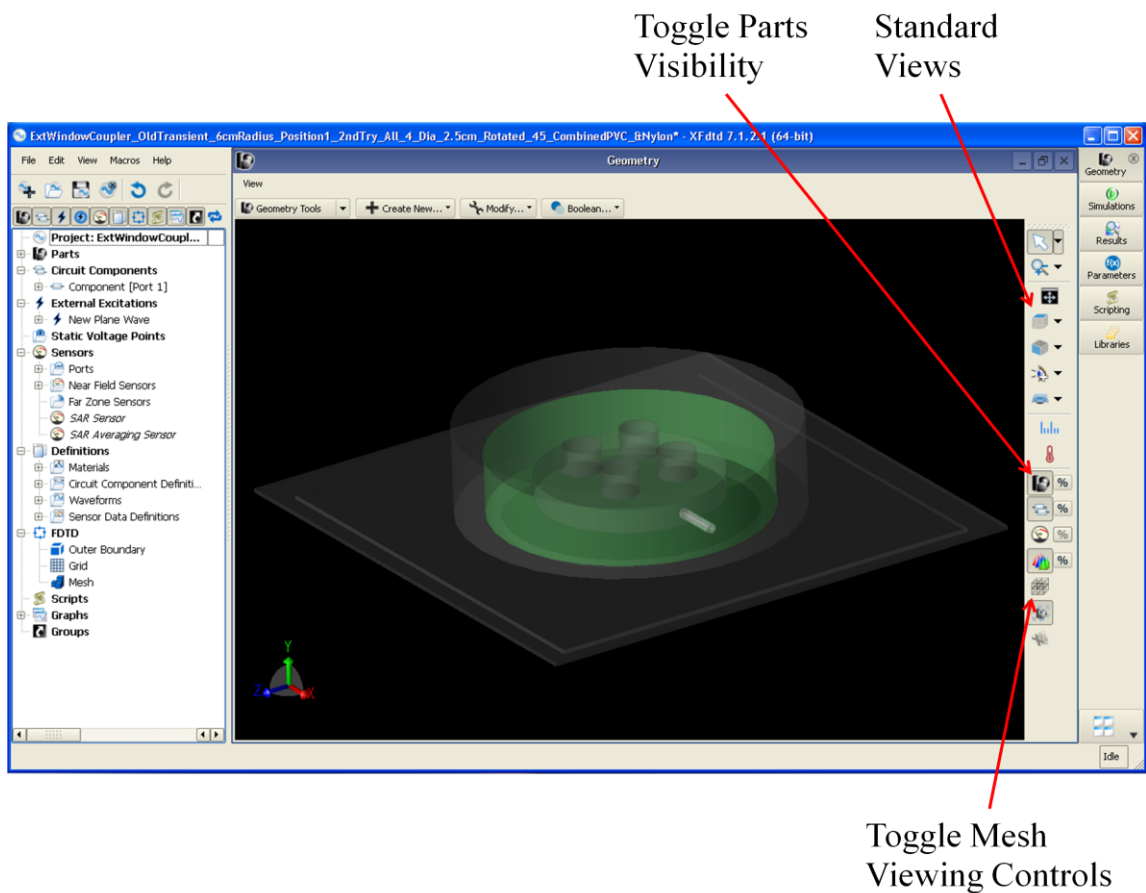


Figure A2.2: The Geometry window

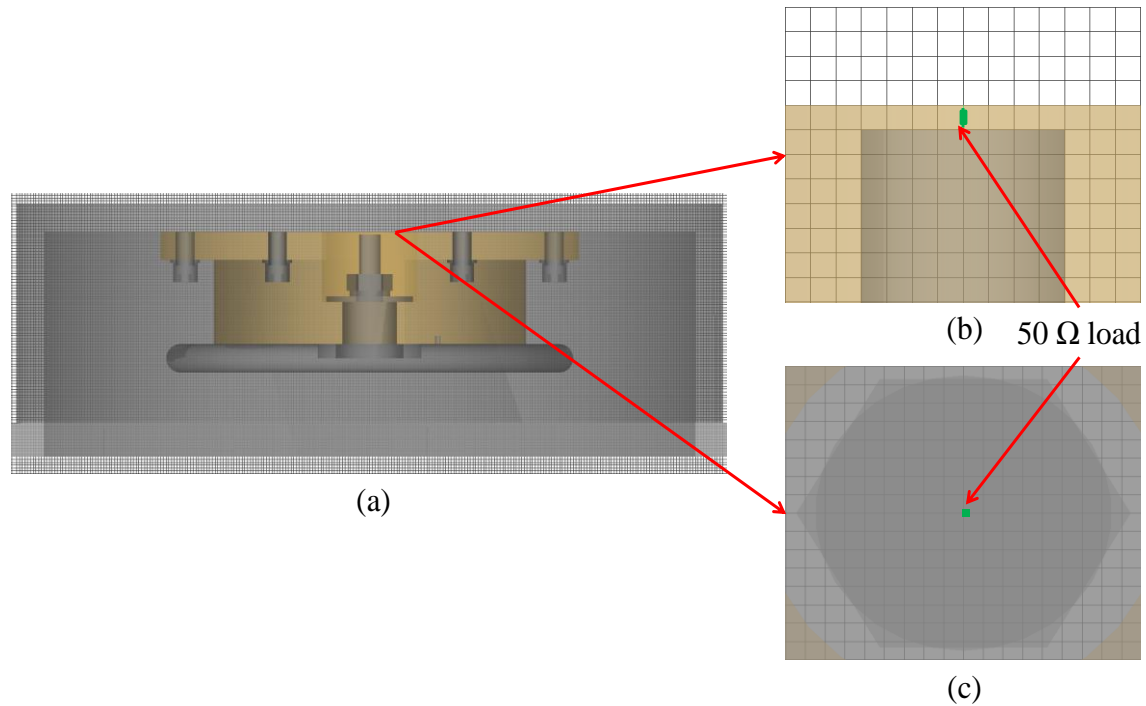


Figure A2.3: The position of $50\ \Omega$ load with one cell gap: (a) side view model of disc-type sensor, (b) one cell gap of $50\ \Omega$ load and (c) centrally located $50\ \Omega$ load at the output of the sensor.

In XFDTD software, Meshing Order setting has been used to specify the level of priority for each object. If objects overlap in one cell, the object that has higher meshing priority will be considered for simulation. To set the meshing order, right-click on Parts and then choose *View Parts List (All Parts)*. Right-click on the object part that needs higher meshing priority and select *Meshing Order > Move Up*.

4. Creating Pulse Excitation

In this simulation, user-defined waveform is used to create the vertically polarized electric field plane wave. The normalized waveform is uploaded into the computer first before the Geometry window, by selecting *My Documents > XFDTD > UserWaveform > UserWaveform*. To upload the waveform into the Geometry window, right-click Waveforms under subheading Definitions (left side of the window) and select *New Waveform Definition*. Choose *User Defined* for the Type of Waveform Editor and then click Import Waveform Data tab. To define the amplitude and the polarization of the

incident plane wave, right-click External Excitation (left side of the Geometry window) and choose *New External Excitation*.

5. Running Simulation and Viewing Output Voltage

After all the setup is completed, the project will start to be simulated by clicking Simulations tab on the right side of the Geometry window. The output voltage of the sensors can be viewed by clicking Results tab.

The General Matlab Instruction to Calculate Frequency Response of the Simulated Sensors

The input electric field and output voltage of the sensors are uploaded into Matlab using Import data tab in Workspace window. The basic Matlab commands for calculating the frequency response of the sensors are as following:

```
e=Efield(:,2);           % the amplitude columns of the electric fields are required
v1=Ovoltage(:,2);       % the amplitude columns of the output voltages are required
v1milli=v1.*1000;       % convert V to mV
t=1.92583e-12;          % sampling time
L=20000;
NFFT=2^nextpow2(L);
Fs=1/t;
NFs=Fs/2;               % Nyquist frequency
NFsG=NFs/1000000;       % Megahertz range
EFFT=fft(e,NFFT);       % Fast Fourier transform for the electric fields
VFFT1=fft(v1milli,NFFT); % Fast Fourier transform for the output voltages
H1=VFFT1./EFFT;         % Sensitivity, H (mV/Vm-1)
f=NFsG*linspace(0,1,NFFT/2+1);
plot(f,abs(H1(1:NFFT/2+1)))
```

References

- [1] "IEEE Standard Terminology for Power and Distribution Transformers," *IEEE Std C57.12.80-2010 (Revision of IEEE Std C57.12.80-2002)*, pp. 1-56, 2010.
- [2] The British Standards Institution, "High-voltage test technique - Partial discharge measurements," *BS EN 60270:2001*, British Standard Committees, 2001.
- [3] The British Standards Institution, "Insulating liquids - Determination of the partial discharge inception voltage (PDIV) - Test procedure," *IEC 61294*, British Standard Committees, 1993.
- [4] N. Pattanadech, F. Pratomosiwi, B. Wieser, M. Baur, and M. Muhr, "Partial Discharge Characteristics of Mineral Oil using Needle-Plane and Needle-Sphere Electrode Configuration base on Pulse Current Measurement," *Annual Report Conference on Electrical Insulation and Dielectric Phenomena, CEIDP*, pp. 64-67, 2012.
- [5] M. Pompili, C. Mazzetti, and R. Bartnikas, "Comparative PD pulse burst characteristics of transformer type natural and synthetic ester fluids and mineral oils," *IEEE Transactions on Dielectrics and Electrical Insulation*, vol. 16, pp. 1511-1518, 2009.
- [6] R. H. Khawaja and T. R. Blackburn, "Partial discharge patterns in oil-impregnated paper and pressboard insulation at high temperature," *Australasian Universities Power Engineering Conference, AUPEC*, pp. 1-5, 2008.
- [7] (20/03/2013) E. Lemke, *Guide for Electrical Partial Discharge Measurements in compliance to IEC 60270*, 2008, [Online]. Available: <http://www.e-cigre.org/bib/366.pdf>
- [8] C. Qingguo, G. Xixiu, G. Wensheng, L. Fuqi, and T. Kexiong, "The UHF method for measurement of partial discharge in oil-impregnated insulation," *Proceedings of the 7th International Conference on Properties and Applications of Dielectric Materials*, vol.1, pp. 451-454, 2003.
- [9] E. Kuffel, W. S. Zaengl, and J. Kuffel, *High Voltage Engineering Fundamentals*: Elsevier Newnes, 2000.
- [10] L. Barbieri, A. Villa, and R. Malgesini, "A step forward in the characterization of the partial discharge phenomenon and the degradation of insulating materials through nonlinear analysis of time series," *IEEE Electrical Insulation Magazine*, vol. 28, pp. 14-21, 2012.
- [11] H. Okubo, S. Yuasa, K. Ota, N. Hayakawa, and M. Hikita, "Discharge characteristics under non-uniform electric field in He, Ar and air at low

- pressures," *IEEE Transactions on Dielectrics and Electrical Insulation*, vol. 4, pp. 450-455, 1997.
- [12] T. Mizuno, K. Morita, Y. Kurata, K. Nagatake, and H. Saitoh, "Electrical insulation performance in air gap with covered electrode," *Proceedings of the 7th International Conference on Properties and Applications of Dielectric Materials*, vol. 1, pp. 133-136, 2003.
- [13] (10/02/2013) R. Arora and W. Mosch, *High Voltage and Electrical Insulation Engineering*, 2011. Available: <http://ieeexplore.ieee.org/xpl/bkabstractplus.jsp?bkn=6047607>
- [14] Suwarno, "Phase-Resolved Properties and Simulation of Partial Discharges in High Voltage Liquid Insulation," *Asia-Pacific Power and Energy Engineering Conference, APPEEC*, pp. 1-4, 2012.
- [15] X. Yi and Z. Wang, "Creepage discharge on pressboards in synthetic and natural ester transformer liquids under ac stress," *IET Electric Power Applications*, vol. 7, 2013.
- [16] M. Hikita, M. Kozako, H. Takada, T. Hirose, M. Higashiyama, S. Nakamura, and T. Umemura, "Partial discharge phenomena in artificial cavity in epoxy cast resin insulation system," *Conference Record of the IEEE International Symposium on Electrical Insulation, ISEI*, pp. 1-5, 2010.
- [17] H. A. Illias, G. Chen, and P. L. Lewin, "Partial discharge measurements for spherical cavities within solid dielectric materials under different stress and cavity conditions," *IEEE Conference on Electrical Insulation and Dielectric Phenomena, CEIDP*, pp. 388-391, 2009.
- [18] A. R. Nosseir, "Calculation of Discharge Inception Voltage Due to the Presence of Voids in Power Cables," *IEEE Transactions on Electrical Insulation*, vol. EI-14, pp. 117-120, 1979.
- [19] D. Adhikari, D. M. Hepburn, and B. G. Stewart, "Characterisation of PD occurring in injected air bubbles in block polymeric insulation," *Annual Report Conference on Electrical Insulation and Dielectric Phenomena, CEIDP*, pp. 48-51, 2012.
- [20] F. H. Kreuger, *Partial discharge detection in high voltage equipment*: Butterworth & Co. Ltd, 1989.
- [21] The British Standards Institution, "Condition monitoring and diagnostics of machines - General guidelines," *BS ISO 17359:2011*, British Standard Committees, 2011.

- [22] CIGRE, "Guidelines for Unconventional Partial Discharge Measurements," *WG D1.33*, 2010.
- [23] S. M. Tetrault, G. C. Stone, and H. G. Sedding, "Monitoring partial discharges on 4-kV motor windings," *IEEE Transactions on Industry Applications*, vol. 35, pp. 682-688, 1999.
- [24] G. C. Stone and J. Kapler, "Condition-based maintenance for the electrical windings of large motors and generators," *Annual Pulp and Paper Industry Technical Conference*, pp. 57-63, 1997.
- [25] (12/02/2010). Available: <http://www.remcom.com/xf7-fdtd-method/>
- [26] The British Standards Institution, "High voltage test techniques - Measurement of partial discharges by electromagnetic and acoustic methods," *Draft BS EN 62478*, British Standard Committees, 2012.
- [27] J. Fuhr, "Condition assessment of power transformers," *International Conference on Condition Monitoring and Diagnosis, CMD*, pp. 9-17, 2012.
- [28] "IEEE Guide for the Interpretation of Gases Generated in Oil-Immersed Transformers," *IEEE Std C57.104-2008 (Revision of IEEE Std C57.104-1991)*, pp. C1-27, 2009.
- [29] The British Standards Institution, "Mineral oil-impregnated electrical equipment in service - Guide to the interpretation of dissolved and free gases analysis," *IEC 60599:1999*, British Standard Committees, 1999.
- [30] M. Duval, "A review of faults detectable by gas-in-oil analysis in transformers," *IEEE Electrical Insulation Magazine*, vol. 18, pp. 8-17, 2002.
- [31] (23/03/2013) E. F. Forney, *KCP&L Brings DGA Testing In-house*, May 2005. Available: <http://business.highbeam.com/137793/article-1G1-132474284/kansas-city-power-amp-light-brings-dga-testing-house>
- [32] C. E. Housecroft and E. C. Constable, *An Introduction to Organic, Inorganic and Physical Chemistry*, 4th ed., Prentice Hall, UK, 2010.
- [33] S. Tominaga, H. Kuwahara, and K. Hirooka, "Influence of Arc-Decomposed SF₆ Gas on Cast EPOXY Insulators for Gas Insulated Switchgears," *IEEE Transactions on Power Apparatus and Systems*, vol. PAS-98, pp. 2107-2114, 1979.
- [34] R. J. Van Brunt and J. T. Herron, "Fundamental processes of SF₆ decomposition and oxidation in glow and corona discharges," *IEEE Transactions on Electrical Insulation*, vol. 25, pp. 75-94, 1990.

- [35] The British Standards Institution, "High-voltage switchgear and controlgear – Part 303: Use and handling of sulphur hexafluoride (SF₆)," *PD CLC/TR 62271-303:2009*, British Standard Committees, 2009.
- [36] L. G. Christophorou, I. Sauers, D. R. James, H. Rodrigo, M. O. Pace, J. G. Carter, and S. R. Hunter, "Recent Advances in Gaseous Dielectrics at Oak Ridge National Laboratory," *IEEE Transactions on Electrical Insulation*, vol. EI-19, pp. 550-566, 1984.
- [37] J. P. Manion, J. A. Philosophos, and M. B. Robinson, "Arc Stability of Electronegative Gases," *IEEE Transactions on Electrical Insulation*, vol. EI-2, pp. 1-10, 1967.
- [38] I. Sauers, H. W. Ellis, and L. G. Christophorou, "Neutral Decomposition Products in Spark Breakdown of SF₆," *IEEE Transactions on Electrical Insulation*, vol. EI-21, pp. 111-120, 1986.
- [39] T. Ju, L. Fan, Z. Xiaoxing, M. Qinghong, and Z. Jiabin, "Partial discharge recognition through an analysis of SF₆ decomposition products part 1: decomposition characteristics of SF₆ under four different partial discharges," *IEEE Transactions on Dielectrics and Electrical Insulation*, vol. 19, pp. 29-36, 2012.
- [40] The British Standards Institution, "Guidelines for the checking and treatment of sulphur hexafluoride (SF₆) taken from electrical equipment and specification for its re-use," *BS EN 60480:2004*, British Standard Committees, 2004.
- [41] S. Tominaga, H. Kuwahara, K. Hirooka, and T. Yoshioka, "SF₆ Gas Analysis Technique and its Application for Evaluation of Internal Conditions in SF₆ Gas Equipment," *IEEE Transactions on Power Apparatus and Systems*, vol. PAS-100, pp. 4196-4206, 1981.
- [42] J. M. Braun and F. Y. Chu, "Novel Low-Cost SF₆ Arcing Byproduct Detectors for Field Use in Gas-Insulated Switchgear," *IEEE Transactions on Power Delivery*, vol. 1, pp. 81-86, 1986.
- [43] Qi Bo, Li Cheng-rong, Wu Zhang-jian, Zhang Yong, and Zheng Shu-sheng, "Experimental study on the relationship between partial discharge and gas decomposition products in SF₆ insulated electrical equipments," *IEEE Conference on Electrical Insulation and Dielectric Phenomena, CEIDP*, pp. 392-395, 2009.
- [44] S. Okabe, S. Kaneko, T. Minagawa, and C. Nishida, "Detecting characteristics of SF₆ decomposed gas sensor for insulation diagnosis on gas insulated switchgears," *IEEE Transactions on Dielectrics and Electrical Insulation*, vol. 15, pp. 251-258, 2008.

- [45] T. Minagawa, M. Kawada, S. Yamauchi, M. Kamei, and C. Nishida, "Development of SF₆ decomposition gas sensor," *Surface and Coatings Technology*, vol. 169–170, pp. 643-645, 2003.
- [46] X. Hu, Y. Li, and Y. Lu, "Study of PD detection and location by means of acoustic measurements transformer," *Proceedings of the 6th International Conference on Properties and Applications of Dielectric Materials*, vol. 2, pp. 753-756, 2000.
- [47] L. E. Lundgaard, "Partial discharge. XIII. Acoustic partial discharge detection-fundamental considerations," *IEEE Electrical Insulation Magazine*, vol. 8, pp. 25-31, 1992.
- [48] R. Meunier and G. H. Vaillancourt, "Propagation behaviour of acoustic partial discharge signals in oil-filled transformers," *12th International Conference on Conduction and Breakdown in Dielectric Liquids, ICDL*, pp. 401-404, 1996.
- [49] C. Su-Yeon, P. Dae-Won, K. Il-Kwon, P. Chan-Yong, and K. Gyung-Suk, "Analysis of acoustic signals generated by partial discharges in insulation oil," *International Conference on Condition Monitoring and Diagnosis, CMD*, pp. 525-528, 2008.
- [50] P. Kundu, N. K. Kishore, and A. K. Sinha, "Frequency domain analysis of acoustic emission signals for classification of partial discharges," *Annual Report - Conference on Electrical Insulation and Dielectric Phenomena, CEIDP*, pp. 146-149, 2007.
- [51] H. N. Nagamani, T. B. Shanker, V. Vaidhyanathan, and S. Neelakantan, "Acoustic emission technique for detection and location of simulated defects in power transformers," *IEEE Power Tech, Russia*, pp. 1-7, 2005.
- [52] R. Menon, S. Kolambekar, N. J. Buch, and M. Ramamoorthy, "Correlation of acoustic emission method and electrical method for detection of partial discharges in transformers," *Proceedings of the IEEE 7th International Conference on Solid Dielectrics, ICSD*, pp. 299-302, 2001.
- [53] K. Sung-Hong, C. Jae-Kwan, Y. Hun-Ju, P. Jae-Jun, and K. Jae-Hwan, "A composite system for simultaneous detection of electrical charge and acoustic emission pulse of partial discharge," *Proceedings of the 5th International Conference on Properties and Applications of Dielectric Materials*, vol. 2, pp. 817-820, 1997.
- [54] B. R. Varlow, D. W. Auckland, C. D. Smith, and J. Zhao, "Acoustic emission analysis of high voltage insulation," *IEEE Proceedings Science, Measurement and Technology*, vol. 146, pp. 260-263, 1999.

- [55] T. R. Blackburn, R. E. James, Q. Su, T. Phung, R. Tychsen, and J. Simpson, "An improved electric/acoustic method for the location of partial discharges in power transformers," *Proceedings of the 3rd International Conference on Properties and Applications of Dielectric Materials*, vol. 2, pp. 1132-1135, 1991.
- [56] "IEEE Trial-Use Guide for the Detection of Acoustic Emissions From Partial Discharges in Oil-Immersed Power Transformers," *IEEE Std C57.127-2000*, 2000.
- [57] F. Ahmed, A. B. Darus, Z. Yusoff, and M. E. Haque, "Characterisation of acoustic signal and pattern recognition of free moving metallic particle motion modes in GIS," *Proceedings of International Conference on Information, Communications and Signal Processing, ICICS*, vol. 2, pp. 750-753, 1997.
- [58] L. E. Lundgaard, "Partial discharge. XIV. Acoustic partial discharge detection-practical application," *IEEE Electrical Insulation Magazine*, vol. 8, pp. 34-43, 1992.
- [59] D. Evagorou, A. Kyprianou, A. Stavrou, V. Efthymiou, P. L. Lewin, and G. E. Georghiou, "Setup and preliminary results of a pilot on-line cable PD monitoring system on an 11 kV switchboard using capacitive couplers," *7th Mediterranean Conference and Exhibition on Power Generation, Transmission, Distribution and Energy Conversion, MedPower*, pp. 1-4, 2010.
- [60] Y. Tian, P. L. Lewin, A. E. Davies, S. J. Sutton, and S. G. Swingler, "Partial discharge detection in cables using VHF capacitive couplers," *IEEE Transactions on Dielectrics and Electrical Insulation*, vol. 10, pp. 343-353, 2003.
- [61] N. H. Ahmed and N. N. Srinivas, "On-line partial discharge detection in cables," *IEEE Transactions on Dielectrics and Electrical Insulation*, vol. 5, pp. 181-188, 1998.
- [62] "IEEE Guide for Partial Discharge Testing of Shielded Power Cable Systems in a Field Environment," *IEEE Std 400.3-2006*, pp. c1-36, 2007.
- [63] F. Wester, E. Gulski, J. Smit, and E. Groot, "Aspect of on-line and off-line PD diagnosis of distribution power cables," *Conference Record of the IEEE International Symposium on Electrical Insulation*, pp. 553-556, 2002.
- [64] E. C. T. de Macedo, J. M. R. de Souza Neto, J. Moises, M. Villanueva, E. C. Guedes, R. C. S. Freire, and I. A. Glover, "Partial discharge estimation based on radiometric and classical measurements," *IEEE International Instrumentation and Measurement Technology Conference, MTC*, pp. 807-811, 2012.
- [65] CIGRE, "On-line Monitoring of MV and HV Distribution Cables using VHF Partial Discharge Detection," *DI - 202*, 2008.

- [66] J. Zhu, L. Yang, J. Jia, and Q. Zhang, "The design of Rogowski coil with wide band using for partial discharge measurements," *Proceedings of International Symposium on Electrical Insulating Materials, ISEIM*, vol. 2, pp. 518-521, 2005.
- [67] IEEE Power Engineering Society, "Practical Aspects of Rogowski Coil Applications to Relaying," *IEEE PSRC Special Report*, 2010.
- [68] P. Brown, "Nonintrusive partial discharge measurements on high voltage switchgear," *IEEE Colloquium on Monitors and Condition Assessment Equipment (Digest No. 1996/186)*, pp. 10/1-10/5, 1996.
- [69] H. Tao, D. Boxue, G. Yu, and X. Yansong, "Partial discharge pattern recognition based on Transient Earth Voltage for 10 kV switchgear in smart grid," *IEEE Innovative Smart Grid Technologies - Asia, ISGT Asia*, pp. 1-4, 2012.
- [70] A. J. Reid, M. D. Judd, and G. Duncan, "Simultaneous measurement of partial discharge using TEV, IEC60270 and UHF techniques," *Conference Record of the IEEE International Symposium on Electrical Insulation, ISEI*, pp. 439-442, 2012.
- [71] K. Raja, F. Devaux, and S. Lelaidier, "Some Fundamental Observations during UHF Partial Discharge Measurement in Transformers," *CIGRE Transformer Colloquium*, Mexico, 2003.
- [72] D. Allan, T. Blackburn, and E. Gulski, "Service Aged Insulation: Guidelines on Managing the Ageing Process," *CIGRE Working Group D1.11*, 2003.
- [73] M. D. Judd, Y. Li, and I. B. B. Hunter, "Partial discharge monitoring of power transformers using UHF sensors. Part I: sensors and signal interpretation," *IEEE Electrical Insulation Magazine*, vol. 21, pp. 5-14, 2005.
- [74] R. Sarathi, A. J. Reid, and M. D. Judd, "Partial discharge study in transformer oil due to particle movement under DC voltage using the UHF technique," *Electric Power Systems Research*, vol. 78, pp. 1819-1825, 2008.
- [75] B. F. Hampton and R. J. Meats, "Diagnostic measurements at UHF in gas insulated substations," *IEEE Proceedings on Generation, Transmission and Distribution*, vol. 135, pp. 137-145, 1988.
- [76] J. S. Pearson, O. Farish, B. F. Hampton, M. D. Judd, D. Templeton, B. W. Pryor, and I. M. Welch, "Partial discharge diagnostics for gas insulated substations," *IEEE Transactions on Dielectrics and Electrical Insulation*, vol. 2, pp. 893-905, 1995.
- [77] M. Hikita, S. Ohtsuka, J. Wada, S. Okabe, T. Hoshino, and S. Maruyama, "Study of partial discharge radiated electromagnetic wave propagation characteristics in

- an actual 154 kV model GIS," *IEEE Transactions on Dielectrics and Electrical Insulation*, vol. 19, pp. 8-17, 2012.
- [78] W. Gao, D. Ding, and W. Liu, "Research on the Typical Partial Discharge using the UHF Detection Method for GIS," *IEEE Transactions on Power Delivery*, vol. 26, pp. 2621-2629, 2011.
- [79] R. Kurrer and K. Feser, "The application of ultra-high-frequency partial discharge measurements to gas-insulated substations," *IEEE Transactions on Power Delivery*, vol. 13, pp. 777-782, 1998.
- [80] M. D. Judd, O. Farish, and B. F. Hampton, "Broadband couplers for UHF detection of partial discharge in gas-insulated substations," *IEE Proceedings on Science, Measurement and Technology*, vol. 142, pp. 237-243, 1995.
- [81] F. Endo, S. Matsumoto, H. Hama, and S. Hironaka, "Innovation of GIS Insulation Monitoring Techniques and Application to Remote Monitoring System," *CIGRE*, Paris, 2002.
- [82] J. B. Kim, J. R. Jung, M. S. Kim, Y. J. Choi, W. P. Song, and H. S. Lee, "Experience of the On-line Intelligent Partial Discharge Monitoring (IPDM) System for GIS using UHF Method," *CIGRE*, Paris, 2006.
- [83] C. G. Azcarraga and V. R. Garcia-Colon, "Experiences on GIS On-Site Evaluation Using High Sensitivity PD Techniques," *Large Engineering Systems Conference on Power Engineering*, pp. 182-186, 2007.
- [84] A. Troeger, U. Riechert, S. Burow, and S. Tenbohlen, "Sensitivity Evaluation of Different Types of PD Sensors for UHF-PD-Measurements," *International Conference on Condition Monitoring and Diagnosis, CMD*, 2010.
- [85] S. Zhang, X. Zheng, J. Zhang, H. Cao, and X. Zhang, "Study of GIS partial discharge on-line monitoring using UHF method," *International Conference on Electrical and Control Engineering*, pp. 4262-4265, 2010.
- [86] J. Tang, Z. Xu, X. Zhang, and C. Sun, "GIS partial discharge quantitative measurements using UHF microstrip antenna sensors," *Annual Report - Conference on Electrical Insulation and Dielectric Phenomena, CEIDP*, pp. 116-119, 2007.
- [87] S. Kaneko, S. Okabe, M. Yoshimura, H. Muto, C. Nishida, and M. Kamei, "Detecting characteristics of various type antennas on partial discharge electromagnetic wave radiating through insulating spacer in gas insulated switchgear," *IEEE Transactions on Dielectrics and Electrical Insulation*, vol. 16, pp. 1462-1472, 2009.

- [88] M. D. Judd, O. Farish, J. S. Pearson, and B. F. Hampton, "Dielectric windows for UHF partial discharge detection," *IEEE Transactions on Dielectrics and Electrical Insulation*, , vol. 8, pp. 953-958, 2001.
- [89] A. Girodet, S. Meijer, and J. J. Smit, "Development of a Partial Discharge Analysis Method to assess the Dielectric Quality of GIS," *CIGRE*, Paris, 2002.
- [90] J. Y. Koo, S. Y. Jung, C. H. Ryu, S. W. Lee, and B. W. Lee, "Identification of insulation defects in gas-insulated switchgear by chaotic analysis of partial discharge," *IET Science, Measurement & Technology*, vol. 4, pp. 115-124, 2010.
- [91] M. Wang, A. J. Vandermaar, and K. D. Srivastava, "Review of condition assessment of power transformers in service," *IEEE Electrical Insulation Magazine*, vol. 18, pp. 12-25, 2002.
- [92] WG 12.05, "An international survey on failures in large power transformers in service," *CIGRE*, Paris, 1983.
- [93] G. P. Cleary and M. D. Judd, "An Investigation of Discharges in Oil Insulation using UHF PD Detection," *Proceedings of 14th International Conference on Dielectric Liquids, ICDL*, pp. 341-344, 2002.
- [94] M. D. Judd, "Experience with UHF partial discharge detection and location in power transformers," *Electrical Insulation Conference, EIC*, pp. 201-205, 2011.
- [95] S. Meijer, P. D. Agoris, J. J. Smit, M. D. Judd, and L. Yang, "Application of UHF Diagnostics to detect PD during Power Transformer Acceptance Tests," *Conference Record of the IEEE International Symposium on Electrical Insulation*, pp. 416-419, 2006.
- [96] M. D. Judd, Y. Li, and I. B. B. Hunter, "Partial Discharge Monitoring for Power Transformers using UHF Sensors. Part 2: Field Experience," *IEEE Transactions on Dielectrics and Electrical Insulation*, vol. 21, pp. 5-13, 2005.
- [97] L. H. Truong, D. J. Swaffield, P. L. Lewin, and M. D. Judd, "The feasibility of using UHF sensors to measure partial discharges in liquid nitrogen," *IEEE International Conference on Dielectric Liquids, ICDL*, pp. 1-4, 2011.
- [98] S. P. Mehta, N. Aversa, and M. S. Walker, "Transforming transformers (superconducting windings)," *IEEE Spectrum*, vol. 34, pp. 43-49, 1997.
- [99] A. Denat, F. Jomni, F. Aitken, and N. Bonifaci, "Thermally and electrically induced bubbles in liquid argon and nitrogen," *IEEE Transactions on Dielectrics and Electrical Insulation*, vol. 9, pp. 17-22, 2002.

- [100] M. Marci and I. Kolcunova, "Electric breakdown strength measurement in liquid dielectrics," *9th International Conference on Environment and Electrical Engineering, IEEEIC*, pp. 427-430, 2010.
- [101] H. H. Sinaga, B. T. Phung, and T. R. Blackburn, "Partial Discharge Localization in Transformers using Monopole and Log-Spiral UHF Sensors," *IEEE 10th International Conference on the Properties and Applications of Dielectric Materials, ICPADM*, 2012.
- [102] L. Mingjun and L. Zhaohui, "An Online UHF PD Monitoring System for Power Transformer and Its Applications," *Asia-Pacific Power and Energy Engineering Conference, APPEEC*, pp. 1-4, 2010.
- [103] S. Tenbohlen, S. M. Hoek, D. Denissov, R. Huber, U. Riechert, S. M. Markalous, T. Strehl, and T. Klein, "Electromagnetic (UHF) PD Diagnosis of GIS, Cable Accessories and Oil-paper Insulated Power Transformers for Improved PD Detection and Localization," *CIGRE*, Paris, 2006.
- [104] A. Pfeffer, S. Coenen, S. Tenbohlen, T. Strehl, and S. Markalous, "Onsite experiences with multi-terminal IEC PD measurements and UHF PD measurements," *International Symposium on High Voltage Engineering*, Cape Town, South Africa, 2009.
- [105] S. Meijer, M. D. Judd, and S. Tenbohlen, "Sensitivity check for radio frequency partial discharge detection for power transformers," *International Conference on Condition Monitoring and Diagnosis, CMD*, pp. 1031-1035, 2008.
- [106] S. Meijer, E. Gulski, J. J. Smit, and H. F. Reijnders, "Sensitivity check for UHF PD detection on power transformers," *Conference Record of the IEEE International Symposium on Electrical Insulation*, pp. 58-61, 2004.
- [107] CIGRE, "Partial Discharge Detection System for GIS: Sensitivity Verification for the UHF Method and the Acoustic Method," *TF 15/33.03.05*, 1999.
- [108] S. Maruyama, T. Hoshino, T. Sakakibara, and N. Kurokawa, "Sensitivity Verification of UHF PD Coupler for 400 kV GIS," *International Conference on Electrical Engineering, ICEE*, pp. 1-4, 2008.
- [109] S. Meijer, E. Gulski, J. J. Smit, and H. F. Reijnders, "Sensitivity check for UHF PD detection on power transformers," *Conference Record of the IEEE International Symposium on Electrical Insulation, ISEI*, pp. 58-61, 2004.
- [110] S. Neuhold, T. Heizmann, R. Braunlich, D. Kochli, U. Riechert, and C. Dehne, "Experiences with UHF PD detection in GIS using external capacitive sensors on windows and disk-insulator," *International Symposium on High Voltage Engineering*, Slovenia, 2007.

- [111] R. Kurrer, K. Feser, and T. Krauß, "Antenna Theory of Flat Sensors for Partial Discharge Detection at Ultra-High-Frequency in GIS," *International Symposium on High Voltage Engineering*, Austria, 1995.
- [112] D. Gautschi and P. Bertholet, "Calibration of UHF sensors for GIS: Comparison of different methods and testing of a calibration system based on a conical antenna," *International Conference on High Voltage Engineering and Application ICHVE*, pp. 28-31, 2010.
- [113] M. D. Judd, O. Farish, and J. S. Pearson, "UHF couplers for gas-insulated substations: a calibration technique," *IEEE Proceedings on Science, Measurement and Technology*, vol. 144, pp. 117-122, 1997.
- [114] F. T. Ulaby, *Electromagnetics for Engineers*, Pearson International Edition, 2005.
- [115] C. Harrison, Jr., "The radian effective half-length of cylindrical antennas less than 1.3 wavelengths long," *IEEE Transactions on Antennas and Propagation*, vol. 11, pp. 657-660, 1963.
- [116] M. D. Judd, "Transient calibration of electric field sensors," *IEEE Proceedings on Science, Measurement and Technology*, vol. 146, pp. 113-116, 1999.
- [117] The National Grid Company plc, "Capacitive Couplers for UHF Partial Discharge Monitoring," *Technical Guidance Note: TGN (T) 121*, issue 1, 1997.
- [118] R. Mishra, H. Muthukrishnan, A. Ramanan, and R. Sarathi, "Understanding partial discharge activity in GIS due to particle movement under high frequency AC voltage adopting UHF technique," *6th IEEE International Conference on Industrial and Information Systems, ICIIIS*, pp. 93-97, 2011.
- [119] M. D. Judd, O. Farish, and B. F. Hampton, "The excitation of UHF signals by partial discharges in GIS," *IEEE Transactions on Dielectrics and Electrical Insulation*, vol. 3, pp. 213-228, 1996.
- [120] R. Sarathi and M. Archana, "Investigation of partial discharge activity by a conducting particle in transformer oil under harmonic AC voltages adopting UHF technique," *IEEE Transactions on Dielectrics and Electrical Insulation*, vol. 19, pp. 1514-1520, 2012.
- [121] M. D. Judd and O. Farish, "A pulsed GTEM system for UHF sensor calibration," *IEEE Transactions on Instrumentation and Measurement*, vol. 47, pp. 875-880, 1998.
- [122] J. P. Bentley, *Principles of Measurement Systems*, 4th ed., Pearson Education Limited, 2005.

- [123] M. D. Judd, "The excitation of UHF signals by partial discharge in gas insulated substations," PhD, Electronic and Electrical Engineering, University of Strathclyde, Glasgow, 1996.
- [124] A. Taflove, *Advances in Computational Electrodynamics: The Finite-Difference Time-Domain Method*, Artech House, USA, 1998.
- [125] Y. Kane, "Numerical solution of initial boundary value problems involving maxwell's equations in isotropic media," *IEEE Transactions on Antennas and Propagation*, vol. 14, pp. 302-307, 1966.
- [126] P. P. Silvester and R. L. Ferrari, *Finite Elements for Electrical Engineers*, 3rd ed., Cambridge University Press, UK, 1996.
- [127] D. M. Sullivan, *Electromagnetic Simulation Using the FDTD Method*, IEEE Press Series on RF and Microwave Technology, New York, 2000.
- [128] A. Taflove, *Computational Electromagnetics: The Finite-Difference Time-Domain Method*, Artech House, 1995.
- [129] M. D. Judd, "Using finite difference time domain techniques to model electrical discharge phenomena," *Annual Report Conference on Electrical Insulation and Dielectric Phenomena*, vol. 2, pp. 518-521, 2000.
- [130] A. Bojovschi, W. S. T. Rowe, and K. L. Wong, "Electromagnetic field intensity generated by partial discharge in high voltage insulating materials," *Progress In Electromagnetics Research, PIER*, vol. 104, pp. 167-182, 2010.
- [131] T. Hoshino, S. Maruyama, and T. Sakakibara, "Simulation of Propagating Electromagnetic Wave Due to Partial Discharge in GIS Using FDTD," *IEEE Transactions on Power Delivery*, vol. 24, pp. 153-159, 2009.
- [132] A. Tacchini, D. Grossi, L. Vincetti, M. Maini, S. Serra, M. Fattori, and L. Sandrolini, "Electromagnetic analysis of PD detection in GIS systems," *Asia-Pacific Symposium on Electromagnetic Compatibility, APEMC*, pp. 889-892, 2012.
- [133] REMCOM, *XFDTD Full-wave 3D Electromagnetic Analysis Software, Reference Manual*, version 7.0 ed., Remcom Inc., 2009.
- [134] R. L. Boylestad, *Introductory Circuit Analysis*, 12th ed., Pearson Education Limited, 2010.
- [135] H. Zainuddin, P. L. Lewin, and P. M. Mitchinson, "Characteristics of leakage current during surface discharge at the oil-pressboard interface," *Annual Report*

- Conference on Electrical Insulation and Dielectric Phenomena, CEIDP*, pp. 483-486, 2012.
- [136] A. Abubakar Mas'ud, B. G. Stewart, S. G. McMeekin, and A. Nesbitt, "Partial discharge pattern classification for an oil-pressboard interface," *Conference Record of the IEEE International Symposium on Electrical Insulation, ISEI*, pp. 122-126, 2012.
- [137] (11/03/2013) TIBTECH, *Properties table of stainless steel, metals and other conductive materials*, 2011. Available: <http://www.tibtech.com/conductivity.php>
- [138] R. E. Bolz and G. L. Tuve, *CRC Handbook of Tables for Applied Engineering Science*, 2nd ed., CRC Press, 1973.
- [139] P. Kakeeto, M. Judd, J. Pearson, and D. Templeton, "Experimental investigation of positional accuracy for UHF partial discharge location," *International Conference on Condition Monitoring and Diagnosis, CMD*, pp. 1070-1073, 2008.
- [140] L. Yang and M. D. Judd, "Propagation characteristics of UHF signals in transformers for locating partial discharge sources," *International Symposium on High Voltage Engineering*, Netherlands, 2003.
- [141] G. W. C. Kaye and T. H. Laby, *Tables of physical and chemical constants*, Longman, 1995.
- [142] J. Watkins, "Circular resonant structures in microstrip," *Electronics Letters*, vol. 5, pp. 524-525, 1969.